Lattice Boltzmann method for contact line dynamics

Sudhir Srivastava

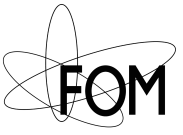

This work is part of the Industrial Partnership Program (IPP) "Contact Line Control during Wetting and Dewetting" (CLC) of the Foundation for Fundamental Research on Matter (FOM), which is part of the Netherlands Organization for Scientific Research (NWO). The CLC IPP is co-financed by ASML and Océ.

Eindhoven University of Technology
Department of Applied Physics
Turbulence and Vortex Dynamics Group
PO Box 513
5600 MB Eindhoven
www.fluid.tue.nl

Printed by Uitgeverij BOXPress, 's-Hertogenbosh, The Netherlands

A catalogue record is available from the Eindhoven University of Technology Library
ISBN: 978-90-386-3608-5

Lattice Boltzmann method for contact line dynamics

PROEFSCHRIFT

ter verkrijging van de graad van doctor aan de Technische Universiteit Eindhoven, op gezag van de rector magnificus prof.dr.ir. C.J. van Duijn, voor een commissie aangewezen door het College voor Promoties, in het openbaar te verdedigen op woensdag 7 mei 2014 om 16:00 uur

door

Sudhir Srivastava

geboren te Bahraich, India

Dit proefschrift is goedgekeurd door de promotoren en de samenstelling van de promotiecommissie is als volgt:

voorzitter:	prof.dr.ir. G.M.W. Kroesen
1e promotor:	prof.dr. F. Toschi
2e promotor:	prof.dr. H.J.H. Clercx
copromotor(en):	dr.ir. J.H.M. ten Thije Boonkkamp
leden:	prof.dr.ir. B. Koren
	prof.dr. D. Lohse (UT)
	prof. L. Biferale (University of Rome "Tor Vergata")
	dr.ir. J.D.R. Harting
adviseur(s):	dr. H.M.A. Wijshoff (Océ Technologies B.V.)

Contents

Nomenclature

Acronyms

1D	one-dimensional
2D	two-dimensional
3D	three-dimensional
BE	Boltzmann equation
BGK	Bhatnagar-Gross-Krook
CIJ	continuous inkjet
DOD	drop-on-demand
FB	force balance
GL	generalized lubrication
HS	Huh and Scriven
LB	lattice Boltzmann
LGCA	lattice gas cellular automata
LLD	Landau-Levich-Derjaguin
LT	lubrication theory
LU	lattice unit
MC	multi-component Shan-Chen
MP	multi-phase Shan-Chen
NS	Navier-Stokes
PIJ	piezoelectric inkjet
RP	Rayleigh-Plateau
SC	Shan-Chen
SI	système international
SJ	slender jet

Characteristic scales

h_{film}	Derjaguin film thickness [m]
h_{LLD}	Landau-Levich-Derjaguin film thickness [m]
ℓ_{c}	capillary length [m]
λ_{s}	slip length [m]

t_{cap}	capillary time [s]
U_{p}	plate velocity [m/s]

Dimensionless numbers

Ca	capillary number
Ca_{c}	critical capillary number
Kn	Knudsen number
Ma	Mach number
Oh	Ohnesorge number
Re	Reynolds number
R_μ	ratio of dynamic viscosities
R_ρ	ratio of densities
We	Weber number
Wo	Womersley number

Operators

$\lvert . \rvert$	absolute value of a real number
$\boldsymbol{\nabla}$	gradient operator with respect to position [1/m]
$\boldsymbol{\nabla}^2$	Laplace operator [1/m^2]
$\boldsymbol{\nabla}_{\mathrm{v}}$	gradient operator with respect to velocity [s/m]
$\lVert . \rVert$	Euclidian norm of a vector
D/Dt	material derivative [1/s]

Subscripts and superscripts

ℓ	liquid
n	normal component
r	radial component
T	transpose of the matrix
t	tangential component (superscript)
t	time (subscript)
z	axial component
eq	equilibrium
g	gas
v	vapor

Scalar variables

c_s	speed of sound [m/s]
Δ	distance between contact line and level of bath [m]
g	gravity [m/s^2]
G_{sc}	interaction strength in SC model [m^3/s/kg]
κ	mean curvature [1/m]

μ	dynamic viscosity [kg/m/s]
ν	kinematic viscosity [m^2/s]
p	pressure [N/m^2]
ψ	pseudo-density function [kg/m^3]
ρ	fluid density [kg/m^3]
γ	surface tension [N/m]
θ	angle [°]
θ_0	microscopic contact angle [°]
θ_e	equilibrium contact angle [°]
θ_w	wedge angle [°]
ζ	second/bulk viscosity [kg/m/s]
m_p	mass of single particle [kg]
T	temperature [K]
t	time [s]

Tensors

$\mathbf{T}$	deviatoric stress tensor
$\mathbf{I}$	identity matrix
$\mathbf{P}$	pressure tensor
$\boldsymbol{\sigma}$	stress tensor
$\mathbf{uu}$	dyadic vector product
$\mathbf{E}$	strain rate tensor
$\mathbf{\Pi}$	momentum flux tensor

Vector variables

$\mathbf{c}_i$	lattice velocity vector along i-direction [m/s]
$\mathbf{F}$	volumetric force [N/m^3]
$\mathbf{F}_{sc}$	Shan-Chen force [N/m^3]
$\mathbf{K}$	force [N]
$\hat{\mathbf{n}}$	unit normal vector [-]
$\hat{\mathbf{t}}$	unit tengential vector [-]
$\mathbf{u}$	fluid velocity [m/s]
$\mathbf{v}$	particle velocity [m/s]
$\mathbf{x}$	position vector [m]

1 | Introduction

Moving contact lines are ubiquitous in nature, drops sliding on surfaces are common examples that we encounter daily in our life. A contact line in fluid dynamics is usually referred to as the common border between a liquid, solid and the surrounding air/vapor. Recent advances in micro-fluidics posed a large demand on the technology and fundamental understanding of the forces and flow conditions that control the dynamics of the contact line.

This thesis involves aspects related to the physics of contact lines, to their analytical and numerical modelling and to their inspiring industrial geometries. The motivating industrial applications are immersion lithography (ASML) and the printhead of an inkjet nozzle (Océ). Both these problems involve several characteristic length- and time-scales, highly curved fluid interfaces, multiphase flows and complex boundary conditions, thus challenging analytical and numerical studies.

1.1 Moving contact lines

1.1.1 Immersion lithography

Photolithography is a complex procedure, which allows to transfer a pattern from a mask onto a silicon wafer with sub-micron accuracy [1]. One of the key steps in the photolithography process is exposing a photoresist coated on the silicon wafer with deep-ultraviolet (DUV) light using a high resolution optical system. The smallest feature or the critical dimension, CD, that can be masked onto the wafer using the optical system is determined the Rayleigh criterion:

$$CD = k\frac{\lambda}{NA}, \tag{1.1}$$

where NA denotes the numerical aperture of the optical system, λ is the wavelength of light used and k is a process-dependent constant. In optics, the numerical aperture, $NA = n\sin\alpha$, of an optical system is a dimensionless number that characterizes the range of angles over which the system can accept

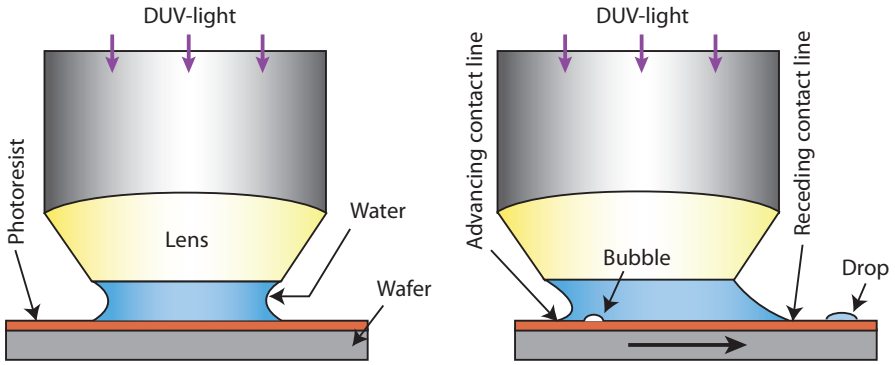

Figure 1.1: Left panel: A schematic of the immersion lithography setup for a static wafer plate. Right panel: A schematic showing the immersion lithography setup for a moving wafer. Above a certain velocity of the wafer the advancing contact line can entrain an air film and the receding contact line can drag a liquid film, which eventually breaks into air bubbles or liquid drops.

or emit light, where α is the angle of acceptance of the lens ($0 < \alpha < \pi/2$) and n is the refractive index of the medium between the lens and the photoresist. Any decrease in the value of CD leads to smaller and faster electronic devices.

According to the Rayleigh criterion given by Eq. (1.1), smaller values of CD can be obtained by decreasing k or λ or by increasing NA. For the current KrF and ArF excimer lasers, the wavelength of light can be decreased up-to 280 nm and 193 nm, respectively [1], while k is a process dependent constant that has been decreased up to 0.4 using resolution enhancement techniques [2]. The numerical aperture can be increased by increasing $\sin\alpha$ or n. Practical limit for $\sin\alpha$ is found to be 0.93, which is very close to the theoretical limit $|\sin\alpha| \leq 1$. Increasing n is the idea behind the use of immersion lithography.

Immersion lithography is a photolithography technique, in which the air gap between the lens and the photoresist is replaced by water, see Figure 1.1 (left panel). The water used in immersion lithography is highly purified deionized water with an index of refraction of 1.44 for 193 nm wavelength [3]. This value of the refractive index increases the resolution of resolvable feature sizes by a factor of approximately 30% [3]. This method is a less expensive way to achieve smaller feature sizes with the advantage of not having to take on big changes towards much more expensive lithography technologies [4].

Since the water is in direct contact with the photoresist on the wafer, the immersion lithography technology brings some challenges, mostly related to possible contamination of the lens and the photoresist. In particular, when the wafer plate moves with velocity U_{p}, relative to the lens, it also moves the

liquid-air-solid contact lines, see Figure 1.1 (right panel). Beyond a certain minimum speed, the advancing and the receding contact lines (see Figure 1.1, right panel) become unstable and may entrain air or drag a liquid film onto the wafer, respectively [5]. The air and the liquid film eventually break into air bubbles or liquid drops [6], negatively affecting the lithography process. In this thesis we contributed to the study of the stability of the advancing and receding contact lines at varying the velocity of the plate, the wetting properties of the wafer and the viscosity of the surrounding air.

1.1.2 Drop-on-demand inkjet printer

Modern inkjet printing technologies can be divided in two main types: continuous inkjet (CIJ) and drop-on-demand (DOD) inkjet. In a CIJ printer, a jet of liquid, coming out of the microscopic nozzle, breaks up into droplets due to the Rayleigh-Plateau (RP) instability. This RP instability is triggered by a piezoelectric crystal, which creates acoustic fluctuations capable to accurately control the stream of liquid and thus the breakup into droplets at regular intervals [7]. While the DOD inkjet printers can be further divided into two categories depending on the working principle [8]. We focus here only on piezoelectric inkjet (PIJ) printers.

In PIJ printers the drop-formation is caused by the pressure waves produced by a piezo element. A schematic of the printhead of a PIJ printer is shown in Figure 1.2. PIJ printers are relatively slow compared to CIJ printers, but have much higher print quality [7]. The quality of a printer is typically measured in dots per square inch (dpi), with modern applications requiring smaller droplets (higher dpi) and better accuracy. Among the many factors affecting the accuracy and size of the drops, the wettability of the nozzle, of the nozzle plate and the frequency of drop-formation, f_{DOD}, plays a crucial role [8]. For a good drop formation, the position of the contact line must be precisely controlled within the nozzle. In this thesis, we focus only on some aspects of the drop-formation in PIJ printer. Our study aims at the development of a numerical tool, thanks to which one can study the effect of nozzle wettability and of the DOD frequency on the drop formation process.

1.2 General framework and contribution of the author

From the modeling point of view, problems that involve contact line motion in immersion lithography and drop-formation in PIJ printers, fall into the

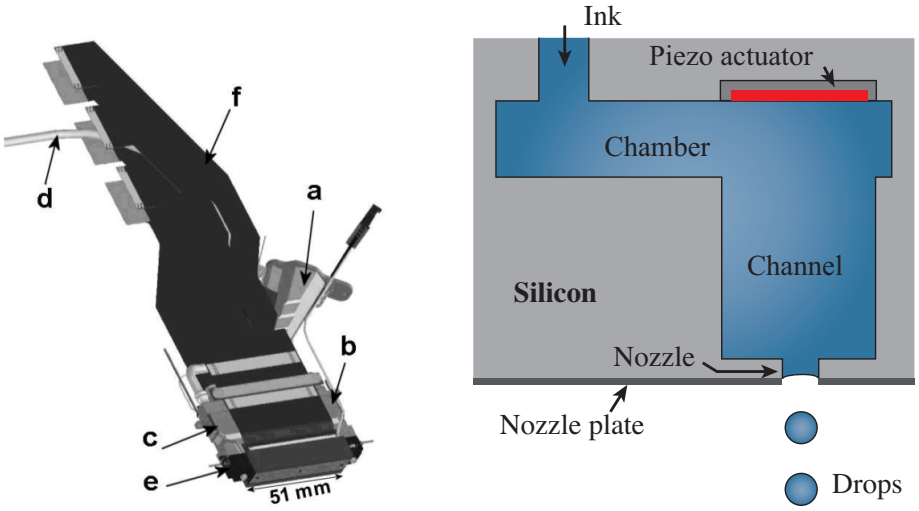

Figure 1.2: Left panel: 3D CAD drawing of a printhead prototype showing (a) the melting unit, (b) the filter units, (c) the reservoir, (d) the static pressure hose, (e) the central part, and (f) the electronic driving supply. Image retrieved from [8]. Right panel: A schematic showing a single nozzle uint in the central part (e) of the printhead shown in the left panel.

general category of the fluid mechanics of advancing and receding contact lines (section 2.3.2). For our study, we consider the contact lines and interfaces that are translational symmetric along one of the coordinate axis i.e. 2D or axisymmetric.

Our 2D numerical setup consists of a smooth plate, vertically immersed in a pool of liquid. The wettability of the plate is measured by the contact angle θ_e (section 2.3.1). We define a surface as being completely wet when $\theta_e = 0$, partially wet when $0 < \theta_e \leq \pi/2$, partially dry when $\pi/2 < \theta_e < \pi$ and completely dry when $\theta_e = \pi$. Depending on whether the plate is being pulled out or pushed into the fluid bath, we have dip-coating (receding contact line) or plunging plate (advancing contact line) problems, respectively. For the receding contact line problem the gas viscosity is irrelevant, on the other hand for the advancing contact line case the second phase must be considered, which makes the study of the problem much more complex.

We apply the lattice Boltzmann (LB) method to both problems, for different contact angles, viscosity ratio and velocities (capillary numbers). The different fluid phases and their contact with the plate are simulated by means of the Shan-Chen model [9, 10]. The LB simulations are validated using a generalized lubrication (GL) model describing the flow phenomena for differ-

ent viscosity ratios, contact angles and for small capillary numbers [11]. We found that for partially wet surfaces the agreement between LB and GL simulations is very good. This work cross-validates the LB and the GL model, and presents the LB method as an effective alternative for the study of contact lines in motion.

The second part of this thesis is devoted to the drop-formation in PIJ printers. For this study we only consider printheads with an axisymmetric nozzle exit, and we developed thus a LB method for axisymmetric multiphase flows. The model is an extension of the classic Shan-Chen multiphase model but restricted to axisymmetric flow problems. We benchmarked this new LB model for its accuracy in reproducing the dynamics of the oscillations of an axially symmetric droplet and on the capillary breakup of a viscous liquid thread. A very good quantitative agreement between the numerical solutions and the analytical results is observed. The method is further developed and used to simulate the drop-formation in the PIJ printer.

1.3 Outline of the thesis

Chapter 2 provides the theoretical background for the study of moving interfaces and contact lines. Here we briefly describe the concepts, definitions, laws and phenomena which are necessary for the understanding of the contact line motion and that are frequently used in the rest of this thesis. We also give a brief overview of the lubrication model and we discuss various characteristic regimes.

Chapter 3 provides an overview of the lattice Boltzmann method for multiphase flows. In this Chapter, we discuss the boundary conditions and force implementation schemes in the lattice Boltzmann method. Furthermore, we discuss the implications of two force incorporation schemes and their implications for multiphase flow simulations. We provide a numerical study of the Shan-Chen multiphase model, which helps us to point out some of the limitation of the model. We conclude this chapter with a short discussion on the spurious effects in the LB method.

We present the application of the LB method to dip-coating and to the plunging plate problems in Chapter 4. The Chapter is divided into two parts. In the first part we validate the boundary conditions and the LB model. In this part, we study the applicability and limitations of the Shan-Chen multiphase LB model for the study of the two problems. In the second part, we present the generalized lubrication (GL) model for the generic case of two fluids with arbitrary viscosity ratio and of a plate moving in either directions (pulled or

pushed in a bath) and compare the LB simulations and the GL results. The GL model shown here includes non-zero air viscosity, which is essential for the study of the plunging plate problem.

We present a novel axisymmetric lattice Boltzmann method for multiphase flow in Chapter 5. This method is capable of accurately modeling flows with variable density. The model presented here is an extension of the classic Shan-Chen multiphase model. We check the validity of the model numerically through several single- and multi-phase test cases, e.g., flow through a cylindrical pipe, dynamics of the oscillations of an axially symmetric droplet and the capillary breakup of a viscous liquid thread.

In Chapter 6, we present an application of the axisymmetric multiphase LB model to PIJ printing. The Chapter shows three important aspects of the LB model to study drop formation: first we show the constraints that must be respected while choosing the LB simulation parameters; second we present the validation for the time varying pressure boundary condition in the LB method; and finally we provide a way to convert the LB simulations in the SI (système international) units.

Finally, in Chapter 7, we draw conclusions from our research and give recommendations that may be used in the future for continuation and extension of the research presented in this thesis.

2 | Theoretical background

This chapter provides the essential theoretical background information frequently used in the rest of this thesis. This includes, the mass and momentum conservation equations for single and multiphase fluids, as well as the essential features of a fluid interface and its interaction with a static and moving solid surface. We report a short derivation of the lubrication theory model, by A. Oron and coworkers [Reviews of Modern Physics, **69***,931-980 (1997)]. Furthermore, we discuss different regimes and length scales that arise in the study of contact line motion due to gravity, inertia and viscous forces.*

2.1 Equations of motion for viscous fluids

The Navier-Stokes (NS) equations are the most used mathematical model for the description of viscous fluids in motion [12]. The NS equations are based on the continuum assumption which means that the fluid is treated as a continuous medium rather than as a collection of discrete molecules. The NS equations in divergence form are given by:

$$\frac{\partial(\rho \mathbf{u})}{\partial t} + \boldsymbol{\nabla} \cdot \boldsymbol{\Pi} \;\; = \;\; \mathbf{F}, \tag{2.1}$$

where $\rho \equiv \rho(\mathbf{x}, t)$ is the fluid density, $\mathbf{u} \equiv \mathbf{u}(\mathbf{x}, t)$ is the fluid velocity, $\mathbf{F} \equiv \mathbf{F}(\mathbf{x}, t)$ is the external body force or the force per unit volume on the fluid, $\boldsymbol{\nabla} \cdot$ is the divergence operator, $\boldsymbol{\Pi} \equiv \boldsymbol{\Pi}(\mathbf{x}, t)$ is the momentum flux tensor. All these quantites are functions of the position $\mathbf{x}$ and time t. The momentum flux tensor $\boldsymbol{\Pi}$ for a viscous fluid is given by:

$$\boldsymbol{\Pi} = p\mathbf{I} + \rho \mathbf{u}\mathbf{u} - \mathbf{T}, \tag{2.2}$$

where $p \equiv p(\mathbf{x}, t)$ is the pressure, $\mathbf{uu}$ is the dyadic vector product, $\mathbf{T}$ is the deviatoric or viscous stress tensor and $\mathbf{I}$ is the identity matrix. The pressure p is the thermodynamic pressure which is related to the density ρ and the temperature T by an equation of state [13].

For a viscous fluid in motion, the total stress $\boldsymbol{\sigma}$ in the fluid consists of two parts: the isotropic stress p, that arises when the fluid is at rest, and the anisotropic viscous stress $\mathbf{T}$, that arises due to fluid motion:

$$\boldsymbol{\sigma} = -p\mathbf{I} + \mathbf{T}. \tag{2.3}$$

The most general form of the viscous stress tensor is given by

$$\mathbf{T} = 2\mu\mathbf{E} + \zeta(\boldsymbol{\nabla}\cdot\mathbf{u})\mathbf{I}, \tag{2.4}$$

where $\mathbf{E}$ is the strain rate tensor*, μ is the dynamic viscosity, and ζ is called the second viscosity [12, 13]. The strain rate tensor is the symmetric part of the Jacobian matrix $\boldsymbol{\nabla}\mathbf{u}$, i.e., $\mathbf{E} = \frac{1}{2}\left(\boldsymbol{\nabla}\mathbf{u} + \boldsymbol{\nabla}\mathbf{u}^{\mathsf{T}}\right)$. Using Eqs. (2.2) and (2.4), the NS equations Eq. (2.1) read:

$$\begin{aligned}\frac{\partial(\rho\mathbf{u})}{\partial t} + \boldsymbol{\nabla}\cdot(\rho\mathbf{u}\mathbf{u}) &= -\boldsymbol{\nabla}p + \boldsymbol{\nabla}\cdot\left[\mu\left(\boldsymbol{\nabla}\mathbf{u} + \boldsymbol{\nabla}\mathbf{u}^{\mathsf{T}}\right)\right] \\ &\quad + \boldsymbol{\nabla}[\zeta(\boldsymbol{\nabla}\cdot\mathbf{u})] + \mathbf{F}.\end{aligned} \tag{2.5}$$

In this thesis, we assume that the fluid viscosities μ and ζ are constant.

The NS equations are the statements on local momentum conservation for a fluid. Conservation of mass must be considered as well and it is given by the continuity equation:

$$\frac{\partial\rho}{\partial t} + \boldsymbol{\nabla}\cdot(\rho\mathbf{u}) = 0. \tag{2.6}$$

A fluid flow is defined as incompressible if the material derivative of ρ is zero, i.e.,

$$\frac{\mathrm{D}\rho}{\mathrm{D}t} \equiv \frac{\partial\rho}{\partial t} + \mathbf{u}\cdot\boldsymbol{\nabla}\rho = 0. \tag{2.7}$$

Using Eq. (2.7) the continuity Eq. (2.6) for incompressible flow reduces to:

$$\boldsymbol{\nabla}\cdot\mathbf{u} = 0. \tag{2.8}$$

Using the vector identity $\boldsymbol{\nabla}\cdot(\rho\mathbf{u}\mathbf{u}) = \rho(\mathbf{u}\cdot\boldsymbol{\nabla})\mathbf{u} + \mathbf{u}[\boldsymbol{\nabla}\cdot(\rho\mathbf{u})]$ and Eqs. (2.6), (2.8), the NS Eqs. (2.5) take the following form for an incompressible flow:

$$\rho\left(\frac{\partial\mathbf{u}}{\partial t} + \mathbf{u}\cdot\boldsymbol{\nabla}\mathbf{u}\right) = -\boldsymbol{\nabla}p + \boldsymbol{\nabla}\cdot\left[\mu\left(\boldsymbol{\nabla}\mathbf{u} + \boldsymbol{\nabla}\mathbf{u}^{\mathsf{T}}\right)\right] + \mathbf{F}. \tag{2.9}$$

*The strain rate tensor in the linear approximation of the velocity is given by $\boldsymbol{\nabla}\mathbf{u}$. Here we only consider the symmetric part of the strain rate tensor. The antisymmetric part, $\frac{1}{2}\left(\boldsymbol{\nabla}\mathbf{u} - \boldsymbol{\nabla}\mathbf{u}^{\mathsf{T}}\right)$ gives the fluid rotation and does not contribute in deforming the fluid [13].

For constant dynamic viscosity μ, Eq. (2.9) further reduces to:

$$\rho\left(\frac{\partial \mathbf{u}}{\partial t} + \mathbf{u}\cdot\boldsymbol{\nabla}\mathbf{u}\right) = -\boldsymbol{\nabla}p + \mu\boldsymbol{\nabla}^2\mathbf{u} + \mathbf{F}, \tag{2.10}$$

where $\boldsymbol{\nabla}^2$ is the Laplace operator.

2.2 Multiphase flows

In the context of this thesis, we will consider fluid systems consisting of one or more immiscible fluids. If the two fluids in the system are a liquid and its equilibrium vapor phase, then we refer to it as a multiphase fluid system; if the properties of the two fluids are different at the molecular level, we call it a multicomponent fluid system.

For a multiphase system the coexistence of the liquid and its vapor phase can be e.g. explained by the van der Waals equation of state [14, p. 14]:

$$p = \frac{RT}{v-b} - \frac{a}{v^2}, \tag{2.11}$$

where p is the pressure, v is the molar volume ($[v] = \mathrm{m}^3/\mathrm{mol}$), T is the temperature ($[T] = \mathrm{K}$), R is the gas constant ($R \approx 8.314\,\mathrm{kg\,m^2/(mol\,s^2\,K)}$). The constants a is a measure of the inter-particle attraction and the constant b is an approximation of the actual volume of the particles. A phase diagram for CO_2, in terms of the van der Waals Eq. (2.11), is shown in Figure 2.1: the liquid CO_2 can coexist with its vapor phase if the system temperature is below the critical temperature ($T < T_c$) and the pressure in the two phases is the same across the interface [14]. The thickness of the interface between the liquid CO_2 and its equilibrium vapor phase becomes infinite at the critical temperature. For $T < T_c$, the equilibrium density in the two phases across the interface can be determined by the Maxwell's equal area rule [15]:

$$\int_{v_\ell}^{v_\mathrm{v}} p\,\mathrm{d}v = p_\mathrm{eq}(v_\mathrm{v} - v_\ell), \tag{2.12}$$

where p_eq is the equilibrium pressure given by $p_\mathrm{eq} = p(v_\mathrm{v}) = p(v_\ell)$, v_v and v_ℓ are the molar volume for the vapor and the liquid phases in equilibrium. The Maxwell equal area allows to find the equilibrium molar volume of the liquid and of its vapor for a given equation of state, we will use it rule in the next chapter to obtain the equilibrium density for the Shan-Chen multiphase model [9].

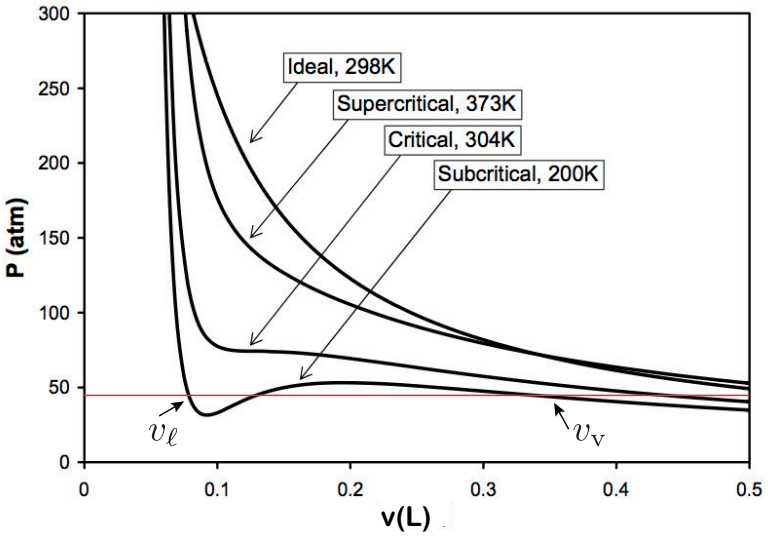

Figure 2.1: Graphical representation of the van der Waals equation of state given by Eq. (2.11) for CO_2. The pressure is measured in scale of atmospheric pressure (atm) and volume is measured in liter (L). Image reproduded from [15]. The phase-diagram shows that below the critical temperature we can find the equilibrium pressure (shown by the red rooted line) for which CO_2 can coexist in liquid and vapor phase. The value of the equilibrium pressure can be determined by Maxwell's equal area rule.

2.2.1 Fluid interfaces

The characteristic difference between the single- and the multi-phase fluid systems is the presence of an interface. A fluid interface can be identified by changes in the physical properties of the system, like its density, viscosity, refractive index etc. At the hydrodynamic scales a fluid interface is a smooth surface, this definition will be used throughout the rest of the thesis. It must be remembered, however, that at the molecular scales the interface is spread over a distance proportional to molecular diameters, and has a roughness of the same order, see Figure 2.2 (a). This implies that the hydrodynamic description cannot be expected to hold below the molecular scale, with important consequences in regularizing otherwise apparently diverging terms at the contact line (see section 2.3.2).

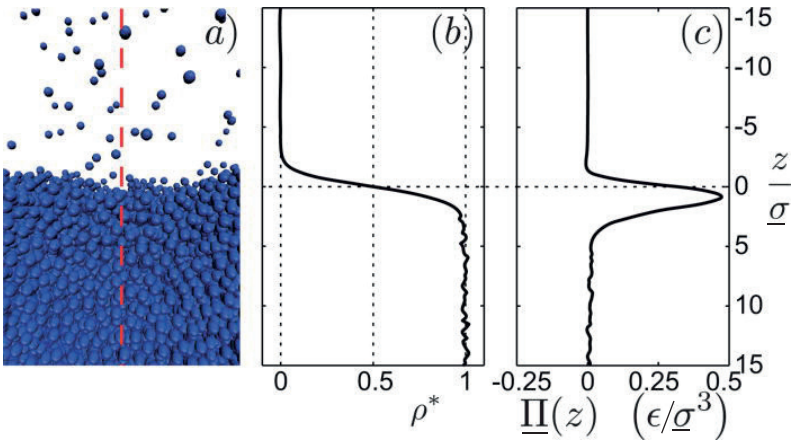

Figure 2.2: The liquid-vapor interface at the microscopic length scale obtained from a molecular dynamics (MD) simulation using Lennard-Jones potential. The vertical axis is in units of the molecular diameter $\underline{\sigma}$ and the stress shown in panel (c) is measured in $\epsilon/\underline{\sigma}^3$. Here, ϵ is the energy scale corresponding to the intermolecular forces. (a) Snapshot of the liquid-vapor interface in the MD simulation. The red dotted line divides the system in two parts: Left and right. (b) Time-averaged normalized density profile $\rho^*(z)$ across the interface. (c) Tangential force per unit area exerted by the left part on the right part of the system. The plot shows the difference between the normal and the tangential components of stress tensor: $\underline{\Pi}(z) = \boldsymbol{\sigma}^{\mathrm{n}} - \boldsymbol{\sigma}^{\mathrm{t}}$. Images reproduced from [16].

Surface tension

From a mechanical point of view, the surface tension can be defined as a force per unit length, acting tangentially to the interface. In a recent study, Marchand et al.[16], show a molecular-dynamics simulation, which supports the idea of interpreting the surface tension as a mechanical force, see figure 2.2 (c). The origin of this force is the attractive anisotropic force within a few molecular lengths from the interface. This anisotropy and the corresponding tangential force occurs at the liquid-solid interfaces as well, where also there is a half-space of liquid missing [16]. The thermodynamic description of the surface tension must consider that a liquid molecule at an interface is surrounded by a relatively small number of molecules as compared to a molecule in the bulk, this leads to a higher free energy at the interface. This excess free

energy per unit are is defined as the surface tension [17]:

$$\gamma = \left(\frac{\partial G}{\partial A}\right)_{T,V,n}, \tag{2.13}$$

where G is the free energy for a fluid system of volume V, number of molecules n and temperature T.

2.2.2 Multiphase flow modelling

A classical way to model an interface is to approximate it by a deformable surface of zero thickness. This kind of interface models are usually referred to as sharp interface models and these are the interfaces that will be considered in the rest of this chapter.

It follows from Eq. (2.13) that, for a given fixed volume of liquid, a curved surface has a higher surface energy than a flat surface. According to the Laplace law, this excess surface energy for a curved interface is compensated by the pressure jump across the interface. In general, the Laplace law states that the normal stress difference across the interface is given by the product of the surface tension, γ, and of the mean curvature, κ, of the interface [12]:

$$\boldsymbol{\sigma}_1^{\mathrm{n}} - \boldsymbol{\sigma}_2^{\mathrm{n}} = \gamma\kappa, \tag{2.14}$$

where $\boldsymbol{\sigma}^{\mathrm{n}} \equiv (\boldsymbol{\sigma}\hat{\mathbf{n}}) \cdot \hat{\mathbf{n}}$, $\boldsymbol{\sigma}$ is the stress tensor, given by Eq. (2.3), and $\hat{\mathbf{n}}$ is the unit normal vector at the interface. In a static situation, the normal stress difference across the interface is given by the pressure difference across it and Eq. (2.14) read as:

$$p_1 - p_2 = \gamma\kappa, \tag{2.15}$$

where p_1, p_2 are the pressures in fluid 1 and 2 close to the interface. For a spherical drop of radius R the curvature is constant and given by $\kappa = 2/R$.

Generally speaking, both with numerical as well as analytical modeling, we will consider a multiphase fluid as made of two incompressible components separated by an interface where appropriate force act. This force depends on the surface tension and on the gradient of the curvature. Furthermore, in what follows and for simplicity, we assume that the fluids across the interface are of the same nature. For such a fluid system, the NS equations can be written as:

$$\rho\left(\frac{\partial \mathbf{u}}{\partial t} + \mathbf{u} \cdot \boldsymbol{\nabla}\mathbf{u}\right) = -\boldsymbol{\nabla}p + \mu\boldsymbol{\nabla}^2\mathbf{u} + \mathbf{f} \tag{2.16}$$

where $\mathbf{f}$ is the force corresponding to the surface tension. Introducing scaling parameters:

$$\begin{aligned} \bar{\mathbf{x}} &= \mathbf{x}/L, & \bar{\mathbf{u}} &= \mathbf{u}/U, & \bar{t} &= tU/L, \\ \bar{p} &= pL/(\mu U), & \bar{\mathbf{f}} &= \mathbf{f}L^2/\gamma, \end{aligned} \tag{2.17}$$

where U and L are the characteristic velocity and length scale for a problem. Using Eqs Eq. (2.17), the NS Eqs. (2.16) read:

$$\mathrm{Re}\left(\frac{\partial \bar{\mathbf{u}}}{\partial \bar{t}} + \bar{\mathbf{u}} \cdot \bar{\boldsymbol{\nabla}}\bar{\mathbf{u}}\right) = -\bar{\boldsymbol{\nabla}}\bar{p} + \bar{\boldsymbol{\nabla}}^2\bar{\mathbf{u}} + \frac{1}{\mathrm{Ca}}\bar{\mathbf{f}}, \tag{2.18}$$

where Re is the Reynolds number and Ca is the capillary number given by:

$$\mathrm{Re} = \frac{\rho U L}{\mu}, \tag{2.19}$$

$$\mathrm{Ca} = \frac{\mu U}{\gamma}, \tag{2.20}$$

respectively. The Reynolds number is the ratio of the inertial and of the viscous forces and the capillary number gives the ratio of the viscous and of the capillary forces. The product of the capillary the Reynolds number gives the ratio of the inertia and capillary forces, and referred to as the Weber number:

$$\mathrm{We} = \mathrm{Ca}\,\mathrm{Re} = \frac{\rho U^2 L}{\gamma}. \tag{2.21}$$

2.3 Interaction between a fluid interface and a solid

2.3.1 Static contact line

Although, the definition of contact line may be applied to include also the common border between three immiscible fluids, here we will restrict ourself to the case of the interaction of a fluid interface with a solid. An example of such contact line is shown in Figure 2.3 (left panel).

Wettability of a solid

When a liquid drop comes in contact with a solid, depending on the relative strength of the interactions, it can either completely spread over the solid or it may form a stable spherical cap. In the first case the solid is said to be

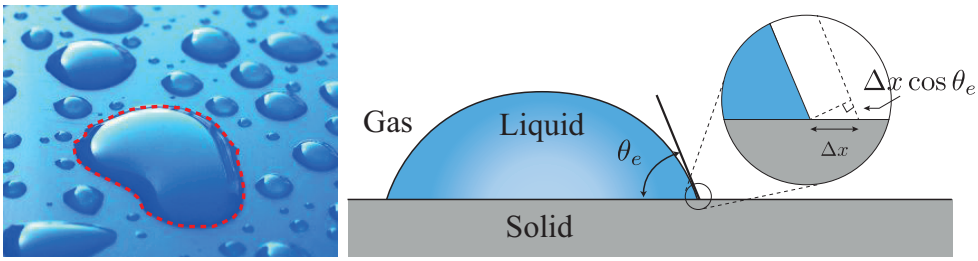

Figure 2.3: Left panel: Water drops on a glass substrate (Image source: `http://way2science.com/molecular-theory-of-surface-tension`*).The red dotted line in the figure shows the position of the contact line. The shape of the big drops is affected by the force due to gravity. Right panel: Schematics of a liquid drop on a smooth non-deformable solid surface. The figure shows the contact angle, θ_e, in thermodynamic equilibrium.*

perfectly wet whereas in the latter it is said to be partial wet. The shape of the drop on the partially wet plate is determined by the angle made between the solid-liquid and the liquid-air interface: this angle is know as the equilibrium contact angle θ_e. If the surface tensions of liquid-gas, solid-liquid and solid-gas interface are denoted by $\gamma_{\ell g}$, $\gamma_{s\ell}$, and γ, respectively, then for an infinitesimally small displacement of the contact line, Δx, the following energy variation takes place: energy loss due to diminishing of the solid-air interface is $\gamma_{\ell g}\Delta x$, energy gain due to the increase in the liquid-solid interface is $\gamma_{s\ell}\Delta x$ and energy gain due to the increase in the solid-liquid interface is $\gamma\Delta x\cos\theta_e$, see Figure 2.3 (right panel). Using the conservation of energy, one obtains the following relation:

$$\gamma_{sg}\Delta x - \gamma_{s\ell}\Delta x - \gamma\cos\theta_e\Delta x = 0,$$

where Δx is the virtual displacement of the contact line, see Figure 2.3 (right panel). Rearranging the term gives the celebrated Young equation:

$$\cos\theta_e = \frac{\gamma_{sg} - \gamma_{s\ell}}{\gamma}. \tag{2.22}$$

As already mentioned, the contact angle is the measure of the wettability of a solid, it is customary to say that a surface is perfectly wet or partially wet if $\theta_e = 0$ or $0 < \theta_e \leq \pi/2$, respectively, and a surface is perfectly dry or partially dry if $\theta_e = \pi$ or $\pi/2 < \theta_e \leq \pi$, respectively ($[\theta_e]$ = rad). The Young relation given by Eq. (2.22) can also be seen as the balance of capillary forces: $\gamma_{s\ell}$, $\gamma_{\ell g}$ and γ at the contact line.

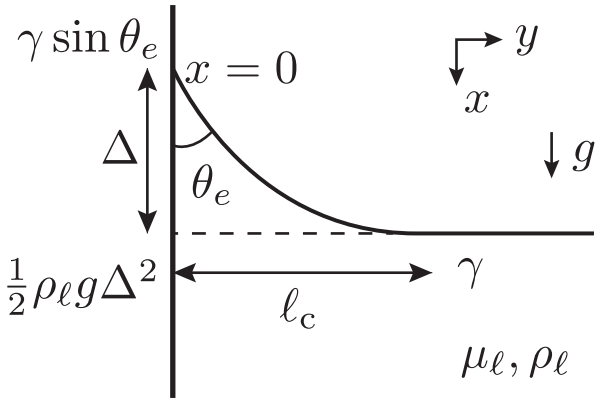

Figure 2.4: Schematic showing the horizontal component of forces acting on the meniscus formed due to the contact between a fluid interface and a partially wettable and chemically smooth solid static plate. The plate is aligned in the direction parallel to the force due to gravitational acceleration g.

The role of gravity in capillarity

In presence of gravity, capillary forces (forces due to surface tension) dominate close to the contact line while away from it these are negligible, as compared to the gravity. Figure 2.3 (left panel) shows an example of an interplay between gravity and capillary forces, where the larger water drops are flattened at the center due to the effect of gravity. Another example of the balance between capillary force and gravity can be noticed by the shape of a meniscus climbing a vertical partially wetting solid wall far from the wall, see Figure 2.4. At the wall the capillary force dominates and deform the liquid-gas interface, while far from the contact line, gravity dominate and the interface flatten.

The rise of the meniscus with respect to the flat interface, Δ, can be obtained by the mechanical balance of forces in the horizontal direction, as shown in Figure 2.4:

$$\Delta = \pm \ell_c \sqrt{2(1 - \sin\theta_e)}, \tag{2.23}$$

where θ_e is the equilibrium contact angle, ρ_ℓ is the density of liquid, g is the acceleration due to gravity and ℓ_c is the capillary length given by:

$$\ell_c = \sqrt{\frac{\gamma}{\rho_\ell g}}. \tag{2.24}$$

In our choice of the coordinates, positive and negative signs of Δ in Eq. (2.23) correspond to dry and wet surfaces, respectively.

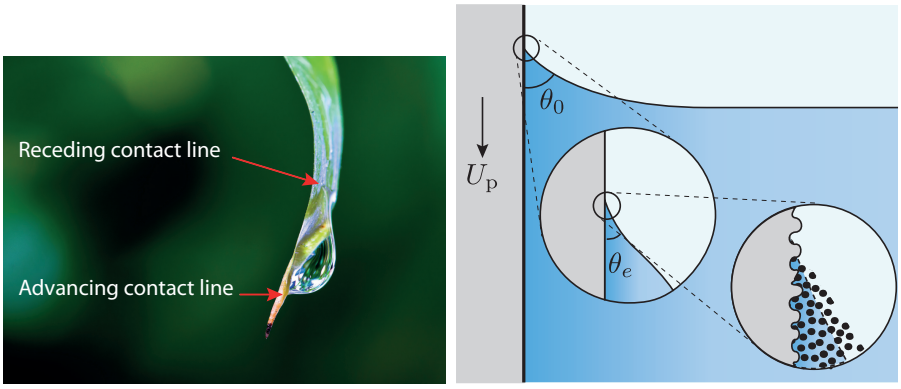

Figure 2.5: Left panel: a water drop sliding on a leaf (Image source `http://robwebb.net/wp-content/uploads/2011/01/IMG_2314-Edit.jpg`*). The figure shows the difference in the contact angles at the receding and the advancing contact lines. Right panel: schematic representation of the advancing contact line, showing the three distinct scales involved in the study of contact line motion. The apparent micoscopic contact angle is denoted by* θ_0*. For the advancing contact line, the apparent contact angle is larger then the equilibrium contact angle* θ_e*. Image adapted from [18].*

The capillary length is the characteristic length-scale over which capillary forces dominate over gravity. If the density of the gas, ρ_g, is not negligible as compared to the density of the liquid, ρ_ℓ, then the capillary length is given by:

$$\ell_c = \sqrt{\frac{\gamma}{(\rho_\ell - \rho_g)g}}. \tag{2.25}$$

2.3.2 Contact line in motion

Drops sliding on a surface, liquid film coating, jets from a nozzle, drop splashing on solid surfaces etc. are just some examples of the problems that involve moving contact lines. Depending on whether the contact line moves towards the dry or the wet position of the surface, we refer to it as to the receding or to the advancing contact line, respectively (see Figure 2.5).

For the static case, a complete description of the contact line can be obtained by balancing gravity and capillary forces. However, as soon as the contact line starts moving, the problem becomes much more complex. For a moving contact line, the local angle measured at the contact line depends on the scale [19]. This is not the case for static situations where the Young relation, given by Eq. (2.22), can be derived by the balance of capillary forces at

the hydrodynamic scale. The hydrodynamic modeling of the moving contact line leads to the Huh-Scriven paradox: i.e. using no-slip boundary condition for the flow near to the contact line leads to an energy dissipation that diverges logarithmically as $r \to 0$ [20], where r is distance from the contact line position. This paradox is clear indication that microscopic effects beyond hydrodynamics cannot be ignored when studying moving contact line (see section 2.2.1).

Typically, problems related to moving contact lines are divided into three distinct regimes: inner regime, the flow description of the contact line at the molecular scale; outer regime, the flow description at the hydrodynamic length scale; and the intermediate regime, where the interface is strongly curved due to the interplay between capillary and viscous forces [19]. A schematic representation of these three length scales is shown in Figure 2.5. In this thesis, we will only focus on the intermediate and the outer regimes.

The nature of the viscous singularity

Huh and Scriven analytically calculated the flow profile in a wedge assuming a perfectly planar liquid-vapor interface [20]. According to their computation, the flow in the "contact line region" is dominated by viscosity and therefore, the fluid flow on either side of the interface is described by the Stokes' equation. In 2D polar coordinates, (r, ϕ), the Stokes' equation transforms in a biharmonic equation for the stream function, $\psi(r, \phi)$:

$$\nabla^4 \psi = 0. \tag{2.26}$$

Subjected to the no-slip boundary condition at the wall ($u_r = U_\mathrm{p}$ for $\phi = 0°$ and $u_\mathrm{r} = -U_\mathrm{p}$ for $\phi = 180°$, see Figure 2.6 (b)) and assuming that the velocity $\mathbf{u} = (u_\mathrm{r}, u_\phi)$ is bounded as $r \to \infty$, the solution of the biharmonic Eq. (2.26) is:

$$\psi(r, \phi) = r(a \sin\phi + b \cos\phi + c\phi \sin\phi + d\phi \cos\phi). \tag{2.27}$$

The constants a, b, c, d are evaluated using impenetrable and no-slip boundary conditions at the solid and impenetrable and continuity of velocity and tangential stress conditions at the fluid-fluid interface. The integration constants a, b, c, d further depend on the viscosity ratio, $R_\mu = \mu_1/\mu_2$, and on the wedge angle θ_w. Finally, the velocity field can be obtained from the stream function using [20]:

$$u_\mathrm{r} = -\frac{1}{r}\frac{\partial \psi}{\partial \phi}, \quad u_\phi = \frac{\partial \psi}{\partial r}.$$

The following conclusions can be drawn from the Huh-Scriven solution:

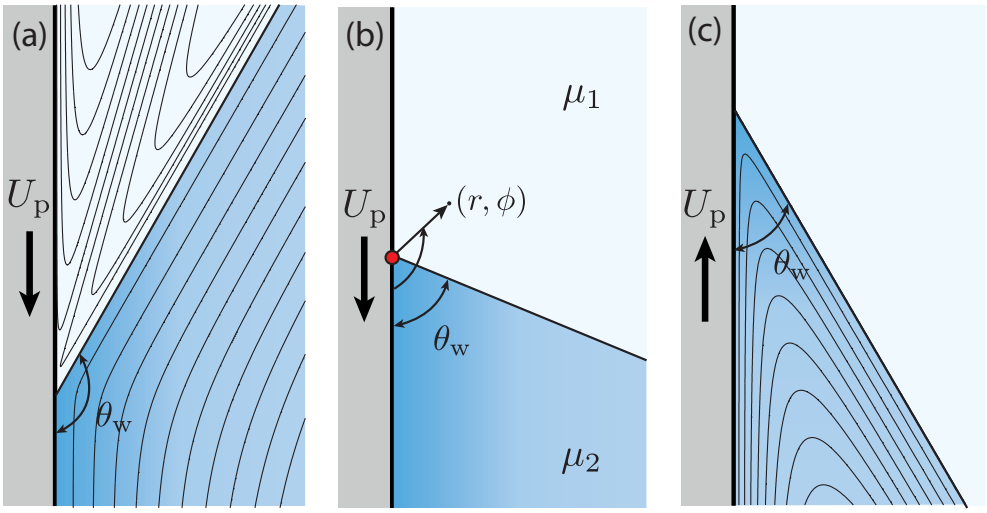

Figure 2.6: Streamlines showing the solution proposed by Huh and Scriven [20]. Middle panel: schematics showing an interface located at $\phi = \theta_w$ and separating two immiscible fluids with viscosities μ_1 and μ_2. Left panel: $\theta_w = 150\,^\circ$, $U_p = 1$; Right panel: $\theta_w = 30^\circ$, $U_p = -1$. The viscosity ratio for both cases is $R_\mu = \mu_1/\mu_2 = 10^{-3}$.

- The shear stress varies as r^{-1} near to the contact line. This implies that the total force exerted on the solid surface is logarithmically infinite for $r \to 0$.
- The velocity field has no intrinsic length scale and hence the Reynolds number, Re, can only be defined locally based on r. This means that Re can be arbitrary small as $r \to 0$ and that the Stokes' flow approximation is self consistent as long as $r \ll \mu/(\rho U_p)$.
- The pressure in the contact line region scales as μ/r. This pressure must be balanced by the capillary pressure, resulting in a highly curved surface near to the contact line. In this respect, the assumption of planar interface cannot fully describe the moving contact line.
- When the plate is pushed into the liquid pool, the viscous force at the contact line is dominated by the strong velocity gradients in fluid 1, see Figure 2.6 (a). Therefore the viscosity of fluid 1 should not be ignored for the problems related to advancing contact lines.

The viscous singularity can be removed by using partial slip boundary conditions at the wall, i.e., instead of applying no-slip boundary conditions

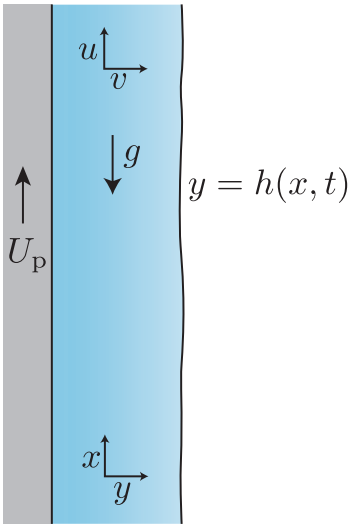

Figure 2.7: Schematics of a fluid interface parallel to a flat solid surface. The figure shows the steady state interface profile $h(x,t)$ (black curve) for a plate moving with the velocity, U_{p} . The plate moves perpendicular to free surface in the direction opposite to the gravity and to the x-axis.

at the wall we apply them at a distance, λ_{s}, in the wall. This distance, λ_{s}, is known as the slip length. Unfortunately there is no analytical solution of the biharmonic equation satisfying both the slip boundary condition and the bounded velocity simultaneously.

2.4 Lubrication theory

Lubrication theory (LT) is a well-established mathematical tool, which has been successfully used in the study of problems involving free surface flows and the contact line motion [21–23].

In what follows, we report the derivation of LT as presented in the work by A. Oron and coworkers [21], we provide the key steps and main assumptions are they are typically used in a lubrication model for free surface flows. For more details on the derivation we refer the reader directly to the work by A. Oron and coworkers [21].

In order to restrict our derivation to the specific context of this thesis, we consider a partially wetting and smooth flat plate, vertically immersed in a pool of liquid of density, ρ, and dynamic viscosity, μ (see Figure 2.7). The continuity and the NS equations for an incompressible flow, in the 2D

Cartesian coordinates, are given by:

$$\partial_{\mathrm{x}} u + \partial_{\mathrm{y}} v = 0, \tag{2.28}$$

$$\begin{aligned} \rho\left(\partial_{\mathrm{t}} u + u\partial_{\mathrm{x}} u + v\partial_{\mathrm{y}} u\right) &= -\partial_{\mathrm{x}} p + \mu\nabla^2 u - \partial_{\mathrm{x}}\varphi, & \text{(2.29a)} \\ \rho\left(\partial_{\mathrm{t}} v + u\partial_{\mathrm{x}} v + v\partial_{\mathrm{y}} v\right) &= -\partial_{\mathrm{y}} p + \mu\nabla^2 v - \partial_{\mathrm{y}}\varphi, & \text{(2.29b)} \end{aligned}$$

where $u \equiv u(x, y, t)$ and $v \equiv v(x, y, t)$ are the fluid velocity in the $x-$ and y-directions, respectively and φ is the gravitational potential given by $\varphi = -\rho g x$. The boundary conditions at $y = 0$ are no penetration through the wall and partial-slip:

$$v = 0, \qquad\qquad u = U_{\mathrm{p}} + \lambda_{\mathrm{s}}\partial_{\mathrm{y}} u, \tag{2.30}$$

where λ_{s} is the slip length. The partial-slip boundary condition at the wall, is used to regularize the viscous singularity at the contact line. The boundary conditions at the free surface $y = h(x, t)$ are, first, the kinematic boundary condition:

$$v = \partial_{\mathrm{t}} h + u\partial_{\mathrm{x}} h, \tag{2.31}$$

and second, the dynamic boundary conditions:

$$\partial_{\mathrm{y}} u = 0, \qquad\qquad \gamma\kappa = -p, \tag{2.32}$$

where

$$\kappa = \frac{\partial_{\mathrm{xx}} h}{\left(1 + (\partial_{\mathrm{x}} h)^2\right)^{3/2}}. \tag{2.33}$$

Integrating equation Eq. (2.28) with respect to y from $y = 0$ to $y = h(x, t)$, and using Eq. (2.31), we get:

$$\partial_{\mathrm{t}} h + \partial_{\mathrm{x}} q = 0, \qquad q = h\tilde{u}, \qquad \tilde{u}(x, t) = \frac{1}{h}\int_0^h u(x, y, t)\,\mathrm{d}y, \tag{2.34}$$

where q represents the mass flux in the x-direction in the film and $\tilde{u}$ is the velocity averaged over the film thickness.

Furthermore we introduce a scaling parameter $\varepsilon = h_0/L$ $(0 < \varepsilon \ll 1)$ where L and h_0 are the characteristic length scales along and perpendicular to the wall, respectively. In addition to the length scales h_0 and L, we use the

plate velocity, U_p, as the characteristic velocity of the problem. Using U_p, h_0, ε and μ, we define the following dimensionless variables:

$$\begin{aligned} &Y = y/h_0, \qquad X = x\,\varepsilon/h_0, \qquad U = u/U_\mathrm{p}, \qquad V = v/(\varepsilon U_\mathrm{p}),\\ &T = t\,\varepsilon U_\mathrm{p}/h_0, \quad P = p\,\varepsilon h_0/(\mu U_\mathrm{p}), \quad \Phi = \varphi\,\varepsilon h_0/(\mu U_\mathrm{p}), \end{aligned} \tag{2.35}$$

In the scaled variables defined by Eqs.(2.35), the system of Eqs. (2.28)-(2.32) reads:

$$\partial_\mathrm{X} U + \partial_\mathrm{Y} V = 0, \tag{2.36}$$

$$\begin{aligned} \varepsilon \mathrm{Re}\Big(\partial_\mathrm{T} U + U\partial_\mathrm{X} U + V\partial_\mathrm{Y} U\Big) &= -\partial_\mathrm{X} P - \partial_\mathrm{X}\Phi + \varepsilon^2\partial_\mathrm{XX} U \\ &\quad +\partial_\mathrm{YY} U, \qquad (2.37a)\\ \varepsilon^3 \mathrm{Re}\Big(\partial_\mathrm{T} V + U\partial_\mathrm{X} V + V\partial_\mathrm{Y} V\Big) &= -\partial_\mathrm{Y} P - \partial_\mathrm{Y}\Phi + \varepsilon^4\partial_\mathrm{XX} V \\ &\quad +\varepsilon^2\partial_\mathrm{YY} V, \qquad (2.37b) \end{aligned}$$

at $Y = 0$,

$$V = 0, \qquad U = 1 + \Lambda_s \partial_\mathrm{Y} U, \tag{2.38}$$

at $Y = h(x,t)/h_0 \equiv H(X,T)$,

$$\partial_\mathrm{Y} U = 0, \qquad \mathrm{Ca}^{-1}\varepsilon^3 \frac{\partial_\mathrm{XX} H}{\Big(1 + \varepsilon^2 \big(\partial_\mathrm{X} H\big)^2\Big)^{3/2}} = -P, \tag{2.39}$$

where $\Lambda_s = \lambda_\mathrm{s}/h_0$, $\mathrm{Re} = U_\mathrm{p} h_0/\nu$ and $\mathrm{Ca} = U_\mathrm{p}\mu/\gamma$. Finally, Eq. (2.34) in the scaled variables is given by:

$$\partial_\mathrm{T} H + \partial_\mathrm{X} Q = 0, \quad Q = H\tilde{U}, \quad \tilde{U}(X,T) = \frac{1}{H}\int_0^H U(X,Y,T)\,\mathrm{d}Y, \tag{2.40}$$

where Q represents the mass flux in the film, and $\tilde{U}$ is the velocity averaged over the film thickness.

Next, we expand U, V and P in a series of ε to obtain a series solution for the governing equations (2.36) and (2.37) [21]:

$$\begin{aligned} U &= U_0 + \varepsilon U_1 + \varepsilon^2 U_2 + O(\varepsilon^3), \qquad (2.41a)\\ V &= V_0 + \varepsilon V_1 + \varepsilon^2 V_2 + O(\varepsilon^3), \qquad (2.41b)\\ P &= P_0 + \varepsilon P_1 + \varepsilon^2 P_2 + O(\varepsilon^3). \qquad (2.41c) \end{aligned}$$

The gravitational potential Φ used here is linear in the spatial variables and can be used as it is in the following derivation. The lubrication approximation when the surface $h(x)$ is parallel to the plate is given by: $\mathrm{Re}\,, \overline{\mathrm{Ca}} \approx O(1)$ for $\varepsilon \to 0$, where $\overline{\mathrm{Ca}} = \mathrm{Ca}\,\varepsilon^{-3}$ [21]. Substituting Eqs. (2.41) in Eqs. (2.37) and takeing the lubrication approximation for a surface parallel to the plate, we get:

$$\partial_{\mathrm{YY}} U_0 - \partial_{\mathrm{X}} P_0 - \partial_{\mathrm{X}} \Phi = 0, \tag{2.42a}$$

$$-\partial_{\mathrm{Y}} P_0 - \partial_{\mathrm{Y}} \Phi = 0. \tag{2.42b}$$

In the linearized and scaled variables, the boundary conditions given by Eqs.(2.38) at $Y = 0$ read:

$$U_0 = 1 + \Lambda_s \partial_{\mathrm{Y}} U_0 \tag{2.43a}$$

$$\partial_{\mathrm{Y}} U_0 = 0, \tag{2.43b}$$

$$\overline{\mathrm{Ca}}^{-1} \partial_{\mathrm{XX}} H = -P_0. \tag{2.43c}$$

$$\partial_{\mathrm{T}} H + \partial_{\mathrm{X}} Q = 0, \qquad \text{where } Q = \int_0^H U_0 \mathrm{d}X \tag{2.44}$$

The resulting equations are consistent with the assumption that the flow in the film is parallel to the plate. Integrating Eq. (2.42a) twice and using the boundary condition Eq. (2.43a) gives us:

$$U_0 = \left(\frac{Y^2}{2} - HY + H\Lambda_s \right) \partial_{\mathrm{X}} (P_0 + \Phi) + 1. \tag{2.45}$$

This implies that:

$$\int_0^H U_0 \mathrm{d}Y = -H^2 (H + 3\Lambda_s) \frac{\partial_{\mathrm{X}} (P_0 + \Phi)}{3} + H. \tag{2.46}$$

Substituting this flux into Eq. (2.44), we obtain the following dynamical equation for $H(X, T)$

$$\partial_{\mathrm{T}} H - \partial_{\mathrm{X}} \left(H^2 (H + 3\Lambda_s) \frac{\partial_{\mathrm{X}} (P_0 + \Phi)}{3} + H \right) = 0, \tag{2.47}$$

where $P_0 = -\overline{\mathrm{Ca}}^{-1} \partial_{\mathrm{XX}} H$. In the steady state $\partial_{\mathrm{T}} H = 0$ and $\partial_{\mathrm{X}} \equiv \mathrm{d}/\mathrm{d}X$, hence Eq. (2.47) becomes

$$H^2 (H + 3\Lambda_s) \frac{1}{3} \frac{\mathrm{d}}{\mathrm{d}X} (P_0 + \Phi) + H = \tilde{U}. \tag{2.48}$$

The thickness average velocity $\tilde{U}$ given by Eq. (2.40) in the limit of $\varepsilon \to 0$ becomes $\tilde{U} = \frac{1}{H}\int_0^H U_0\, dY$. Rearranging the terms of Eq. (2.48) we get:

$$\frac{\mathrm{d}^3 H}{\mathrm{d}X^3} - \overline{\mathrm{Ca}}\frac{\mathrm{d}\Phi}{\mathrm{d}X} + \frac{3\overline{\mathrm{Ca}}(1-\tilde{U})}{H(H+3\Lambda_s)} = 0. \tag{2.49}$$

Reverting back to the original variables gives us

$$\frac{\mathrm{d}^3 h}{\mathrm{d}x^3} - \frac{1}{\gamma}\frac{\mathrm{d}\phi}{\mathrm{d}x} + \frac{3\mathrm{Ca}}{h(h+3\lambda_\mathrm{s})}\left(1 - \frac{\tilde{u}}{U_\mathrm{p}}\right) = 0. \tag{2.50}$$

In the frame of reference of a moving plate, the velocity $\tilde{u}$ is replaced by $\tilde{u} - U_\mathrm{p}$. If we fix the position of the contact line at $x = 0$, then using $\varphi = -\rho g x$ Eq. (2.50) becomes:

$$\frac{\mathrm{d}^3 h}{\mathrm{d}x^3} + \frac{1}{\ell_\mathrm{c}^2} - \frac{3\mathrm{Ca}\,(\tilde{u}/U_\mathrm{p})}{h(h+3\lambda_\mathrm{s})} = 0, \tag{2.51}$$

where, $\ell_\mathrm{c} = \sqrt{\gamma/(\rho g)}$, is the capillary length. The first, second and third term of Eq. (2.51), represent effect of capillary, gravity and viscosity, respectively, on the interface shape. For the advancing contact line $U_\mathrm{p} < 0$. The derivation presented here is only valid for $\varepsilon = \mathrm{Ca}^{1/3} \ll 1$, $\mathrm{Re} \ll 1$ and $\mathrm{Ca}^{2/3}(\partial_\mathrm{X} H)^2 \ll 1$, see Eq. (2.43c), where we implicitly assumed that $|\partial_\mathrm{X} H| \ll 1$. The assumption, $|\partial_\mathrm{X} H| \ll 1$, may not be valid for the coating of a hydrophobic plate or when a hydrophilic plate is pushed into a liquid pool. An extension of this one dimensional, single-phase, lubrication model, applicable to curved surfaces, can be found in [23]. A further extension of the LT model which is applicable to highly curved surface and that includes the effect of air viscosity, has already been derived [11]. We will present this extension in Chapter 4.

Interface profile for the static contact line

For the static plate, $\mathrm{Ca} = 0$, the lubrication equation (2.51) becomes:

$$\frac{\mathrm{d}\kappa}{\mathrm{d}x} = -\frac{1}{\ell_\mathrm{c}^2}. \tag{2.52}$$

Here we use the general definition of the curvature, κ, as given by Eq. (2.33). One can solve Eq. (2.52) analytically and obtain the interface profile, $h(x)$, for the stationary contact line [17, Eq. 2.21]:

$$h(x) - h_\Delta = \ell_\mathrm{c}\mathrm{arcosh}\left(\frac{2\ell_\mathrm{c}}{x-\Delta}\right) - 2\ell_\mathrm{c}\left[1 - \left(\frac{x-\Delta}{2\ell_\mathrm{c}}\right)^2\right]^{1/2}, \tag{2.53}$$

where the constant h_Δ can be obtained by using the condition $h(0) = 0$:

$$h_\Delta = -\ell_c \text{arcosh}\left[2/(1-\sin\theta_e)\right]^{1/2} + \ell_c\left[2(1+\sin\theta_e)\right]^{1/2}.$$

The analytical solution given by Eq. (2.53) is referred to as to the "Landau solution" in the rest of this thesis. It will be used in Chapter 4, as a reference for the validation of the boundary conditions for the lattice Boltzmann simulations.

2.4.1 Characteristic regimes for the moving contact line

In the static case, as we saw earlier, the interface shape is determined by the balance between capillary and the gravitational forces. When the plate moves with respect to the fluid, viscous forces comes into effect. These viscous forces tend to drag the contact line with the solid, which is opposed by the capillary forces near the contact line and by the gravity far from the contact line. The competition between viscous and capillary forces is measured by the capillary number:

$$\text{Ca} = \frac{\text{Viscous force}}{\text{Capillary force}} = \frac{\mu U_p}{\gamma}, \tag{2.54}$$

where U_p is the velocity of the solid, μ is the dynamic viscosity and γ is the interfacial tension at the liquid-air interface.

Visco-capillary regime

For a partially wetting plate, when the plate is pulled out of the pool (receding contact line case), two distinct regimes can be observed. For small plate velocities, the position of the contact line raises up to a finite distance, with respect to the bath, and then attains an equilibrium, while the contact line slips over the plate. Instead, if the plate velocity is higher than a critical value, the plate entrains a continuous liquid film. The transition between the two regimes is often known as "dynamical wetting transition" or "forced wetting". This process of forcedly wetting a plate, is a common technique for coating thin liquid films on solid substrates [24] (dip-coating). In their seminal works on film coating, Landau and Levich [25] and Derjaguin, LLD [26] showed that the thickness of the coating film is uniquely determined by the plate velocity and in particular, it is given by:

$$h_{\text{LLD}} = 0.94\ell_c\,\text{Ca}^{2/3}. \tag{2.55}$$

This relation is only valid in the limit of small capillary numbers.

For capillary numbers below the wetting transition, gravity is negligible as compared to viscous and capillary forces and therefore one can omit the second term from Eq. (2.51). Furthermore, we assume that in this regime the thickness averaged velocity, $\tilde{u}$, can be approximated by the plate velocity; under these assumptions the steady state Eq. (2.51) becomes:

$$\frac{\mathrm{d}^3 h}{\mathrm{d}x^3} = \frac{3\mathrm{Ca}}{h(h+3\lambda_\mathrm{s})}. \tag{2.56}$$

The first thing that can be identified between Eq. (2.56) and the hydrodynamic modeling of the contact line motion is the viscous singularity in the limit of $h \to 0$ (for the case when $\lambda_\mathrm{s} = 0$) [20]. Secondarily, since the flow near the contact line has no intrinsic length scale [20], the solution to Eq. (2.56) is of the form $h = l\,H(x\,\mathrm{Ca}^{1/3}/l)$, where the characteristic length scale, l, depends on the mechanism of regularization of the viscous singularity [19, 27]. The analytical solution of the third order nonlinear Eq. (2.56) was first derived by Duffy and Wilson [28]. This analytical solution under specific asymptotic matching conditions is equivalent to the solution given by Voinov [19, 29]:

$$\left(\frac{\mathrm{d}h}{\mathrm{d}x}\right)^3 = \theta_0^3 - 9\mathrm{Ca}\,\ln\left(\frac{x}{l}\right), \tag{2.57}$$

where l is the microscopic length scale, Ca is the capillary number and θ_0 is the microscopic contact angle.

Visco-gravitational regime

If the capillary number is high, the LLD film thickness increases and gravity comes into play. In this regime viscous forces dominates over the capillary forces therefore we can drop the first term in equation Eq. (2.51). For the case of a perfect wetting plate, we can assume that $\tilde{u} \sim U_\mathrm{p}$. Furthermore, if we assume that $\lambda_\mathrm{s} = 0$ then Eq. (2.51) becomes

$$\frac{1}{\ell_\mathrm{c}^2} = \frac{3\mathrm{Ca}}{h^2}, \tag{2.58}$$

which gives us the film thickness $h_\mathrm{film} = \ell_\mathrm{c}\sqrt{3\mathrm{Ca}}$ corresponding to the visco-gravitational regime. This is consistent with the Derjaguin law [26].

3 | Lattice Boltzmann method

In this thesis, we use the lattice Boltzmann method as numerical tool to solve the Navier-Stokes equations. This chapter provides an overview of the lattice Boltzmann method in general and of the Shan-Chen multi-phase model in particular [9, 10]. Starting from the discretization of the Boltzmann equation, we discuss the boundary conditions and the schemes to incorporate forces in the lattice Boltzmann method. Furthermore, we discuss the implications of the different forcing schemes for the multi-phase flow simulations. In the end of this chapter, we provide a short discussion on the artifacts of the method such as the presence of spurious currents and of checker-board effect.

3.1 Introduction

In the last two decades, the lattice Boltzmann (LB) method has emerged as a popular numerical tool in computational fluid dynamics [30, 31]. The method has been successfully employed for single and multi-phase laminar flow applications, viz. contact line motion [11, 32–37], flow in porous media [38, 39] to mention only a few, as well as for turbulent flow applications [40–48]. Apart from fluid flow modeling, the method has also been used to study granular flow [49], acoustics [50, 51], the Schrödinger equation [52], magnetohydrodynamics [53, 54], etc..

In most of the fluid applications the LB method is used as an alternative numerical tool that gives an approximate solution of the Navier-Stokes (NS) Eq. (2.10) for incompressible flow. Instead of solving directly the macroscopic mass and the nonlinear momentum conservation equations, one solves a discretized version of the linear Boltzmann equation. However, the convergence towards the NS equation is only valid in the low Mach number and small Knudsen number regime (the Mach number, Ma, is defined as the ratio of the characteristic speed in the problem and the speed of sound in the fluid and the Knudsen number, Kn, is defined as the ratio of mean free path to the characteristic length scale). The condition of small Mach number ensures that

the flow remains incompressible while the small Knudsen number condition is essential to ensure that the continuum description at the macroscopic length scale holds.

The LB method is based on the kinetic theory of gases. This gives the LB method several advantages over conventional numerical methods: the advection (streaming) operator in the LB method is a linear operator which simplifies the complication that arises in the discretisation of the non-linear advection operator in the NS Eq. (2.10); the discrete Boltzmann equation converges to the incompressible NS equations, where the pressure is given by an equation of state (this avoids the solution of the Poisson equation for the pressure); the implementation of the boundary conditions in the LB method is relatively easy as compared to the traditional numerical methods (especially for the case of multicomponent and multi-phase flow); and the LB method is easy to parallelize.

This chapter is organized as follows: in section 3.2, we present a brief description of the Boltzmann equation and the BGK collision operator. In section 3.3 we discuss the lattice Boltzmann method as a space and time finite-difference approximation of the discrete velocity Boltzmann equation. Furthermore, we discuss the boundary conditions and the force incorporation schemes in the LB method. In Section 3.4 we present a brief description and a numerical study of the Shan-Chen model for multi-phase simulations. In section 3.5.2, we will discuss some artifact of the method.

3.2 The Boltzmann equation

Consider a system of N indistinguishable particles enclosed in a spatial volume X. At room temperature these particles are in continuous state of random motion, during which they collide with each other and as well as with the wall of the container. In classical mechanics, the state of each particle can be completely described by specifying its position, $\mathbf{x}$, and momentum, $\mathbf{p}$, at a given time. Typically a box of volume $X \approx 1\text{cm}^3$ at room temperature T contains approximately 10^{20} interacting particles. This makes the numerical description of such a classical system impossible at the macroscopic scales.

On the other hand, in statistical mechanics we are interested in the distribution of particles in phase-space, rather than in their individual microscopic state. The phase-space of a system is the collection of all positions $\mathbf{x}$ and momentum vectors $\mathbf{p}$. Based on the Boltzmann equation and on the Boltzmann H-theorem, one can show that the distribution of particles asymptotically converges to a Maxwellian distribution [55].

If all the particles in the system are identical, then one can define mass density function as:

$$f(\mathbf{x}, \mathbf{v}, t) \equiv m_{\mathrm{p}} N f_1(\mathbf{x}_1, \mathbf{p}_1, t), \tag{3.1}$$

where $f_1(\mathbf{x}_1, \mathbf{p}_1, t)$ is the single particle probability distribution function, $\mathbf{x} = \mathbf{x}_1$, $\mathbf{v} = \mathbf{p}_1/m_{\mathrm{p}}$, m_{p} is the mass of the single particle and N is the number of particles in the spatial volume X [56]. The Boltzmann equation (BE) is a partial differential equation for the function f, that describes the statistical behavior of a system of particles, in general out of thermodynamic equilibrium. The function $f(\mathbf{x}, \mathbf{v}, t)$ is a positive and real valued function of position $\mathbf{x}$, velocity $\mathbf{v}$ and time t. Physically, the function $f(\mathbf{x}, \mathbf{v}, t)$ is interpreted by means of the quantity, $f(\mathbf{x}, \mathbf{v}, t)\,\mathrm{d}\mathbf{x}\,\mathrm{d}\mathbf{v}$, which gives the total mass of particles in the spatial volume $[\mathbf{x}, \mathbf{x} + \mathrm{d}\mathbf{x}]$ and have velocity in $[\mathbf{v}, \mathbf{v} + \mathrm{d}\mathbf{v}]$ at time t. Using the property of the single particle distribution function f_1 one gets the following normalization condition on f:

$$\frac{1}{m_{\mathrm{p}} N} \int_{X \times V} f(\mathbf{x}, \mathbf{v}, t)\,\mathrm{d}\mathbf{v}\,\mathrm{d}\mathbf{x} = 1, \tag{3.2}$$

where V is an arbitrary volume in the velocity space. If these particles are subject to an external force field $\mathbf{K}$, then the evolution of the function $f(\mathbf{x}, \mathbf{v}, t)$ can be described by the Boltzmann equation [56]:

$$\frac{\partial f}{\partial t} + \mathbf{v} \cdot \boldsymbol{\nabla} f + \frac{\mathbf{K}}{m_{\mathrm{p}}} \cdot \boldsymbol{\nabla}_{\mathbf{v}} f = Q(f)\,, \tag{3.3}$$

where $f \equiv f(\mathbf{x}, \mathbf{v}, t)$ $\boldsymbol{\nabla}$ and $\boldsymbol{\nabla}_{\mathbf{v}}$ are the gradients with respect to the position vector and velocity vector, respectively and $Q(f)$ is the Boltzmann collision operator. The collision operator $Q(f)$ is based on the assumptions of molecular chaos and given by [55]:

$$Q(f) = \frac{1}{m_{\mathrm{p}}} \int_{V^3} \int_{\Omega} \|\mathbf{v} - \mathbf{v}_2\| \left(\frac{\mathrm{d}\sigma}{\mathrm{d}\Omega}\right) (f'\, f_2' - f\, f_2)\,\mathrm{d}\Omega\,\mathrm{d}\mathbf{v}_2\,\mathrm{d}\mathbf{v}'\,\mathrm{d}\mathbf{v}_2', \tag{3.4}$$

where $\mathrm{d}\sigma/\mathrm{d}\Omega$ is the differential cross section, $f \equiv f(\mathbf{x}, \mathbf{v}, t)$, $f_2 \equiv f(\mathbf{x}, \mathbf{v}_2, t)$, $f' \equiv f(\mathbf{x}, \mathbf{v}', t)$ and $f_2' \equiv f(\mathbf{x}, \mathbf{v}_2', t)$. The differential cross section of the collision is a region in space, in which the relative momentum of the particle, $\mathbf{v} - \mathbf{v}_2$, changes its direction by an angle θ into the solid angle $\mathrm{d}\Omega$, after collision. The post-collision variables are represented by the super-script "$\prime$" in Eq. (3.4).

The Boltzmann collision operator shown in Eq. (3.4) has three main physical properties: 1) conservation of local mass, momentum and energy (collision invariants); 2) Galilean invariance; and 3) the local dissipation relation:

$$\int_{X \times V} Q(f) \log f\,\mathrm{d}\mathbf{v}\,\mathrm{d}\mathbf{x} \leq 0, \tag{3.5}$$

for all t [57]. Furthermore, it can be shown that, there exist a unique positive function $f = f^{\mathrm{eq}}$ such that $Q(f^{\mathrm{eq}}) = 0$ [57]. This distribution function is known as the Maxwell-Boltzmann (MB) distribution function:

$$f^{\mathrm{eq}}(\mathbf{x}, \mathbf{v}, t) = \rho(\mathbf{x}, t) \left(\frac{m_{\mathrm{p}}}{2\pi\, k_{\mathrm{B}} T} \right)^{n/2} \exp\left(-\frac{m_{\mathrm{p}}}{2 k_{\mathrm{B}} T} \|\mathbf{v} - \mathbf{u}(\mathbf{x}, t)\|^2 \right), \tag{3.6}$$

where n is the dimension of the position space, k_{B} is the Boltzmann constant, T is the temperature and $\rho(\mathbf{x}, t)$ is the local mass density given by:

$$\rho(\mathbf{x}, t) = \int_V f(\mathbf{x}, \mathbf{v}, t)\, \mathrm{d}\mathbf{v}\,. \tag{3.7}$$

The equilibrium velocity, $\mathbf{u}$, is given by:

$$\mathbf{u}(\mathbf{x}, t) = \int_V \mathbf{v}\, f(\mathbf{x}, \mathbf{v}, t)\, \mathrm{d}\mathbf{v} \Big/ \int_V f(\mathbf{x}, \mathbf{v}, t)\, \mathrm{d}\mathbf{v}\,. \tag{3.8}$$

The above mentioned properties of the Boltzmann collision operator lead to the Boltzmann H-theorem(1872) [58], i.e., the entropy of a system defined as:

$$S(f) = -\int_X \int_V f(\mathbf{x}, \mathbf{v}, t) \log[f(\mathbf{x}, \mathbf{v}, t)]\, \mathrm{d}\mathbf{v}\, \mathrm{d}\mathbf{x},$$

can only increase in time, i.e. $\mathrm{d}S/\mathrm{d}t \geq 0$, and the state of maximum entropy, corresponding to $\mathrm{d}S/\mathrm{d}t = 0$ is uniquely given by $f = f^{\mathrm{eq}}$.

The collision operator of the BE must satisfies the local mass and momentum conservation in order for the same to hold macroscopic scales. Using a formal asymptotic expansion Chapman and Cowling [59] showed that for dilute gases the zeroth and the first moment of the Boltzmann Eq. (3.3) result into macroscopic mass (continuity equation) and momentum (NS equation) conservation.

For dense gases and liquids the mean free path λ_m is very small, as compared to the characteristic macroscopic length scale L, and the ratio $\varepsilon = \mathrm{Kn} = \lambda_m / L$ is known as the Knudsen number. For small Knudsen numbers the distribution function f remains "close" to the MB distribution. More importantly, for dense gases and liquids the Boltzmann collision operator given by Eq. (3.4) can be approximated by a linear collision operator. A short discussion on this linear collision operator is given in the next section (sec. 3.2.1). Using the Chapman-Enskog (CE) expansion on the Boltzmann equation with the linear collision operator and under the low Mach number conditions, it can be shown that only the first order approximation of f is sufficient to recover the continuity Eq. (2.6) and the NS Eq. (2.10) for liquids [55, 58].

3.2.1 Linear collision operator

For dense gases and liquids the Knudsen number ε is very small. This means that the number of collisions per unit volume is very high, which leads to fast relaxation of the distribution function to the local MB distribution, f^{eq}. Under these assumptions, one can expand f in the following series in ε:

$$f = f^{(0)} + \varepsilon f^{(1)} + O(\varepsilon^2), \tag{3.9}$$

where $f^{(0)} = f^{\mathrm{eq}}$. The linear collision operator can be obtained by using the Taylor series expansion of Q at $f = f^{\mathrm{eq}}$ [60]:

$$Q(f) = Q(f^{\mathrm{eq}}) + \mathbf{S}(f - f^{\mathrm{eq}}) + O(\varepsilon^2), \tag{3.10}$$

where $\mathbf{S} = \left(\mathrm{d}Q/\mathrm{d}f\right)_{f=f^{\mathrm{eq}}}$ is commonly known as the linear scattering operator [60]. The first term of the above series vanished as $Q(f^{\mathrm{eq}}) = 0$. In the limit of small Knudsen number ($\varepsilon \ll 1$), the collision operator Q reduces to the linear scattering operator $\mathbf{S}$:

$$\lim_{\varepsilon \to 0} Q(f) = \mathbf{S}(f - f^{\mathrm{eq}}). \tag{3.11}$$

The scattering operator $\mathbf{S}$ inherits the two main characteristics of the Boltzmann collision operator Q: local conservation of mass, momentum and energy (collisional invariance); $\lim_{t\to\infty} Q(f) = \lim_{t\to\infty} \mathbf{S}(f - f^{\mathrm{eq}}) = 0$ (asymptotic limit). If the scattering of particles is restricted to m directions then $\mathbf{S}$ is a square matrix of order m. The eigenvalues of this linear scattering operator are all non-positive [61]. The non-zero eigenvalues of the scattering operator are connected to transport coefficient at the hydrodynamic scale [60, 62].

Bhatnagar-Gross-Krook collision operator

If one assumes that all non-zero eigenvalues are identical, say $-\omega$ ($\omega > 0$), then the collisional operator reduces to the celebrated BGK form [63]:

$$Q_{\mathrm{BGK}}(f) = -\omega(f - f^{\mathrm{eq}}), \tag{3.12}$$

named after P. L. Bhatnagar, E. P. Gross and M. Krook. Physically, ω can be interpreted as the collision frequency [63] and the eigenvalue of the linear BGK collision operator is inversely proportional to the local relaxation time τ, i.e., $\omega = 1/\tau$ [63]. Standard von Neumann stability analysis by Lallemand et al. [60] shows that for the discrete nine-velocity and two-dimensional (D2Q9) the LB-BGK model has stability issues close to $\tau \leq 0.5$. Since we are using D2Q9 LB-BGK model throughout this thesis, we will restrict our selves $\tau > 0.5$.

The advantage of the BGK collision operator is that it is the simplest collision operator that inherits all the properties of the collision operator shown in Eq. (3.4) [57]. Furthermore, the BGK collision operator is valid for fluids with high densities [55, 63] and the Chapman-Enskog expansion of LB equation with the BGK operator satisfies hydrodynamic mass and momentum conservation relations. For all LB simulations presented in this thesis, we will employ the BGK form of the collisional operator.

3.3 Lattice Boltzmann method

Historically, the LB method is a descendant of lattice-gas cellular automata (LGCA) [64]. The main difference between the LGCA and the LB method is that the LB method directly uses the particle distribution function, which allows real values for the number of particles, whereas LGCA only allows for integers [65]. Using distribution functions in the LB method substantially reduces the statistical noise observed in LGCA [65] and makes the LB method a better choice for fluid dynamics simulations. Sterling and Chen [66] interpreted the LB method as a finite difference discretization of the Boltzmann equation with the BGK collision operator. This interpretation of the LB method allows us to use mathematical tools like linear stability analysis [67], that give more insight into the stability of the method.

3.3.1 Lattice Boltzmann equation

In absence of any external force, the Boltzmann Eq. (3.3) with the BGK collision operator and for a finite set of velocity m vectors $\mathbf{v}_i$ can be written as:

$$\frac{\partial f_i}{\partial t} + \mathbf{v}_i \cdot \boldsymbol{\nabla} f_i = -\frac{1}{\tau}(f_i - f_i^{\mathrm{eq}}), \qquad (i = 0, 1, \ldots, m-1), \tag{3.13}$$

where $f_i \equiv f(\mathbf{x}, \mathbf{v}_i, t)$, m is the number of discrete velocities, τ is the relaxation time, and f_i^{eq} is the second order accurate Maxwell-Boltzmann equilibrium velocity distribution function given by Eq. (3.6), i.e.

$$f_i^{\mathrm{eq}} = \rho \left[a + b(\mathbf{v}_i \cdot \mathbf{u}) + c(\mathbf{v}_i \cdot \mathbf{u})^2 + d\|\mathbf{u}\|^2 \right]. \tag{3.14}$$

The macroscopic mass density, ρ, and the velocity, $\mathbf{u}$, are defined as:

$$\rho(\mathbf{x}, t) = \sum_{i=0}^{m-1} f_i(\mathbf{x}, t), \qquad \mathbf{u}(\mathbf{x}, t) = \frac{1}{\rho(\mathbf{x}, t)} \sum_{i=0}^{m-1} \mathbf{v}_i f_i(\mathbf{x}, t). \tag{3.15}$$

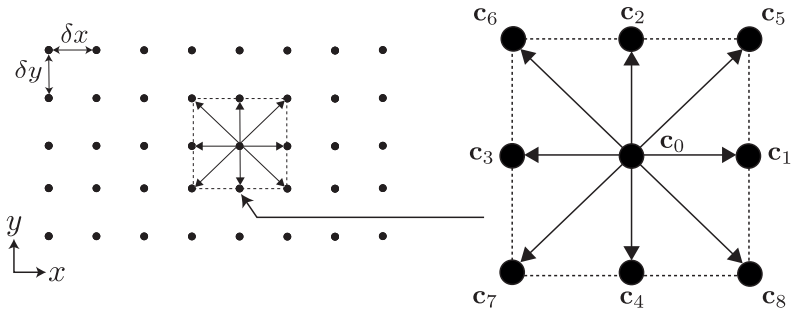

Figure 3.1: Schematics of the D2Q9 lattice. Circles represents the discretization of spatial positions and the arrows in the dotted box represent the discrete velocity space.

From here onwards, we will use the $\sum_i$ to represent the summation operator $\sum_{i=0}^{m-1}$. The constants a, b, c and d depend on the choice of the lattice. The second order approximation of the MB distribution is necessary to ensure the incompressibility and the Galilean invariance of the asymptotically obtained NS equation [58].

For a particular choice of the lattice dependent velocity vectors $\mathbf{v}_i = \mathbf{c}_i$ (see Figure 3.1), the BE Eq. (3.13) can be rewritten as:

$$\frac{\partial f_i}{\partial t} + \mathbf{c}_i \cdot \boldsymbol{\nabla} f_i = -\frac{1}{\tau}(f_i - f_i^{\mathrm{eq}}), \qquad (i = 0, 1, \ldots, m-1). \tag{3.16}$$

Using the forward finite difference approximation for the time derivative and the upwind scheme for the spatial derivative we get:

$$\begin{aligned} &\frac{f_i(\mathbf{x}, t+\delta t) - f_i(\mathbf{x}, t)}{\delta t} + \|\mathbf{c}_i\| \frac{f_i(\mathbf{x}, t) - f_i(\mathbf{x} - \mathbf{e}_i\, \delta x_i, t)}{\delta x_i} \\ &\qquad = -\frac{1}{\tau}\big[f_i(\mathbf{x} - \mathbf{e}_i\, \delta x_i, t) - f^{\mathrm{eq}}(\mathbf{x} - \mathbf{e}_i\, \delta x_i, t)\big], \end{aligned} \tag{3.17}$$

where $\mathbf{e}_i = \mathbf{c}_i / \|\mathbf{c}_i\|$ and $\delta x_i = \|\mathbf{x} - \mathbf{x}_i\|$, $\mathbf{x}_i$ is the nearest grid point in the $\mathbf{e}_i$ direction. Rearranging Eq. (3.17) gives

$$\begin{aligned} &f_i(\mathbf{x}, t+\delta t) + (\mathrm{Cr} - 1)\, f_i(\mathbf{x}, t) - \mathrm{Cr}\, f_i(\mathbf{x} - \mathbf{e}_i\, \delta x_i, t) \\ &= -\frac{\delta t}{\tau}\big[f_i(\mathbf{x} - \mathbf{e}_i\, \delta x_i, t) - f^{\mathrm{eq}}(\mathbf{x} - \mathbf{e}_i\, \delta x_i, t)\big], \end{aligned} \tag{3.18}$$

where the Courant number Cr is given by, $\mathrm{Cr} = \|\mathbf{c}_i\|\, \delta t / \delta x_i$. If the lattice velocity $\mathbf{c}_i$ satisfies

$$\mathbf{c}_i = \frac{\mathbf{e}_i \delta x_i}{\delta t}, \tag{3.19}$$

then Cr = 1, which is a necessary condition for the stability of the LB method [67]. Furthermore, for Cr = 1 Eq. (3.18) reduces to:

$$f_i(\mathbf{x}, t+\delta t) - f_i(\mathbf{x}-\mathbf{c}_i\delta t, t) = -\frac{\delta t}{\tau}\left[f_i(\mathbf{x}-\mathbf{c}_i\delta t, t) - f^{\mathrm{eq}}(\mathbf{x}-\mathbf{c}_i\delta t, t)\right]. \quad (3.20)$$

An equivalent and more popular form of the LB equation is given by:

$$f_i(\mathbf{x}+\mathbf{c}_i\delta t, t+\delta t) - f_i(\mathbf{x}, t) = -\frac{\delta t}{\tau}\left[f_i(\mathbf{x}, t) - f_i^{\mathrm{eq}}(\mathbf{x}, t)\right]. \quad (3.21)$$

The equilibrium distribution function satisfying all the lattice constraints is given by

$$\begin{aligned} f_i^{\mathrm{eq}}(\mathbf{x}, t) &= w_i\,\rho(\mathbf{x}, t)\Bigg[1 + \frac{1}{c_s^2}(\mathbf{c}_i\cdot\mathbf{u}(\mathbf{x}, t)) \\ &\quad + \frac{1}{2c_s^2}\left(\frac{1}{c_s^2}(\mathbf{c}_i\cdot\mathbf{u}(\mathbf{x}, t))^2 - \|\mathbf{u}(\mathbf{x}, t)\|^2\right)\Bigg], \end{aligned} \quad (3.22)$$

for the index $i = 0, 1, \ldots, m-1$. For the D2Q9 lattice shown in Figure 3.1, the weights w_i and velocity $\mathbf{c}_i$ are given by:

i	0	1	2	3	4	5	6	7	8
w_i	4/9	1/9	1/9	1/9	1/9	1/36	1/36	1/36	1/36
$c_{i\mathrm{x}}$	0	1	0	-1	0	1	-1	-1	1
$c_{i\mathrm{y}}$	0	0	1	0	-1	1	1	-1	-1

,

and $c_s = 1/\sqrt{3}$ [58].

The macroscopic density, $\rho(\mathbf{x}, t)$, and the velocity, $\mathbf{u}(\mathbf{x}, t)$, are given by:

$$\rho(\mathbf{x}, t) = \sum_i f_i(\mathbf{x}, t), \qquad \mathbf{u}(\mathbf{x}, t) = \frac{1}{\rho(\mathbf{x}, t)}\sum_i \mathbf{c}_i f_i(\mathbf{x}, t). \quad (3.23)$$

The velocity, space and time discrete Boltzmann equation (3.21) is commonly known as the lattice Boltzmann equation. A formal asymptotic technique known as the Chapman-Enskog (CE) method, in the limit of small Knudsen number Kn and low Mach number Ma, gives us the continuity Eq. (2.8) and the NS Eq. (2.10):

$$\begin{aligned} \boldsymbol{\nabla}\cdot\mathbf{u} &= 0, \\ \rho\left(\frac{\partial\mathbf{u}}{\partial t} + \mathbf{u}\cdot\boldsymbol{\nabla}\mathbf{u}\right) &= -\boldsymbol{\nabla}p + \boldsymbol{\nabla}\cdot\left[\mu\left(\boldsymbol{\nabla}\mathbf{u} + \boldsymbol{\nabla}\mathbf{u}^{\mathsf{T}}\right)\right], \end{aligned}$$

for the incompressible flows [58], where, the bulk pressure p is the thermodynamic pressure:

$$p = c_s^2 \rho, \tag{3.24}$$

and the dynamic viscosity μ is given by:

$$\mu = \nu\rho = \rho c_s^2 \left(\tau - \frac{\delta t}{2}\right), \tag{3.25}$$

where ν represents the kinematic viscosity. If $\tau \leq \delta t/2$ the method becomes unstable [60]. The square root of the density gradient of Eq. (3.24) gives us $c_s = \sqrt{\mathrm{d}p/\mathrm{d}\rho}$, which can be physically interpreted as the speed of sound.

So far we have only considered the LB model without any external force. In the next section we will discuss the force incorporation scheme in the LB method.

3.3.2 Adding forces in LB

The Boltzmann Eq. (3.3) can be rewritten as:

$$\frac{\partial f}{\partial t} + \mathbf{v} \cdot \boldsymbol{\nabla} f = Q'(f), \tag{3.26}$$

where

$$Q'(f) = Q(f) - \frac{\mathbf{K}}{m_\mathrm{p}} \cdot \boldsymbol{\nabla}_\mathrm{v} f. \tag{3.27}$$

The discrete and lattice dependent form of Eq. (3.26) with BGK collision operator is given by:

$$\begin{aligned} f_i(\mathbf{x} + \mathbf{c}_i \delta t, t + \delta t) - f_i(\mathbf{x}, t) \quad &= \quad -\frac{\delta t}{\tau}\left[f_i(\mathbf{x}, t) - f_i^{\mathrm{eq}}(\mathbf{x}, t)\right] \\ &\quad + \delta t\, S_i(\mathbf{x}, t), \end{aligned} \tag{3.28}$$

where S_i is the source term, $f_i^{\mathrm{eq}}(\mathbf{x}, t) \equiv f_i^{\mathrm{eq}}\big(\rho(\mathbf{x}, t), \mathbf{u}(\mathbf{x}, t)\big)$ and $\mathbf{u}$ is the local equilibrium velocity. In this section we will use $\mathbf{u}^{\mathrm{eq}}$ to represent the local equilibrium velocity. The streaming part of Eq. (3.28) remains the same, whereas the collision operation depends on the choice of S_i and $\mathbf{u}^{\mathrm{eq}}$. If the volumetric force $\mathbf{F} = \rho\mathbf{K}/m_\mathrm{p}$ is not constant, depending on the choice of S_i and $\mathbf{u}^{\mathrm{eq}}$, the resulting hydrodynamic equations are different. A detailed discussion on the different choices of S_i and $\mathbf{u}^{\mathrm{eq}}$ and on the resulting continuity and NS equations can be found in [68, 69]. Here, we use the force addition schemes as proposed by X. Shan and H. Chen [9] (SC-forcing) and by Z. Guo et al. [68] (Guo-forcing) to add forces to the LB model.

The SC-forcing scheme

According to the SC-forcing scheme, an external or internal force $\mathbf{F}$ (force per unit volume) can be incorporated by shifting the equilibrium velocity:

$$\mathbf{u}^{\mathrm{eq}}(\mathbf{x},t) = \frac{1}{\rho(\mathbf{x},t)}\sum_i \mathbf{c}_i f_i(\mathbf{x},t) + \tau\,\frac{\mathbf{F}(\mathbf{x},t)}{\rho(\mathbf{x},t)}, \tag{3.29}$$

and the source term in Eq. (3.28) $S_i = 0$ [9]. Finally, the local density is given by Eq. (3.23) and the hydrodynamic velocity at the next time step is obtained by using:

$$\mathbf{u}(\mathbf{x},t^*) = \frac{1}{2\rho}\left(\sum_i \mathbf{c}_i f_i(\mathbf{x},t) + \sum_i \mathbf{c}_i f_i(\mathbf{x},t+\delta t)\right), \tag{3.30}$$

where $t < t^* < t+\delta t$. Using the Taylor expansion for $f_i(\mathbf{x},t+\delta t)$ and Eq. (3.30) for the velocity, Eq. (3.30) becomes:

$$\mathbf{u}(\mathbf{x},t^*) = \mathbf{u}(\mathbf{x},t) + \frac{\delta t}{2}\frac{\partial \mathbf{u}(\mathbf{x},t)}{\partial t} + O(\delta t^2). \tag{3.31}$$

In this sense, we can say that the hydrodynamic velocity and density in the SC-forcing scheme are evaluated at staggered time levels, i.e, the hydrodynamic density and velocity are evaluated at time t and $t+\delta t/2$, respectively.

It can be shown that the hydrodynamic density, $\rho(\mathbf{x},t)$, and velocity defined by Eq. (3.30) satisfy the following mass and momentum conservation equations [68]:

$$\frac{\partial \rho}{\partial t} + \boldsymbol{\nabla}\cdot(\rho\mathbf{u}) = -\delta t\left(\tau-\frac{1}{2}\right)\boldsymbol{\nabla}\cdot\mathbf{F}, \tag{3.32a}$$

$$\begin{aligned}\frac{\partial(\rho\mathbf{u})}{\partial t} + \boldsymbol{\nabla}\cdot(\rho\mathbf{u}\mathbf{u}) &= -\boldsymbol{\nabla}p + \boldsymbol{\nabla}\cdot\left[\mu\left(\boldsymbol{\nabla}\mathbf{u}+\boldsymbol{\nabla}\mathbf{u}^{\mathsf{T}}\right)\right] + \mathbf{F} \\ &\quad -\delta t\left(\tau-\frac{1}{2}\right)\left[\frac{\partial \mathbf{F}}{\partial t} + \boldsymbol{\nabla}\cdot(\mathbf{u}\mathbf{F}+\mathbf{F}\mathbf{u})\right] \\ &\quad -\left[\delta t\left(\tau-\frac{1}{2}\right)\right]^2\boldsymbol{\nabla}\cdot\left(\frac{1}{\rho}\mathbf{F}\mathbf{F}\right) \\ &\quad +\frac{\delta t}{2}\left(\tau-\frac{1}{2}\right)\boldsymbol{\nabla}\cdot\left[\mu\left(\boldsymbol{\nabla}\mathbf{F}+\boldsymbol{\nabla}\mathbf{F}^{\mathsf{T}}\right)\right],\end{aligned} \tag{3.32b}$$

respectively, where $p = c_s^2\rho$.

If the force $\mathbf{F}$ is constant, the additional terms on the right hand side of Eqs. (3.32) vanish and we obtain the exact continuity Eq. (2.6) and NS Eq. (2.9).

The Guo-forcing scheme

According to the Guo-forcing scheme [68], an external/internal force $\mathbf{F}$ (force per unit volume) can be incorporated by shifting the equilibrium velocity:

$$\mathbf{u}^{\mathrm{eq}}(\mathbf{x},t) = \frac{1}{\rho(\mathbf{x},t)}\sum_i \mathbf{c}_i f_i(\mathbf{x},t) + \delta t\,\frac{\mathbf{F}(\mathbf{x},t)}{2\rho(\mathbf{x},t)}, \tag{3.33}$$

and by using the source term S_i as

$$S_i = w_i\left(1-\frac{\delta t}{2\tau}\right)\left(\frac{(\mathbf{c}_i-\mathbf{u})\cdot\mathbf{F}}{c_s^2} + \frac{(\mathbf{c}_i\cdot\mathbf{u})(\mathbf{c}_i\cdot\mathbf{F})}{c_s^4}\right), \tag{3.34}$$

where

$$\mathbf{u}(\mathbf{x},t^*) = \frac{1}{\rho(\mathbf{x},t)}\sum_i \mathbf{c}_i f_i(\mathbf{x},t) + \delta t\,\frac{\mathbf{F}(\mathbf{x},t)}{2\rho(\mathbf{x},t)}. \tag{3.35}$$

In the Guo scheme the hydrodynamic and the equilibrium velocities are the same. The hydrodynamic density and velocity given by Eq. (3.23) and Eq. (3.35) give the following hydrodynamic equations as a result of the CE expansion [68]:

$$\frac{\partial\rho}{\partial t} + \boldsymbol{\nabla}\cdot(\rho\mathbf{u}) = 0, \tag{3.36a}$$

$$\frac{\partial(\rho\mathbf{u})}{\partial t} + \boldsymbol{\nabla}\cdot(\rho\mathbf{u}\mathbf{u}) = -\boldsymbol{\nabla}p + \boldsymbol{\nabla}\cdot\left[\mu\left(\boldsymbol{\nabla}\mathbf{u} + \boldsymbol{\nabla}\mathbf{u}^{\mathsf{T}}\right)\right] + \mathbf{F}, \tag{3.36b}$$

where $p = c_s^2\rho$. Unlike the SC scheme, the hydrodynamic Eqs. (3.36) have no additional terms with respect to the continuity Eq. (2.6) and to the NS Eq. (2.9).

The hydrodynamic and the post-collision velocity for both the SC and Guo scheme are the same, moreover, for both Guo and SC scheme, the hydrodynamic velocity and density in the SC scheme are evaluated at the staggered time steps.

3.3.3 Boundary conditions

In order to obtain a unique solution of the NS equations for a given problem, we have to specify boundary conditions for the hydrodynamic variables ρ, p and $\mathbf{u}$. Similarly, in the LB method, we need boundary conditions for the distribution functions. The main challenge here is in converting back from the hydrodynamic variables to the particle distribution functions. Many studies have shown that, due to the kinetic nature of the method, the no-slip and the free-slip boundary conditions at the flat as well as at the curved boundaries,

can be easily imposed in the LB method [15, 70]. In fact, this is one of the major advantages of using the LB method for complex geometries like porous media [39]. Details of these boundary conditions can be found in [15, 31, 71, 72].

In this section, we provide the details for the various boundary conditions in a two-dimensional (2D) lattice of size $N_\mathrm{x} \times N_\mathrm{y}$ and for simplicity, we consider that the fluid domain is aligned with the coordinate axes and that there is no curved boundary in the domain. The distances between two nearest nodes in x and y-direction are $\delta x = 1$ and $\delta y = 1$, respectively. The collection of fluid nodes is represented by X, and defined as $X = \{\mathbf{x} : \mathbf{x} \equiv (k, j)\}$, where $k = 1, 2, \ldots, N_\mathrm{x}$ and $j = 1, 2, \ldots, N_\mathrm{y}$. The boundary of this rectangular domain can be divided in four parts: A, B, C and D. The collection of fluid nodes at these boundaries are defined as: $X_\mathrm{A} = \{\mathbf{x}_{\mathrm{A},j} : \mathbf{x}_{\mathrm{A},j} \equiv (1, j)\}$, $X_\mathrm{B} = \{\mathbf{x}_{\mathrm{B},k} : \mathbf{x}_{\mathrm{B},k} \equiv (k, 1)\}$, $X_\mathrm{C} = \{\mathbf{x}_{\mathrm{C},j} : \mathbf{x}_{\mathrm{C},j} \equiv (N_\mathrm{x}, j)\}$ and $X_\mathrm{D} = \{\mathbf{x}_{\mathrm{D},k} : \mathbf{x}_{\mathrm{D},k} \equiv (k, N_\mathrm{y})\}$. The nodes outside of the fluid domain will be referred as to ghost nodes in this thesis. The collection of ghost nodes for the boundaries A, B, C and D are denoted by $X'_\mathrm{A}, X'_\mathrm{B}, X'_\mathrm{C}$ and X'_D, respectively. For the ghost nodes the index runs over $k = 0, 1, \ldots, N_\mathrm{x} + 1$ and $j = 0, 1, \ldots, N_\mathrm{y} + 1$; a schematic representation is shown in Figure 3.2.

Periodic boundary condition

For a periodic flow along the x-axis, shown in Figure 3.2, the flow properties at the boundary A are exactly the same as the flow properties at the boundary C of the domain and vice-versa. In order to impose the periodic boundary condition in the LB method, we simply copy the distribution function from the fluid nodes at the boundary C to the ghost nodes at the boundary A, and similarly the distribution function from fluid nodes at the boundary A to the ghost nodes at boundary C. In our notation, this boundary condition can be implemented as:

$$f_i(\mathbf{x}'_{\mathrm{A},j}, t) = f_i(\mathbf{x}_{\mathrm{C},j}, t), \qquad f_i(\mathbf{x}'_{\mathrm{C},j}, t) = f_i(\mathbf{x}_{\mathrm{A},j}, t). \tag{3.37}$$

The above relation holds for all times t, velocity directions i and indices j for the boundaries A and C. The periodic boundary conditions is the simplest boundary condition that can be used for the LB simulation. Furthermore, the boundary condition conserves mass and momentum in the system.

No-slip boundary condition

The hydrodynamic no-slip boundary condition means that the velocity components of the fluid node at the boundary are exactly the same as the velocity

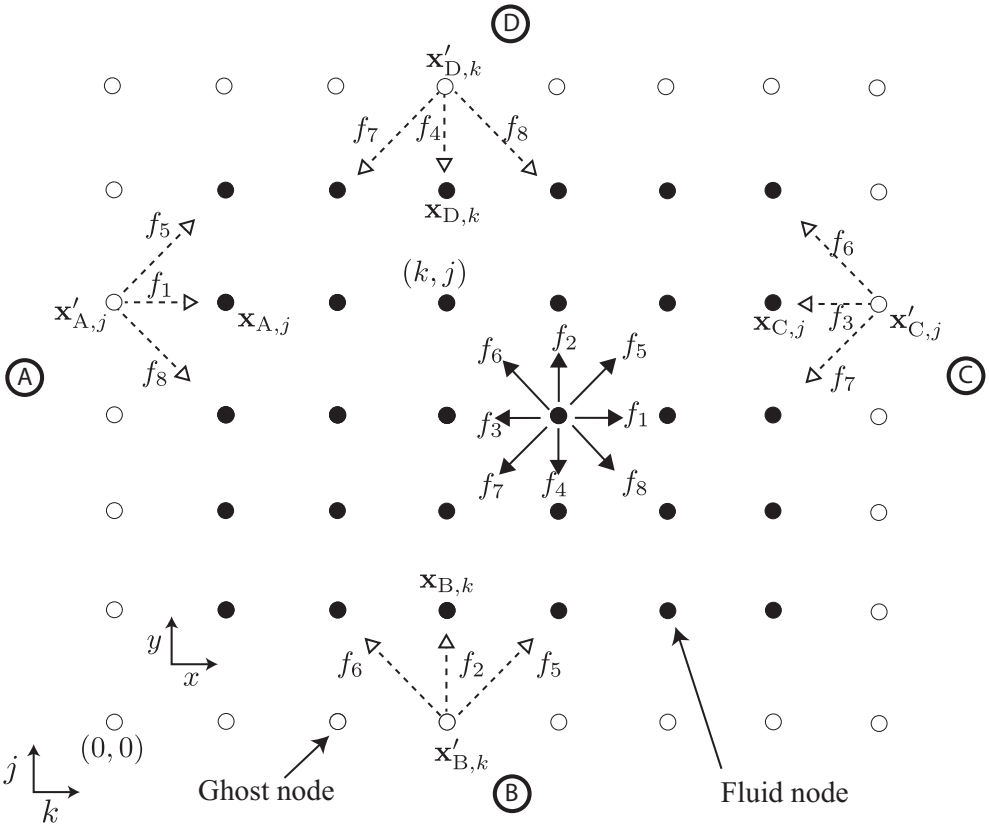

Figure 3.2: A schematics showing the unknown distribution functions, f_i, (dashed arrows) at one of the ghost nodes from each boundary, that must be initialized before the streaming step at the fluid nodes in the LB algorithm. The solid and hollow nodes represent the fluid and ghost nodes, respectively. The value assigned to the unknown f_i depends on the particle distribution function and/or the hydrodynamic variables ρ, $\mathbf{u}$ at the nearest fluid node.

of the solid node. In general, these boundary conditions are referred to as the Dirichlet boundary condition for the velocity. In our notation, we consider a solid flat plate at the boundary B, moving along the horizontal axis with velocity U_{p}. The unknown distribution functions, that need to be initialized before streaming, are f_6, f_2 and f_5. We impose the mid-grid bounce back scheme for the no-slip boundary condition at the fluid nodes on the boundary [31]. In our notation, the implementation of the mid-grid bounce back looks

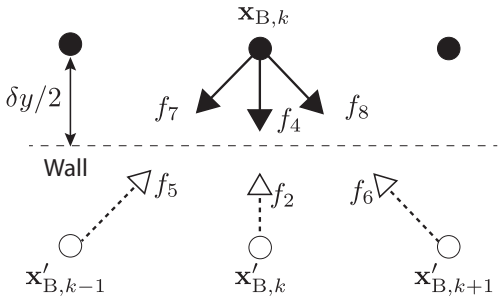

Figure 3.3: A schematic representation of the mid-grid bounce back (no-slip) boundary condition.

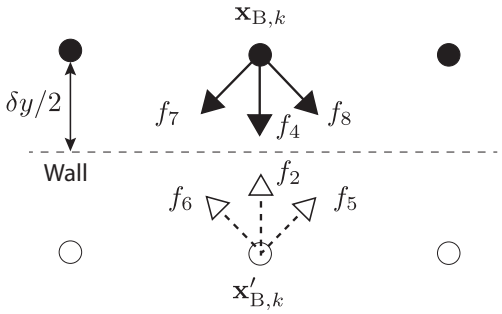

Figure 3.4: A schematics representation of the mid-grid specular reflection (free-slip) boundary condition.

like, see Figure 3.3:

$$f_2(\mathbf{x}'_{\mathrm{B},k}, t) = f_4(\mathbf{x}_{\mathrm{B},k}, t), \tag{3.38a}$$

$$f_5(\mathbf{x}'_{\mathrm{B},k-1}, t) = f_7(\mathbf{x}_{\mathrm{B},k}, t) + 0.5\, c_s^2\, \rho(\mathbf{x}_{\mathrm{B},k}, t)\, U_{\mathrm{p}}, \tag{3.38b}$$

$$f_6(\mathbf{x}'_{\mathrm{B},k+1}, t) = f_8(\mathbf{x}_{\mathrm{B},k}, t) - 0.5\, c_s^2\, \rho(\mathbf{x}_{\mathrm{B},k}, t)\, U_{\mathrm{p}}. \tag{3.38c}$$

The above relations hold for all nodes X_{B} at the boundary B. As the name suggests, the mid-grid bounce back boundary conditions effectively gives the no-slip boundary conditions at $y = 0.5\,\delta y$. Advantages of using the mid-grid bounce back condition are that it is second order accurate in space and conserves mass and momentum [31].

Free-slip boundary condition

The free-slip hydrodynamic boundary condition means that $v = 0$ and $\mathrm{d}u/\mathrm{d}y = 0$, where u, v are the velocity components along and perpendicular to the wall.

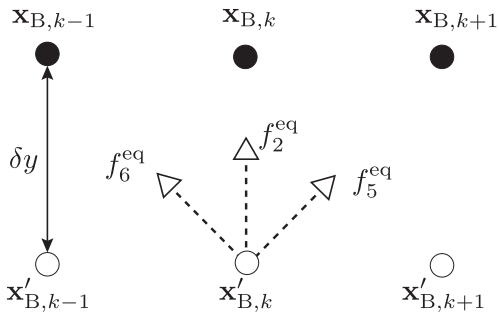

Figure 3.5: A schematic representation of the open boundary conditions. The values assigned to the f_i (dotted arrows) depend on the hydrodynamic variables $\rho, \mathbf{u}$ at the nearest fluid node.

The free-slip boundary condition in the LB method can be imposed by applying specular reflection boundary conditions on the distribution function [31]. In our notations, the implementation of the specular-reflection boundary condition in the LB method at the boundary B, looks like (see Figure 3.4):

$$f_2(\mathbf{x}'_{\mathrm{B},k}, t) = f_4(\mathbf{x}_{\mathrm{B},k}, t), \tag{3.39a}$$

$$f_5(\mathbf{x}'_{\mathrm{B},k}, t) = f_8(\mathbf{x}_{\mathrm{B},k}, t), \tag{3.39b}$$

$$f_6(\mathbf{x}'_{\mathrm{B},k}, t) = f_7(\mathbf{x}_{\mathrm{B},k}, t). \tag{3.39c}$$

The above relation holds for all fluid nodes at the boundary B. Similar to the bounce back boundary conditions, this boundary condition gives the free-slip boundary condition at $y = 0.5\,\delta y$ with second order accuracy in space and conservation of mass and momentum.

Open boundary condition

In this thesis, we use open boundary conditions to impose: 1) hydrodynamic pressure gradient across the flow domain, 2) mass flux and 3) zero-stress conditions. The issue here is that these boundary conditions depend on the hydrodynamic variables, but for the LB simulations we need boundary condition for the distribution functions. We use the equilibrium distribution function given by Eq. (3.22) for the unknown values $f_5(\mathbf{x}'_{\mathrm{B},k}, t), f_2(\mathbf{x}'_{\mathrm{B},k}, t), f_6(\mathbf{x}'_{\mathrm{B},k}, t)$ at the ghost nodes X'_{B}, see Figure 3.5. The evaluation of the equilibrium distribution function requires the density and velocity at ghost nodes. For different choices of density and velocity at the ghost nodes X'_{B} we get different hydrodynamic boundary conditions.

Let us assume that we need to impose a constant pressure gradient along the x-axis of the domain shown in Figure 3.2. The pressure in the LB model is related to the density via the equation of state ($p = c_s^2\rho$). In order to impose the pressure gradient, we use a constant density ρ_{in} on the nodes X'_{A}, and a density ρ_{out} at the nodes X'_{C}. The velocity values at the ghost nodes X'_{A} and X'_{C} are kept exactly the same as the velocity at fluid nodes X_{A} and X_{C}, respectively. Finally, we use the discrete equilibrium distribution function given by Eq. (3.22) to evaluate the unknown distribution at the nodes X'_{A} and X'_{C}.

3.4 Shan-Chen model

This section presents an overview of the Shan-Chen (SC) model for the multi-phase flows simulations [9, 10], and modeling of the contact angle in the SC model [73]. The SC model is based on the long-range interaction between particles, with an interaction potential given by [9]:

$$V(\mathbf{x}, \mathbf{x}', t) = G(\mathbf{x}, \mathbf{x}')\psi(\mathbf{x}, t)\psi(\mathbf{x}', t), \tag{3.40}$$

where $G_{\mathrm{sc}}(\mathbf{x}, \mathbf{x}')$ is a Green's function, and $\psi(\mathbf{x}, t) \equiv \psi[\rho(\mathbf{x}, t)]$ is a pseudo-mass density function. In order to simulate multi-phase flows using the SC LB model, it is sufficient to choose only the first neighbor particle interactions [74]:

$$G(\mathbf{x}, \mathbf{x}') = \begin{cases} G_{\mathrm{sc}} & \text{if } \|\mathbf{x} - \mathbf{x}'\| = \|\mathbf{c}_i\|, \\ 0 & \text{if } \|\mathbf{x} - \mathbf{x}'\| \neq \|\mathbf{c}_i\|, \end{cases} \tag{3.41}$$

where $i = 1, \ldots, m-1$, $\mathbf{x}$, $\mathbf{x}'$ are lattice cites in the LB model, G_{sc} is referred to as interaction strength in the SC model. The magnitude of G_{sc} gives the interaction strength between the fluids phases, and the sign of the G_{sc} models the repulsive ($G_{\mathrm{sc}} > 0$) or the attractive ($G_{\mathrm{sc}} < 0$) forces. The effective force due to the nearest neighbor interaction on a lattice is given by [74]:

$$\mathbf{F}_{\mathrm{sc}}(\mathbf{x}, t) = -G_{\mathrm{sc}}\psi(\mathbf{x}, t) \sum_i w_i \psi(\mathbf{x} + \mathbf{c}_i\delta t, t)\, \mathbf{c}_i. \tag{3.42}$$

The pseudo-density function that we use for the SC simulations in this thesis is [9]:

$$\psi(\rho) = \rho_0[1 - \exp(-\rho/\rho_0)], \tag{3.43}$$

where ρ_0 is a constant. The phase transition in the SC model is triggered by the density gradients and the special choice of ψ helps to obtain saturated

high- and low-density regions in the SC LB simulations. In this thesis, we refer to these high- and low-density regions as to the liquid and the vapor phases. The SC model is a diffuse interface model. where the thickness of the interface with increases with $G_{\rm sc}$. The physical interpretation of the SC force, $\mathbf{F}_{\rm sc}$, can be given by the following expession:

$$\mathbf{F}_{\rm sc} = -G_{\rm sc} c_s^2\, \delta t\, \psi \boldsymbol{\nabla}\psi - \frac{G_{\rm sc}}{2} c_s^4 (\delta t)^3 \psi \boldsymbol{\nabla}\left(\boldsymbol{\nabla}^2\psi\right) + O((\delta t)^5). \tag{3.44}$$

This expression is obtained by using the Taylor expansion for $\psi(\mathbf{x} + \mathbf{c}_i\delta t)$ and by the isotropy condition on w_i in Eq. (3.42). The first term contributes into the non-ideal pressure and the second terms models the surface tension in the SC model.

3.4.1 Fluid properties in the SC model

The pressure tensor for non-ideal fluids at equilibrium is given by [75]:

$$\boldsymbol{\nabla}\cdot\mathbf{P} = \boldsymbol{\nabla}(p\mathbf{I}) - \mathbf{F}_{\rm sc}, \tag{3.45}$$

where $p = c_s^2\rho$ is the pressure corresponding to the ideal gas. Substituting Eq. (3.44), with $\delta t = 1$, into Eq. (3.45) and integrating, one obtains the following pressure tensor [75]:

$$\begin{aligned} P_{\alpha\beta} &= \left(c_s^2\rho + \frac{c_s^2 G_{\rm sc}}{2}\psi^2 + \frac{c_s^4 G_{\rm sc}}{2}\psi\boldsymbol{\nabla}^2\psi + \frac{c_s^4 G_{\rm sc}}{4}\|\boldsymbol{\nabla}\psi\|^2\right)\delta_{\alpha\beta} \\ &\quad - \frac{c_s^4 G_{\rm sc}}{2}\partial_\alpha\psi\partial_\beta\psi, \end{aligned} \tag{3.46}$$

The first two terms of the pressure tensor, given by Eq. (3.46), correspond to the equation of state for the SC multi-phase model:

$$p(\rho) = c_s^2\rho + \frac{c_s^2}{2} G_{\rm sc}\, \psi^2(\rho). \tag{3.47}$$

A graphical representation of the non-ideal equation of state is shown in Figure 3.6 (left panel). Using the Maxwell's construction and the equation of state one can estimate the equilibrium liquid and vapor densities in the multi-phase SC model, see Figure 3.6 (right panel). A table showing the values of equilibrium densities and surface tension for different values of $G_{\rm sc}$ is shown in Table 3.1. The pressure tensor given by Eq. (3.46) depends on the force incorporation schemes used in the LB method. The bulk pressure in the fluid is independent of force incorporation schemes, however the value of the surface tension depends on the forcing scheme in the LB method [10].

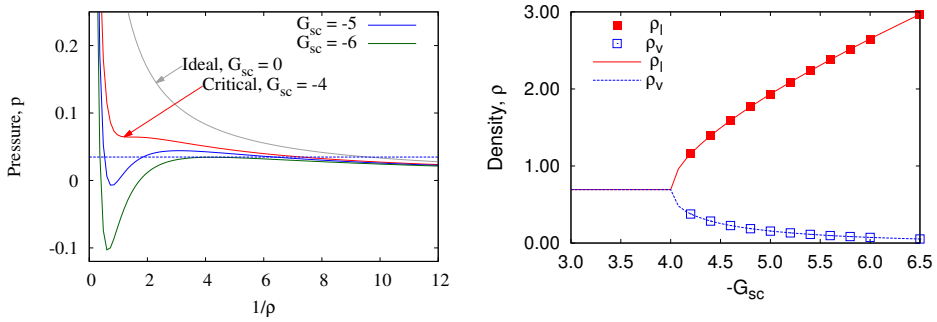

Figure 3.6: Left panel: the gray curve shows the equation of state for the ideal gas, Eq. (3.24). The colored lines show the equation of state given by the SC multi-phase model, Eq. (3.47). The blue dotted line shows the bulk pressure corresponding to $G_{\rm sc} = -5$ in the equilibrium state. The minimum and maximum values of ρ at which the dotted blue line intersect the solid blue curve, correspond to the equilibrium phase densities of the vapour $\rho_{\rm v}$ and liquid ρ_ℓ, respectively (Maxwell construction). Right panel: dependence of the equilibrium densities, $\rho_\ell, \rho_{\rm v}$ on the interaction parameter $G_{\rm sc}$. The LB results are shown by square symbols whereas the curves represents the results obtained from the Maxwell construction. The LB simulation parameters: $N_{\rm x} \times N_{\rm y} = 80 \times 1$, $\tau = 1$.

Surface tension

For a given pressure tensor, $\mathbf{P}$, the following mechanical condition can be used to estimate the surface tension in a LB model [14]:

$$\boldsymbol{\nabla}\gamma_{\ell{\rm v}} \cdot \hat{\mathbf{n}} = P^{\rm n} - P^{\rm t}, \tag{3.48}$$

where γ is the surface tension between the two fluids, $\hat{\mathbf{n}}$ and $\hat{\mathbf{t}}$ are the unit vectors normal and tangential to the interface, $P^{\rm n} \equiv (\mathbf{P}\hat{\mathbf{n}}) \cdot \hat{\mathbf{n}}$ is the normal and $P^{\rm t} \equiv (\mathbf{P}\hat{\mathbf{n}}) \cdot \hat{\mathbf{t}}$ is the tangential component of the pressure tensor.

For a flat interface perpendicular to the y-axis all the derivatives of ψ with respect to x vanish, thus the pressure tensor given by Eq. (3.46) become:

$$P_{\rm yy} = c_s^2\rho + \frac{c_s^2 G_{\rm sc}}{2}\psi^2 + \frac{c_s^4 G_{\rm sc}}{2}\psi\partial_{\rm yy}\psi - \frac{c_s^4 G_{\rm sc}}{4}(\partial_{\rm y}\psi)^2, \tag{3.49a}$$

$$P_{\rm xx} = c_s^2\rho + \frac{c_s^2 G_{\rm sc}}{2}\psi^2 + \frac{c_s^4 G_{\rm sc}}{2}\psi\partial_{\rm yy}\psi + \frac{c_s^4 G_{\rm sc}}{4}(\partial_{\rm y}\psi)^2, \tag{3.49b}$$

and Eq. (3.48) becomes $\partial_{\rm y}\gamma_{\ell{\rm v}} = P_{\rm yy} - P_{\rm xx}$. This leads to the surface tension

in the multi-phase SC-LB model [73]:

$$\gamma_{\ell \mathrm{v}} = -\frac{1}{2} c_s^4 G_{\mathrm{sc}} \int_{y_{\mathrm{v}}}^{y_\ell} \left(\frac{\mathrm{d}\psi}{\mathrm{d}y} \right)^2 \mathrm{d}y, \tag{3.50}$$

where the interval $[y_{\mathrm{v}}, y_\ell]$ is the location of the diffused interface and $\gamma_{\ell \mathrm{v}}$ the surface tension between liquid-vapor interface.

However, if we use the SC-forcing scheme to incorporate the SC force, the pressure tensor is given by [10]:

$$\begin{aligned} P_{\alpha\beta} &= \left(c_s^2 \rho + \frac{c_s^2 G_{\mathrm{sc}}}{2} \psi^2 + \frac{c_s^4 G_{\mathrm{sc}}}{2} \psi \boldsymbol{\nabla}^2 \psi + \frac{c_s^4 G_{\mathrm{sc}}}{4} |\boldsymbol{\nabla} \psi|^2 \right) \delta_{\alpha\beta} \\ &\quad - \frac{c_s^4 G_{\mathrm{sc}}}{2} \partial_\alpha \psi \partial_\beta \psi + \left(\tau - \frac{1}{2} \right)^2 \frac{1}{\rho} F_\alpha F_\beta, \end{aligned} \tag{3.51}$$

In this case, the surface tension corresponding to the pressure tensor shown in Eq. (3.51) becomes:

$$\tilde{\gamma}_{\ell \mathrm{v}} = -\frac{1}{2} c_s^4 G_{\mathrm{sc}} \int_{y_{\mathrm{v}}}^{y_\ell} \left(\frac{\mathrm{d}\psi}{\mathrm{d}y} \right)^2 \mathrm{d}y + \left(\tau - \frac{1}{2} \right)^2 \int_{y_{\mathrm{v}}}^{y_\ell} \frac{1}{\rho} (F_{\mathrm{sc},y})^2 \, \mathrm{d}y, \tag{3.52}$$

where $F_{\mathrm{sc},y}$ is the Shan-Chan force along the y-axis. The LB simulations showing the surface tension as a function of the interaction parameter G_{sc} is shown in Figure 3.7.

The Laplace test

The Laplace Eq. (2.15) can be used to both validate and estimate the surface tension for the multi-phase LB simulations. For a 2D drop of radius R_{D}, the radius of curvature is given by $\kappa = 1/R_{\mathrm{D}}$, hence, using the Laplace Eq. (2.15), the surface tension between the liquid-vapor interface $\gamma_{\ell \mathrm{v}}$ is given by:

$$p_{\mathrm{in}} - p_{\mathrm{out}} = \frac{\gamma_{\ell \mathrm{v}}}{R_{\mathrm{D}}}, \tag{3.53}$$

where p_{in} and p_{out} are the pressure inside and outside of the drop, respectively. The SC model is a diffuse interface model, therefore the radius of the drop needs to be approximated appropriately. We use the following mass balance condition to estimate the radius of a 2D drop:

$$M_t = \pi R_{\mathrm{D}}^2 \rho_\ell + (L^2 - \pi R_{\mathrm{D}}^2) \rho_{\mathrm{v}}, \tag{3.54}$$

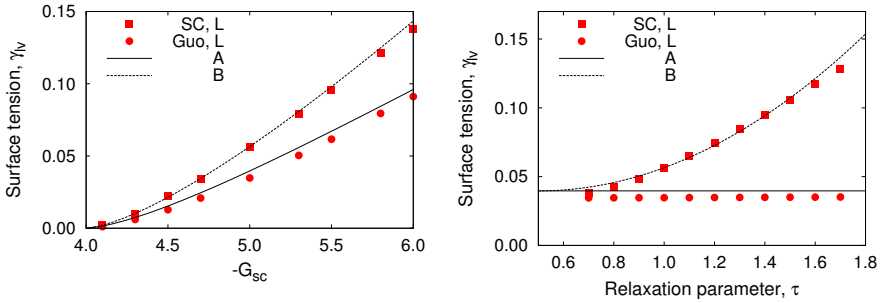

Figure 3.7: Surface tension $\gamma_{\ell v}$ as a function of the interaction parameter G_{sc} (left panel) and of the relaxation parameter τ (right panel) in the SC two-phase model. The labels A and B represent the surface tension using Eq. (3.50) and Eq. (3.52) for the flat interface, respectively. The label L represents the surface tension from the Laplace test on a 2D drop of radius 20 with center at (40.5, 40.5). The label SC and Guo represents the Shan-Chen [10] and Guo [68], force implementation schemes, respectively. For the analytical expression Eq. (3.52) shown by label B in the left panel we use $\tau = 1$, and the results in the right panel corresponds to $G_{sc} = -5$. The initial fluid densities $\rho_\ell = 1.9324$ and $\rho_v = 0.1564$ are kept fixed for both SC and Guo schemes. All the LB simulations are performed in a domain of size $N_x \times N_y = 80 \times 80$, until the steady state is reached.

where M_t is the total mass of the fluid in the domain $N_x \times N_y = L \times L$ and ρ_ℓ and ρ_v are the densities of the liquid and the vapor in the steady state, respectively. Eq. (3.54) can be rearranged to give an approximate radius of a drop with diffuse interface:

$$R_D = \sqrt{\frac{M_t - L^2\rho_v}{\pi(\rho_\ell - \rho_v)}}. \tag{3.55}$$

An estimate of the surface tension using the Laplace test and its validation using Eqs. (3.53) and (3.55) for the MP-LB model, is shown in Figure 3.7.

3.4.2 Modeling wettability

In this thesis, we are using the schemes proposed by Benzi et al.[73] and Huang et al.[76] to the wettability of a solid in multi-phase and multico-mponent SC model, respectively. In this section we only present results for the contact angle modelling in the multi-phase SC model.

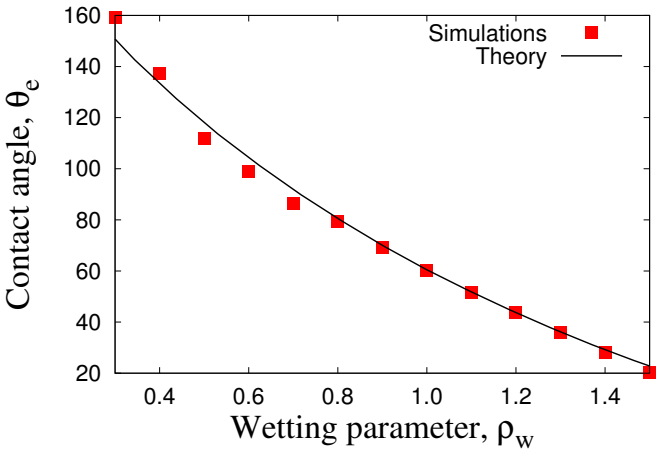

Figure 3.8: Contact angle as a function of the wetting parameter for the SC multi-phase model. Simulation parameters: $N_\mathrm{x} \times N_\mathrm{y} = 180 \times 55$, $G_\mathrm{sc} = -5$, $\tau = 1$.

In the model proposed by Benzi et al. [73], the force between the wall and the fluid is given by:

$$\mathbf{F}_\mathrm{ads} = -G_\mathrm{sc}\psi \sum_i w_i \Psi(\mathbf{x} + \mathbf{c}_i \delta t)\mathbf{c}_i, \tag{3.56}$$

where $\Psi(\mathbf{x}', t) = \psi(\rho_w)$ or $\psi[\rho(\mathbf{x}', t)]$ if $\mathbf{x}'$ is a wall node or fluid node. Here, the parameter ρ_w is varied to control the equilibrium contact angle at the wall in the liquid phase. The analytical estimate of the contact angle measured in the liquid phase is given by [73]:

$$\cos\theta_\mathrm{e} = \frac{\int_{y_\mathrm{v}}^{y_\mathrm{s}} (\boldsymbol{\nabla}\psi \cdot \hat{\mathbf{n}}_\mathrm{sv})^2 \, \mathrm{d}n - \int_{y_\mathrm{s}}^{y_\ell} (\boldsymbol{\nabla}\psi \cdot \hat{\mathbf{n}}_{\mathrm{s}\ell})^2 \, \mathrm{d}n}{\int_{y_\mathrm{v}}^{y_\ell} (\boldsymbol{\nabla}\psi \cdot \hat{\mathbf{n}}_{\ell\mathrm{v}})^2 \, \mathrm{d}n}, \tag{3.57}$$

where $\hat{\mathbf{n}}_{\mathrm{s}\ell}$, $\hat{\mathbf{n}}_\mathrm{sv}$ and $\hat{\mathbf{n}}_{\ell\mathrm{v}}$ are the normal vectors along the solid-liquid, the solid-vapor and the liquid-vapor interfaces. We adapt the numerical solution given in [73] to approximate the integrals in Eq. (3.57), a comparison of the MP-LB simulations to model the contact angle and Eq. (3.57) is shown in Figure 3.8.

The 2D MP LB simulations are initialized with a semicircular drop on the plate, which changes its shape depending on the wetting parameter ρ_w. No-slip boundary conditions are used for the walls parallel to each other and

periodic boundary condition are used at other two boundaries. The contact angle is measured by fitting a quadratic function to the interface profile at the contact line. Here we use the threshold value of the density $(\rho_\ell + \rho_\mathrm{v})/2$ to approximate the interface profile. The error in the measurement of the contact angle is $\pm 5^\circ$, which goes up to $\pm 10^\circ$ for the contact angle measurement close to $0^\circ$and 180°.

While we do not include contact angle hysteresis in this thesis, the model has been proposed to include it in the SC model [77].

3.5 Numerical artifacts in the LB method

3.5.1 Spurious velocities

The spurious velocities are a common inconvenience in diffuse interface models, a review of the spurious velocity in different LB multi-phase models is shown in [78], while a comparision between LB and phase field model can be found in [79].

The spurious currents typically arises near curved interface, see Figure 3.9 (left panel). In the SC LB simulations they arises due to the insufficient isotropy in calculating the density gradients [80]. Although, the spurious currents can be reduce by using higher order lattices [75], this approach make the LB simulation more expensive [80]. A comparison of the magnitude of the spurious velocity in the SC model using the Guo-forcing scheme and the SC-forcing scheme is shown in Figure 3.9 (right panel).

3.5.2 The checker-board effect

If the hydrodynamic velocity or pressure fluctuation in a fluid simulations have high frequency oscillations, the grid resolution used in the standard LB scheme may not be sufficient to get a good approximation of the derivatives. These inaccurate derivatives leads to inaccurate values of the equilibrium velocity, which usually does not damp out in time: this numerical artifact is know as the checker-board effect. In this section, we will discuss the Lax-Wendroff (LW) streaming scheme proposed by Guo [81], to eliminate the checkerboard effects.

The checkerboard effect for single phase and the multi-phase flow is shown in the left and in the right panels of Figure 3.10, respectively. In some cases the effect is found to be dependent on the parity of the number of grid points used in the simulation. Even if we use a uniform density and velocity to initialize the LB simulation, the checkerboard effect can still be induced by the bounce

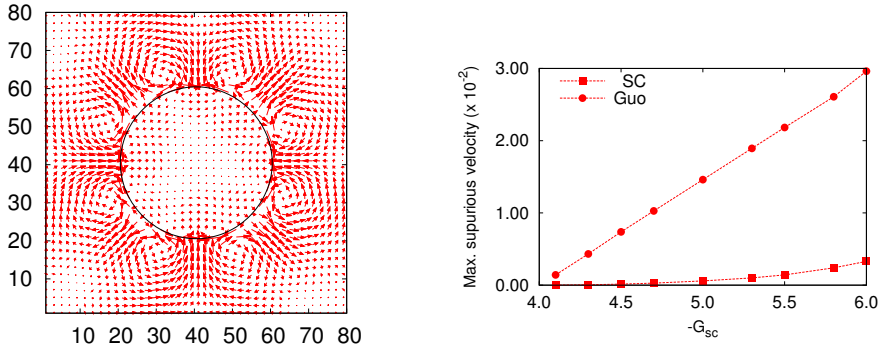

Figure 3.9: Velocity vectors showing the spurious velocities at the interface of a 2D drop. The interface shown as the black curve is defined by choosing the threshold density, $(\rho_\ell + \rho_\mathrm{v})/2$. Right panel: amplitude of the maximum spurious velocity is 5×10^{-3}. Parameters for the LB simulation: $N_\mathrm{x} \times N_\mathrm{y} = 80 \times 80$, $\tau = 1$, $G_\mathrm{sc} = -5$, centre of the drop (40.5, 40.5) and drop radius, $R_\mathrm{D} = 20$.

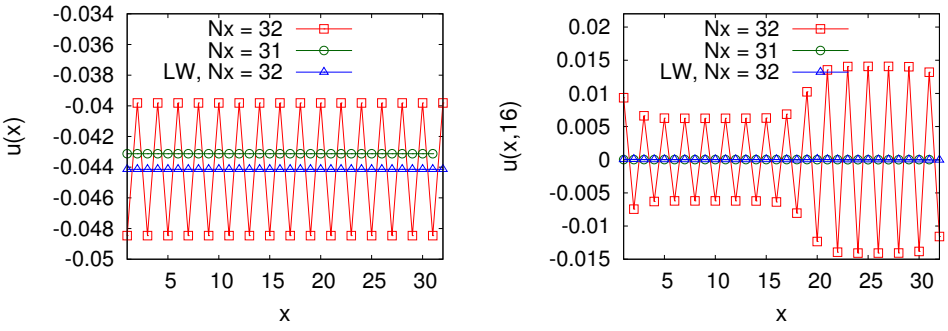

Figure 3.10: The checkerboard effect for single phase (left panel) and the multi-phase (right panel) LB simulations. Simulation parameter (left panel): $N_\mathrm{x} \times N_\mathrm{y} = N_\mathrm{x} \times 1$, $\tau = 1$. Simulation parameter (right panel): $N_\mathrm{x} \times N_\mathrm{y} = N_\mathrm{x} \times 32$, $\tau = 1$, $G_\mathrm{sc} = -5$. The parameter Cr *used for the LW LB simulation is* $\mathrm{Cr} = 0.999$. *The single phase simulation shown in the left panel is initialized using $\rho = 1$ and a perturbed velocity field $\mathbf{u}$. The multi-phase simulation is initialized using equilibrium densities and zero velocities. The LB simulation performed using the LW scheme (shown by label LW) effectively eliminates the checkerboard effect shown in the standard LB scheme.*

back boundary condition at the curved boundaries for single-phase flow. For multi-phase flows the effect is usually triggered by spurious velocities at the interface. A detailed study of the checkerboard effect in the LB method can be fond in [81, 82]. Here we show the Lax-Wendroff (LW) scheme to eliminate the checkerboard effects in the single and multi-phase LB simulations [81].

The LB Eq. (3.21) can be divided into two parts, collision and streaming:

$$\frac{\partial f_i}{\partial t} = -\frac{1}{\tau'}\left[f_i(\mathbf{x},t) - f^{\mathrm{eq}}(\rho,\mathbf{u})\right], \tag{3.58a}$$

$$\frac{\partial f_i}{\partial t} + \mathbf{c}_i \cdot \boldsymbol{\nabla} f_i = 0. \tag{3.58b}$$

The approximate solution of Eq. (3.58a) is given by the explicit Euler method:

$$f_i'(\mathbf{x},t) = f_i(\mathbf{x},t) - \frac{\delta t'}{\tau'}\left[f_i(\mathbf{x},t) - f^{\mathrm{eq}}(\rho,\mathbf{u})\right]. \tag{3.59}$$

Using $f_i'(\mathbf{x},t)$ as initial condition, the solution of Eq. (3.58b) is given by [81]:

$$f_i(\mathbf{x},t+\delta t') = \alpha_{-1} f_i'(\mathbf{x}-\mathbf{e}_i\delta x_i,t) + \alpha_0 f_i'(\mathbf{x},t) + \alpha_1 f_i'(\mathbf{x}+\mathbf{e}_i\delta x_i,t), \tag{3.60}$$

where $\delta t' = \mathrm{Cr}\,\delta t$, $\alpha_{-1} = \mathrm{Cr}(\mathrm{Cr}+1)/2$, $\alpha_0 = 1-\mathrm{Cr}^2$ and $\alpha_1 = \mathrm{Cr}(\mathrm{Cr}-1)/2$, with $\mathrm{Cr} = \|\mathbf{c}_i\|\,\delta t/\delta x_i$ and $0 < \mathrm{Cr} \leq 1$. The CE expansion on the LW LB scheme under appropriate conditions on velocity and lattice symmetry, results in the incompressible NS equation, with kinematic viscosity [81]:

$$\nu = c_s^2\,\delta t'\left(\tau' - \frac{1}{2}\right). \tag{3.61}$$

In order to have the same hydrodynamic viscosity as the standard LB model in Eq. (3.25), we define τ' as:

$$\tau' = \frac{1}{2} + \frac{1}{\mathrm{Cr}}\left(\tau - \frac{1}{2}\right). \tag{3.62}$$

For $\mathrm{Cr} = 1$ we get $\tau' = \tau$, $\alpha_{-1} = 1, \alpha_0 = 0$ and $\alpha_1 = 0$ and therefore the Lax-Wendroff (LW) LB scheme reduces to the standard LB scheme, given by Eq. (3.21). The results of the LB simulations using the LW scheme are shown in Figure 3.10. For the LB simulations shown in this thesis we are using the LW scheme with $\mathrm{Cr} = 0.999$, which effectively removes the checkerboard effect from the standard LB model.

$-G_{\mathrm{sc}}$	ρ_ℓ	ρ_{v}	$\rho_{\mathrm{v}}/\rho_\ell$	$\gamma_{\ell\mathrm{v}}$
$-G_{\mathrm{sc}} \leq 4.0$	ln(2)	ln(2)	1	0
4.1	1.0043	0.4557	0.4537	0.0020
4.2	1.1558	0.3774	0.3265	0.0057
4.3	1.2806	0.3248	0.2536	0.0103
4.4	1.3915	0.2851	0.2049	0.0156
4.5	1.4935	0.2534	0.1697	0.0215
4.6	1.5892	0.2273	0.1430	0.0277
4.7	1.6799	0.2052	0.1221	0.0345
4.8	1.7668	0.1863	0.1054	0.0415
4.9	1.8505	0.1699	0.0918	0.0489
5.0	1.9314	0.1560	0.0808	0.0566
5.5	2.3067	0.1041	0.0451	0.0981
6.0	2.6500	0.0755	0.0285	0.1435
6.5	2.9695	0.0534	0.0180	0.1920
7.0	3.2600	0.0412	0.0126	0.2431

Table 3.1: Equilibrium liquid and vapor densities, density ratios and surface tensions for different values of interaction parameter G_{sc} for the SC force incorporation scheme. The value of the surface tension is evaluated using Eq. (3.52) ($\tau = 1$).

4 | Plunging Plate Problem *

In this Chapter, we present the validation of the LB method for contact line motion and for moving interfaces, and we compare it with the generalized lubrication (GL) model. The Chapter is divided in the following two parts: in the first part, the static and dynamical behavior of the contact line, between two fluids and a solid plate, has been studied by means of the LB method. The different fluid phases and their contact with the plate are simulated by means of the standard Shan-Chen (SC) model. We study different regimes and compare the MC vs. the MP LB models near the contact line. We qualitatively study the influence of wall and open boundary conditions on the equilibrium shape of the meniscus, the boundary condition that model the free end of the interface in our LB simulations. In the second part, we present the GL model for the generic case of two fluids with arbitrary viscosity ratio and of a plate moving in either direction (pulled or pushed in the bath). We find a good agreement between the LB and GL simulations, particularly for small capillary numbers. The GL model developed here includes non-zero air viscosity that allows us to study the dependence of the critical capillary number for air entrainment on the other parameters in the problem, i.e. contact angle and viscosity ratio.

4.1 Introduction

The motion of the contact line, the common boundary between a solid, a liquid, and its equilibrium vapor, is key to several important applications like coating, painting or oil recovery [21, 83, 84]. The dynamics of the contact line has stimulated theoretical studies and experimental investigations [22, 85–89]. The dynamics is controlled by a rather subtle competition between the interfacial interactions amongst the three phases, the dissipation in the fluid, and the geometrical or chemical patterning and irregularities of the surface.

*Published as: S. Srivastava et al. *A Study of Fluid Interfaces and Moving Contact Lines Using the Lattice Boltzmann Method*, Comm. Comput. Phys. **13**, 725-740 (2012), and T. S. Chan et al. *Hydrodynamics of air entrainment by moving contact lines*, Phys. Fluids **25**, 074105 (2013).

The first fundamental steps in the field are due to Landau and Levich [25] and Deryaguin [26], who studied the problem of liquid film coating on a fully wetting substrate ($\theta_e = 0$, Figure 4.1, right panel red curve). In the case of a wetting plate moving with velocity U_p, one observes a film deposition whose thickness is controlled by the balance between viscous forces and surface tension. The relative effect of the viscous and the capillary force is measured in terms of the capillary number, $\mathrm{Ca} = \mu_2 U_p/\gamma_{12}$, where μ_2 is the dynamic viscosity of fluid 2 and γ_{12} is the surface tension between two fluids. The sign of the capillary number shown in Figure 4.1 indicates the direction of the plate motion with respect to the x-axis. The thickness of this film h_{LLD} is given by Eq. (2.55). The film thickness and the problem is referred to as the "LLD film" and "LLD problem" hereafter.

The problem of a liquid film coating was further investigated by de Gennes [90] for the case of partial wetting. This problem is referred to as the "dip-coating problem" hereafter. When the liquid partially wets the plate ($0 < \theta_e < 180°$) with a non-vanishing dynamic contact angle, a steady state is achieved only for the capillary number smaller than a certain critical value $\mathrm{Ca_c}$. Beyond the critical value of the capillary number ($\mathrm{Ca} > \mathrm{Ca_c}$) a film of fluid 2 is deposits on the plate. More recently, it was shown that partial wetting substrates allow for the existence of a second admissible solution for the thickness of the film [86] and it was shown experimentally that in the case a of partially-wetting plate, a remarkable ridge-like structure is produced during the entrainment process [22]. The solution of the dip-coating problem has also been generalized to non-Newtonian fluids by Tallmadge [91], plastic-viscous fluids by Deryaguin and Levi [92], to include the effects of inertia by de Ryck and Quere [93], as well as the effects of Marangoni stresses by Ramdane and Quere [94].

Another case of interest is when the solid plate is plunged into the bath instead of being pulled (see Figure 4.1, left panel). The dip-coating problem has got considerable attention in the past including some of the seminal contributions form Landau, Deryaguin and Bretherton [25, 26, 95]. However, much less is known about the reverse case (plate vertically pushed into the liquid bath). In this thesis this problem is referred to as the plunging plate problem. Similar to the dip-coating experiments, a dynamical wetting transition has been observed for the plunging plate problem. But instead of a liquid film, the wetting transition now results into the entrainment of an air film or air bubbles [96–101]. Despite the viscosity contrast between the liquid in the reservoir and that of the surrounding air, the dynamics inside the air is very important for this process. The perturbation analysis by Cox [27] suggested that the critical speed is inversely proportional to the viscosity of the liquid,

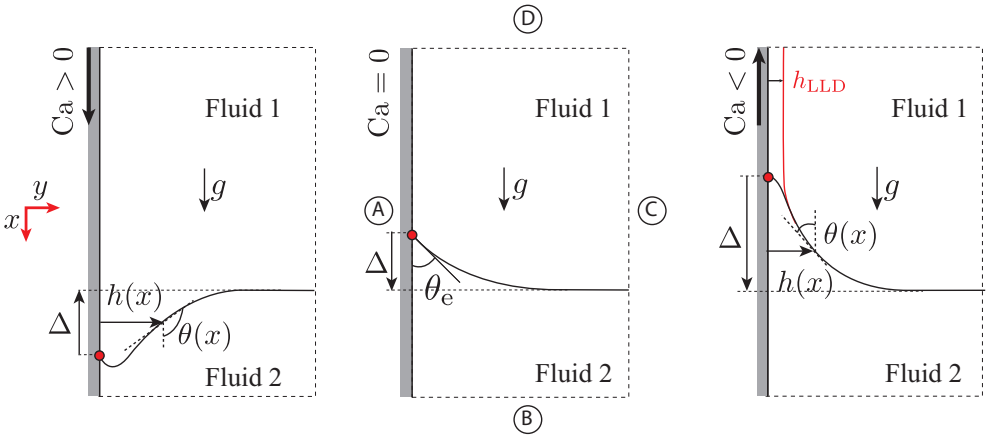

Figure 4.1: A schematic view of the plunging plate problem (left panel) and the dip-coating problem (right panel). The gray rectangular region represents a solid flat plate. The direction of the arrow drawn on the plate, represents the direction of the plate motion. The middle panel shows the situation for static plate Ca = 0*, and the schematics for the LB simulation domain. The position of the contact line has been emphasized by putting a red dot on it.*

$1/\mu_2$, with logarithmic corrections due to the viscosity of the air, μ_1. This is similar to the scenario for air entrainment by viscous cusps [102], such as observed for impacting liquid jets [103].

Recently, in the experiment of a plunging a plate into reservoirs of different liquids Marchand *et al.* [98] observed that the dependence on μ_2 is much weaker than predicted; enforcing a power-law fit to their data would give a small exponent, in between -1/2 and -1/3 rather than the expected -1. This implies that air viscosity plays an important role on the onset of air entrainment even if it is orders of magnitude smaller than the liquid viscosity. The importance of air was already highlighted in similar dip-coating experiments, where a reduction of the ambient pressure was shown to significantly enhance the critical speed of entrainment [96].

In this Chapter, we present the LB simulations for the dip-coating and the plunging plate problem. Here we consider a smooth, partially wettable, chemically homogeneous and flat plate immersed in the pool of liquid (fluid 2, see Figure 4.1). We assume that the dynamic viscosity of fluid 1 (μ_1) is smaller or equal to the dynamic viscosity of fluid 2 (μ_2), i.e., $R_\mu = \mu_1/\mu_2 \leq 1$, the equilibrium contact angle (θ_e) is always measured in the fluid 2 and the gravity g always acts along the x-axis. We use the dip-coating problem for the validation of the MP and MC-LB simulations. The validation and the results

from LB and GL simulations are divided into two parts.

In the first part of this Chapter, we present the numerical study based on the multiphase Shan-Chen (MP) and the multicomponent Shan-Chen (MC) versions of the LB method, and investigate the applicability of the LB method to study the dynamics of the three phase contact line. We use the analytical solution given by Eq. (2.53) to validate the the MP-LB and MC-LB models for the static plate (Ca = 0).

The boundary conditions for simulation of the dip-coating and the plunging plate problems should be employed at sufficiently large distance from the contact line, so that they do not influence the meniscus shape and the interface dynamics. However, the LB simulations need to be carried out in a finite domain, and size of the domain influences the computational cost for the simulation. The infinite bath at the right boundary maps the setup to the LLD

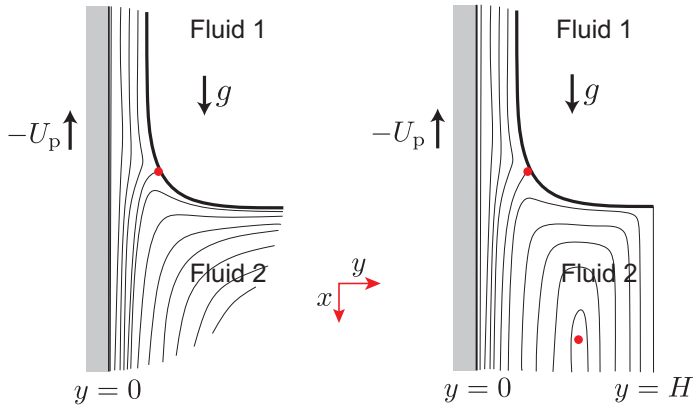

Figure 4.2: Schematic of the streamlines when a solid plate is vertically pulled out from fluid 1 into a fluid 2, and the stagnation points (red dots). The plate is located at $y = 0$. Left panel: infinite bath along y-axis has only one stagnation point (LLD problem). Right panel: a fictions wall placed in the simulation at $y = H$ has two stagnation points (Bretherton problem).

problem whereas a no-slip, neutral wetting, right boundary maps the setup onto a problem similar to the Bretherton problem [95]. The fundamental geometrical difference between the Bretherton and the LLD problems, a channel instead of a semi-infinite bath, has important implications on the flow topology, with one stagnation point for the LLD case versus two for the Bretherton problem (see Figure 4.2). The open boundary conditions are more sensitive to the initial conditions and takes much longer computational time to reach the steady state. However, the no-slip boundary condition are computationally

more efficient, but only applicable as long as the domain width (H) is much larger then the capillary length (ℓ_c).

We show the boundary conditions that can be used to effectively reduce the size of the flow domain and hence the computational cost per simulation. In this part, we also discuss the limitations and applicability of the SC MP model to study the plunging plate problem. In the last section of the first part, we employ our LB model for the dip-coating and the plunging plate problem for small capillary number and compare it with the GL model.

In the second part (starting from section 4.3), we present the generalized lubrication (GL) model. The GL model presented here is an extension of the LT model shown in section 2.4, that includes the MP character of the plunging plate problem. We compare our LB simulations with the simulation form GL model to ensure the validity of both GL and LB model for the dip-coating as well as the plunging plate problem. Here we compare the interface shape, deformation and the meniscus displacement between the two models till the dynamical wetting transition takes place $\mathrm{Ca} = \mathrm{Ca_c}$. After this, the GL model is used to study the plunging plate problem for small viscosity ratios, $R_\mu \ll 1$. Finally, we study the dependence of $\mathrm{Ca_c}$ on R_μ and the microscopic parameter slip-length λ_s. Finally, we present a discussion on the comparison of the GL model with the experiments and draw the conclusions from this Chapter.

4.2 LB simulations for the static and the moving contact line

In this section, we present results from both the MP and the MC-LB simulations. For the static case $U_p = 0$, where U_p is the plate velocity. We use the Landau solution Eqn. (2.53) to benchmark the results from the LB simulations at varying the domain width, H, and the equilibrium contact angle, θ_e. Furthermore, we also compare the interface profile in the LB simulations using two different boundary conditions at boundary C. The numerical study for the moving plate problem is divided into two parts: *i.e.*, the dip-coating problem ($U_p < 0$) and the plunging plate problem ($U_p > 0$). The steady state interface profile obtained from the MC-LB simulations are compared with the interface profile obtained from GL model (section 4.3.2).

We are using the Shan-Chen multiphase/multiphase LB method for the LB simulations shown in this Chapter. The implementation details for the method and the boundary conditions can be found in Chapter 3 of this thesis. A schematics of the LB simulation domain is shown in Figure 4.1 (middle panel). The size of the flow domain in the LB simulations is given by $N_x \times N_y =$

$L \times H$. We mimic an infinite bath at the boundaries B and D, by imposing the pressure boundary conditions described in Section 3.3.3. The pressure boundary conditions at boundary B and D are used to sustain the hydrostatic pressure due to the weight of the liquid column. This allows us to control the interface position inside the flow domain. At the boundary A, we impose a no-slip wetting wall which moves with velocity U_{p}. At the boundary C, we either use an open boundary to mimic an infinite bath or a no-slip static wall. From here onwards, the boundaries of the LB simulation domain: A, B, C and D will be referred as to the left, bottom, right and top boundaries, respectively (see Figure 4.1). We use the following coordinate transformation to compare the interface profiles obtained in the LB simulation and the GL simulations: $x = (x - x_0)/\ell_{\mathrm{c}}, y = y/\ell_{\mathrm{c}}$, where x_0 is the position of the contact line. The contact line position is given by the intersection point of the three interfaces: fluid 1 - fluid 2, fluid 1 - solid, fluid 2 - solid. Since the interface in the SC LB model is diffused, we choose the threshold density $(\rho_1 + \rho_2)/2$ to approximate the three interfaces.

For the MC-LB simulations, we need to solve two LB equations, one for each component. The distribution function f_i, relaxation parameter τ, density ρ, velocity $\mathbf{u}$, pressure p, kinematic viscosity ν and dynamic viscosity μ of the two components are distinguished by suffix α and β. The physical properties of fluid 1 and fluid 2 used in this Chapter are weighted average of the physical properties of the two components α, β. The properties of two component system in fluid 1 and 2 are represented by the suffixes '1' and '2', respectively. Using these notations the density, the kinematic viscosity and the velocity for the MC-LB simulations shown in this Chapter are defined as:

$$\rho_1 = \sum_{\xi \in \{\alpha,\beta\}} \rho_{\xi,1}, \qquad \rho_2 = \sum_{\xi \in \{\alpha,\beta\}} \rho_{\xi,2}, \tag{4.1a}$$

$$\nu_1 = \sum_{\xi \in \{\alpha,\beta\}} \nu_\xi \rho_{\xi,1}/\rho_1, \qquad \nu_2 = \sum_{\xi \in \{\alpha,\beta\}} \nu_\xi \rho_{\xi,2}/\rho_2, \tag{4.1b}$$

$$\mathbf{u}_1 = \sum_{\xi \in \{\alpha,\beta\}} \mathbf{u}_\alpha \rho_{\xi,1}/\rho_1, \qquad \mathbf{u}_2 = \sum_{\xi \in \{\alpha,\beta\}} \mathbf{u}_\alpha \rho_{\xi,2}/\rho_2, \tag{4.1c}$$

where $\nu_\xi = c_s^2(\tau_\xi - 0.5)$, $\xi = \alpha, \beta$. The pressure and the dynamic viscosity can be calculated using the density and kinematic viscosities in the respective fluids. The surface tension values for both the MP and MC simulations are obtained using the Laplace test (section 3.4.1), and denoted by γ from here onwards. The capillary length for the MC simulations is obtained using $\ell_{\mathrm{c}} = \sqrt{\gamma/((\rho_{\alpha,1} - \rho_{\alpha,2})g)}$, whereas for the MP simulations the capillary length has been obtained using $\ell_{\mathrm{c}} = \sqrt{\gamma/((\rho_1 - \rho_2)g)}$. Here ρ_1, ρ_2 are the densities of

fluid 1 and fluid 2.

The viscosity ratio for the MP-LB simulation is same as the ratio of density, i.e., $R_\mu = \rho_1/\rho_2$, and for the MC-LB simulations is given by $R_\mu = \mu_1/\mu_2$. For the MP-LB simulations shown in this Chapter, we use $\tau = 1$. For the MC-LB simulations shown in the first part of this Chapter, we use $\tau_\alpha = \tau_\beta = 1$. However, for the second part we change the relaxation parameter to get a non-unit viscosity ratio. A detailed study of the LB model based on different values of relaxation parameters is beyond the scope of this Chapter.

4.2.1 Static meniscus

As a first step we proceed with the validation of the LB method for the static case (Ca = 0). We focus on both open and wall bounded baths and on both the MP and MC models. In the case of the MP-LB model a body force g applies everywhere. In the MP-LB the kinematic viscosity of two fluid phases are the same and hence the dynamic viscosity ratio is given by, $R_\mu = \rho_1/\rho_2$. Moreover, the MP-LB method is restricted to compute interface dynamics between two fluids with high density ratio (e.g. water in air). For the MC-LB model, instead, the density ratio cannot be easily pushed to large values, while the viscosity ratio can be taken easily to be of order unity. Thus it is necessary to devise a different procedure to give rise to the static meniscus. For the MC-LB simulation our approach consists in keeping the densities of

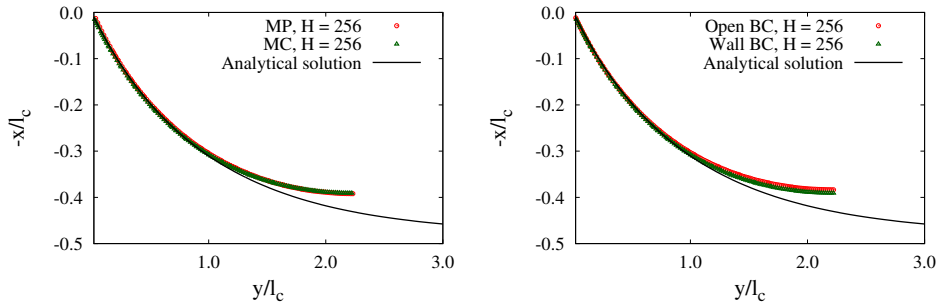

Figure 4.3: A comparison of interface profiles for Ca = 0. *(Left panel) Comparison of the analytical solution Eqn. (2.53), the MC-LB and the MP-LB simulations for the no-slip boundary conditions at the right boundary. (Right panel) Comparison of analytical solution Eqn. (2.53) and the MC-LB simulations for two different boundary conditions on the right boundary.*

the two component equal, therefore we apply pressure and gravity only on one fluid component, ρ_α. In this test we validate this assumption by comparing

the MC-LB simulation with the MP-LB simulation where we apply pressure and gravity on both fluids.

The simulation parameters in lattice units, for the MP-LB simulation are: system size $L \times H = 640 \times 256$, $G_{\rm sc}$ = -6.0, $\rho_2 = \rho_\ell = 2.65$, $\rho_1 = \rho_{\rm v} = 0.075$, $\tau = 1$, $\nu = 0.1666$, $\gamma = 0.1444$, body force $g = 4.271{\times}10^{-6}$, initial density difference at bottom boundary $\Delta\rho = 0.027$. The simulation parameters in lattice units, for the MC-LB simulation are: System size $L \times H = 640 \times 256$, interaction parameter $G_{\rm sc}^{(\beta,\alpha)} = G_{\rm sc}^{(\alpha,\beta)} = -0.9$, $\rho_{\alpha,2} = \rho_{\beta,1} = 0.06$, $\rho_{1,\alpha} = \rho_{\beta,2} = 2.00$ the initial densities, for both fluid components, relaxation parameters $\tau_\alpha = \tau_\beta = 1$, body force $g = 6.82{\times}10^{-6}$, initial density difference at bottom boundary is $\Delta\rho_\alpha = 0.02$, $\Delta\rho_\beta = 0$, the surface tension $\gamma = 0.183$ and the dynamic viscosities $\mu_1 = \mu_2 = 0.34$. The capillary length and the equilibrium contact angle for both the MP and MC simulations are the same and given by $\ell_{\rm c} = 114.73$ and $\theta_{\rm e} = 62^\circ \pm 5^\circ$, respectively. The viscosity ratios for the MP and the MC simulation is 0.03 and 1.0, respectively.

The result for this test show a very good agreement between the two approaches (Figure 4.3 (left panel)). This indicates that the both the MP and the MC-LB models can be employed to study capillarity effects. We stress here that the combined possibility to use either a MP or a MC-LB model is key to investigate the meniscus dynamics at both large or small values for the viscosity ratios.

In order to investigate the effect of boundary conditions at the right boundary, we are using the open and the wall boundary conditions at the right boundary. The implementation details of the open and the wall boundary conditions in the LB method can be found in section 3.3.3 of this thesis. A short description of the contact angle modeling in the MP and MC-LB model can be found in section 3.4.2 of this thesis.

The first observation, using the open boundaries, is that this boundary condition is very sensitive to the initialization and its convergence times are extremely long. This is probably due to relatively slow velocity dissipation, as compared to the no-slip boundary condition on the right boundary. Once the interface reaches a stationary state we compare the profiles obtained with the two boundary conditions. As shown in Figure 4.3 (right panel) the result from the two simulations are in good agreement with each other as well as with the Landau's solution close to the contact line. To further validate the MC-LB for the study of the static meniscus, we investigate systems with different bath width, H (with respect to the capillary length, $\ell_{\rm c}$) and with different wall wettability. We compare all these cases with the Landau's solution Eq. (2.53). The parameters used for the MC-LB simulations are same as the parameter used for the previous MC simulation, except now we are varying the domain

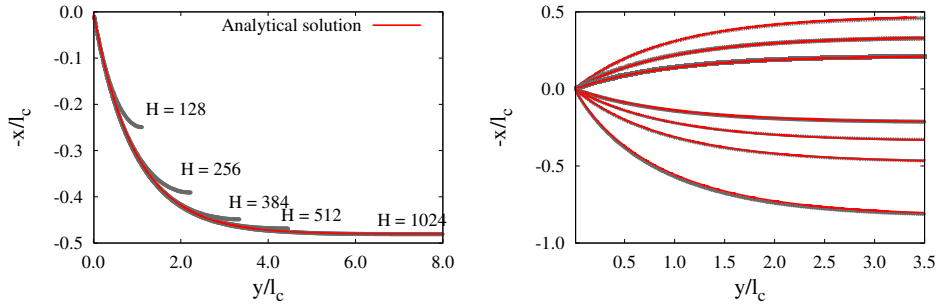

Figure 4.4: A comparison of interface profiles for Ca $= 0$. *(Left panel) The analytical solution Eqn.* (2.53) *(solid red curve) versus the MC-LB solution for different channel width* H *and* $R_\mu = 1$. *(Right panel) Validation of the LBM solution for different static contact angles against the analytical solution Eqn.* (2.53) *(solid red curve). For the Landau's solution shown for different contact angle (right panel) we use the* $\theta_e = 41^\circ, 53^\circ, 62^\circ, 70^\circ, 77^\circ, 117^\circ, 102^\circ$ *and* 109° *from bottom to top.*

width H as shown in the left panel of Figure 4.4. As already stated, the body force g and the pressure jump ($\propto \Delta\rho_\alpha$) to counter balance the hydrostatic pressure are only applied on one fluid component (ρ_α). The results for the test with different domain widths H are shown in Figure 4.4 (left panel). We notice that close to the contact line the solution is always in good agreement with the analytical solution, but only for larger system sizes the accuracy extends up to well outside the static meniscus. In particular, the reference simulation with width as large as $H = 1024$ is matching the analytic solution well inside the domain.

The second validation involves the MC-LB simulation with different static contact angles as shown in the right panel of Figure 4.4. The LBM results for these tests are in good agreement with Landau's solution Eqn. (2.53). Again, the parameters used for the MC-LB simulations for this test is same as for the simulation shown in Figure 4.4 (left panel), except here we fix $H = 512$ and change the wetting parameter $G^\alpha_{\text{ads}} = -G^\beta_{\text{ads}}$ = -0.20, -0.15, -0.10, 0.10, 0.15, 0.20 and 0.30 to model different equilibrium contact angles.

4.2.2 Results for moving plate (dry regime)

In this section, we discuss the case when the plate is either pulled (Ca < 0) or plunged (Ca > 0) into a liquid bath of viscosity μ_2. For small capillary number, one does not expect the formation of a liquid or gas film, we refer to

this regime as to the dry regime. We report two sets of simulations for the steady state interface profile for the case of a moving contact line.

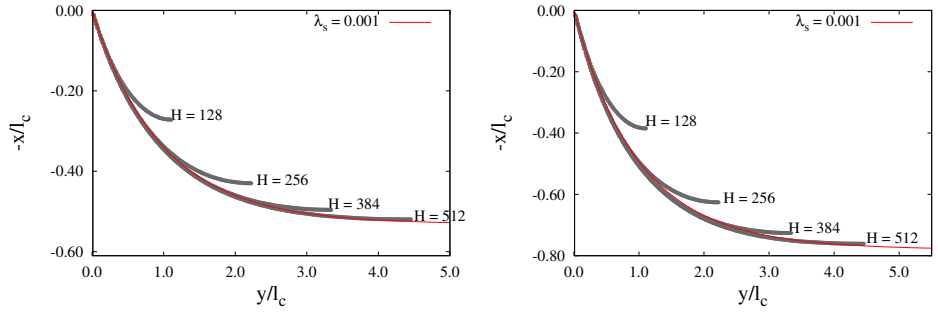

Figure 4.5: Comparison of the steady state interface profile between the MC-LB (gray dots) and the GL simulations (solid red curve) for for $\mathrm{Ca} = -0.0187$ *(left panel)* $\mathrm{Ca} = -0.0938$ *(right panel), for different* H*. For these simulation* $R_\mu = 1$*, and* $\theta_\mathrm{e} = 62.9°$*.*

In this first set of simulations we show the MC-LB simulations for the dip-coating problem ($\mathrm{Ca} < 0$), and compare these results against the GL approximation (section 4.3.2). The MC-LB simulation parameters used here are the same as the parameter used for the simulations shown in Figure 4.3 (left panel), except now the plate is moving with constant velocity (U_p), in the direction parallel but opposite to x-axis, and the density difference at the bottom boundary is $\Delta\rho_\alpha = 0.008, \Delta\rho_\beta = 0.0$. Figure 4.5 show the results for $\mathrm{Ca} = -0.0187$ (left panel) and $\mathrm{Ca} = -0.0938$ (right panel) for different H. The MC-LB results are in good agreement, for higher H, with the corresponding result from GL model with slip length $\lambda_\mathrm{s} = 10^{-3}$. We are using the no-slip wall boundary condition on the right boundary for these simulations.

One can estimate a-priori that the slip length, λ_s, for the LB will be of the order of one grid cell (in lattice units). For a quantitative comparison between the LB and the GL simulations, one needs to tune the value of the slip length in the two cases. We are doing this for one particular wall velocity $U_\mathrm{p} = 5 \times 10^{-3}$ (see Figure 4.6, left panel). This value of λ_s for the GL was then used for quantitative matching for all the higher values of the capillary numbers.

In Figure 4.6 (left panel) we report the steady state interface profile in the case of the plunging plate problem for $\mathrm{Ca} = 0.0187$. To compare the simulation from the LB and the GL model, we need the slip-length λ_s for the GL model. In the case of the LB method, we can estimate λ_s as being in the order of

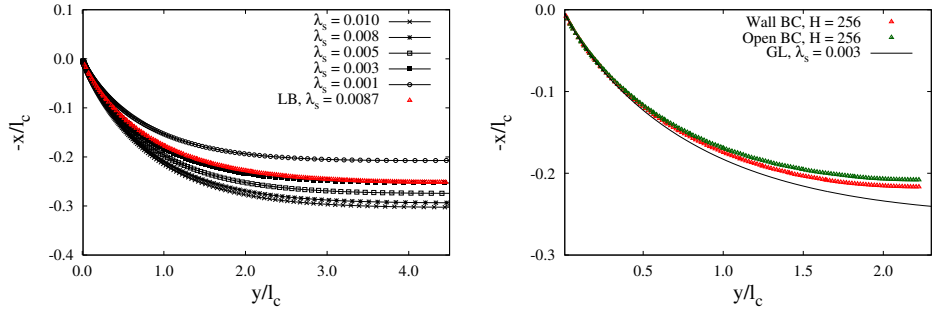

Figure 4.6: (Left panel) Comparison of the steady state interface profile between the GL simulation for different λ_s and the MC-LB simulation (solid red curve) with $\lambda_s = 1/\ell_c$. (Right panel) Comparison of steady state interface profile for different boundary conditions at the right boundary. For these simulation $R_\mu = 1$, $\theta_e = 62.9°$ and $\mathrm{Ca} = 0.0187$.

one lattice cell; the agreement with the GL model is quite good once λ_s is better tuned (roughly a factor 3 with respect to our estimate). In Figure 4.6 (right panel), we show that for $\mathrm{Ca} = 0.0187$ the interface profile obtained in the LB simulations is sensitive to the boundary conditions used on the right boundary of the flow domain. It is further shown in Figure 4.7 (left panel), that the LB simulations converge quite rapidly to the solution for an infinite bath obtained from the GL model, similar to what was found for the case of a static wall. However, when the capillary number is increased ($\mathrm{Ca} = 0.0374$), see Figure 4.7 (right panel), we not only observe important deviations from the GL simulation, but also significant dependence on the width H.

4.2.3 Limitations and applicability

In this section we discuss some of the issues that emerge when using MP and MC-LB models to the dip-coating and the plunging plate problem. To study these two problems, one is interested in small ($|\mathrm{Ca}| \ll 1$), as well as in large values of the capillary numbers i.e., $|\mathrm{Ca}| \approx \mathrm{Ca_c}$, where $\mathrm{Ca_c}$ is the critical capillary number. There are constraints on the possibility to increase the capillary number within the LB method: the increase of the plate velocity cannot be pushed too close to the lattice sound speed; the viscosity cannot be increased too much, otherwise LB model becomes collision-less. The value of the surface tension in both the MP and MC model monotonically increases with the magnitude of the interaction strength (G_{sc}, $G_{\mathrm{sc}}^{(\xi,\xi)}, \xi = \alpha, \beta$). In order to get smaller values of surface tension, we need to decrease the magnitude G_{sc}

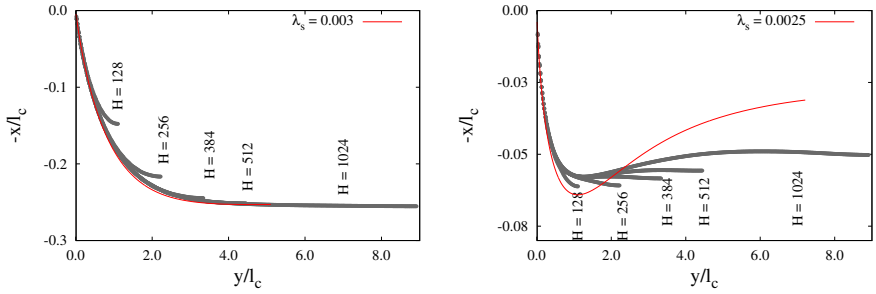

Figure 4.7: (Left panel) Comparison between the GL simulation (solid red curve) and the MC-LB simulations at Ca = 0.0187 *and varying* H. *(Right panel) Same as in the left panel but for* Ca = 0.0374. *For these simulation* R_μ = 1, *and* $\theta_e = 62.9°$.

in the MP-LB and $G_{sc}^{(\xi,\xi)}(\xi = \alpha, \beta)$ in the MC-LB. This leads to high diffusivity of fluids in the the MC model [76, 104] and high condensation/evaporation of vapor/liquid in the MP model [105] (see Figure 4.8, right panel). Hence we can not decrease the surface tension too much while avoiding the undesirable effects at the same time.

A common inconvenience with the SC LB model [9, 10] (as well as Cahn-Hilliard models [79]) is the spurious velocity in the vicinity of the interface (see Figure 3.9). These spurious velocities arise due to insufficient isotropy in the calculation of the density gradient. Despite these spurious velocities at the interface, the Shan-Chen MP and MC-LBM models have shown a very good agreement with the sharp interface models [35]. Figure 4.9 shows that despite the discontinuity at the interface the velocity field in MC SC LBM is in good agreement with the Huh-Scriven model [20]. The wedge angle in Huh-Scriven model [20] is the angle made by the straight interface with the plate in the fluid 1.

Another issue with the standard SC model is that the surface tension, density ratio and the spurious velocities depends on the magnitude of the interaction strength, cannot be changed independent of each other.

For some of these issues partial solutions have been proposed, e.g., the use of multi-range models can provide an independent, and thus more flexible, control of the density ratio and surface tension [75], but this involves reverting to more complex LB methods than the usual first-neighbor SC model.

Using the collocated grid for pressure and velocity fields in LB can also produce spurious checker-board oscillations of important amplitude [81]. These oscillations may be controlled by reverting to a Lax-Wendroff streaming scheme

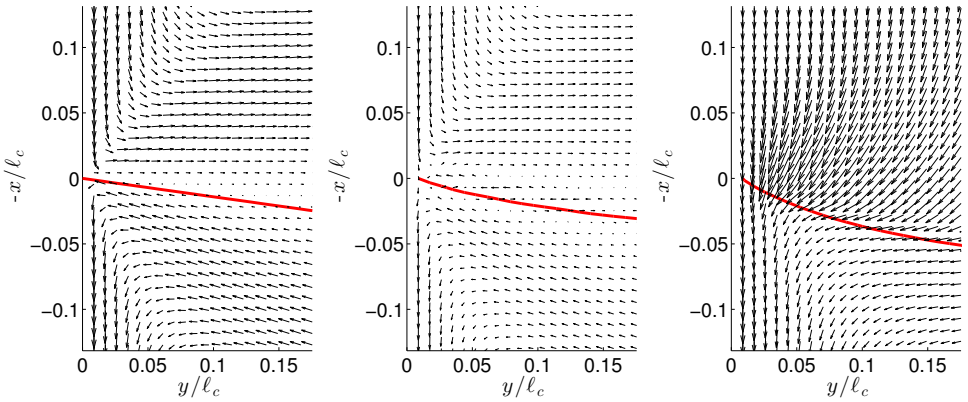

Figure 4.8: The velocity field (black arrows) and interface position (solid red curve) near the contact line for: the Huh-Scriven (HS) model (left panel, $R_\mu = 1$, $\theta_w = 84°$), the MC-LB simulation (middle panel, $R_\mu = 1$, $\theta_e = 62°$), and the MP-LB simulation (right panel, with $R_\mu = 0.17$, $\theta_e = 62°$). In all three cases, the plate is moving with velocity $U_p = 0.01$, and the capillary length for the MP and MC-LB simulations is 114 LU. The MP-LB simulation shows a significant mass flux across the interface (right panel), which is absent in the case of the MC-LB simulation (middle panel).

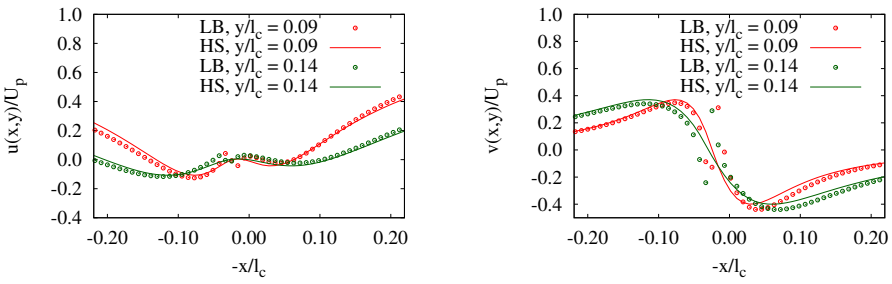

Figure 4.9: Comparison of velocity $u(x, 10)$ (left panel), and $v(x, 10)$ (right panel) between the MC-LB, and the HS solution shown in Figure 4.8. The discontinuity in the velocity field for the MC-LB simulations is due to the spurious velocities at the interface.

(section 3.5.2). The presence of an open boundary poses important issues for what concerns the stability, the convergence and thus the usability of the method.

In conclusion, we can say that the multicomponent Shan-Chen LB method

is a suitable tool to investigate a two fluid system with nearly equal viscosities, for both dip-coating and the plunging plate problem. The multiphase Shan-Chen LB method is a suitable tool to study the dip-coating problem and the plunging plate problem with low viscosity ratio. However, due to enhanced mass flux across the interface at higher capillary number, it is not possible to obtain the wetting transition in the plunging plate problem using the standard MP-LB model [33]. We will see this result in the next part of this Chapter.

Note: *For the rest of this Chapter, we will use radian [rad] to measure angle.*

4.3 Hydrodynamics of air entrainment by moving contact lines

In this section, we provide a new framework to study air entrainment by advancing contact lines, in which the two-phase character of the flow is taken into account. The usual lubrication approximation is valid for small equilibrium contact angles and does not take into account the flow inside the gas (see section 2.4). Since both assumptions are no longer valid near the onset of air entrainment, we extend the lubrication approximation such that it allows for large angles and a nonzero gas viscosity. This generalized lubrication (GL) theory is validated by comparison to the lattice Boltzmann simulations. We show that the meniscus shapes obtained from the GL model agree well with the simulations. Note, however, that such simulations are limited in terms of viscosity ratio and spatial resolution (i.e. the separation between the capillary length and the microscopic cutoff given by the interface width or, equivalently, by the effective slip length [35]), and cannot achieve experimental conditions for air entrainment. The generalized lubrication model developed and studied here, incorporates the effect of the air viscosity μ_1. This make the GL model a better choice for understanding the experiments for the plunging plate problem. Moreover, the model can be used to explore the parameter space, i.e., the contact angle and the arbitrary small viscosity ratio.

4.3.1 Formulation of the problem

We consider a smooth, chemically homogeneous solid plate translating across an interface of two immiscible fluids at a constant speed U_p (positive/negative for plunging/withdrawing). As sketched in Figure 4.10, the two liquids are contained in a reservoir much larger than all the lengths of the problem and the plate can be inclined to an angle $\alpha = \pi/2$. If the plate is not moving

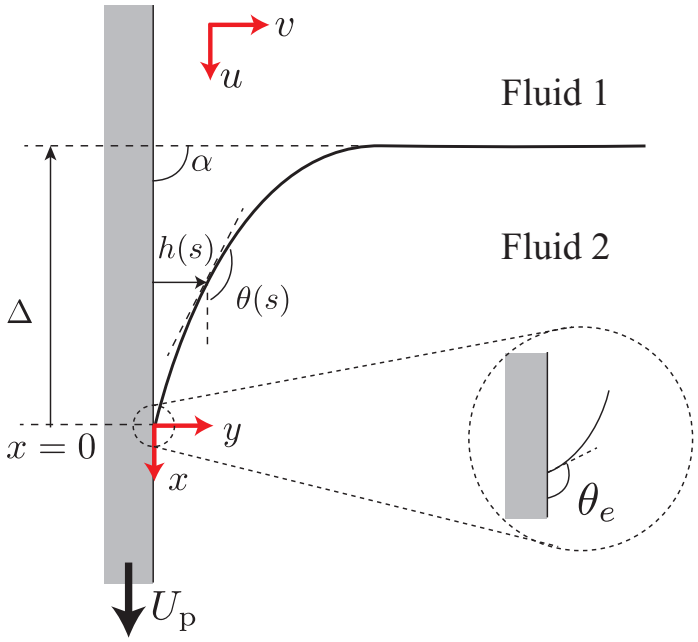

Figure 4.10: Schematic diagram showing a plate moving with speed U_p with respect to an interface of two immiscible fluids. The plate has an inclination α, here drawn with $\alpha = \pi/2$ for the case of a vertical plate. The interface touches the wall at the contact line with an angle assumed to be the same as the equilibrium contact angle θ_e. The meniscus profile is described by $h(s)$ or the local angle $\theta(s)$, where s is the arc length of the interface measured from the contact line. The total meniscus deformation is quantified by Δ, the distance between the contact line and the level of the bath.

($U_\mathrm{p} = 0$) there is no flow in the fluids, and the interface equilibrates to a static shape due to the balance between the capillary and gravity forces (see section 2.4). The interface makes an equilibrium angle θ_e with the solid as a result of intermolecular interaction between the three phases at the contact line. Neglecting the contact angle hysteresis, θ_e takes a well-defined value determined by Young's law. The contact line equilibrates at a distance Δ from the bath, which can be expressed as

$$\Delta = \pm \ell_\mathrm{c} \sqrt{2\,(1 - \cos(\alpha - \theta_\mathrm{e}))}. \tag{4.2}$$

Here, $\ell_\mathrm{c} = \sqrt{\gamma/((\rho_2 - \rho_1)g)}$, is the capillary length, determined by the surface tension γ, gravity g and the density difference $\rho_2 - \rho_1$. The $\pm$ sign depends on whether θ_e is smaller (+) or larger (-) than the plate inclination α. When addressing the transition to air entrainment, we will consider the upper fluid 1 in Figure 4.10 to be gaseous, while fluid 2 is a liquid. We therefore use subscripts 'ℓ' and 'g' to indicate liquid and gas phase, respectively.

When the plate is moving, the viscous drag generated by the moving plate gradually deforms the interface between the two fluids (fluid 1 and 2, see Figure 4.10). As long as the speed of the plate is lower than a threshold value, the meniscus equilibrates at a new distance Δ from the bath level. For positive U_p the plate is moving downwards so that Δ is lower than the static equilibrium height, while the opposite holds for negative U_p. The contact line is assumed to be straight so that the problem can be treated as two-dimensional. The interface is described by the film thickness profile $h(s)$. The origin $(x, y) = (0, 0)$ is chosen at the contact line. When the plate is moving beyond a critical speed, the meniscus can no longer equilibrate to a steady state. In the case of receding contact lines this leads to the deposition of a liquid film [22, 106–111], while air will be entrained for advancing contact lines [96–100, 112–114].

In this Chapter, we only focus on viscous flows, for which the Reynolds number is assumed to be zero. Thus, for incompressible fluids the flow in the two phases is described by the Stokes' equation and the continuity equation, i.e.,:

$$\mu_\mathrm{g} \nabla^2 \mathbf{u}_\mathrm{g} - \nabla p_\mathrm{g} - \nabla \Phi_\mathrm{g} = 0, \quad \nabla \cdot \mathbf{u}_\mathrm{g} = 0, \tag{4.3}$$

and

$$\mu_\ell \nabla^2 \mathbf{u}_\ell - \nabla p_\ell - \nabla \Phi_\ell = 0, \quad \nabla \cdot \mathbf{u}_\ell = 0, \tag{4.4}$$

where $\mathbf{u}_\mathrm{g} \equiv (u_\mathrm{g}, v_\mathrm{g})$ and $\mathbf{u}_\ell \equiv (u_\ell, v_\ell)$, p_g and p_ℓ, $\Phi_\mathrm{g} = -\rho_\mathrm{g}\, g\, x$, and $\Phi_\ell = -\rho_\ell\, g\, x$, are the corresponding velocity fields, pressures and gravitational potentials in the gas and the liquid phases, respectively. When considering air

entrainment, the dynamic viscosity of the gas and the liquid phases are μ_{g} and μ_ℓ, respectively. The relative viscosity is expressed by the viscosity ratio $R_\mu = \mu_{\mathrm{g}}/\mu_\ell$ which, in practical situations, can be very small, e.g., the viscosity ratio between the air and the water at room temperature is $R_\mu \approx 10^{-3}$.

To solve for the velocity fields and the interface shape, we need to specify appropriate boundary conditions at the flow domain and the liquid-gas interface, respectively. At the steady interface, the velocities parallel to the interface $\mathbf{u}^{\mathrm{t}}$ are continuous and the velocities normal to the interface $\mathbf{u}^{\mathrm{n}}$ vanish, so

$$\mathbf{u}_{\mathrm{g}}^{\mathrm{t}} = \mathbf{u}_\ell^{\mathrm{t}} \tag{4.5a}$$

and

$$\mathbf{u}_{\mathrm{g}}^{\mathrm{n}} = \mathbf{u}_\ell^{\mathrm{n}} = 0. \tag{4.5b}$$

In each phase, we define the normal stress, $\sigma^{\mathrm{n}} \equiv (\boldsymbol{\sigma}\hat{\mathbf{n}}) \cdot \hat{\mathbf{n}}$, at the interface, where $\hat{\mathbf{n}}$ is the unit vector normal to the interface and the stress tensor σ is defined as (in cartesian coordinates)

$$\sigma_{ij} \equiv -p\delta_{ij} + \mu \left(\frac{\partial u_i}{\partial x_j} + \frac{\partial u_j}{\partial x_i} \right). \tag{4.6}$$

The normal stress discontinuity across the interface is related to the curvature κ and to the surface tension γ by Laplace's law

$$\sigma_\ell^{\mathrm{n}} - \sigma_{\mathrm{g}}^{\mathrm{n}} = \gamma\kappa. \tag{4.7}$$

By contrast, the tangential stress component, $\sigma^{\mathrm{t}} \equiv (\sigma\hat{\mathbf{n}}) \cdot \hat{\mathbf{t}}$, is continuous across the interface,

$$\sigma_g^{\mathrm{t}} = \sigma_\ell^{\mathrm{t}}. \tag{4.8}$$

At the boundary $y = 0$, the velocity normal to the wall vanishes in the gas and liquid phases, as no penetration of fluid through the solid is allowed, i.e.

$$v_\ell(x, 0) = 0, \qquad v_{\mathrm{g}}(x, 0) = 0. \tag{4.9}$$

Regarding the velocity component parallel to the wall, $u_\ell(x, 0), u_{\mathrm{g}}(x, 0)$, the situation is more subtle because of the moving contact line singularity [19, 20]: imposing a no-slip boundary condition leads to diverging stress fields and calls for a microscopic mechanism of regularization. In this Chapter, we use two independent approaches to solve the flow equations (GL and LB), which naturally involve different regularizations of the singularity at the contact line. The microscopic boundary condition will therefore be discussed separately below.

In the following section we present the generalized Lubrication (GL) model to determine the meniscus shape sketched in Figure 4.10.

4.3.2 Generalized lubrication model

The lubrication approximation has been a very efficient framework to deal with thin film flows [21]. This systematic reduction of the NS equations is very suitable for numerical simulations and in many cases allows for analytical results [19]. It is usually derived for flows that involve a single phase that constitutes a "thin" film, with the slopes $|\mathrm{d}h/\mathrm{d}x| \ll 1$. However, the expansion parameter underlying the analysis is not the interface slope, but the capillary number $\mathrm{Ca} = U_\mathrm{p}\mu_\ell/\gamma$ [21]. This means that a lubrication-type analysis can be performed whenever surface tension dominates over viscosity. Indeed, it was shown in [22] that the lubrication approximation can be generalized to large interface angles θ, giving a perfect agreement with the perturbation results by Voinov [29] and Cox [27]. Here we further extend this approach by taking into account, besides of the effect of a large slope, also of the viscous flows on both sides of the interface. The goal is to provide a model that can deal with moving contact lines in cases where both phases are important (as in Figure 4.10). In particular, this will allow us to study the air entrainment transition. Let us now derive this generalized lubrication model. According to Eq. (4.7) (Laplace law), the interface curvature κ is determined by the normal stress difference across the interface. In curvilinear coordinate, curvature is given by:

$$\kappa = \frac{\mathrm{d}\theta}{\mathrm{d}s}, \tag{4.10}$$

where θ is the local interface angle, s the arc length measured from the contact line, i.e., at $s = 0$ at the contact line (see Figure 4.10). The normal stresses have to be determined from the flows in the fluids, which themselves depend on the shape of the interface. For the usual lubrication theory in which the interface slope is small, the leading order contribution to the flow reduces to a parabolic Poiseuille flow inside the film. This can be generalized to two-phase flows and large interface slopes: as long as the capillary number is small, the interface curvature is small as well and the leading order velocity field is given by the flow in a wedge (Figure 4.11). The wedge solutions have been obtained analytically by Huh and Scriven (HS) [20], for any viscosity ratio R_μ and for any wedge angle θ_w. Figure 4.11 shows the corresponding streamlines. Based on these exact solutions, the local normal stress can be determined, thus giving the local curvature of the interface through Eq. (4.7).

We denote the quantities derived from the Huh-Scriven solutions by capital symbols, e.g., the normal stress is denoted by Σ^n, velocity by $\mathbf{U}$ and pressure by P. For the HS model, the anisotropic part of the normal stress at the

interface vanishes so that

$$\Sigma^{\mathrm{n}} = -P. \tag{4.11}$$

Approximating the normal stresses by the HS solutions, Eq. (4.7) becomes

$$\gamma \frac{\mathrm{d}\theta}{\mathrm{d}s} = \Sigma^{\mathrm{n}}_{\ell} - \Sigma^{\mathrm{n}}_{\mathrm{g}} = P_{\mathrm{g}} - P_{\ell}. \tag{4.12}$$

Since $P_{\mathrm{g}} - P_{\ell}$ is defined up to an integration constant, it is convenient to differentiate Eq. (4.12) once with respect to s, giving

$$\gamma \frac{\mathrm{d}^2\theta}{\mathrm{d}s^2} = \frac{\mathrm{d}P_{\mathrm{g}}}{\mathrm{d}s} - \frac{\mathrm{d}P_{\ell}}{\mathrm{d}s} = \left(\nabla P_{\mathrm{g}} - \nabla P_{\ell}\right)_{\mathrm{int}} \cdot \hat{\mathbf{e}}_s. \tag{4.13}$$

where

$$\hat{\mathbf{e}}_s = \left(\frac{\mathrm{d}x}{\mathrm{d}s}, \frac{\mathrm{d}y}{\mathrm{d}s}\right),$$

is the unit vector tangent to the interface, i.e., $\hat{\mathbf{e}}_s = \hat{\mathbf{t}}$ (see Figure 4.10). The index "int" indicates that the quantities inside the brackets are to be evaluated on the interface.

When Stokes equation (4.3) is applied, Eq. (4.13) can be rephrased in terms of velocity field obtained from the HS model

$$\gamma \frac{\mathrm{d}^2\theta}{\mathrm{d}s^2} = \Big(\mu_{\mathrm{g}} \nabla^2 \mathbf{U}_{\mathrm{g}} - \mu_{\ell} \nabla^2 \mathbf{U}_{\ell} - \nabla(\Phi_{\mathrm{g}} - \Phi_{\ell})\Big)_{\mathrm{int}} \cdot \hat{\mathbf{e}}_s. \tag{4.14}$$

The viscous contributions on the right hand side can be expressed in terms of R_μ and θ in the form

$$\mu_{\ell} \left(\frac{\mu_{\mathrm{g}}}{\mu_{\ell}} \nabla^2 \mathbf{U}_{\mathrm{g}} - \nabla^2 \mathbf{U}_{\ell}\right)_{\mathrm{int}} \cdot \hat{\mathbf{e}}_s = \frac{3\mu_{\ell} U_{\mathrm{p}} f(\theta, R_\mu)}{h^2}, \tag{4.15}$$

where

$$\begin{aligned} f(\theta, R_\mu) &\equiv \frac{2\sin^3\theta [R_\mu^2 f_1(\theta) + 2R_\mu f_3(\theta) + f_1(\pi - \theta)]}{3[R_\mu f_1(\theta) f_2(\pi - \theta) - f_1(\pi - \theta) f_2(\theta)]} \\ f_1(\theta) &\equiv \theta^2 - \sin^2\theta \\ f_2(\theta) &\equiv \theta - \sin\theta\cos\theta \\ f_3(\theta) &\equiv (\theta(\pi - \theta) + \sin^2\theta). \end{aligned} \tag{4.16}$$

The gravity terms in (4.14) can be simplified to

$$\nabla \left(\Phi_{\mathrm{g}} - \Phi_{\ell}\right)_{\mathrm{int}} \cdot \hat{\mathbf{e}}_s = -(\rho_{\ell} - \rho_{\mathrm{g}}) g \sin(\theta - \alpha). \tag{4.17}$$

Substituting Eq. (4.15) and Eq. (4.17) into Eq. (4.14) gives a generalized form of the lubrication equation, which after scaling all lengths with the capillary length ℓ_c becomes

$$\frac{\mathrm{d}^2\theta}{\mathrm{d}s^2} = \frac{3\mathrm{Ca}}{h^2} f(\theta, R_\mu) + \sin(\theta - \alpha). \tag{4.18}$$

In the remainder we will use the same symbols for rescaled lengths. Once more, the capillary number is defined based on the viscosity of the liquid, $\mathrm{Ca} = \mu_\ell U_\mathrm{p}/\gamma$. This equation must be complemented by the geometrical relations

$$\frac{\mathrm{d}h}{\mathrm{d}s} = \sin\theta, \qquad \frac{\mathrm{d}x}{\mathrm{d}s} = \cos\theta \tag{4.19}$$

Note that for all numerical examples in the rest of the Chapter, we consider a vertical plate, for which $\alpha = \pi/2$.

One easily verifies that for $R_\mu = 0$, $\alpha = \pi/2$ and $\theta \to 0$, $f(0,0) = -1$ and (4.18) the standard LT equation for small slopes (see Eq. (2.51)) is recovered:

$$\frac{\mathrm{d}^3 h}{\mathrm{d}x^3} = \frac{3\mathrm{Ca}}{h^2} - 1. \tag{4.20}$$

When considering a single phase with arbitrary angle, one recovers the equation previously proposed in [23, Eq. (14)], with $f(\theta, 0)$ instead of $f(\theta, R_\mu)$.

It is important to note that Eq. (4.18) is derived from the solution of the HS model with no-slip boundary condition at the plate. Near the contact line, this induces a divergence of the pressure and of the shear stress, which scale as $\mu_\ell U_\mathrm{p}/h$ and $\mu_\mathrm{g} U_\mathrm{p}/h$ in the liquid and the gas, respectively. A purely hydrodynamic approach to regularize the singularity is to impose a slip boundary condition on the solid wall. Unfortunately, there is no direct extension of the HS model, which solves the Stokes' equation in a wedge satisfying both the slip boundary condition and the condition of bounded velocity [20]. However, as contact line flows are only mildly affected by the details of the microscopic conditions [19, 115], we proceed by a phenomenological regularization. We therefore consider the standard lubrication equation, which can be derived including a Navier slip boundary condition. The regularized LT equation is given by:

$$\frac{\mathrm{d}^3 h}{\mathrm{d}x^3} = \frac{3\mathrm{Ca}}{h(h + 3\lambda_\mathrm{s})} - 1, \tag{4.21}$$

where λ_s is the slip length (see section 2.4). In comparison to (4.20), the effect of slip can be summarized by a correction factor $h/(h + 3\lambda_\mathrm{s})$ for the viscous

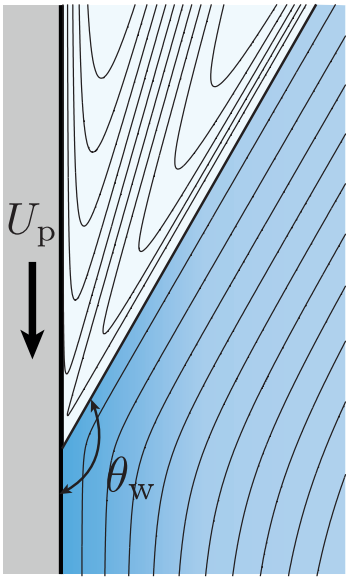

Figure 4.11: Streamlines showing the solution obtained form the HS model for the flow in a wedge of angle $\theta_\mathrm{w} = 0.83\pi$, $R_\mu = 10^{-3}$ and $U_\mathrm{p} = 1$. The wedge angle in this case is close to π. This flow solution has been used here to derive the GL model.

term. Indeed, this weakens the singularity such that the equations can be integrated to $h = 0$ [116]. We simply propose to use the same regularization factor for the viscous term in (4.18):

$$\frac{\mathrm{d}^2\theta}{\mathrm{d}s^2} = \frac{3\mathrm{Ca}}{h(h+3\lambda_\mathrm{s})} f(\theta, R_\mu) - \cos\theta, \tag{4.22}$$

where we have assumed the slip length to be independent of R_μ. Finally, in order obtain the complete information of the steady state interface profile, we solve the following system of ordinary differential equations:

$$\frac{\mathrm{d}\kappa}{\mathrm{d}s} = \frac{3\mathrm{Ca}}{h(h+3\lambda_\mathrm{s})} f(\theta, R_\mu) - \cos\theta, \tag{4.23a}$$

$$\frac{\mathrm{d}\theta}{\mathrm{d}s} = \kappa, \tag{4.23b}$$

$$\frac{\mathrm{d}h}{\mathrm{d}s} = \sin\theta, \tag{4.23c}$$

$$\frac{\mathrm{d}x}{\mathrm{d}s} = \cos\theta. \tag{4.23d}$$

In order to obtain a unique solution of Eq. (4.23) for the given Ca, R_μ, θ_e and λ_s, we need initial conditions on h, x, θ and κ at $s = 0$. The initial condition on h, x and θ can be obtained by the choice of our reference frame:

$$h(0) = 0, \qquad x(0) = 0, \qquad \theta(0) = \theta_e, \qquad \kappa(0) = \kappa_0. \tag{4.24}$$

However, κ_0 is not known in advance. To fix the value of κ_0 and to obtain a unique solution of Eq. (4.23), we use the constraint that far from the contact line the interface remains flat i.e.:

$$\theta(s \to \infty) = \pi/2, \tag{4.25}$$

(see Figure 4.10). We solve Eq. (4.23) with the boundary conditions given by Eq. (4.24) for arbitrary values of κ_0 until the constraint Eq. (4.25) is satisfied. In the following sections, we use the explicit 4th order Runge-Kutta numerical scheme, to compute the shape of the meniscus for different parameters $(\theta_e, R_\mu, \lambda_s)$.

4.4 Comparing the GL and LB simulations

In this section we compare the results of the GL model and the LB method. Since the latter are limited to moderate viscosity ratios R_μ, the comparison is done for R_μ=0.03, 0.83 and 1. We further explore the parameter space in section 4.3.2, using only the GL model. The results for this section are computed for θ_e=$\pi/2$ and $\alpha = \pi/2$.

The LB simulations are performed using the LB simulation setup that we established and validated in the first part of this Chapter. However, for the LB simulations shown in the rest of this Chapter, we restrict ourself to the no-slip/no-wetting boundary condition at the right boundary. Let us stress that all LB methods, independent of the underlying kinetic model, describe the multi-phase or the multi-component dynamics via a *diffuse interface* approach. There exist therefore a natural regularizing microscopic length which is of the order of the interface width, typically a few grid points. Such a length scale is also of the order of the *effective* slip length, λ_s, that must be used whenever a quantitative comparison between the hydrodynamical behavior of the LB and the evolution of the equivalent Navier-Stokes system is made, as shown for example recently in [35].

4.4.1 Meniscus rise

We first compare the meniscus rise Δ for viscosity ratios $R_\mu = 0.03, 0.83$ and 1 in Figure 4.12. When the plate is at rest, Ca = 0, the meniscus is perfectly

horizontal, i.e., $\Delta = 0$, due to the choice of θ_e and α. Let us first consider the case where both liquids have identical viscosity, $R_\mu = 1$, but are still immiscible due to the nonzero surface tension. This case is perfectly symmetric in the sense that $\mathrm{Ca} \to -\mathrm{Ca}$ gives $\Delta \to -\Delta$: there is no difference between plunging and withdrawing. This symmetry is indeed observed in Figure 4.12. Blue circles represent the LB simulations, while the dash-dotted line is the GL model. We use this symmetric case to calibrate the microscopic parameter of the GL model. A nearly perfect fit is achieved for slip length $\lambda_s = 0.002$, which is a reasonable value given that the grid size used in the LB simulation is 0.01. As Ca increases, the viscous forces increasingly deform the interface, leading to a change in Δ.

It is interesting to see to what extent the same microscopic parameter λ_s is able to describe different viscosity ratios. We first mildly decrease the viscosity ratio to $R_\mu = 0.83$ and still find a very good agreement between LB and the GL (red squares and dotted line respectively). With respect to the case $R_\mu = 1$ we see that $|\Delta|$ is slightly smaller at a given value of Ca. This means that for the same speed, the meniscus is deformed by a smaller amount due to the lower viscosity of the upper phase. When further decreasing the viscosity ratio to $R_\mu = 0.03$ (green diamonds, dashed line), some differences between LB and GL become apparent (the same value for λ_s is maintained). The meniscus in GL is systematically below the value obtained in LB. A possible explanation for this difference is the sensitivity of the result on the microscopic contact angle imposed as a boundary condition. Still, both models agree reasonably well and display very similar trends. In particular, we find that much larger values of Ca can be achieved due to the strong reduction of the viscosity in the upper phase. This effect is most pronounced for the plunging case, for which the liquid is advancing. This is consistent with experimental observations that advancing contact lines can move much more rapidly than receding contact lines [18, 19, 98]. The breakdown of the steady solutions, which signals the transition to air/liquid entrainment, will be discussed in details in section 4.3.2.

4.4.2 Shape of the meniscus

A much more detailed test for the two models is to investigate the detailed structure of the interface: How well do the shapes of the menisci compare between GL and LB? In Figure 4.13, we show the dynamical meniscus profiles for $\mathrm{Ca} = 1.9 \times 10^{-2}, 2.8 \times 10^{-2}$ and 3.6×10^{-2}, in the case of equal viscosities, $R_\mu = 1$. Note that the contact line position is held constant at $x = 0$, so that the bath appears at different heights due to the increase in magnitude

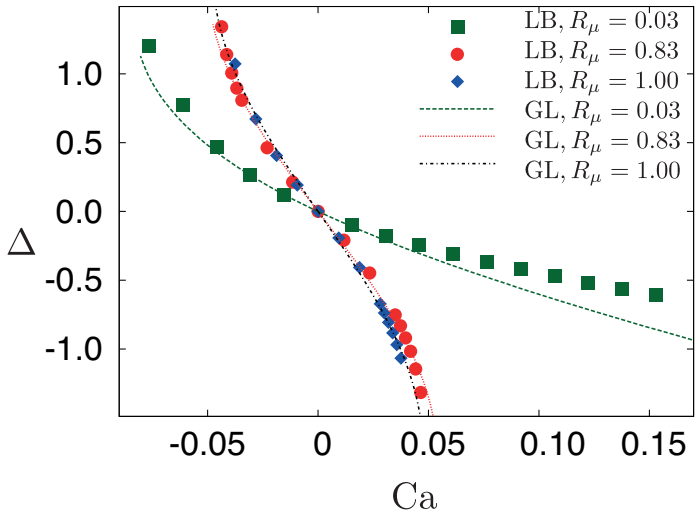

Figure 4.12: (Color online) Meniscus rise Δ *as a function of* Ca *for* $\theta_e = \pi/2$. Ca *is negative/positive when the plate is moving upward/downward. Symbols: results of lattice Boltzmann (LB) simulation. Curves: results of the lubrication-type (GL) model with a slip length* $\lambda_s = 2 \times 10^{-3}$. *All lengths are scaled by the capillary length* ℓ_c.

of Δ with speed. The agreement of the results of the GL model and the LB simulations is very good, in particular for Ca $= 1.9 \times 10^{-2}$ and 2.8×10^{-2}, even down to the contact line region (Figure 4.13b). For larger plate velocities some differences become apparent. These differences may be due to different reasons. First, one has to notice that a large Ca is also accompanied by a large viscous stress contribution, leading to a larger bending of the interface and therefore to the possibility to leave the realm of applicability of the GL model. Second, as said, in the LB approach the *effective* slip length is an output and not an input as for the GL method, and it is not clear that one would need a finer tuning of it as a function of the capillary number, in order to match the GL behavior.

An even more detailed characterization of the meniscus shape is provided by the local angle of the interface θ vs h, see Figure 4.14. Clearly, both the GL model and the LB simulation exhibit the same nontrivial variation of the contact angle. At small scales, the angle approaches $\theta_e = \pi/2$, while at large scale the meniscus evolves towards the reservoir $\theta = \alpha = \pi/2$. In between, the angle changes significantly due to the well-known effect of "viscous bending" [19]: the balance of viscosity and surface tension leads to a curvature of the interface. Very similar variations of the meniscus angle have been obtained

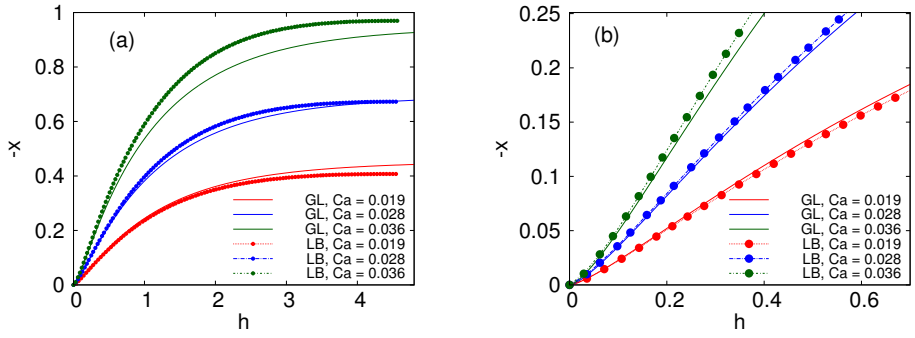

Figure 4.13: (Color online) Dynamical meniscus profiles $-x$ vs h for $R_\mu = 1$ ($\theta_e = \pi/2$ and $\lambda_s = 0.002$ for the GL model, lattice separation $= 0.01$ for the LB simulation). All lengths have been scaled by the capillary length. The contact line is at $x = 0$ so that the bath is at different x for different Ca. *(a) Solid curves: results of GL model. Dots: results of LB simulation. (b) Zoom on the contact line region.*

experimentally [117].

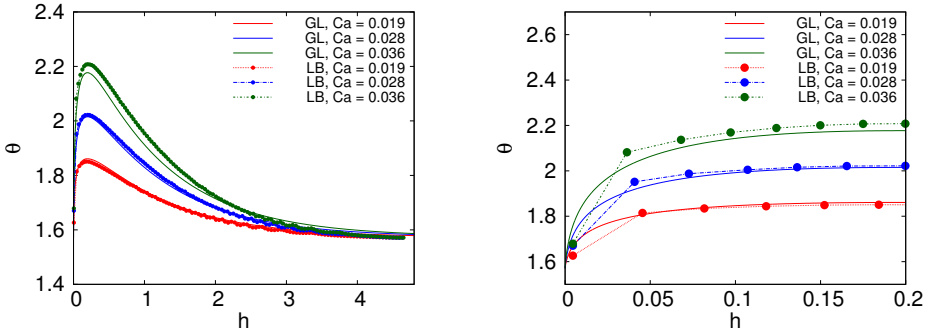

Figure 4.14: (Color online) Local meniscus angle θ (rad) vs h for $R_\mu = 1$. Identical parameters as in Figure 4.13.

4.5 Maximum speeds and transition to air entrainment

In this section and for the result of this Chapter, we discuss the physics of air entrainment in the case of a plunging plate ($\mathrm{Ca} > 0$) using the GL model. For realistic situations the viscosity ratio R_μ is typically very small, of order 10^{-2} for water and much smaller for very viscous liquids. This regime can be accessed by the GL model only, as LB is restricted to moderate viscosity contrasts. In the first part of this section we discuss how the transition to air entrainment is captured in our model in terms of a bifurcation diagram. Next, we study the effect of viscosity ratio on the critical speed. In the last part we investigate how the critical speed depends on the microscopic parameters such as the slip length and the static contact angle.

4.5.1 Maximum speed for advancing contact lines

We first consider the case where the equilibrium contact angle is close to π. For such a hydrophobic substrate we expect air entrainment to occur at relatively small Ca [99, 100], and therefore relatively weak curvature of the interface. This is important, since the assumption underlying the GL model is that the interface curvature is weak [22]. We will therefore focus on $\theta_\mathrm{e} = 2.8$ and explicitly verify how strongly the interface is curved for the numerical solutions using the GL model. Figure 4.15 shows the drop of the meniscus Δ as function of Ca for a viscosity ratio $R_\mu = 10^{-2}$ ($\lambda_\mathrm{s} = 10^{-5}$, i.e., of the order of 10 nm). As Ca increases, the contact line equilibrates at a lower position resulting in a more negative value of Δ. However, when Ca achieves a certain critical value, stationary solutions cease to exist. This corresponds to a maximum plate velocity, or critical capillary number $\mathrm{Ca_c}$. By analogy to deposition of liquid films for plate withdrawal [22, 86, 110, 111, 118], this can be identified as the onset of air entrainment: above $\mathrm{Ca_c}$, unsteady solutions will develop, with a downward motion of the contact line [98]. As can be seen in Figure 4.15, the critical point arises close to $\Delta = -\sqrt{2}$, which according to (4.2) corresponds to a meniscus with apparent contact angle π. This is the analogue of the withdrawal case, for which $\Delta = +\sqrt{2}$ and the apparent contact angle vanishes at the transition [107, 110]. Note that viscous effects push the system slightly below this maximum extent of deformation for a perfectly static meniscus, with the critical point slightly below $\Delta = -\sqrt{2}$.

Interestingly, for a range of speeds $\mathrm{Ca} < \mathrm{Ca_c}$ one actually finds more than one solution (Figure 4.15). Upon decreasing Δ, the capillary number first increases and then decreases close to the critical point. We refer to the solution

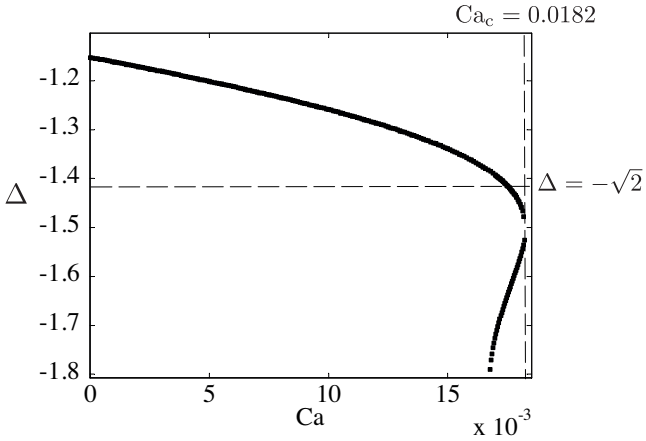

Figure 4.15: Meniscus fall Δ *versus* Ca ($\theta_e = 2.8$, $R_\mu = 10^{-2}$, $\lambda_s = 10^{-5}$). *The horizontal dashed line indicates the minimum value of* Δ *for a static meniscus* ($\Delta = -\sqrt{2}$, *with* $\theta_e = \pi$), *and the vertical dashed line indicates the critical capillary number* ($\mathrm{Ca_c} = 0.0182$).

branches around $\mathrm{Ca_c}$ as the upper and lower branch respectively. Once again, an identical bifurcation structure was previously observed for the withdrawing plate case [110, 119, 120]. To compare these two types of solutions, we show the corresponding meniscus profiles for $\mathrm{Ca} = 1.7 \times 10^{-2}$ in Figure 4.16. At a large distance from the contact line, the solutions are almost identical in shape. Zooming in on the contact line region, however, we see the lower branch (red dashed curve) solution displays a "finger" that explains the larger magnitude of Δ with respect to the upper branch.

4.5.2 Effect of viscosity ratio

A key parameter for the transition to air entrainment is the viscosity ratio R_μ. Figure 4.17 shows the meniscus fall Δ as function of Ca for different viscosity ratios: $R_\mu = 0$, 10^{-4}, 10^{-3} and 10^{-2}. At $\mathrm{Ca} = 0$, all cases have the same value of $\Delta = -1.15$ corresponding to a static bath with contact angle $\theta_e = 2.8$. Now we consider the result for $R_\mu = 0$, for which there are no viscous effects in the air ($\mu_g = 0$). We observe that Δ decreases with Ca, but without any bifurcation. It appears that steady meniscus solutions can be sustained up to arbitrarily large plate velocities. In fact, the curve is consistent with the scaling $\Delta \sim -\sqrt{\mathrm{Ca}}$ at large Ca, corresponding to a simple balance between gravity and viscosity. For $R_\mu \neq 0$, however, the situation becomes

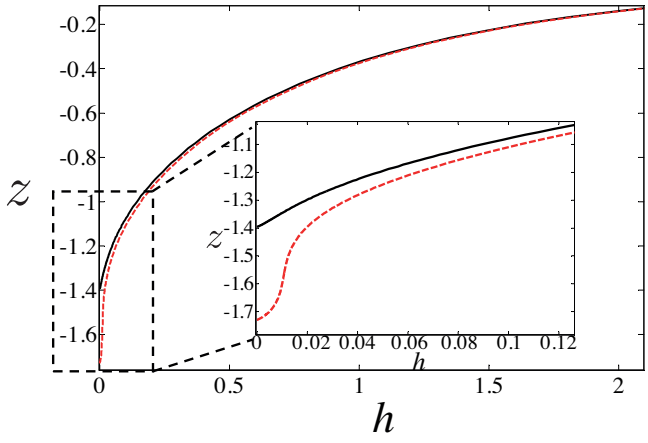

Figure 4.16: (Color online) Meniscus profiles for the upper branch (black solid curve) and the lower branch (red dashed curve) solutions for $\mathrm{Ca} = 1.7 \times 10^{-2}$ *(*$\theta_\mathrm{e} = 2.8$*,* $R_\mu = 10^{-2}$*,* $\lambda_\mathrm{s} = 10^{-5}$*). Here we define* $z = \Delta - x$*. So the bath level is at* $z = 0$*.*

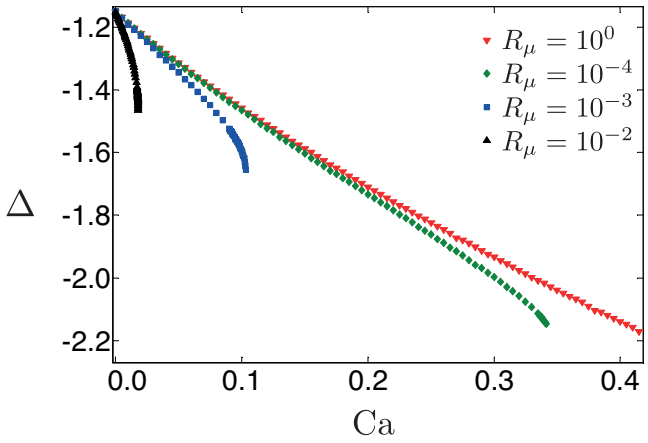

Figure 4.17: (Color online) Meniscus fall Δ *versus* Ca *for different viscosity ratios (*$\theta_\mathrm{e} = 2.8$ *,* $\lambda_\mathrm{s} = 10^{-5}$*). For the case the gas phase has no viscosity,* $R_\mu = 0$*, steady-state menisci can be maintained to arbitrarily large velocity (within our numerical resolution).*

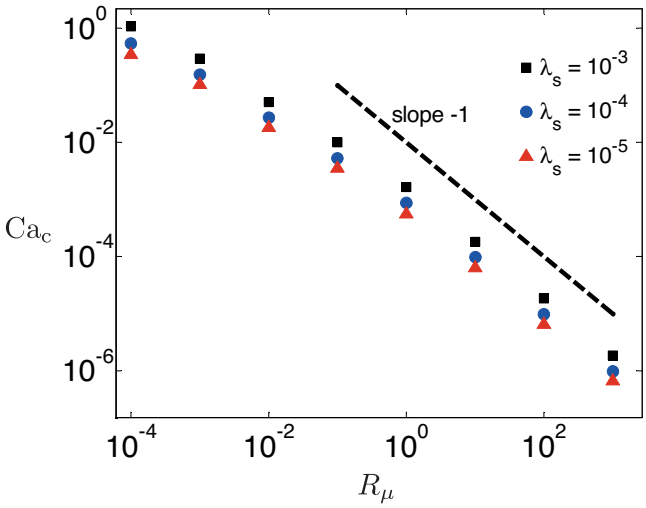

Figure 4.18: (Color online) Critical capillary number $\mathrm{Ca_c}$ *versus viscosity ratio* R_μ *for different slip lengths* λ_s *(*$\theta_e = 2.8$*). The dashed line indicates a power law with exponent -1, which is valid for large* R_μ*.*

fundamentally different. While the curves follow the same trend as for $R_\mu = 0$ at small Ca, a deviation appears at larger speeds that ultimately leads to a critical point. Each nonzero viscosity ratio has a well-defined critical speed, with $\mathrm{Ca_c}$ increasing when the viscosity ratio R_μ is reduced.

These observations can be interpreted as follows. As long as the viscosity of the air has a negligible effect on the flow, the curves are indistinguishable from the case $R_\mu = 0$. Deviations from the $R_\mu = 0$ curve signal that the air flow starts to influence the shape of the meniscus. Physically, this arises because the interface slope approaches π, leaving only a narrow wedge angle for the air flow. Figure 4.11 illustrates that the recirculation in the air induces significant velocity gradients: despite the small air viscosity, the stresses in the small wedge of air become comparable to those in the liquid. Mathematically, this can be derived from the function $f(\theta, R_\mu)$ as defined in (4.16). For small R_μ, θ close to π and the Taylor's series, we can approximate:

$$f(\theta, R_\mu) \simeq f(\theta, 0) - 4R_\mu \simeq -\frac{2(\pi - \theta)^3}{3\pi} - 4R_\mu \tag{4.26}$$

as long as $\pi - \theta \gg 2\pi R_\mu$ (see appendix I). For θ very close to π, $f(\theta, R_\mu)$ has a different asymptotic form, see the appendix for details. The first term in (4.26) represents the (relative) viscous contribution inside the liquid, which vanishes in the limit $\theta \to \pi$. The second term represents the viscous contribution in

the air, which will be significant once $(\pi - \theta) \sim R_\mu^{1/3}$. Noting that the contact line is *receding* from the point of view of the air phase, one understands that a critical speed appears when the effect of the air becomes important.

From here onwards, we adapt the following notions to represent the dip-coating problem: The direction of plate motion is along x-axis (see Figure 4.10). However for the dip-coating problem the viscosity ratio $R_\mu = \mu_1/\mu_2 \geq 1$, and the equilibrium contact angle is given by $(\pi - \theta_e)$. The notations used for the plunging plate problem remains same as before.

The dependence of the critical capillary number $\mathrm{Ca_c}$ on the viscosity ratio R_μ is shown in Figure 4.18 (for various slip lengths). First we consider the limit $R_\mu \gg 1$, for which the upper fluid is actually much more viscous than the bottom fluid. This is the usual case of a receding contact line that is completely dominated by the upper (receding) phase. In this limit we expect the critical plate velocity (U_p^*) to scale with the viscosity of the upper phase (μ_1), such that $U_\mathrm{p}^* \sim \gamma/\mu_1$. Since we have defined the capillary number based on the viscosity μ_2, we obtain $\mathrm{Ca_c} \equiv U_\mathrm{p}^* \, \mu_2/\gamma \sim R_\mu^{-1}$. This is indeed observed in Figure 4.18 at $R_\mu \gg 1$. However, our main interest here lies in the opposite limit, i.e., $R_\mu \ll 1$, as for air entrainment. As already mentioned, the critical capillary number seems to increase indefinitely by reducing the viscosity ratio. This suggests that for the limiting case of $R_\mu = 0$, steady menisci can be sustained at arbitrarily large capillary numbers. Our numerical resolution does not allow for a perfect determination of the asymptotics for $R_\mu \ll 1$. Enforcing a power law fit, $\mathrm{Ca_c} \sim (R_\mu)^\beta$, in the range $R_\mu = 10^{-4} - 10^{-1}$, one obtains $\beta = -0.67$. This (effective) exponent suggests that both phases play an important role in determining the critical speed. Namely, the exponent would be $\beta = -1$ if only μ_1 were important, while $\beta = 0$ corresponds to the case where μ_2 is the only relevant viscosity.

Finally, we briefly verify the assumption of small curvature, necessary for the strict validity of the model. In Figure 4.19 we plot the dimensionless curvature, $h|\mathrm{d}\theta/\mathrm{d}s|$, as function of h in the vicinity of the critical point ($R_\mu = 10^{-4}, 10^{-3}$ and 10^{-2}, $\lambda_\mathrm{s} = 10^{-5}$). At small scales, $h|\mathrm{d}\theta/\mathrm{d}s| \ll 1$ for all Ca, consistent with the assumption of small curvature. However, the curvature increases significantly when approaching the bath due to the bending of interface from a large contact angle to $\pi/2$. The magnitude is acceptable in this regime, in particular since viscous effects becomes less important at large scales. Inclining the plate angle to values close to π would further reduce this bending effect, and extend the range of validity of the GL model.

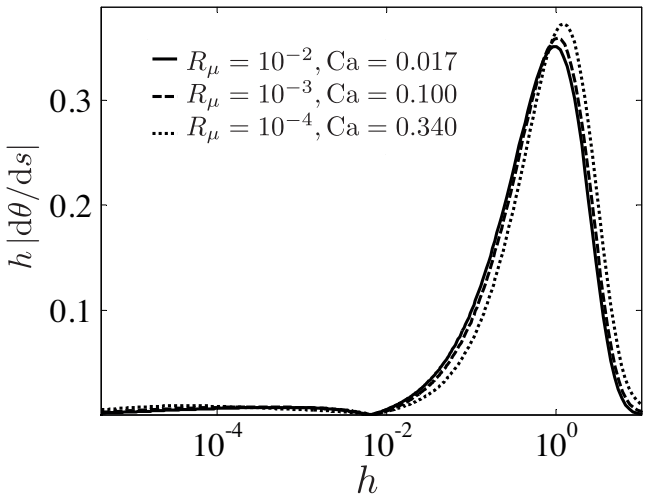

Figure 4.19: Scaled curvature $h|\mathrm{d}\theta/\mathrm{d}s|$ vs h for Ca *very close to* $\mathrm{Ca_c}$ *($\lambda_\mathrm{s} = 10^{-5}$).*

4.5.3 Dependence of the critical speed on microscopic parameters

Apart from the viscosity ratio, the GL model contains two parameters: the slip length λ_s and the microscopic (equilibrium) contact angle θ_e. Here we discuss the dependence of $\mathrm{Ca_c}$ on these parameters. The slip length was varied already in Figure 4.18, with values $\lambda_\mathrm{s} = 10^{-5}$, 10^{-4} and 10^{-3}. As expected for wetting problems, we see a weak increase of $\mathrm{Ca_c}$ with increasing λ_s. A larger λ_s reduces the range over which viscous dissipation is effective. This leads to a (logarithmic) reduction of the viscous dissipation, while the capillary forces remains unaltered. Hence, larger velocities can be achieved before air entrainment occurs.

The dependence of the critical speed on θ_e is investigated in Figure 4.20. The figure reveals that there is no obvious universal scaling behavior for Ca_c down to viscosity ratios as small as $R_\mu = 10^{-4}$. Enforcing a power-law fit, different θ_e would give rise to different exponents. We do clearly see that $\mathrm{Ca_c}$ decreases with increasing θ_e, which is further emphasized in Figure 4.21. Consistent with [99, 100], the critical speed vanishes in the hydrophobic limit where $\theta_\mathrm{e} \to \pi$. We note that for contact angles that are not close to π, the shape of the meniscus displays significant curvatures. In this sense, we expect that our results are not fully quantitative solutions of the Stokes flow problem.

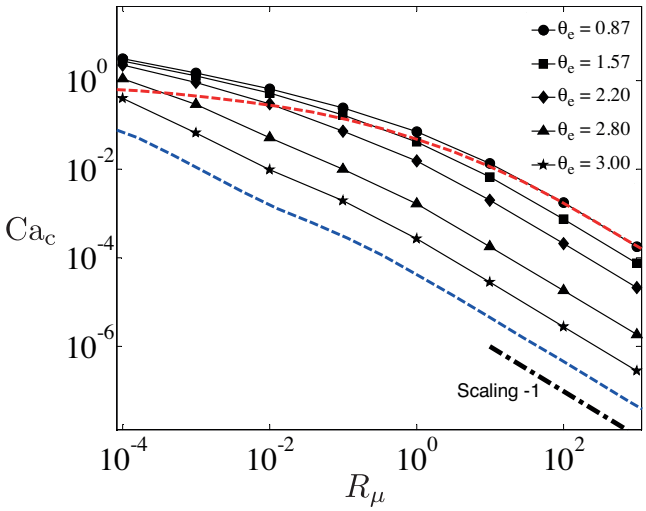

Figure 4.20: (Color online) Critical capillary number $\mathrm{Ca_c}$ *as a function of* R_μ *for different static contact angle* θ_e *(*$\lambda_\mathrm{s} = 10^{-3}$*). Symbols are results of the GL model. Dashed curves are predictions of Cox's model (top one for* $\theta_\mathrm{e} = 0.87$*, bottom one for* $\theta_\mathrm{e} = 3.0$*), from [27, Eq. (8.3)], for which we take the ratio between the microscopic length scale and macroscopic length scale to be* 10^{-3} *(the same value as our slip length scaled by the capillary length* λ_s*). The dashed-dotted line indicates slope of -1.*

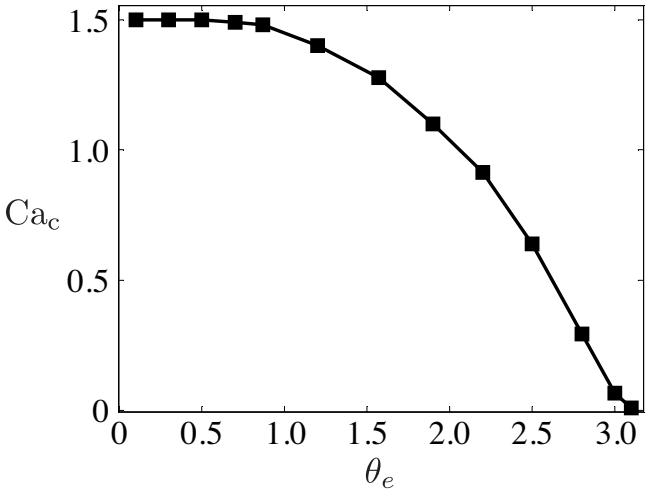

Figure 4.21: Critical capillary number $\mathrm{Ca_c}$ *as a function of static contact angle* θ_e *for* $R_\mu = 10^{-3}$ *and* $\lambda_\mathrm{s} = 10^{-3}$.

4.6 Discussion and conclusions

In the first part of this Chapter, we studied the behavior of a fluid at the three-phases contact, e.g. amongst a solid a liquid and its vapor, by means of the LB method. Here we discussed the possibility to employ simple and standard implementations of the LB method for multiple phases or components in order to study the problem under both static and dynamic (i.e. moving wall) conditions. We showed that the MC-LB method can effectively replace the MP modeling by applying the gravitational field, along with balancing hydrostatic pressure at the bottom, on only one fluid component. The MC-LBM is less sensitive to condensation and evaporation phenomena at the contact line and thus outperforms the MP method for the case of small viscosity ratio between the two fluids.

In the second part of this Chapter, we have presented, compared and employed two distinct models to study the meniscus deformation and the onset of air entrainment in a dip-coating geometry. The first model is a generalization of the lubrication theory to a two-phase flow situation, in which a slip length is introduced to resolve the viscous singularity. The second model is the lattice Boltzmann method for multiphase/multicomponent fluids. In the LB model the viscous singularity is removed by lattice discretization, which effectively introduces an effective slip length to the system [37]. Therefore,

the effective slip length in the LB method depends on the choice of multiphase/multicomponent model.

The results of the GL model and the LB model have shown a good agreement, in particular when Ca is relatively small. When exploring larger values of Ca, the two models start to differ as shown in Figure 4.12, which can be attributed to different physics at microscopic and hydrodynamical scales (e.g. the non-zero interface thickness in the LB or strong viscous bending of the interface violates the hypothesis of small interface curvatures in the GL model). Yet, qualitative features, such as the bending of the meniscus and the dependence on viscosity ratio, are consistent for the two models. The transition to air entrainment for θ_e close to π involves relatively weak curvatures and is thus captured by the GL model. For the LB simulations the main challenge is given by the small viscosity ratio between the two phases, something that is still not fully achievable for the MP/MC-LB model used here.

Furthermore, in the second part of this Chapter, the critical speed of air entrainment is investigated by the GL model. We have found a strong dependence of critical speeds on the air viscosity, which is consistent with the experiments performed by Marchand *et al.* [98]. Remarkably, both our theoretical results and the experimental results from [98] differ from Cox's model in which $\mathrm{Ca_c}$ is predicted to depend only logarithmically on air viscosity [27]. For comparison, we have added in Figure 4.20 the predictions of the Cox's model [27, Eq. (8.3)], represented by the dashed curves (top curve for $\theta_e = 0.87$, bottom one for $\theta_e = 3.0$). For the dip-coating problem, we find that both models predict $\mathrm{Ca_c}$ scales as R_μ^{-1}. This regime corresponds to the usual dewetting case for which the critical speed only depends on the viscosity of the more viscous fluid [107, 110, 111]. Note that in Cox's model, there is an undetermined factor ϵ which is defined as the ratio of the microscopic length scale to the macroscopic length scale. Here we take ϵ to be the same value as λ_s, which is 10^{-3}. Interestingly, both the models predict exactly the same values of $\mathrm{Ca_c}$ for $\theta_e = 0.87$ when R_μ is large, which we consider as an coincidence since ϵ is an adjustable parameter. For $\theta_e = 3.0$, Cox's and our results differ by a factor. More interesting things occur at small R_μ, it is clearly shown in Figure 4.20 that for Cox's model (red top curve) $\mathrm{Ca_c}$ increases extremely slowly (logarithmically) as R_μ is decreased. By contrast, our model predicts a moderate increase of $\mathrm{Ca_c}$. Interestingly, such a weak logarithmic relation has been observed in the case of liquid impacting on liquid [102, 103], for which there is no moving contact line. Both our theoretical results and experimental results from [98] therefore suggest that the mechanism leading to air entrainment can be fundamentally different depending on whether a contact line is present or not.

The GL model is directly compared with experiments in [98], and shows that the model is able to qualitatively capture the dependence of Ca_c on the viscosity ratio R_μ. Quantitatively, however, the agreement is not satisfactory [98, Figure 3]. We believe this is due to the relatively large meniscus curvatures encountered in the experiments (static contact angle of the substrate ≈ 0.87), pushing the problem beyond the assumptions of the model. It would be interesting to explore other methods to achieve a more quantitative description of air entrainment by an advancing contact line, in particular for large values of Ca. From an experimental perspective, more insight could be obtained by varying the gas viscosity or by replacing the air by a liquid of low viscosity. It would also be interesting to perform experiments with a substrate of large static contact angles.

5 | Axisymmetric lattice Boltzmann method *

In this chapter, a novel lattice Boltzmann method for axisymmetric multi-phase flows is presented and validated. The novel method is capable of accurately modelling flows with variable density. We extend the classic Shan-Chen multi-phase model [Physical Review E **47***, 1815 (1993)] to axisymmetric flows. The model can be used to efficiently simulate single- and multi-phase flows. The convergence to the axisymmetric Navier-Stokes equations is demonstrated analytically by means of a Chapman-Enskog expansion and numerically through several test-cases. In particular, the model is benchmarked for its accuracy in reproducing the dynamics of the oscillations of an axially symmetric droplet and on the capillary breakup of a viscous liquid thread. Very good quantitative agreement between the numerical solutions and the analytical results is observed.*

5.1 Introduction

Multiphase flows occur in a large variety of phenomena, in nature and industrial applications alike. In both type of applications it is often necessary to accurately and efficiently simulate the dynamics of interfaces under different flow conditions. A paradigmatic industrial application concerns the formation of small ink droplets from inkjet printer nozzles [8]. When both flow geometry and initial conditions display axial symmetry, one expects that the flow will preserve that symmetry at any later time. Under such conditions it is advantageous to employ numerical methods capable of exploiting the symmetry of the problem. The computational costs of a three-dimensional (3D) axisymmetric simulation is very close to that of a two-dimensional (2D), presenting thus a considerable advantage over fully 3D simulations. When one deals with multiphase methods characterized by diffuse interfaces, such as the ones common

*Published as: S. Srivastava et al. *Axisymmetric multi-phase lattice Boltzmann method*, Phys. Rev. E **88**, 013309 (2013), and S. Srivastava et al. *Lattice Boltzmann method to study the contraction of viscous ligament*, Int. J. Mod. Phys. C (2013).

in the lattice Boltzmann method, the availability of additional computational resources allows one to decrease the interface width with respect to the other characteristic length-scales in the problem. The possibility to get closer to the "sharp-interface" limit has thus a direct impact on the accuracy of the numerical solutions for diffuse interface multi-phase solvers. In recent years several implementations of axisymmetric LBM for single-phase systems have been proposed [121–126], while, in comparison, relatively little attention has been devoted to the case of the multi-phase flow [127, 128].

The aim of the present chapter is to introduce a novel, accurate and efficient algorithm to study generic axisymmetric, density-varying flows and in particular multi-phase flows. The proposed algorithm is easy to implement, is accurate and its multi-phase model builds upon the widely used Shan-Chen model [9, 10]. One particular advantage of having the axisymmetric implementation of the Shan-Chen model is that it allows one to retain the same parameters of the fully 3D model (e.g., coupling strength, surface tension and phase diagram) thus allowing to easily switch between axisymmetric and full 3D Shan-Chen investigations, according to what is needed.

The chapter is organized as follows. In section 5.2 we present the new lattice Boltzmann method. In section 5.3 and section 5.4 we present the results of several benchmarks of the method against single and multi-phase flows, respectively. In section 5.5, we present an application of the multi-phase axisymmetric LB model to study the contraction of a viscous ligament. In section 5.6 conclusions are drawn. The derivation of the additional terms for the axisymmetric LB model is presented in Appendix II.

5.2 Axisymmetric LB method

When the boundary conditions, the initial configuration and all external forces are axisymmetric, one does expect that the solution of the Navier-Stokes (NS) equations will preserve the axial symmetry at any later time. The rotationally symmetric continuity and NS equations in cylindrical coordinates (z, r, θ), in absence of external forces reads:

$$\frac{\partial \rho}{\partial t} + \boldsymbol{\nabla} \cdot (\rho \mathbf{u}) = -\frac{1}{r}\rho u_{\mathrm{r}}, \tag{5.1}$$

and

$$\rho\left(\frac{\partial \mathbf{u}}{\partial t} + \mathbf{u} \cdot \boldsymbol{\nabla}\mathbf{u}\right) = -\boldsymbol{\nabla} p + \boldsymbol{\nabla}\Big[\mu(\boldsymbol{\nabla}\mathbf{u} + \boldsymbol{\nabla}\mathbf{u}^{\mathsf{T}})\Big] + \mathbf{F}^{\mathrm{axis}}, \tag{5.2}$$

where $\mathbf{u} = (u_{\mathrm{z}}, u_{\mathrm{r}})$ is the velocity and $\boldsymbol{\nabla} \equiv (\partial_{\mathrm{z}}, \partial_{\mathrm{r}})$ is the gradient operator in the 2D Cartesian coordinate system $(z \to x, r \to y)$. The additional term,

$\mathbf{F}^{\text{axis}} \equiv (F_z^{\text{axis}}, F_r^{\text{axis}})$, is the contribution due to axisymmetry and given by:

$$F_{\text{z}}^{\text{axis}} = \frac{\mu}{r}\left(\frac{\partial u_{\text{z}}}{\partial r} + \frac{\partial u_{\text{r}}}{\partial z}\right), \qquad F_{\text{z}}^{\text{axis}} = 2\mu\frac{\partial}{\partial r}\left(\frac{u_{\text{r}}}{r}\right). \tag{5.3}$$

respectively, where $\mu = \nu\rho$, is the dynamic viscosity and ν is the kinematic viscosity of the fluid. In principle an axisymmetric flow may have an azimuthal component of the velocity field, u_θ. In Eqs. (5.1) and (5.2) we assume that the flows that we consider have no swirl , *i.e.*, $u_\theta = 0$, and that other hydrodynamic variables are independent of θ. We can thus write, $u_{\text{r}} = u_{\text{r}}(z, r; t)$, $u_\theta = 0$, $u_{\text{z}} = u_{\text{z}}(z, r; t)$ and $\rho = \rho(z, r; t)$.

Eqns. (5.1) and (5.2) easily highlight the similarities with respect to 2D flows in a (z, r)-plane. The continuity equation (5.1) differs from the purely 2D equation because of the presence of a source/sink term on the right hand side; this term is responsible for a locally increasing mass whenever fluid is moving towards the axis, and for decreasing mass, when moving away. The physical role of this term is to maintain 3D mass conservation (a density ρ at a distance r must be weighted with a $2\pi r$ factor).

The NS equations have also been rewritten in a way to highlight the 2D equations. The additional contributions that make the 3D axisymmetric equations differ from the 2D ones are the terms $r^{-1}\mu(\partial_{\text{r}} u_{\text{z}} + \partial_{\text{z}} u_{\text{r}})$ and $2\mu\partial_{\text{r}}(r^{-1}u_{\text{r}})$ on the right hand side of the Eq. (5.2). Our approach employs a 2D LB model to solve for the 2D part of the equations and explicitly evaluate and adds the additional force terms given in Eq. (5.3).

The idea to model the 3D axisymmetric LB method with a 2D LB model supplemented with appropriate source-terms has already been employed in a number of studies, for single-phase axisymmetric LBM models [121, 122, 129, 130] and for multi-phase LB model as well [127, 128]. Here we will develop an axisymmetric version of the Shan-Chen model [9, 10].

In the reset of this Chapter, we will use $\mathbf{x} = (z, r)$, where the z-axis is the horizontal axis and the r-axis is the vertical axis. Details of the standard LB model and the multi-phase SC model can be found in Chapter 3 of this thesis. Here, we will only describe the axisymmetric variant of the single- and multi-phase LB method. The axisymmetric multi-phase model developed here is an axisymmetric variant of the standard Shan-Chen model [9, 10].

5.2.1 LB model for axisymmetric single-phase flow

The first step in deriving a LB model for axisymmetric multi-phase flow is to derive a model that can properly deal with density variations. In particular, the LBM should recover the axisymmetric continuity Eq. (5.1) and

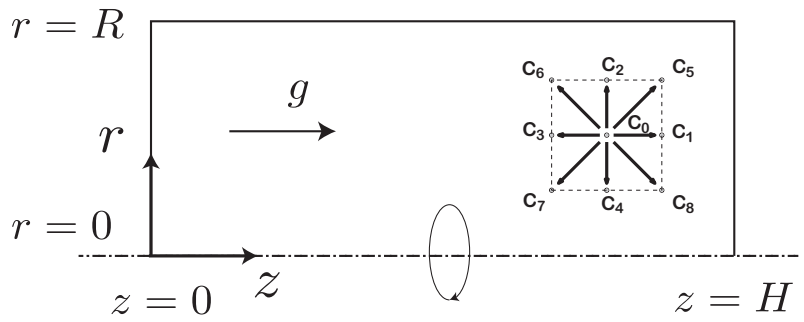

Figure 5.1: Schematic of the axisymmetric geometry, eventually in presence of gravity or an external force aligned with the z-axis. Schematic also shows the lattice velocities for the D2Q9 model.

NS Eqs. (5.2) by means of a Chapman-Enskog (CE) expansion in the long-wavelength and long-time scale limit. In order to derive such a model we start from the 2D LB model with the addition of appropriate space- and time-varying microscopic sources h_i (see also [121, 122, 129, 130]). We employ the following lattice Boltzmann equation:

$$\begin{aligned} &f_i(\mathbf{x}+\mathbf{c}_i\delta t, t+\delta t) - f_i(\mathbf{x},t) = -\frac{1}{\tau}\big(f_i(\mathbf{x},t) - f_i^{\mathrm{eq}}(\rho,\mathbf{u}^{\mathrm{eq}})\big) \\ &+ \delta t\; h_i(\mathbf{x}+\mathbf{c}_i\delta t/2, t+\delta t/2), \qquad \text{for } i=0,1,\dots 8, \end{aligned} \tag{5.4}$$

where the source terms h_i, are evaluated at fractional time steps, and τ is non-dimensional ($\tau = \tau/\delta t$). It can be shown, that when the additional term h_i in Eq. (5.4) has the following form:

$$h_i = w_i\Big(-\frac{\rho u_{\mathrm{r}}}{r} + \frac{1}{c_s^2}\big(c_{i\mathrm{z}}H_{\mathrm{z}} + c_{i\mathrm{r}}H_{\mathrm{r}}\big)\Big), \tag{5.5}$$

with $\mathbf{c}_i = (c_{i\mathrm{z}}, c_{i\mathrm{r}})$, and

$$H_{\mathrm{z}} = \frac{c_{i\mathrm{z}}}{r}\Big(\mu\big(\partial_{\mathrm{r}}u_{\mathrm{z}} + \partial_{\mathrm{z}}u_{\mathrm{r}}\big) - \rho u_{\mathrm{r}}u_{\mathrm{z}}\Big), \tag{5.6a}$$

$$H_{\mathrm{r}} = \frac{c_{i\mathrm{r}}}{r}\Big(2\mu\Big(\partial_{\mathrm{r}}u_{\mathrm{r}} - \frac{u_{\mathrm{r}}}{r}\Big) - \rho u_{\mathrm{r}}^2\Big), \tag{5.6b}$$

the CE expansion of Eq. (5.4) provides the axisymmetric version of the continuity and the NS Eqs. (5.1) and (5.2). Details on the CE expansion are reported in Appendix II. The equations introduced here are enough to describe a fluid with variable density in axisymmetric geometry.

5.2.2 LB model for axisymmetric multi-phase flow

With a lattice Boltzmann method capable of handling density variations the additional steps towards the definition of the axisymmetric version of the SC multi-phase model only consists in the correct definition of the SC force.

The standard Shan-Chen model in the continuous form is given by Eq. (3.44):

$$\mathbf{F}_{\mathrm{sc}}(\mathbf{x}) = -G_{\mathrm{sc}} c_s^2\, \delta t\, \psi(\mathbf{x}) \boldsymbol{\nabla} \psi(\mathbf{x}) - \frac{G_{\mathrm{sc}}}{2} c_s^4 (\delta t)^3 \psi(\mathbf{x}) \boldsymbol{\nabla} (\boldsymbol{\nabla}^2 \psi(\mathbf{x})) \tag{3.44}$$

This continuum expression is accurate up to $5th$-order in space and time, lattice independent and holds true for any coordinate system and dimension. We restrict Eq. (3.44) to the case of axisymmetric flows by expressing both the gradient, $\boldsymbol{\nabla}$ and the Laplace, $\boldsymbol{\nabla}^2$ operators in cylindrical coordinates given by $\boldsymbol{\nabla} \equiv (\partial_{\mathrm{z}}, \partial_{\mathrm{r}})$ and $\boldsymbol{\nabla}^2 \equiv (\partial_{\mathrm{zz}} + \partial_{\mathrm{rr}} + r^{-1}\partial_{\mathrm{r}})$. Thus, in the axisymmetric case, Eq. (3.44) reduces to:

$$\begin{aligned} \mathbf{F}_{\mathrm{sc}}(\mathbf{x}) \;=\; & -G_{\mathrm{sc}} c_s^2\, \delta t\, \psi(\mathbf{x}) \boldsymbol{\nabla} \psi(\mathbf{x}) - \frac{G_{\mathrm{sc}}}{2} c_s^4 (\delta t)^3 \psi(\mathbf{x}) \boldsymbol{\nabla} (\boldsymbol{\nabla}^2 \psi(\mathbf{x})) \\ & + \mathbf{F}_{\mathrm{sc}}^{\mathrm{axis}}(\mathbf{x}). \end{aligned} \tag{5.7}$$

where $\boldsymbol{\nabla}^2 = \partial_{\mathrm{zz}} + \partial_{\mathrm{rr}}$ is the Laplace differential operator in 2D ($z \to x, r \to y$),

$$\mathbf{F}_{\mathrm{sc}}^{\mathrm{axis}}(\mathbf{x}) = -\frac{G_{\mathrm{sc}}}{2} c_s^4 (\delta t)^3 \psi(\mathbf{x}) \boldsymbol{\nabla} \left(r^{-1} \partial_{\mathrm{r}} \psi(\mathbf{x})\right). \tag{5.8}$$

From Eq. (5.7), we immediately see that the first two terms on the right hand side give the Shan-Chen force in 2D. The last term in Eq. (5.7), $\mathbf{F}_{\mathrm{sc}}^{\mathrm{axis}}$, is the additional term responsible for the three-dimensionality. This extra contribution needs to be accurately taken into account in order to model the axisymmetric Shan-Chen multi-phase systems in 3D. In particular, this term is extremely important in order to correctly implement a 3D surface tension force which responds to curvatures, both along the axis and in the azimuthal direction. The two components of the additional term can be rewritten as:

$$F_{\mathrm{sc,z}}^{\mathrm{axis}} = -\frac{G_{\mathrm{sc}}}{2} c_s^4 (\delta t)^3 \psi r^{-1} \partial_{\mathrm{zr}} \psi, \tag{5.9a}$$

$$F_{\mathrm{sc,r}}^{\mathrm{axis}} = -\frac{G_{\mathrm{sc}}}{2} c_s^4 (\delta t)^3 \psi \Big(r^{-1} \partial_{\mathrm{rr}} \psi - r^{-2} \partial_{\mathrm{r}} \psi \Big). \tag{5.9b}$$

The evaluation of the terms $F_{\mathrm{sc,z}}^{\mathrm{axis}}$ and $F_{\mathrm{sc,r}}^{\mathrm{axis}}$ requires an approximation for the derivatives accurate up to order $(\delta t)^4$ or higher. Such an accuracy ensures the isotropy of the "reconstructed" 3D axisymmetric Shan-Chen force and thus

the isotropy of the resulting surface tension along the interface. The pressure tensor for the SC model is given by:

$$\begin{aligned} P_{\alpha\beta} =& \Big(c_s^2\rho + \frac{c_s^2 G_{\rm sc}}{2}\psi^2 + \frac{c_s^4 G_{\rm sc}}{2}\psi\boldsymbol{\nabla}^2\psi + \frac{c_s^4 G_{\rm sc}}{4}|\boldsymbol{\nabla}\psi|^2 \Big)\delta_{\alpha\beta} \\ & - \frac{c_s^4 G_{\rm sc}}{2}\partial_\alpha\psi\partial_\beta\psi + \left(\tau - \frac{1}{2}\right)^2 \frac{1}{\rho} F_{{\rm sc},\alpha} F_{{\rm sc},\beta}, \end{aligned} \tag{3.51}$$

where the suffix α, β range over the set $\{z, r\}$. The equation of state remains same as the standard SC model

$$p(\rho) = c_s^2\rho + \frac{c_s^2}{2} G_{\rm sc}\,\psi(\rho)^2. \tag{3.47}$$

Our choice for the pseudo density function remains the same throughout this thesis:

$$\psi(\rho) = \rho_0[1 - \exp(-\rho/\rho_0)],$$

where ρ_0 is a constant ($\rho_0 = 1$).

In our implementation we used the following isotropic $5th$-order accurate finite difference approximations on D2Q9 lattice (see Figure 5.1). For a scalar valued function $\phi(\mathbf{x})$ it reads:

$$\begin{aligned} \partial_{\rm r}\phi(\mathbf{x}) &= \frac{1}{36}\sum_{i=1}^{8}\Big(8\phi(\mathbf{x}+\mathbf{c}_i\delta t) - \phi(\mathbf{x}+2\mathbf{c}_i\delta t)\Big)c_{i{\rm r}} \\ &\quad + O((\delta t)^5), \end{aligned} \tag{5.10a}$$

$$\begin{aligned} \partial_{\rm rr}\phi(\mathbf{x}) &= \frac{1}{36}\sum_{i=1}^{8}\Big(8\partial_{\rm r}\phi(\mathbf{x}+\mathbf{c}_i\delta t) - \partial_{\rm r}\phi(\mathbf{x}+2\mathbf{c}_i\delta t)\Big)c_{i{\rm r}} \\ &\quad + O((\delta t)^5), \end{aligned} \tag{5.10b}$$

$$\begin{aligned} \partial_{\rm zr}\phi(\mathbf{x}) &= \frac{1}{12}\Big(- \partial_{\rm r}\phi(\mathbf{x}+2\mathbf{c}_1\delta t) + 8\partial_{\rm r}\phi(\mathbf{x}+\mathbf{c}_1\delta t) \\ &\quad - 8\partial_{\rm r}\phi(\mathbf{x}+\mathbf{c}_3\delta t) + \partial_{\rm r}\phi(\mathbf{x}+2\mathbf{c}_3\delta t)\Big) \\ &\quad + O((\delta t)^6), \end{aligned} \tag{5.10c}$$

where $\partial_{\rm r}\phi(\mathbf{x})$ in Eq. (5.10c) is approximated as

$$\begin{aligned} \partial_{\rm r}\phi(\mathbf{x}) &= \frac{1}{12}\Big(- \phi(\mathbf{x}+2\mathbf{c}_2\delta t) + 8\phi(\mathbf{x}+\mathbf{c}_2\delta t) \\ &\quad - 8\phi(\mathbf{x}+\mathbf{c}_4\delta t) + \phi(\mathbf{x}+2\mathbf{c}_4\delta t)\Big) \\ &\quad + O((\delta t)^6). \end{aligned} \tag{5.10d}$$

From the SC model the present axisymmetric implementation does inherit all advantages as well as the limitations. One of the limitations is the relatively small density contrast that can be achieved. Other multi-phase LB models, for which similar axisymmetric extensions can be worked out, may allow to achieve larger density contrasts. In the SC model both the density ratio, $R_\rho = \rho_\ell/\rho_\mathrm{v}$, and the surface tension, γ, depend upon a single parameter, G_sc. Decreasing the value of G_sc increases both the surface tension and the density ratio between two phases. Higher surface tension gives smaller interface width that leads to higher truncation error in the gradient approximation at the interface. This makes the numerical scheme unstable for too high values of G_sc. As a rule of thumb, a density ratio of $R_\rho \leq 35$, ($-6.0 \leq G_\mathrm{sc} < -4.0$) still ensures the stability of the SC model. Therefore, the current axisymmetric SC model, as much as the standard SC model, is limited to density ratio smaller then 35.

5.2.3 Boundary conditions

In axisymmetric flows the boundary conditions for the distribution functions, f_i, need to be prescribed at all boundaries including at the axis. In our approach we impose boundary conditions before the streaming step (pre-streaming). We use mid-grid point specular reflection boundary conditions on the axis [15], this choice allows us to avoid the singularity due to the force terms containing $1/r$. Mid-grid bounce-back or mid-grid specular reflection boundary conditions are used to impose either hydrodynamic no-slip or free-slip conditions at the other walls, respectively [15]. In order to impose a prescribed velocity or pressure at the inlet and outlet boundaries, we impose the equilibrium distribution functions, f_i^eq, evaluated using the desired hydrodynamic velocity and density values. For our LB simulations we use unit time step ($\delta t = 1$) and unit grid spacing ($\delta z = \delta r = 1$), hence the length can be measured in terms of the number of nodes. We are using symmetry boundary condition for the derivative evaluation in (5.6) and (5.8) at the axis. For the other three boundaries we impose the derivative terms to be zero.

5.3 Numerical validation for single-phase axisymmetric LB model

Here we present the validation of the axisymmetric LB model for single-phase flow simulations by comparing it with analytical solutions for the test cases: the axial flow through a tube and the outward radial flow between two parallel

discs. These two tests complement each other because they correspond to flows parallel and orthogonal to the axis, respectively. Both flow problems have analytical steady state solutions that help us to validate the accuracy of the axial and radial component of the velocity.

All physical quantities in this chapter, unless otherwise stated, are reported in lattice units (LU), the relaxation time has been keep fixed for all the simulations, $\tau = 1$, and the simulations have been carried out on a rectangular domain of size $H \times R = N_{\mathrm{z}} \times N_{\mathrm{r}}$. The steady state in the following single-phase simulations is defined when the total kinetic energy of the system, $E_{\mathrm{kin}} = \pi \sum_{N_z} (\sum_{N_r} r\rho \|\mathbf{u}\|^2)$, becomes constant up to the machine precision.

5.3.1 Flow through a pipe

In this test we consider the constant-density flow of a fluid with density, ρ, kinematic viscosity, ν, flowing inside a circular pipe of radius R. The flow is driven by a constant body force, ρg, along to the axis of the pipe. The schematic illustration of the flow geometry is presented in Figure 5.1. Assuming $u_{\mathrm{r}}(z, r) = 0$ and no-slip condition on the inner surface ($r = R$) of the pipe, the steady state solution for the axisymmetric NS Eq. (5.2) for this problem is given by [131]:

$$u_{\mathrm{z}}(z, r) = U_1 \left[1 - \left(\frac{r}{R} \right)^2 \right], \tag{5.11}$$

where $U_1 = u_{\mathrm{r}}(z, 0) = gR^2/(4\nu)$, is the maximum velocity in the pipe. For the LB simulation we used the no-slip boundary condition at the inner surface of the pipe, and periodic boundary conditions at the open ends of the pipe. The body force $g = 10^{-5}$ is applied at each node of the simulation domain. The LB simulations are carried out till the simulation reaches its steady state. The result of the LB simulation shown in Figure 5.2, is in very good agreement with the analytical solution in Eq. (5.11). This validates the single phase axisymmetric LB model for the case where there is no velocity in the radial direction.

5.3.2 Outward radial flow between two parallel discs

Another important test to validate the single-phase axisymmetric LB model is the simulation of the outward radial flow between two parallel discs separated by a distance H. The schematic of the flow setup for this problem is reported in Figure 5.3. Assuming $u_{\mathrm{z}}(z, r) = 0$ for $R_i \leq r \leq R$, the no-slip boundary

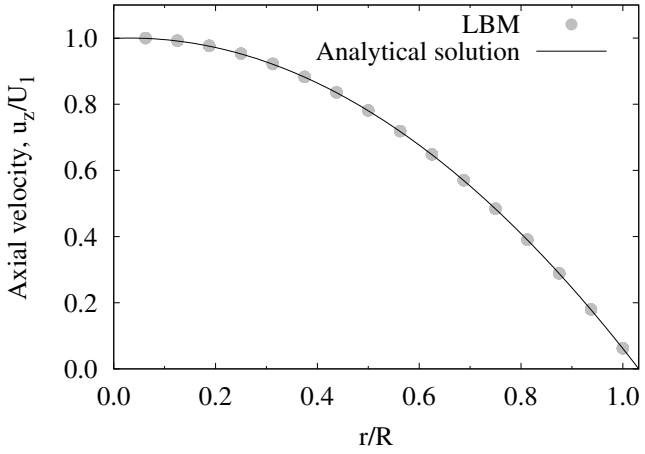

Figure 5.2: A comparison of the axial velocity profile as obtained form the LB simulations (circles) versus the analytical solution (solid line) Eq. (5.11). Simulation parameters: $N_z \times N_r = 16 \times 16$, $R = N_r$, $\rho = 1$, $\nu = 0.167$, $g = 10^{-5}$, $U_1 = u_z(0) = 3.84 \times 10^{-3}$.

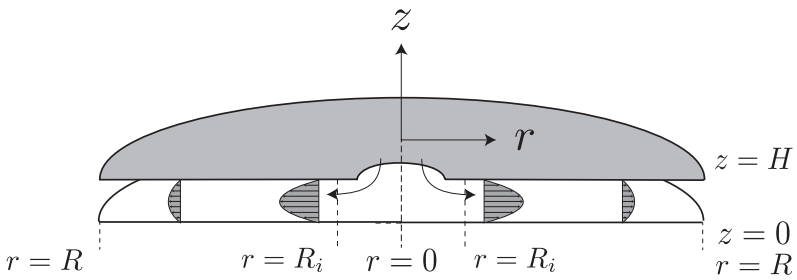

Figure 5.3: Schematic of the physical setup to study outward radial flow between two parallel discs. The arrows show the direction of the inlet mass flow. The LB method is used to simulate the flow domain $0 \leq z \leq H$, $R_i \leq r \leq R$. *We assume that the flow is fully developed for* $r \geq R_i$ *and hence the axial velocity* u_z *vanishes in this region.*

condition on the discs and a constant mass flow rate Q along the radial direction, the solution of the NS Eq. (5.2) corresponding to this problem is given by [131]:

$$u_r(z,r) = -U_2 \left(\frac{4R_i}{H^2}\right) \frac{z(z-H)}{r}, \tag{5.12}$$

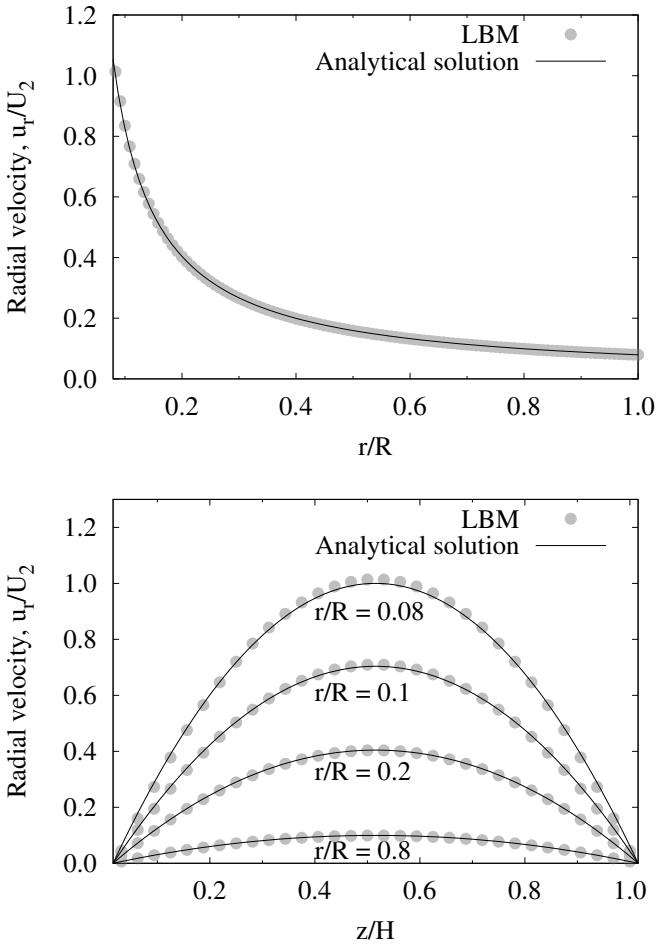

Figure 5.4: A comparison of the radial velocity profile, u_{r}, as obtained form LB simulations (circles) versus the analytical solution (solid lines) of Eq. (5.12). Simulation parameters: $N_{\mathrm{z}} \times N_{\mathrm{r}} = 32 \times 120$, $R = N_r - 0.5$, $H = N_z$, $R_i = 9.5$, $\rho = 1$, $\nu = 0.167$, $Q = 0.5$ and $U_2 = 3.93 \times 10^{-4}$. Top figure shows the comparison at $z = 15.5$. Bottom figure from top to bottom shows the curves correspond to the radial distances $r/R = 0.8, 0.2, 0.1$ and 0.08.

where $U_2 = u_{\mathrm{r}}(H/2, R_i) = 3Q/(4\pi R_i H)$. The LB simulations shown in Figure 5.4 are carried out for the flow domain $R_i \leq r \leq R, 0 \leq z \leq H$ and using the no-slip boundary condition along the discs. The velocity profile given by Eq. (5.12) is applied at the inlet boundary while the outlet is considered as an open boundary. The LB simulations shown in Figure 5.4 are in a very good

agreement with the analytical solution Eq. (5.12). This validates the single phase axisymmetric LB model for the case of a radial velocity.

5.4 Numerical validation for axisymmetric multi-phase model

In this section we present the validation for our axisymmetric multi-phase LB model for three standard test cases: Laplace law, oscillation of a viscous drop and the Rayleigh-Plateau (RP) instability. We also show a test to validate the volume conservation in our model.

The volume conservation in our multi-phase model is checked by observing the behavior of a fluid drop in the shape of an axisymmetric torus. We assume that the axis of rotation of the torus is aligned with the axis of the cylinder ($r = 0$). Due to the surface tension, the torus contract into a spherical drop, which in our simulation can be depicted by a 2D drop moving towards the r-axis. In our LB simulation, we find that the volume of the spherical drop is in a good agreement with the initial volume of the torus (see Figure 5.5). The LB simulation parameters used for this test are: $N_{\mathrm{z}} \times N_{\mathrm{r}} = 180 \times 100$, $(z_0, r_0) = (50.5, 0.5)$ and $G_{\mathrm{sc}} = -5$. The initial volume of toroid is given by, $V = \pi R_1^2 2\pi R_2$, where $R_1 = 15.0, R_2 = 50.0$. Radius of spherical drop in the final stage is given by $R_{\mathrm{D}} = (3V/(4\pi))^{1/3} = 37.7$, which agrees well with the drop radius obtained in the LB simulation.

5.4.1 Laplace test

In this validation we compare the in-out pressure differences for different droplet radii. According to the Laplace law the in-out pressure difference, Δp, for a droplet of radius R_{D} is given by

$$\Delta p = \frac{2\gamma}{R_{\mathrm{D}}}, \tag{5.13}$$

where γ is the liquid-vapor interfacial tension. For this validation we first estimate the value of the surface tension using Eq. (3.50) (Guo scheme [68]) and Eq. (3.52) (SC scheme [10]) for both 2D and axisymmetric LB method. The data obtained from these simulations are reported in Table 5.1. Both the Guo and SC scheme are consistent with the fact that for the SC model the surface tension should only depend on the value of the interaction parameter, G_{sc}.

In the next step we do a series of axisymmetric LB simulation for different droplet radii and measure the in-out pressure difference. When comparing the

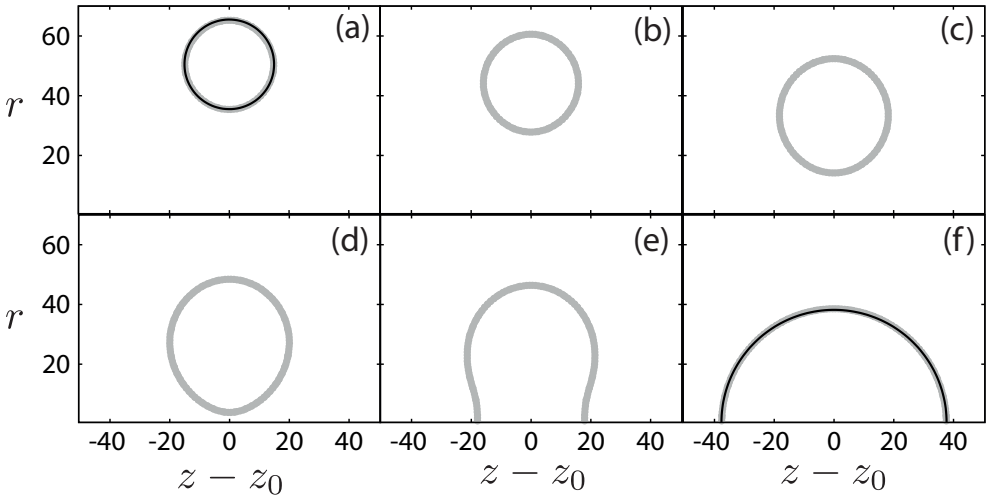

Figure 5.5: Volume conservation in the axisymmetric LB model. Initial (top left) and final (bottom right) shape of the toroid are shown by the black curve. The LB simulation are shown by gray circles, where the labels (a), (b), (c), (d), (e) and (f) represent the interface at time step $100, 700, 1200, 1400, 1500$ *and* 20000*, respectively.*

	SC		Guo	
G_{sc}	$\tilde{\gamma}^{\mathrm{2D}}$	$\tilde{\gamma}^{\mathrm{axis}}$	γ^{2D}	γ^{axis}
-4.5	0.0220	0.0220	0.0135	0.0136
-5.0	0.0579	0.0579	0.0376	0.0378
-5.5	0.0995	0.0996	0.0681	0.0683

Table 5.1: Surface tension evaluated using Eq. (3.52) (column 2,3) and Eq. (3.50) (column 4,5). Here $\gamma^{\mathrm{2D}}, \gamma^{\mathrm{axis}}$ *denote the surface tensions obtained from the 2D and axisymmetric SC LB model, respectively. Simulation parameters:* $N_{\mathrm{z}} \times N_{\mathrm{r}} = 1 \times 64$*,* $\tau = 1$*, initial interface position,* $r = 32$*.*

in-out pressure difference for a drop (Laplace test) and the pressure drop given by Eq. (5.13), we find that the maximum relative error in pressure difference for Guo scheme [68] and SC scheme [10] is 2% and 20%, respectively. This difference might be due to following reason. The external force, $\mathbf{F} \equiv (F_{\mathrm{z}}, F_{\mathrm{r}})$, can be incorporated in the LB model in several ways [68, 69, 132]. However, depending on the chosen forcing scheme, the Chapman-Enskog (CE) expansion has different truncation error terms in the continuity and Navier-Stokes equations. For instance, if one use the force addition scheme as proposed

by Guo et al. [68] one obtains the continuity equation given by Eq. (5.1), whereas by using the scheme proposed by Shan and Chen [9] the CE gives us the following axisymmetric continuity equation:

$$\frac{\partial \rho}{\partial t} + \nabla \cdot (\rho \mathbf{u}) = -\delta t \left(\tau - \frac{1}{2}\right) \nabla \cdot \mathbf{F}. \tag{3.32a}$$

Different right hand side terms in the continuity equation result in different densities inside the droplet (in the Laplace test) and one may obtain different values of the pressure, via the equation of state given by Eq. (3.47).

In the axisymmetric continuity equation, with the SC forcing scheme (section 3.3.2), the gradient operator has an additional term $-(\tau - \frac{\delta t}{2})\frac{F_r}{r}$. Because this term goes as r^{-1} we expect that this may be responsible for the larger numerical errors, thus leading to the departure of about 20% for what concerns the pressure difference. However, only the gradient of the pressure enters into the NS Eq. (5.2), therefore the axisymmetric LB simulations and fully 3D LB simulations for axisymmetric flow gives same results with the SC forcing scheme. In the rest of this chapter, we are using the SC forcing scheme for the SC-LB simulation and symbol γ to represent the surface tension.

5.4.2 Oscillating droplet

Here we consider the dynamics of the oscillation of a droplet in order to validate the axisymmetric multi-phase LB method. Among different drop oscillation modes, only the second mode of the oscillation is rotationally symmetric. Hence, our validation is restricted only for the axisymmetric drops. We compare the frequency of the second mode of the drop oscillation, ω_2, obtained from the LB simulation with the analytical solution reported in Miller and Scriven [133]. The frequency ω_2 of the oscillation of a liquid droplet immersed in another fluid is given by:

$$\omega_2 = \omega_2^* - 0.5\alpha(\omega_2^*)^{1/2} + 0.25\alpha^2, \tag{5.14}$$

where

$$\omega_2^* = \sqrt{\frac{24\gamma}{R_{\mathrm{D}}^3(2\rho_{\mathrm{v}} + 3\rho_\ell)}},$$

and R_{D} is the radius of the drop at equilibrium, γ is the surface tension, $\rho_\ell, \rho_{\mathrm{v}}$ are the densities of the liquid and vapor phases, respectively. The parameter α is given by:

$$\alpha = \frac{25\sqrt{\nu_\ell \nu_{\mathrm{v}}}\,\rho_\ell \rho_{\mathrm{v}}}{\sqrt{2} R_{\mathrm{D}}(2\rho_{\mathrm{v}} + 3\rho_\ell)(\sqrt{\nu_\ell}\rho_\ell + \sqrt{\nu_{\mathrm{v}}}\rho_{\mathrm{v}})},$$

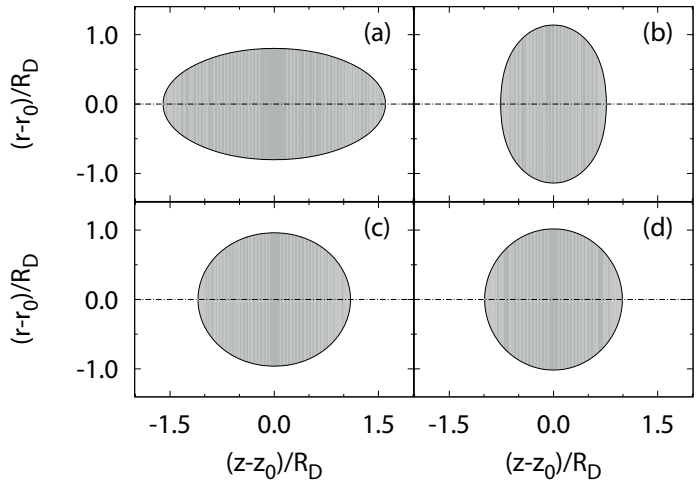

Figure 5.6: Time evolution of the shape of an ellipsoidal droplet immersed in a fluid with different density. Simulation parameters: $N_z \times N_r = 320 \times 128$, $G_{sc} = -6$. $\rho_\ell = 2.65$, $\rho_v = 0.075$, $(z_0, r_0) = (160.0, 0.5)$. *The labels (a),(b),(c) and (d) indicate the droplet shapes for time* $t = 0, 1 \times 10^2, 8 \times 10^2$ *and* 5×10^4, *respectively.*

where ν_ℓ, ν_v are the kinematic viscosities of the liquid and vapor phase [133].

In the LB simulations for this test we use the free-slip boundary condition at the top boundary and periodic boundary conditions at the left and right boundaries. The LB simulations are initialized with an axisymmetric ellipsoid, $(z/R_a)^2 + (r/R_b)^2 = 1$, where R_a, R_b are the intercepts on the z and r-axis, respectively, with total volume $4\pi R_a R_b^2/3$. Due to the surface tension, the ellipsoidal droplet oscillates and due to viscous damping it does finally attain an equilibrium spherical shape with radius $R_D = (R_a R_b^2)^{1/3}$ (due to volume conservation). The time evolution of one of these LB simulations is shown in Figure 5.6. The LB simulations are performed to validate the effect of the droplet size, R_D, on the frequency of oscillation, ω_2. In order to calculate the frequency of the oscillation we first measure the length of the intercept on the r-axis as a function of time, $A(t)$ with $A(t = 0) = R_b$, and then we fit the function $g(t) = R_D + a \exp(-bt) \sin(\omega_2 t + d)$, (see Figure 5.7). We find that the numerical estimation of the frequency of the oscillation of the droplet is in excellent agreement with the theoretically expected value, with a maximum relative error of approximatly 1% (see Figure 5.7).

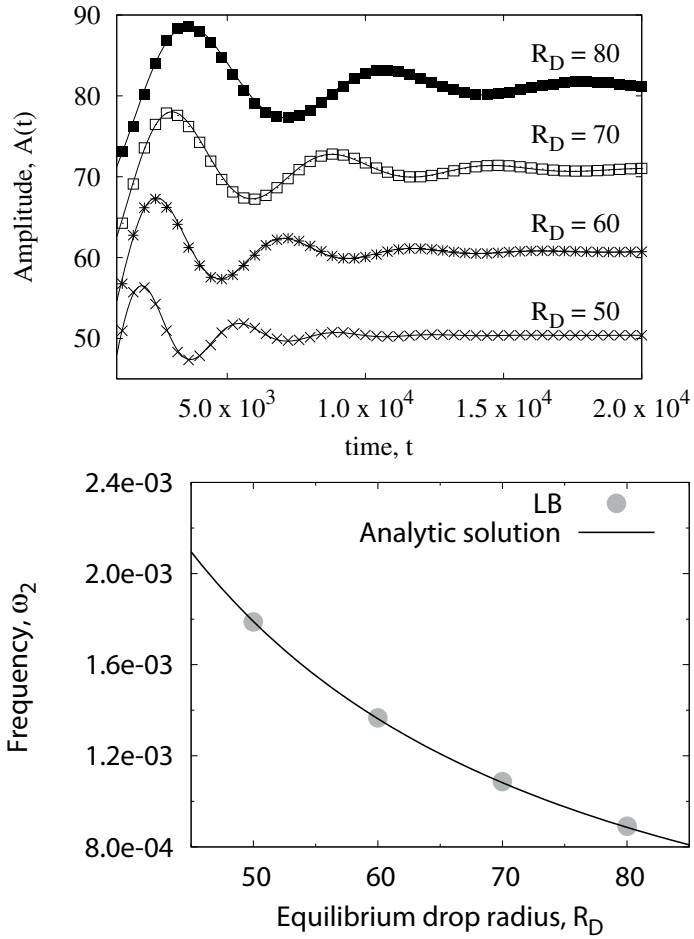

Figure 5.7: Top panel: amplitude, $A(t)$, of the oscillations versus time, t, for different equilibrium droplet radii, R_{D}. Solid lines are obtained by fitting the function, $g(t) = R_{\mathrm{D}} + a\exp(-bt)\sin(\omega_2 t + d)$, to the data obtained from LB simulations. Bottom panel: dimensionless frequency of the second mode of oscillation, ω_2, versus the equilibrium droplet radius, R_{D}. Simulation parameters: $N_{\mathrm{z}} \times N_{\mathrm{r}} = 320 \times 128$, $G_{\mathrm{sc}} = -6$.

5.4.3 Rayleigh - Plateau (RP) instability

The last problem that we consider for the validation is the breakup of a liquid thread into multiple droplets. The problem was first studied experimentally by Plateau [134] and later theoretically by Lord Rayleigh [135], and is currently

referred to as Rayleigh-Plateau (RP) instability. The RP instability has been extensively studied experimentally, theoretically and numerically [134–137]. Moreover, the problem is fully axisymmetric and therefore suitable for the validation of our multi-phase axisymmetric LB model.

In this validation we check the instability criterion: a liquid cylinder of radius R_c is unstable, if the wavelength of a disturbance, λ, on the surface of a liquid cylinder is longer then its circumference $2\pi R_c$. Moreover, we compare the radius of the resulting drops with experimental [138] and numerical data [139].

For the LB simulations we use free-slip boundary condition at the top boundary and periodic boundary conditions at left and right boundaries. The LB simulations are performed in a domain of size $N_z \times N_r = \lambda \times 450$. The wavelength, λ, of the noise runs over 576, 768, 1024, 1280, 1536 and 1792 for different wavenumbers, $\kappa = 2\pi/\lambda$. We represent the wavenumbers in dimensionless form as $\kappa^* = \kappa R_c$. The SC interaction parameter, $G = -6.0$, liquid density $\rho_\ell = 2.68$, vapor density $\rho_v = 0.078$, surface tension $\gamma = 0.141$ and kinematic viscosity $\nu = 0.016$ are fixed for these simulations. For these parameters the Ohnesorge number, $\mathrm{Oh} = \nu\sqrt{\rho_\ell/(\gamma R_c)} = 0.09$. The axial velocity field in the liquid cylinder is initialized as a sinusoidal velocity field, $u_z(z, r) = \epsilon_u \sin(2\pi z/\lambda)$. For our LB simulation we use $\epsilon_u < 5 \times 10^{-3}$.

The time evolution of the RP instability corresponding to two different wavenumbers $\kappa^* = 2\pi R_c/\lambda$ is shown in Figure 5.8. The time is measured in the capillary time scale, $t_{\mathrm{cap}} = \sqrt{R_c^3 \rho_\ell/\gamma}$. In our simulations we find that the cylinder breaks up into two or more droplets as long as the condition $\kappa^* < 1$ is satisfied (corresponding to the RP instability criterion, $2\pi R_c < \lambda$). Furthermore, the comparisons of drop sizes for different wavenumber shown in Figure 5.9 is in excellent agreement with the results of the slender jet approximation model (SJ) [139] and with experimental data [138].

5.5 Contraction of a viscous ligament

The formation of liquid ligaments is ubiquitous, it basically happens whenever there is a droplet fragmentation [140]. Examples of fragmentation processes are the breakup of a liquid ligament stretched from a bath [141] or the collapse of a liquid film [142]. The formation of these liquid ligaments is very common in the breakup of ocean spume where they influence the properties of the marine aerosols [143]. In industry, the dynamics of ligaments are a key issue for the print quality in inkjet printing [8], where elongated liquid ligaments are ejected from the nozzle (see Figure 5.10). For optimal print quality the ligaments

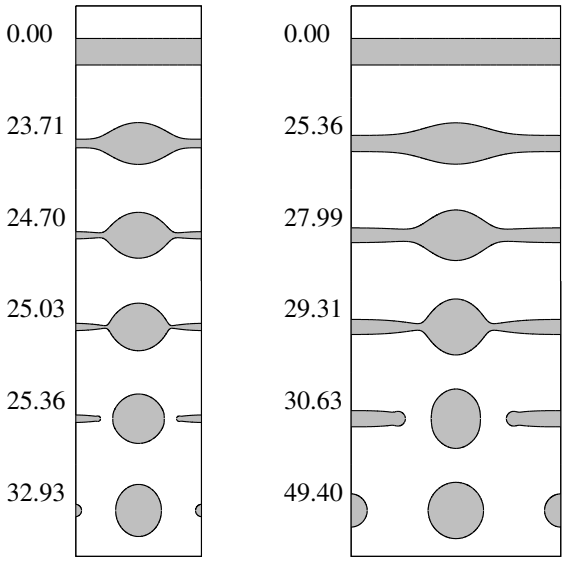

Figure 5.8: Growth of the Rayleigh-Plateau instability with time. Left panel: $\kappa^* = 0.65$; right panel: $\kappa^* = 0.39$. Labels on figures indicate the corresponding dimensionless time, t/t_{cap}.

should contract to a single droplet before they hit the paper. Depending on the fluid properties, size and shape of the ligament, it may collapse into a single droplet (stable contraction), or it may break up into several droplets (unstable contraction) [144]. The contraction of the ligament crucially depends on the Ohnesorge number [145–147] $\text{Oh} = \nu_\ell \sqrt{\rho_\ell/(\gamma R_0)}$, where ν_ℓ, ρ_ℓ, γ, and R_0 are the kinematic viscosity, density, surface tension and radius of the ligament, respectively. It has been shown that[147], for $\text{Oh} = O(0.1)$ the contraction of the ligament remains stable regardless of the length of the ligament, L_0. In this work we use the axisymmetric multi-phase LB model to simulate the stable contraction of the ligament. We validate the LB model by comparing it against the one-dimensional (1D) numerical slender jet (SJ) model of [139], an analytic model based on force balance (FB), and the Flow3D† simulation.

Lubrication theory model

The stability of an axisymmetric viscous liquid ligament is modeled using the slender jet approximation [139, 147–151]. For this study we use the previously developed numerical model by Driessen and Jeurissen [139]. If we use

†Flow3D$^{\text{TM}}$ is CFD software developed by Flow Science Inc., Santa Fe, New Mexico

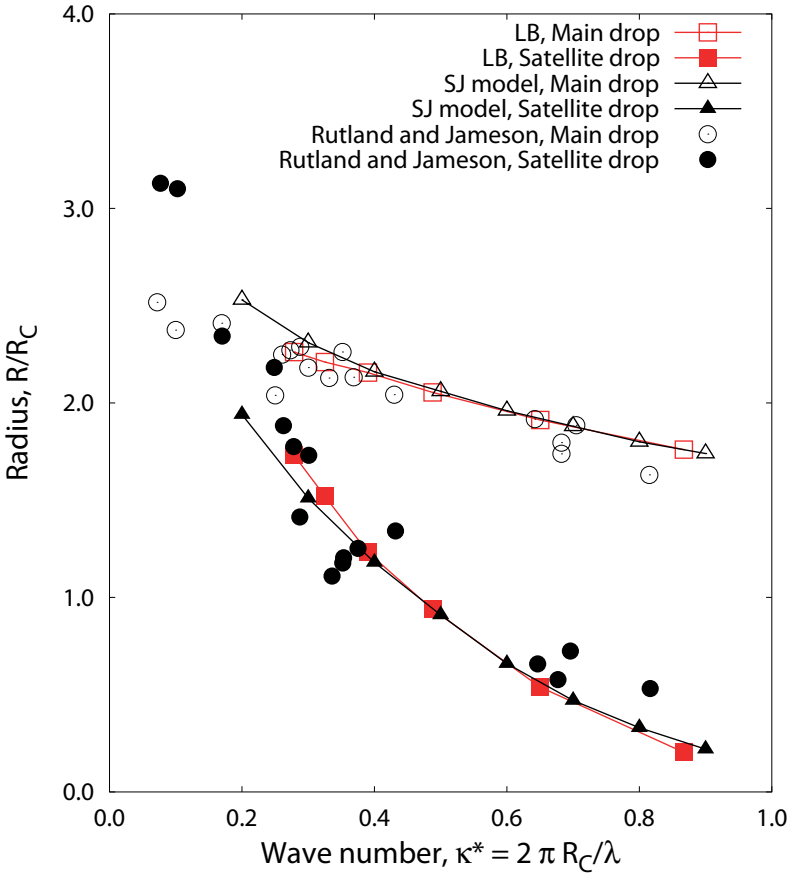

Figure 5.9: Dimensionless wave-number κ^* versus dimensionless droplet radius, R/R_c. Triangles markers represents the data obtained from the SJ model for $Oh = 0.1$ [139], circle markers represents the data from experiments [138] and square markers represents data from the axisymmetric LB simulations for $\mathrm{Oh} = 0.09$.

the initial radius of ligament, R_0, as the length scale and the capillary time, $t_{\mathrm{cap}} = \sqrt{\rho_\ell R_0^3/\gamma}$ as the time scale, then the model based on the slender jet approximation in the dimensionless form is given by:

$$\partial_t r = -u_z \partial_z r - \frac{1}{2} r \partial_z u_z, \tag{5.15a}$$

$$\partial_t u_z = -u_z \partial_z u_z - \partial_z p + 3\mathrm{Oh}\, r^{-2} \partial_z (r^2 \partial_z u_z), \tag{5.15b}$$

$$p = \left\{ r^{-1}[1 + (\partial_z r)^2]^{-1/2} - [1 + (\partial_z r)^2]^{-3/2} \partial_{zz} r \right\},$$

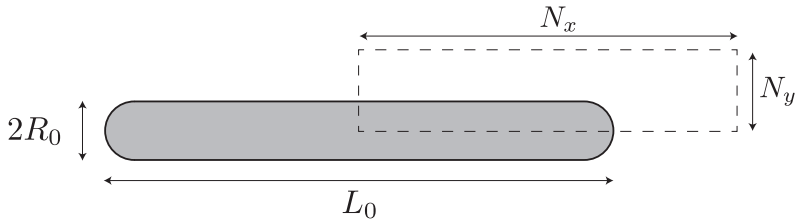

Figure 5.10: A schematic of the initial configuration of the axisymmetric viscous ligament. The rectangular dotted box of size $N_z \times N_r$ represents the simulation domain.

where r is the radius, u_z is the axial velocity, z is the axial coordinate, t is the time, p is the Laplace pressure, and $\mathrm{Oh} = \nu\sqrt{\rho_\ell/(\gamma R_0)}$ is the Ohnesorge number. The solutions to these equations are singular at each pinchoff [148], and at each collision of liquid bodies. To allow the described physical system to transfer across the singularities that occur at pinchoff and coalescence, the surface tension term is regularized by a modification at a radius of the order of the cutoff radius, r_c. The cutoff radius, r_c is a control parameter of the regularization, and is chosen to scale with the spatial step. In the rest of this chapter, we will use the abbreviation SJ to represent the model given by Eq. (5.15). For the SJ simulations presented in this Chapter $r_c = R_0/60$.

Results and discussion

In this section we show the comparison of simulation from the axisymmetric LB model and the SJ model Eq. (5.15), for the contraction of a viscous ligament. The LB simulation is carried out for the following parameters (LU): system size, $N_z \times N_r = 1600 \times 256$, $L_0 = 2000$, $R_0 = 49.5$, relaxation parameter, $\tau = 1$, kinematic viscosity $\nu = 0.16667$, Shan-Chen interaction parameter, $G_{sc} = -5$, liquid density, $\rho_\ell = 1.95$, vapour density, $\rho_v = 0.16$, and surface tension, $\gamma = 0.0568$. For our study it was sufficient to simulate only half of the liquid ligament (see Figure 5.10). We use symmetry boundary condition at left and right boundary and free slip at the top boundary.

In order to make a comparison between the two models we need to have a common system for measuring the physical quantities and we opted for expressing quantities in dimensionless units. We choose the initial radius of the ligament, R_0, and the capillary time, t_{cap}, to scale length and time in LB simulations. For both the LB and SJ simulations we use the aspect ratio, $\Gamma_0 = L_0/(2R_0) = 20$, and the $\mathrm{Oh} = 0.13888$.

First we compare the time evolution of the ligament shape obtained from

the LB and the SJ simulation (see Figure 5.11). During the collapse there is a perfect agreement of all the models. When the tail droplets merge into one big droplet, the models start to differ most probably because of the different assumptions made. The SJ model is 1D axisymmetric, whereas the LB is 2D axisymmetric. For the second validation we compare our LB simulations

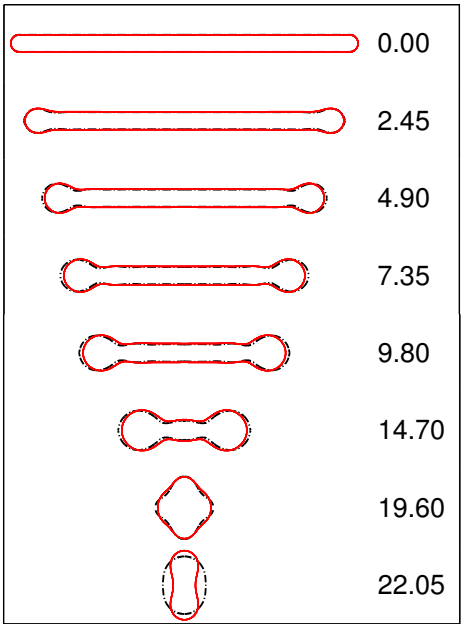

Figure 5.11: Time evolution of interface profile of the liquid ligament. The labels on the figure show the dimensionless time, t/t_{cap}. The data points from the LB simulation are shown in red color, whereas the data from the SJ model given by Eq. (5.15) is shown in black color. During the collapse the agreement is good while the oscillation of the final drop is different, due to the different assumptions in the SJ model.

to the SJ model and the Flow3D simulation. Additionally, we estimate the position of the tail-end of the ligament by an analytical model based on the force balance (FB).

In the FB model the rate of change of the mass, m, and momentum,

$P = mu$, of the tail-drop is given by:

$$\frac{\mathrm{d}m}{\mathrm{d}t} = \rho_\ell \pi R^2 u, \tag{5.16a}$$

$$\frac{\mathrm{d}P}{\mathrm{d}t} = -\pi R^2 \frac{\gamma}{R} = -\pi \gamma R, \tag{5.16b}$$

$$\frac{\mathrm{d}x}{\mathrm{d}t} = u, \tag{5.16c}$$

where u is the velocity of the tail-drop, $2x$ and R are the length and the radius of the ligament at time t, respectively. The solution of Eq. (5.16) subject to the initial conditions $m(0) = \rho_\ell (2/3)\pi R_0^3$, $P(0) = 0$, and $x(0) = 0.5L_0 - R_0$ gives us the length of the ligament, $2x(t)$. In absence of any external force, the net force given by Eq. (5.16) must vanish, i.e., $u\,\mathrm{d}m/\mathrm{d}t + \mathrm{d}P/\mathrm{d}t = 0$. If we assume that the change in radius of the ligament is negligible during its contraction, i.e., $R = R_0$, then the velocity of the tail end of the ligament is given by:

$$u = \sqrt{\frac{\gamma}{\rho_\ell R_0}}. \tag{5.17}$$

The solutions from the FB model, the SJ model, the Flow3D simulation and the LB simulation are in very good agreement with each other (see Figure 5.12). Furthermore, the slope of the curves shown in Figure 5.12 for the LB, SJ and Flow3D simulation is -1, which agrees with the estimate velocity given by Eq. (5.17).

5.6 Conclusions

In the present chapter we introduced a novel axisymmetric LB model that can be employed for single-phase as well as for multi-phase flows. The multi-phase model is the widely employed Shan-Chen model and the axisymmetric version here described is particularly convenient as it allows one to easily switch from 3D to 2D axisymmetric simulations while maintaing the usual Shan-Chen parameters (i.e. densities and coupling strength). The lattice Boltzmann axisymmetric model allows for the solution of multi-phase flows at the computational cost of a 2D simulation. One particular interesting application comes from the possibility of increasing the system size, thus reducing the relative size of the diffuse interface with respect to all other length scales in the flow in the SC-LB model. We presented several validations for single-phase as well as for multi-phase flows. In the case of multi-phase flows we have quantitatively validated the mass conservation and the dynamics of an axially symmetric oscillating droplet. We have also studied the breaking of a liquid thread into

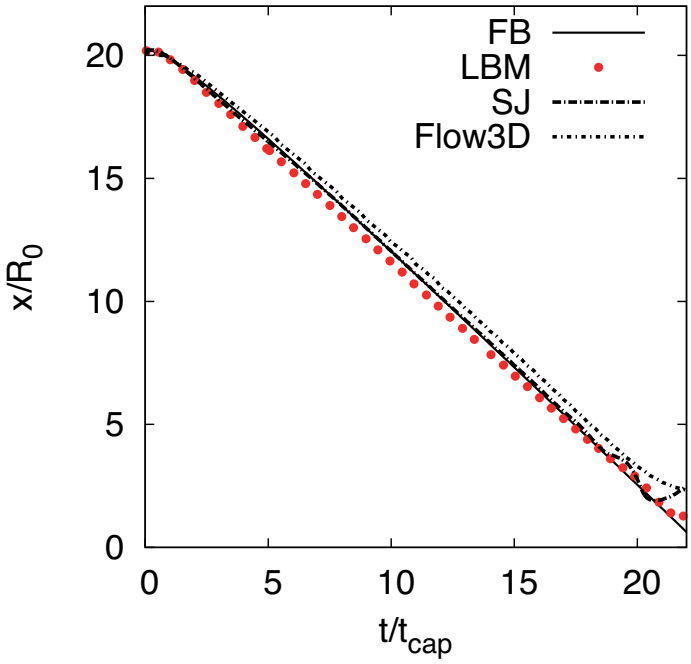

Figure 5.12: The tip location of the collapsing filament as a function of time in the presented models. The differences between the LB simulation, SJ simulation and FB model is smaller than the interface thickness in the LB simulation. The simulations and the analytical result agree well with each other, up to the moment when the tail droplets merge.

main and secondary droplets and we could quantitatively compare these simulations with existing literature results. The constraint of axis-symmetry may partially be relaxed by models that keep into account azimuthal perturbation to lowest order, this will be the subject of future work.

The axisymmetric multi-phase SC LB model (section 5.2) has been applied on the test problem of the stable contraction of liquid ligament. For this validation the LB simulation was compared to the SJ, FB models, and Flow3D simulations. Furthermore the position of the tail-end of the drop was compared with a model based on the balance of forces. We found that the proposed axisymmetric multi-phase SC LB model can accurately simulate the collapse of a viscous liquid ligament.

6 Analysis of lattice Boltzmann method for simulation of drop-formation in inkjet printers

In this chapter, we present an application of the axisymmetric multiphase lattice Boltzmann method to simulate drop formation in inkjet printers. We show, given several geometrical and physical constraints, how one can choose the parameters for the lattice Boltzmann simulation. We validate the time varying pressure boundary condition in the LB model and show that under some geometrical constraints the compressibility effects in the LB simulations are negligible. We present the unit conversion procedure, which helps to compare the LB simulation with realistic jetting cases. Finally, we show a qualitative comparison between the LB and Flow3D simulation for a drop-formation in an inkjet nozzle.

6.1 Introduction

Inkjet printing is a highly accurate technique to deposit very small droplets at very high speed [8]. The inkjet printing technology has been used in various industrial applications other then just graphics printing. Recently, innovative applications started to explore a whole new world of possibilities, in biology it can be used to transport cells [152], in semiconductor industries to print IC chips [153, 154], solar cells [155, 156] and OLED (organic light-emitting diode) displays [157]. The market demand for complex applications, as well as for higher speed and accuracy with smaller and smaller droplets, pushes the technology and raises several fundamental and technical challenges for scientists and engineers [7, 8].

The inkjet printing technology can be classified in two main categories: continuous inkjet (CIJ) and drop-on-demand (DOD) inkjet [158]. Among, the various types of DOD inkjet printers, we are interested here in piezoelectric inkjet (PIJ) printers.

Many experimental and numerical studies have been conducted to under-

stand various issues related to the PIJ printing (for reviews see [7, 8]). From experiments carried out at Océ B.V., it is clear that the wetting properties of the nozzle can play a significant role in the drop-formation. Here we want to investigate same aspects in this direction.

Our aim is to provide a numerical tool for the study of drop-formation in a PIJ printer that includes the interaction between the fluid interface and the nozzle structure (the contact line). The development of the axisymmetric multiphase lattice Boltzmann model presented in Chapter 5 was the first step towards this goal. There the model has been validated for two important problems relevant to inkjet printers, i.e., the Rayleigh-Plateau instability and the contraction of a viscous ligament; see Chapter 5. The multiphase model used in Chapter 5 is an axisymmetric variant of the Shan-Chen (SC) model. Consequently it employs the same fluid-surface interaction as the one discussed in Chapter 3.

The simulation of drop-formation in PIJ printers using the LB model presents some challenges. The first issue is due to the Shan-Chen (SC) multiphase model [9], for which the surface tension, γ, and the density, ρ_ℓ, depend on a single parameter $G_{\rm sc}$ (interaction strength) and thus cannot be changed independently [75]. Furthermore, the interaction strength, $G_{\rm sc}$, needs to be restricted to a certain range to avoid spurious effects. The kinematic viscosity, ν, in the LB models depends on the relaxation parameter, τ, see Chapter 3, thus for a stable SC LB simulation, $G_{\rm sc}$ and τ must be chosen correctly. Furthermore, to simulate an incompressible flow the fluid velocity must be much smaller than the sound speed, c_s, in the LB models [58]. From this it follows that to find the parameters that satisfies any given We, Re and Ma simultaneously is not trivial. The Weber number, We, the Reynolds number, Re, and the Mach number, Ma, are given by:

$$\mathrm{We} = \frac{\rho_\ell U_{\rm n}^2 R_{\rm n}}{\gamma}, \qquad \mathrm{Re} = \frac{U_{\rm n} R_{\rm n}}{\nu}, \qquad \mathrm{Ma} = \frac{U_{\rm n}}{c_s}, \tag{6.1}$$

where $U_{\rm n}$ is the maximum fluid velocity in the nozzle and $R_{\rm n}$ is the radius of the nozzle. The Reynolds number is $\mathrm{Re} = 75$, the Weber number is $\mathrm{We} = 21.4$, and the mach number is $\mathrm{Ma} = 0.008$ in the printhead under consideration. In order to validate the LB simulation we compare the results with the results from Flow3D simulations*. A second issue comes when comparing the LB results with the Flow3D simulations or any other existing numerical tool. The system of units used in the LB model and in Flow3D are different. Hence, we need to convert them.

*Flow3D$^{\rm TM}$ is CFD software developed by Flow Science Inc., Santa Fe, New Mexico

We start with a short discussion of the drop-formation process in an inkjet printer in section 6.2. In section 6.3, we discuss the boundary conditions and the implementation details for the LB model. We show the constraints on the parameter selection for the LB simulations. Furthermore, we describe the procedure to convert lattice units (LU) in international system (SI) of units. Finally, we present conclusions of this work and provide few recommendations for the future studies in section 6.4.

6.2 Nozzle geometry and drop-formation

Figure 6.1 (left panel) shows a single nozzle unit of a printhead in a PIJ printer. The schematic shows a piezo actuator, ink chamber, cylindrical channel, nozzle section and the nozzle plate. The nozzle plate and nozzle can have different wetting properties. The piezo actuator controlled by an electric voltage deforms the channel walls, which induces pressure fluctuations of amplitude 2-3 bar, in the channel. The pressure fluctuation in the channel results into a pressure difference across the nozzle which causes the drop-formation. The equilibrium pressure, p_c, (pressure when the piezo element is not actuated) in the channel is constant and kept slightly smaller then the ambient pressure, p_o, (pressure outside the nozzle), which prevents the leakage of ink out of the nozzle.

The pressure fluctuation and the resulting inertia of the ink in the nozzle is time-dependent. The necessary condition for drop-formation is that the transient inertia of the ink in the nozzle dominates the steady inertia of the fluid in the nozzle, viscous effects and surface tension. We define the angular frequency of the pressure fluctuations, ω, as the reciprocal value of the characteristic time scale for the problem. The relative effect of the transient inertia and the of viscous forces is given by the Womersley number [159]:

$$\mathrm{Wo} = R_{\mathrm{n}}\sqrt{\frac{2\pi\,\omega}{\nu}}. \tag{6.2}$$

6.2.1 Pressure fluctuations in the nozzle

Figure 6.1 (right panel) shows the schematic of the flow domain we use for the LB simulations. The choice of a subdomain here is most relevant to the study of the contact line motion while keeping the geometry of the domain rotationally symmetric. The channel length in the subdomain for the LB simulations should be chosen such that compressibility effects in the LB model are negligible (section 6.3.1). Due to this constraint, the inlet of our simulation

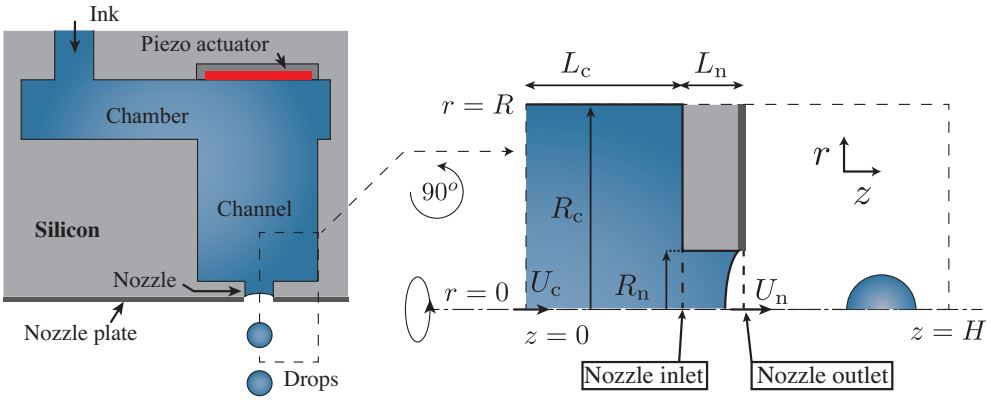

Figure 6.1: Left panel: schematic of a single nozzle unit in the printhead. Right panel: schematic of the channel-nozzle section of the printhead. The axisymmetric channel-nozzle section (right panel) is the simulation domain for our LB simulation ($R = R_c$).

domain is located at a distance L_c from the nozzle inlet, as shown in Figure 6.1 (left panel). The length L_c should be at least large enough to avoid contact between the simulation domain boundary ($z = 0$) and the meniscus, when the meniscus retracts.

In order to simulate a realistic drop formation, we need the boundary conditions at the domain boundaries. Due to technical difficulties in the real printhead, one cannot measure the pressure or the velocity of the ink in the channel experimentally. Therefore, the boundary condition at the channel inlet is not known precisely. On the other hand, it is possible to measure the velocity of the ink at the nozzle exit [160] and we will use the fluid velocity at the nozzle exit to obtain the approximate boundary condition at the channel inlet. Let us consider the following axial velocity at the nozzle exit:

$$u_n(t) = U_n \exp\left[-\xi^2(t - t_0)^2\right] \cos\left[\omega(t - t_0)\right], \tag{6.3}$$

where ξ is a time constant that sets the pulse width. A graphical representation of such a velocity pulse is shown in Figure 6.2 (left panel). This velocity profile is an approximation of the nozzle velocity obtained in experiments [161].

For a given nozzle velocity, we can find the velocity of the fluid at the channel inlet, U_c (using incompressibility and mass conservation). If we impose U_c as velocity at the channel inlet, we do not obtain the desired velocity at

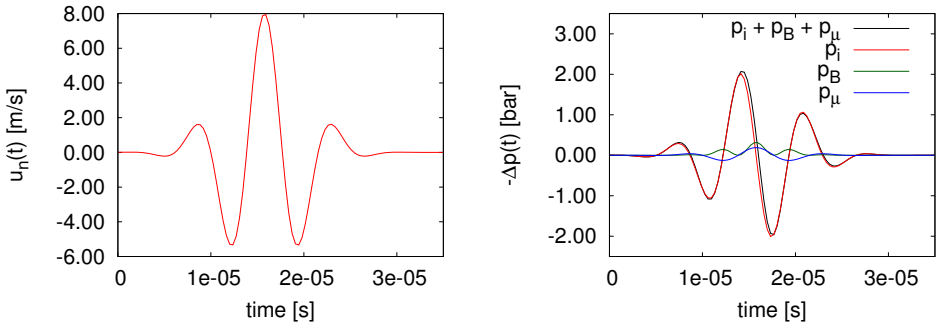

Figure 6.2: Left panel: Graphical representation of the velocity pulse given by Eq. (6.3) with $U_\mathrm{n} = 8\,\mathrm{m/s}$, $\xi = 1.71 \times 10^5$ Hz, $\omega = 8.17 \times 10^5$ Hz, $t_0 = 1.577 \times 10^{-5}$s. *Right panel: The pressure difference,* $\Delta p_\mathrm{n} = p_\mathrm{n}^\mathrm{out} - p_\mathrm{n}^\mathrm{in}$, *across the nozzle versus time,* $p_\mathrm{n}^\mathrm{out}$ *is the pressure at the nozzle outlet* ($p_\mathrm{n}^\mathrm{out} = p_o$) *and* $p_\mathrm{n}^\mathrm{in} = p_\mathrm{i} + p_\mathrm{B} + p_\mu$ *(see Eqs. (6.4)) is the pressure at the nozzle inlet. The capillary pressure given by Eq. (6.4c), for these parameters is bounded above by* $2\gamma/R_\mathrm{n} = 0.093$ bar.

the nozzle inlet due to the compressibility of the fluid in the LB model. Thus we rather use the pressure boundary condition at the channel inlet to avoid compressibility effects in the channel.

If the pressure drop over the channel due to inertia is negligible and the channel length is smaller than a quarter of the wavelength of the pressure fluctuation, i.e. $L_\mathrm{c} < 2\pi c_s/(4\omega)$, then the pressure at the channel inlet is the same as the pressure at the nozzle inlet. In this case it is sufficient to know the pressure jump across the nozzle, $\Delta p_\mathrm{n} = p_\mathrm{n}^\mathrm{out} - p_\mathrm{n}^\mathrm{in}$, where $p_\mathrm{n}^\mathrm{out}$ is the constant ambient pressure in the channel and p_n^in is the pressure at the nozzle inlet.

The pressure at the nozzle inlet, p_n^in, consists of the pressure due to unsteady inertia, p_i, the pressure due to steady inertia, p_B, the capillary pressure, p_cap and the pressure loss due to viscous friction, p_μ, given by [8]:

$$p_\mathrm{i}(t) = \rho_\ell L'_\mathrm{n} \frac{\mathrm{d}}{\mathrm{d}t}[u_\mathrm{n}(t)], \tag{6.4a}$$

$$p_\mathrm{B}(t) = \frac{1}{2}\rho_\ell \left[u_\mathrm{n}(t)\right]^2, \tag{6.4b}$$

$$p_\mathrm{cap}(t) = \gamma\kappa(t), \tag{6.4c}$$

$$p_\mu(t) = \frac{8\mu_\ell L'_\mathrm{n} u_\mathrm{n}(t)}{R_\mathrm{n}^2}. \tag{6.4d}$$

Here $\kappa(t)$ is the instantaneous mean curvature of the dynamic meniscus, γ is

the surface tension, ρ_ℓ is the density of the liquid, $L'_{\rm n}$ is the effective nozzle length and $R_{\rm n}$ is the nozzle radius.

The unsteady inertia is channel is larger than just the inertia in the nozzle. The extra component is due to the inertia of the flow towards the nozzle. In order to model this additional inertia, we use the nozzle length $L'_{\rm n} = L_{\rm n} + 1.22R_{\rm n}$ [162], where $L_{\rm n}$ is the actual length of the nozzle. A graphical representation of this pressure jump across the nozzle for $R_{\rm n} = 15\,\mu$m, $L_{\rm n} = 15\,\mu$m, $U_{\rm n} = 8\,$m/s, $\mu_\ell = 2 \times 10^{-3}\,$kg/m/s and $\gamma = 7 \times 10^{-2}\,$N/m is shown in Figure 6.2 (right panel).

For high values of $U_{\rm n}$, $p_{\rm i}$ dominates and $p_{\rm cap}$ can be ignored. However, for small $U_{\rm n}$, $p_{\rm cap}$ dominates and hence it must be considered. Here we use the latter case for the validation of the boundary conditions in our LB simulations. For small $U_{\rm n}$ one can approximate the time dependent curvature, $\kappa(t)$ (see section 6.3.1), while for large $U_{\rm n}$ the capillary pressure given by Eq. (6.4c) is bounded form above by $2\gamma/R_{\rm n}$. Although we expect it to be a reasonable approximation for the pressure, it is not rigorously valid for large amplitude.

6.3 LB method for inkjet printing

As anticipated we use the axisymmetric multiphase lattice Boltzmann model presented in Chapter 5 to simulate drop-formation in inkjet nozzles.

The flow domain for the LB simulations is shown in Figure 6.1 (right panel). The simulation domain of size $H \times R = N_{\rm z} \times N_{\rm r}$ consists of four parts: channel section of radius $R_{\rm c} = R$ and length $L_{\rm c}$, a wettable nozzle of length $L_{\rm n}$ and radius $R_{\rm n}$, a wettable nozzle plate and the rest of the flow domain of length $H - (L_{\rm c} + L_{\rm n})$ and radius R. The possible choices of nozzle radius depends on We, Re, $U_{\rm n}$, τ and $G_{\rm sc}$, as shown in Figure 6.3. Besides the reasons mentioned in the previous section, the length of the channel for the LB simulations is restricted below a critical value in order to avoid any reflection of pressure waves from the nozzle surface. Moreover, $L_{\rm c}$ is bounded from below to avoid a large pressure gradients at the channel inlet.

We use the no-slip boundary condition at the nozzle and channel surfaces, the no-stress boundary condition at the exit ($z = H$) and the pressure boundary condition at the channel inlet ($z = 0$). The wetting properties of the nozzle plate and the nozzle surface are modeled using a wetting parameter, as shown in section 3.4.2.

A-priori estimates of the SC LB simulation parameters

As mentioned in section 6.1, the SC LB model has some stability issues, which restrict the choice of the parameters G_{sc} and τ. Thus, one needs to check which parameter values are allowed for the simulation of the drop-formation in the inkjet nozzles. Using Eq. (3.25) we can obtain τ as a function of kinematic viscosity ν ($\delta t = 1$):

$$\tau = \frac{1}{2} + \frac{\nu}{c_s^2}, \tag{6.5}$$

and Eq. (6.1) can be used to express ν and ρ_ℓ/γ as a functions of R_{n} and U_{n}, Re and We:

$$\nu = \frac{U_{\mathrm{n}} R_{\mathrm{n}}}{\mathrm{Re}}, \qquad\qquad \frac{\gamma}{\rho_\ell} = \frac{U_{\mathrm{n}}^2 R_{\mathrm{n}}}{\mathrm{We}}, \tag{6.6}$$

where $U_{\mathrm{n}} \ll c_s$. In the SC model, G_{sc} can be expressed as an invertible function of γ/ρ_ℓ, see Table 3.1. First we evaluate G_{sc} for a given ratio γ/ρ_ℓ and then we can find ρ_ℓ and γ for given G_{sc}. Figure 6.3 shows the contour lines for $G_{\mathrm{sc}} = -4.5, -5.5$ and $\tau = 0.9, 1.2$ as a function of U_{n} and R_{n} for $\mathrm{Re} = 75$ and $\mathrm{We} = 21.4$. The region enclosed between these contour lines gives the appropriate values of R_{n} and U_{n} for the LB simulations.

6.3.1 Validation for small amplitude fluctuations

This validation is accurate as long as nonlinear effects in the channel and in the nozzle are negligible (no drop-formation). This is achieved by choosing the velocity given in Eq. (6.3) with a very small amplitude. For small U_{n}, We and Re are small, which means that the flow in the nozzle is parabolic and there is no drop formation. Furthermore, ω and ξ should be chosen such that the capillary pressure dominates the pressure in the channel, see Eqs. (6.4). For small amplitude fluctuations we can assume the shape of the meniscus is a paraboloid:

$$Z(r,t) = Z(0,t)\left[1 - \left(\frac{r}{R_{\mathrm{n}}}\right)^2\right], \tag{6.7}$$

where $Z(0,t)$ is the position of the meniscus at the axis. Using Eq. (6.7) and $\partial Z/\partial r \ll 1$, the mean curvature of the meniscus reads:

$$\kappa(t) = \frac{4\,Z(0,t)}{R_{\mathrm{n}}^2}. \tag{6.8}$$

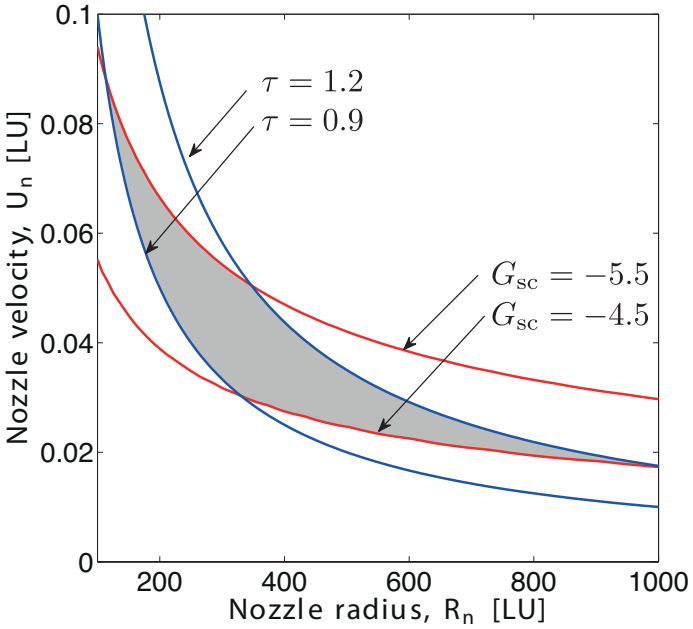

Figure 6.3: Phase diagram showing the parameter space accessible for LB simulations, enclosed by the red and blue curves, with Re = 75, We = 21.4 *and* Ma $\ll 1$. *The red and the blue curves show the values of* G_{sc} *and* τ, *respectively. For every point in the gray region, we get a unique value of* U_n, R_n, τ *and* G_{sc} *in lattice units.*

Using the capillary pressure given by Eq. (6.4c), we obtain the capillary pressure as a function of the meniscus displacement:

$$p_{cap}(t) = \gamma \frac{4\, Z(0,t)}{R_n^2}. \tag{6.9}$$

The problem of approximating p_{cap} is now reduced to the approximation of the average meniscus displacement. In order to obtain the meniscus displacement, we use

$$\frac{\mathrm{d}Z(0,t)}{\mathrm{d}t} = U(t), \tag{6.10}$$

where $U(t)$ is the average fluid velocity in the nozzle:

$$U(t) = \frac{1}{\pi R_n^2} \int_0^{R_n} 2\pi r\, u_z(r,t)\, \mathrm{d}r. \tag{6.11}$$

In the Stokes' limit the average velocity in a cylinder is half of the maximum velocity, i.e. $U(t) = u_{\mathrm{z}}(0,t)/2 = u_{\mathrm{n}}(t)/2$. Finally, we have the following initial value problem:

$$\frac{\mathrm{d}Z(0,t)}{\mathrm{d}t} = \frac{1}{2}u_{\mathrm{n}}(t), \tag{6.12}$$

where the initial condition $Z(0,0)$ is given by the position of the interface at $t = 0$. We use the 4-*th* order explicit Runge-Kutta method [163] to solve Eq. (6.12), which gives the meniscus displacement and hence the capillary pressure.

The following parameters are used for the LB simulation shown in Figure 6.4: $N_{\mathrm{z}} \times N_{\mathrm{r}} = 128 \times 40, R_{\mathrm{c}} = 40, L_{\mathrm{c}} = 40, R_{\mathrm{n}} = 20, L_{\mathrm{n}} = 20, G_{\mathrm{sc}} = -5(\rho_\ell = 1.9314, \rho_{\mathrm{v}} = 0.155, \gamma = 0.053), \nu = 0.167(\tau = 1)$, $\theta_{\mathrm{e}} = 90^\circ$ at the nozzle plate and $\theta_{\mathrm{e}} = 0^\circ$ at the nozzle surface. Moreover, for the velocity pulse we have : $U_{\mathrm{n}} = 4.08 \times 10^{-3}, \xi = 1.85 \times 10^{-4}, \omega = 9.25 \times 10^{-4}$. The characteristic time scale is $t^* = 1/\omega$. The nozzle velocity and pressure difference are evaluated at $z = 45$ and $r = 0.5$ (all parameters are in lattice units). The results of the LB simulation are reported in Figure 6.4. The pressure imposed at the channel inlet is the same as at the nozzle inlet, and the velocity obtained at the nozzle is a good approximation of the velocity ansatz given by Eq. (6.3).

The channel dimensions should be taken such that the compressibility effects are negligible. The compressibility effect in the LB model due to the time dependent pressure variations is proportional to $L_{\mathrm{c}}\omega/c_s$, (the ratio of the characteristic fluid speed in the channel and the speed of sound) [164]. For incompressible flow in a channel, $L_{\mathrm{c}}\omega/c_s < 1$, or $L_{\mathrm{c}} < c_s/\omega$. This sets the limit for L_{c} in the LB simulation. This estimate for the channel length is consistent with our assumption for the pressure boundary conditions mentioned in section 6.2.1. A result of the LB simulation showing compressibility effects is shown in Figure 6.5: varying the channel radius ($R_{\mathrm{c}} > R_{\mathrm{n}}$), does not show any compressibility effect.

6.3.2 Unit conversion

So far we presented the LB simulations either in dimensionless form or in lattice units (LU). However, for an industrial application like PIJ printing, it is very useful to express results and parameters in the international system of units, SI (Système Internationale). Here we provide a procedure to convert the parameter values from LU to SI units. No unit conversion procedure could be found in the literatures that exactly matched our requirements.

For the problem considered in this chapter it is sufficient to consider only three basic physical dimensions: mass [M], length [L] and time [T]. For a given

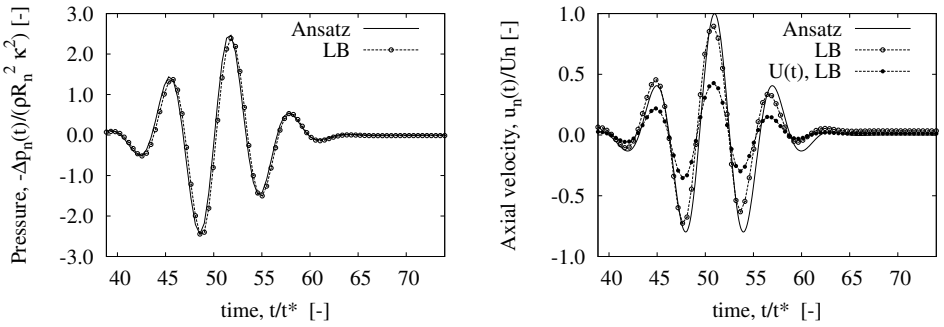

Figure 6.4: Left panel: the pressure difference imposed at the channel inlet (solid curve), and the pressure obtained in the LB simulation at the nozzle entrance. The pressure at the nozzle entrance is the same as the pressure at the channel inlet. Right panel: the axial velocity given by Eq. (6.3) at the nozzle exit (solid line), the axial and the average velocity, $U(t)$ determined by Eq. (6.11), at the nozzle exit obtained from the LB simulations.

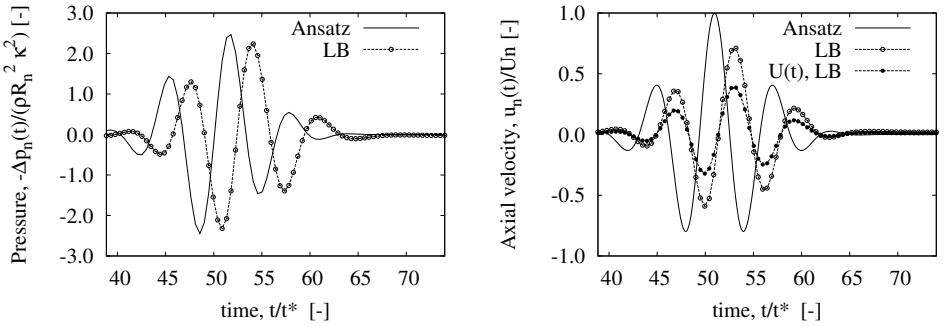

Figure 6.5: Same as Figure 6.4, except $N_z = 768$ and $L_c = 650$. Figure shows the compressibility effects induced by the length of the channel. For this simulation $L_c > c_s/\omega = 624.2$.

physical quantity q its dimension $[q]$ can be expressed as a product of M, L and T, i.e., $[q] = \mathrm{M}^\alpha \mathrm{L}^\beta \mathrm{T}^\delta$.

The first step of the procedure is the selection of the characteristic scales for the basic physical dimensions. For our problem the characteristic length, mass and time scales are R_n, $\rho_\ell R_\mathrm{n}^3$ and ω^{-1}, respectively. Using these we can non-dimensionalize the physical quantity q as:

$$q^* = \frac{q}{(\rho_\ell R_\mathrm{n}^3)^\alpha (R_\mathrm{n})^\beta (\omega^{-1})^\delta} = \frac{q}{(\rho_\ell)^\alpha (R_\mathrm{n})^{3\alpha+\beta} (\omega)^{-\delta}}, \tag{6.13}$$

where q^* is dimensionless and α, β, δ are determined by the dimensions of q. We assign some values to the characteristic parameters in SI units: $U_{\mathrm{n}} = 10\,\mathrm{m/s}$, $R_{\mathrm{n}} = 15\,\mu\mathrm{m}$, $\rho_\ell = 10^3\,\mathrm{kg/m^3}$, $\gamma = 0.07\,\mathrm{N/m}$, $\mu_\ell = 0.002\,\mathrm{kg/m/s}$ and $\omega = 7.54 \times 10^5\,\mathrm{Hz}$. For these parameters we have We = 21.4, Re = 75.0 and Wo = 23.1. In the second step, we use the phase diagram shown in Figure 6.3 for Re = 75 and We = 21.4 and choose $G_{\mathrm{sc}} = -4.9$, $\tau = 1$, which gives $R_{\mathrm{n}} = 270$ and $U_{\mathrm{n}} = 4.56 \times 10^{-2}$ in LU. Furthermore, G_{sc} and τ are used to estimate $\rho_\ell = 1.85$, $\rho_{\mathrm{v}} = 0.17$, $\gamma = 0.048$ and $\mu_\ell = 0.304$ for the LB simulations, which together with Wo can be used to obtain $\omega = 1.91 \times 10^{-4}$ in LU. In the third and last step, we use the values of ρ_ℓ, R_{n} and ω in LU and SI units to obtain the scaling rules between LU and SI units or vice-versa. We do it by first converting one unit system in dimensionless form using Eq. (6.13) and using the same relation to convert the dimensionless values to different unit systems. A list showing all the parameters used for the LB simulations is presented in Table 6.1.

6.3.3 Comparison with Flow3D simulations

Figure 6.6 shows a qualitative comparison of the LB and Flow3D simulation. The geometry used for this simulation is shown in Figure 6.1 and for the LB simulations we use parameters in LU, whereas in the Flow3D simulations we use parameters in SI units. A complete list of parameters used for the LB and Flow3D simulation is presented in Table 6.1.

In the initial ($t < 14\omega$) and final ($t > 30\omega$) stages of the drop-formation, where the meniscus is close to the nozzle end, the agreement between the LB and Flow3D simulation is good. At the stage where a jet of fluid is coming out of the nozzle, the drop-formation in the LB simulation is delayed. We attribute this to the presence of vapor outside the nozzle. Slow breakup of a liquid thread in presence of the vapor has been studies in the SC LB method [165], as well as in experiments [166]. In the final stages, the vapor inertia creates a clear difference between the LB and the Flow3D simulation. Furthermore, the satellite drop in the LB simulation decreases and eventually disappears presumably due to numerically enhanced evaporation [167].

6.4 Conclusions and recommendations

The LB model used here is an axisymmetric model with the axis of symmetry aligned with the axis of the nozzle. We found that the SC LB method is a viable tool for industrial applications under some restrictions on Re, We, and Ma. For a given Re, We, we can only use a limited range of the SC LB parameters.

q	LU	q^*	SI (m, kg, s)	$[q]$
Δx	1.0	3.70×10^{-3}	5.56×10^{-8}	L
Δm	1.0	2.75×10^{-8}	9.27×10^{-20}	M
Δt	1.0	5.41×10^{-1}	2.53×10^{-10}	T
p_o	0.0366	7.45	9.53×10^{5}	$\mathrm{ML^{-1}T^{-2}}$
p_c	0.0365	7.42	9.50×10^{5}	$\mathrm{ML^{-1}T^{-2}}$
R_n	270	1.0	1.50×10^{-5}	L
L_n	270	1.0	1.50×10^{-5}	L
R_c	405	1.5	2.25×10^{-5}	L
L_c	540	2.0	3.00×10^{-5}	L
H	4352	16.1	2.40×10^{-4}	L
U_n	0.046	8.84×10^{-1}	1.00×10^{1}	$\mathrm{LT^{-1}}$
ρ_ℓ	1.830	1.0	1.00×10^{3}	$\mathrm{M\,L^{-3}}$
ρ_v	0.170	9.19×10^{-2}	9.19×10^{1}	$\mathrm{M\,L^{-3}}$
γ	0.048	3.65×10^{-2}	7.00×10^{-2}	$\mathrm{MT^{-2}}$
μ_ℓ	0.304	3.04×10^{-1}	2.00×10^{-3}	$\mathrm{ML^{-1}T^{-1}}$
c_s	0.342	6.63	7.50×10^{1}	$\mathrm{LT^{-1}}$
ω	1.91×10^{-4}	1.0	7.54×10^{5}	$\mathrm{T^{-1}}$
ξ	4.33×10^{-5}	2.27×10^{-1}	1.71×10^{5}	$\mathrm{T^{-1}}$
t_0	7.47×10^{4}	1.43×10^{1}	1.89×10^{-5}	T

Table 6.1: Table showing LB simulation parameters and their corresponding values in SI units. The physical quantities shown in blue are obtained using the phase diagram for $\mathrm{Re} = 75$, $\mathrm{We} = 21.4$, $\mathrm{Wo} = 23.1$. *The rows corresponding to the gray cell represent the characteristic physical parameters and their values in different system of units. The speed of sound,* c_s, *shown in the SI units is 75* m/s, *which is much smaller then the speed of sound in the ink* ($\approx 1250\,\mathrm{m/s}$).

Many of the conditions encountered are intrinsic to the choice of using the classical SC model and not to LB method in general. The explanation of other LB multi-phase models was out of the scope of this thesis. Furthermore, the maximum jetting velocity that we can simulate in the LB model is restricted by the finite speed of sound in the LB method ($\mathrm{Ma} = U_\mathrm{n}/c_s \ll 1$), this is a general condition of the LB model. Although we use the SC LB model in this chapter, the results are applicable to the diffuse interface LB models in general. The model presented in this Chapter can be used to study the contact line motion. The "satellite drop evaporation" observed in the multi-phase SC model can be improved by using a multi-component SC model or other type

of multi-phase LB models.

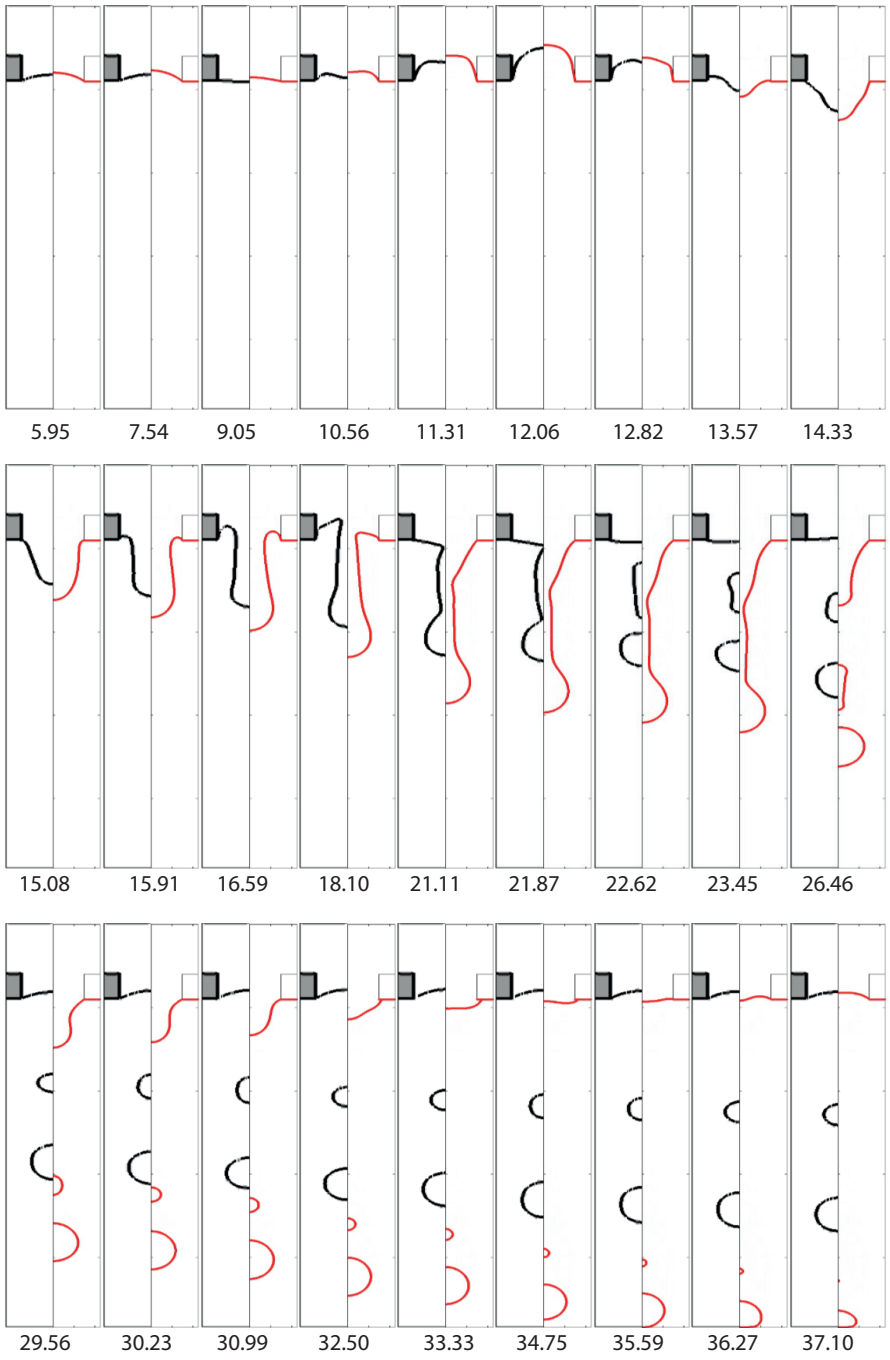

Figure 6.6: A qualitative comparison between the LB simulation (red curve) and Flow3D simulations (black curve). The label below each plot represents the time step in dimensionless units ($t * \omega$). The initial retraction and small amplitude motion is very similar. The jetting and droplet formation is different.

7 | Conclusions

The research presented in this thesis is a part of FOM Industrial Partnership Program (IPP) "Contact line control during wetting and de-wetting" conducted in collaboration with ASML and Océ. In our study, we addressed questions motivated by immersion lithography (ASML) as well as to drop formation in inkjet printers (Océ).

We have studied the moving contact lines and fluid interfaces by using the lattice Boltzmann (LB) method and the lubrication theory (LT) models. The standard LT model shown in Chapter 2 provides the basic framework to study the problems related to the contact line motion. The details of the LB methods have been provided in Chapters 3 and 5, respectively. The standard LT model is a single-phase model and valid only for interfaces with small slopes thus it cannot be used for the study of advancing contact lines or interfaces with large slope. The generalized lubrication (GL) model that includes the multiphase character of the advancing contact line and fluid interfaces with large slopes has been described in Chapter 4.

Based on the geometrical assumptions, the study of the contact lines and of the interfaces has been divided into two categories: first, the contact line motion in 2D (Chapter 4) and second, contact lines and interfaces that are rotationally symmetric (Chapter 5 and 6). For the first category, we used the standard Shan-Chen (SC) multiphase and multicomponent model for the LB simulations [9]. For the second category, we developed a novel axisymmetric variant of the LB model based on the SC multiphase LB model [168].

In Chapter 4, we studied interfaces and contact lines in 2D. In particular, we considered a 2D geometry made of: a solid, partially wettable and chemically homogeneous plate that is vertically immersed in a pool of liquid with viscosity, μ_ℓ. Using this setup, we investigated two different problems: the dip-coating problem (plate pulled out of the liquid) and the plunging plate problem (plate pushed into the liquid). We validated the LB simulations using the GL model at small capillary numbers, Ca. The two most important parameters for which we carried out our studies were the viscosity ratio and

the contact angle. The viscosity ratio, R_μ, is the ratio of viscosities between the surrounding fluid and the liquid in which the plate is immersed, while the contact angle is the equilibrium contact angle, θ_e, measured in the liquid. We found that the multiphase LB method is more suitable for viscosity ratios up to $R_\mu \approx O(10^{-2})$, whereas the multicomponent LB model is the most appropriate tool for the case of two fluids with nearly identical viscosities. An important parameter λ_s (slip-length) has been used to avoid the viscous singularity at the contact line in the GL models. In order to compare the LB and GL simulations, we calibrated the value of λ_s in the GL model. In the regime close to the wetting transition, $\mathrm{Ca} \approx \mathrm{Ca_c}$, the results for the plunging plate problem contributed to the validation of the GL model. After these steps the GL model has been used to study the plunging plate problem for different viscosity ratios. The GL model showed that for the dip-coating problem $\mathrm{Ca_c} \propto R_\mu^{-1}$ while for the plunging plate problem $\mathrm{Ca_c} \propto R_\mu^{-2/3}$. The multiphase LB simulations did not show any wetting transition for the plunging plate problem, due to the enhanced condensation/evaporation present at high capillary numbers.

In Chapter 5, we presented a novel axisymmetric multiphase LB model. We validated our model for single-phase as well as for multiphase flows. In particular we focused on a flow inside a cylindrical pipe, on the axisymmetric oscillations of a drop and on the Rayleigh-Pleatau instability. Using this method we also studied the contraction of the viscous ligament and the results have been compared with those from the LT model [139], an analytical force balance model and form the Flow3D solver [169]. Despite of the modeling differences, all these models showed a very good agreement with each other. The axisymmetric LB model requires computational costs typically of a 2D simulation, thus much less that the cost of a full 3D simulation. Furthermore, the axisymmetric multiphase model developed relies on the widely employed SC model, thus allowing to easily switch from 3D to 2D while maintaining the same values for the SC parameters (i.e. densities and coupling strength). This axisymmetric SC multiphase LB model was used further to study the drop-formation though an inkjet printer nozzle.

In Chapter 6, we employed our axisymmetric multiphase LB model for the study of the drop formation through an inkjet nozzle. Due to the complexity of the geometry and to the boundary conditions, the main challenge here was to develop a framework where the LB simulations can be quantitatively compared to experiments. The main difficulty was the restricted range of applicability of LB parameters and the system of units in which the LB models work.

In our comparisons we found that the LB study not only provides an efficient alternative to the existing analytical and numerical models and com-

mercial flow solvers, but also provides more insight into the regimes where the physics is challenging. Using the LB method for the above mentioned problems also revealed some drawback of the multi-phase and multi-component Shan-Chen LB method. The multiphase model used is a diffuse interface method and introduces an interface width as an additional parameter in the problem, However, the GL models used are based on the assumption of sharp interfaces. The range of viscosity ratios and capillary numbers restricts the range of applicability of the Shan-Chen model for the case of plunging plate problem. Finite sound speed and the dependence of the density and of the surface tension on the single parameter in the Shan-Chen model, gives the geometrical restriction in using the axisymmetric LB method for the inkjet nozzle simulations.

Appendices

I Asymptotic behavior of the GL model

We discuss the behavior of the function $f(\theta, R_\mu)$ when θ is close to π and R_μ close to zero. As presented in Section 4.5, $f(\theta, R_\mu)$ is defined as:

$$\begin{aligned} f(\theta, R_\mu) &\equiv \frac{2\sin^3\theta[R_\mu^2 f_1(\theta) + 2R_\mu f_3(\theta) + f_1(\pi-\theta)]}{3[R_\mu f_1(\theta) f_2(\pi-\theta) - f_1(\pi-\theta) f_2(\theta)]}, \\ f_1(\theta) &\equiv \theta^2 - \sin^2\theta, \\ f_2(\theta) &\equiv \theta - \sin\theta\cos\theta, \\ f_3(\theta) &\equiv (\theta(\pi-\theta) + \sin^2\theta). \end{aligned} \tag{I.1}$$

First, we expand the terms in both the numerator and the denominator in Taylor series about $\theta = \pi$ and keep the leading order terms only. We end up with

$$f(\theta, R_\mu) = \frac{-2[\pi^2 (R_\mu)^2 + 2\pi R_\mu(\pi-\theta) + (\pi-\theta)^4/3]}{2\pi^2 R_\mu + \pi(\pi-\theta)}. \tag{I.2}$$

The asymptotic behavior of $f(\theta, R_\mu)$ depends on the relative magnitude between $(\pi-\theta)$ and R_μ. For $R_\mu \ll \pi - \theta$, $f(\theta, R_\mu)$ can be approximated as:

$$f(\theta, R_\mu) \simeq f(\theta, 0) - 4R_\mu \simeq \frac{-2(\pi-\theta)^3}{3\pi} - 4R_\mu. \tag{I.3}$$

The contribution of air viscosity, represented by $-4R_\mu$, will become significant once $(\pi-\theta) \approx (R_\mu)^{1/3}$.

When θ is very close to π such that $\pi - \theta \ll R_\mu$, $f(\theta, R_\mu)$ has a different asymptotic form, i.e.,

$$f(\theta, R_\mu) \simeq -R_\mu. \tag{I.4}$$

If we substitute this asymptotic form of $f(\theta, R_\mu)$ into the generalized lubrication equation (4.22), we see the liquid viscosity cancels out in the product

Ca R_μ, so that the asymptotic equation does not depend on liquid viscosity anymore. This means in this asymptotic limit, air viscosity completely dominates the flow.

II Chapman-Enskog expansion

Here we present the Chapmann-Enskog (CE) expansion procedure to recover the axisymmetric continuity and NS equations Eq. (5.1) and Eq. (5.2), respectively, form the modified lattice Boltzmann equation Eq. (5.4). The modified lattice Boltzmann Eq. (5.4) for the distribution function $f_i(\mathbf{x}, t)$ reads

$$\begin{aligned} f_i(\mathbf{x} + \mathbf{c}_i\delta t, t + \delta t) - f_i(\mathbf{x}, t) = -\frac{1}{\tau}\big(f_i(\mathbf{x}, t) - f_i^{\text{eq}}(\mathbf{x}, t)\big) \\ + \delta t\ h_i(\mathbf{x} + \mathbf{c}_i\delta t/2, t + \delta t/2). \end{aligned} \tag{5.4}$$

where h_i are the source terms, $\mathbf{c}_i$ are the lattice velocities, τ is the relaxation parameter and $f_i^{\text{eq}}(\mathbf{x}, t) \equiv f_i^{\text{eq}}(\rho(\mathbf{x}, t), \mathbf{u}(\mathbf{x}, t))$ are the discrete second order approximation of the Maxwell-Boltzmann distribution function

$$f_i^{\text{eq}}(\rho, \mathbf{u}) = w_i\rho\bigg(1 + \frac{1}{c_s^2}(\mathbf{c}_i \cdot \mathbf{u}) + \frac{1}{2c_s^4}(\mathbf{c}_i \cdot \mathbf{u})^2 - \frac{1}{2c_s^2}\|\mathbf{u}\|^2\bigg), \tag{3.22}$$

where c_s is the speed of sound and w_i's are the weight factors to ensure the symmetry of the lattice and $\mathbf{u}$ is the local equilibrium velocity. For the D2Q9 LB model with BGK collision operator the speed of sound, $c_s = \sqrt{1/3}$, $w_0 = 4/9$, $w_i = 1/9$ for $i = 1, 2, 3, 4$ and $w_i = 1/36$ for $i = 5, 6, 7, 8$. In general these weights are positive and satisfy following symmetry conditions [58]

$$\begin{gathered} \sum_i w_i = 1, \qquad \sum_i w_i c_{i\alpha} = 0, \\ \sum w_i c_{i\alpha} c_{i\beta} = c_s^2\delta_{\alpha\beta}, \quad \sum w_i c_{i\alpha} c_{i\beta} c_{i\gamma} = 0, \\ \sum_i w_i c_{i\alpha} c_{i\beta} c_{i\gamma} c_{i\delta} = c_s^4(\delta_{\alpha\beta}\delta^i_{\gamma\delta} + \delta_{\alpha\gamma}\delta_{\beta\delta} + \delta_{\alpha\delta}\delta_{\beta\gamma}), \\ \sum_i w_i c_{i\alpha} c_{i\beta} c_{i\gamma} c_{i\delta} c_{i\eta} = 0. \end{gathered} \tag{II.1}$$

The hydrodynamic density, ρ and momentum, $(\rho\mathbf{u})$ are given by the zeroth and first moment of the distribution function respectively, *i.e.*,

$$\rho(\mathbf{x}, t) = \sum_i f_i(\mathbf{x}, t), \tag{II.2a}$$

$$(\rho\mathbf{u})(\mathbf{x}, t) = \sum_i \mathbf{c}_i f_i(\mathbf{x}, t). \tag{II.2b}$$

In order to establish a relation between the LB Eq. (5.4), the continuity Eq. (5.1) and the NS equations (5.2) it is necessary to separate different time scales. We distinguish between slow and fast varying quantities by using two time scales and one space scale [58]. We expand the time and space derivative using a formal parameter ε as

$$\partial_{\mathrm{t}} = \varepsilon\partial_{\mathrm{t}}^{(1)} + \varepsilon^2\partial_{\mathrm{t}}^{(2)} + O(\varepsilon^3), \qquad \boldsymbol{\nabla} = \varepsilon\boldsymbol{\nabla}^{(1)} + O(\varepsilon^2), \tag{II.3}$$

and the distribution function, f_i as

$$f_i = f_i^{(0)} + \varepsilon f_i^{(1)} + \varepsilon^2 f_i^{(2)} + O(\varepsilon^3). \tag{II.4}$$

The expansion parameter is formal in the sense that it allows us to keep the track of the terms with different order of magnitude with respect to $f_i^{(0)}$. The zeroth order contribution, $f_i^{(0)}$, is exactly the same as the equilibrium distribution function, f_i^{eq}. The first and second order perturbations in f_i do not contribute to hydrodynamic density and momentum [58] :

$$\sum_i f_i^{(1)} = \sum_i f_i^{(2)} = 0, \tag{II.5a}$$

$$\sum_i \mathbf{c}_i f_i^{(1)} = \sum_i \mathbf{c}_i f_i^{(2)} = \mathbf{0}. \tag{II.5b}$$

The source term h_i does not have any zeroth order contribution and is expanded as

$$h_i = \varepsilon h_i^{(1)} + \varepsilon^2 h_i^{(2)} + O(\varepsilon^3). \tag{II.6}$$

Taylor series of f_i and h_i around $(\mathbf{x}, t)$ are given by

$$\begin{aligned} f_i(\mathbf{x} + \mathbf{c}_i\delta t, t + \delta t) &= f_i(\mathbf{x}, t) + \delta t(\partial_{\mathrm{t}} + c_{i\alpha}\partial_\alpha) f_i(\mathbf{x}, t) \\ &\quad + \frac{(\delta t)^2}{2}(\partial_{\mathrm{t}} + c_{i\alpha}\partial_\alpha)^2 f_i(\mathbf{x}, t) \\ &\quad + O((\delta t)^3), \end{aligned} \tag{II.7}$$

$$\begin{aligned} h_i(\mathbf{x} + \mathbf{c}_i\delta t/2, t + \delta t/2) &= h_i(\mathbf{x}, t) + \frac{\delta t}{2}(\partial_{\mathrm{t}} + c_{i\alpha}\partial_\alpha) h_i(\mathbf{x}, t) \\ &\quad + \frac{1}{2}\left(\frac{\delta t}{2}\right)^2 (\partial_{\mathrm{t}} + c_{i\alpha}\partial_\alpha)^2 h_i(\mathbf{x}, t) \\ &\quad + O((\delta t)^3), \end{aligned} \tag{II.8}$$

where $c_{i\alpha}$ is the α-*th* component of $\mathbf{c}_i$, and ∂_α represents the partial derivative with respect to α-*th* component of $\mathbf{x}$. Indices $\alpha, \beta, \gamma, \delta$ used in the following

derivation ranges over the set $\{z, r\}$, and when an index appears twice in a single term it represents the standard Einstein summation convention. Using Eq. (II.3),(II.4),(II.7), and (II.8) in (5.4) and rearranging the terms we obtain a series in ε

$$\begin{aligned}
&\varepsilon\Big[\delta t\Big(\partial_{\mathrm{t}}^{(1)} f_i^{(0)} + c_{i\alpha}\partial_\alpha^{(1)} f_i^{(0)}\Big)\Big] + \varepsilon^2\Big[\delta t\Big(\partial_{\mathrm{t}}^{(2)} f_i^{(0)} + \partial_{\mathrm{t}}^{(1)} f_i^{(1)} + c_{i\alpha}\partial_\alpha^{(1)} f_i^{(1)}\Big)\\
&+ \frac{(\delta t)^2}{2}\Big(\partial_{\mathrm{t}}^{(1)}\partial_{\mathrm{t}}^{(1)} f_i^{(0)} + c_{i\alpha}c_{i\beta}\partial_\alpha^{(1)}\partial_\beta^{(1)} f_i^{(0)} + 2c_{i\alpha}\partial_{\mathrm{t}}^{(1)}\partial_\alpha^{(1)} f_i^{(0)}\Big)\Big]\\
&= \varepsilon\Big[-\frac{1}{\tau} f_i^{(1)} + \delta t\ h_i^{(1)}\Big]\\
&+ \varepsilon^2\big[-\frac{1}{\tau} f_i^{(2)} + \delta t\ h_i^{(2)} + \frac{(\delta t)^2}{2}\Big(\partial_{\mathrm{t}}^{(1)} + c_{i\alpha}\partial_\alpha^{(1)}\Big) h_i^{(1)}\Big] + O(\varepsilon^3).
\end{aligned} \tag{II.9}$$

Comparing the coefficients of ε, ε^2 and omitting ε^3 terms in Eq. (II.9) gives us

$$\delta t\left(\partial_{\mathrm{t}}^{(1)} f_i^{(0)} + c_{i\alpha}\partial_\alpha^{(1)} f_i^{(0)}\right) = -\frac{1}{\tau} f_i^{(1)} + \delta t\ h_i^{(1)}, \tag{II.10}$$

$$\begin{aligned}
\delta t\left(\partial_{\mathrm{t}}^{(2)} f_i^{(0)} + \partial_{\mathrm{t}}^{(1)} f_i^{(1)} + c_{i\alpha}\partial_\alpha^{(1)} f_i^{(1)}\right) + \frac{(\delta t)^2}{2}\Big(\partial_{\mathrm{t}}^{(1)}\partial_{\mathrm{t}}^{(1)} f_i^{(0)}\\
+ c_{i\alpha}c_{i\beta}\partial_\alpha^{(1)}\partial_\beta^{(1)} f_i^{(0)} + 2c_{i\alpha}\partial_{\mathrm{t}}^{(1)}\partial_\alpha^{(1)} f_i^{(0)}\Big)\\
= -\frac{1}{\tau} f_i^{(2)} + \delta t\ h_i^{(2)} + \frac{(\delta t)^2}{2}\Big(\partial_{\mathrm{t}}^{(1)} + c_{i\alpha}\partial_\alpha^{(1)}\Big) h_i^{(1)},
\end{aligned} \tag{II.11}$$

respectively. In the following steps of the CE expansion we will take the zeroth and first lattice velocity moments of Eqs. (II.10) and (II.11). The zeroth moment of Eqs. (II.10) and (II.11) will give us the mass conservation up to ε and ε^2 order terms, respectively, and the first moment of Eqs. (II.10) and (II.11) will give us the momentum conservation up to ε and ε^2 order terms, respectively. Finally by using Eq. (II.3) we will obtain equations that conserve the hydrodynamic mass and momentum up to $O(\varepsilon^2)$ perturbations in f_i.

Mass conservation

The zeroth order moment is obtained by taking summation of Eq. (II.10) over index i, and the first order moment is obtained by multiplying Eq. (II.10) by $\mathbf{c}_i$ and taking summation over index i. The zeroth and first order moments of Eq. (II.10) along with Eqs. (II.2) and (II.5) gives us

$$\partial_{\mathrm{t}}^{(1)}\rho + \partial_\alpha^{(1)}(\rho u_\alpha) = \sum_i h_i^{(1)}, \tag{II.12}$$

$$\partial_{\mathrm{t}}^{(1)}(\rho u_\beta) + \partial_\alpha^{(1)}\Pi_{\alpha\beta}^{(0)} = \sum_i c_{i\beta} h_i^{(1)}, \tag{II.13}$$

respectively. $\Pi^{(0)}_{\alpha\beta}$ in Eq. (II.13) is the zeroth order stress tensor, and using Eq. (3.22) it can be expressed in term of hydrodynamic variables [58]

$$\Pi^{(0)}_{\alpha\beta} \equiv \sum_i c_{i\alpha} c_{i\beta} f_i^{(0)} = \rho \left(c_s^2 \delta_{\alpha\beta} + u_\alpha u_\beta \right). \tag{II.14}$$

Using Eq. (II.14) in Eq. (II.13) gives us

$$\partial_{\mathrm{t}}^{(1)}(\rho u_\beta) + \partial_\alpha^{(1)}(\rho u_\alpha u_\beta) = -\partial_\beta(c_s^2 \rho) + \sum_i c_{i\beta} h_i^{(1)}, \tag{II.15}$$

Eq. (II.12) gives us the density change in convective time scale. In order to estimate the density change in diffusive time scale, we take the zeroth moment of Eq. (II.11)

$$\begin{aligned}
&\delta t \Big(\partial_{\mathrm{t}}^{(2)} \sum_i f_i^{(0)} + \partial_{\mathrm{t}}^{(1)} \sum_i f_i^{(1)} + \partial_\alpha^{(1)} \sum_i c_{i\alpha} f_i^{(1)} \Big) \\
&+ \frac{(\delta t)^2}{2} \Big(\partial_{\mathrm{t}}^{(1)} \partial_{\mathrm{t}}^{(1)} \sum_i f_i^{(0)} + \partial_\alpha^{(1)} \partial_\beta^{(1)} \sum_i c_{i\alpha} c_{i\beta} f_i^{(0)} + 2 \partial_{\mathrm{t}}^{(1)} \partial_\alpha^{(1)} \sum_i c_{i\alpha} f_i^{(0)} \Big) \\
&= -\frac{1}{\tau} \sum_i f_i^{(2)} + \delta t \sum_i h_i^{(2)} + \frac{(\delta t)^2}{2} \Big(\partial_{\mathrm{t}}^{(1)} \sum_i h_i^{(1)} + \partial_\alpha^{(1)} \sum_i c_{i\alpha} h_i^{(1)} \Big).
\end{aligned}$$

Using Eqs. (II.5), (II.2) and (II.14) we get

$$\begin{aligned}
&\partial_{\mathrm{t}}^{(2)} \rho + \frac{\delta t}{2} \left(\partial_{\mathrm{t}}^{(1)} \partial_{\mathrm{t}}^{(1)} \rho + \partial_\alpha^{(1)} \partial_\beta^{(1)} \Pi^{(0)}_{\alpha\beta} + 2 \partial_{\mathrm{t}}^{(1)} \partial_\alpha^{(1)} (\rho u_\alpha) \right) \\
&= \sum_i h_i^{(2)} + \frac{\delta t}{2} \Big(\partial_{\mathrm{t}}^{(1)} \sum_i h_i^{(1)} + \partial_\alpha^{(1)} \sum_i c_{i\alpha} h_i^{(1)} \Big). \\
&\partial_{\mathrm{t}}^{(2)} \rho + \frac{\delta t}{2} \Big(\partial_{\mathrm{t}}^{(1)} \left(\partial_{\mathrm{t}}^{(1)} \rho + \partial_\alpha^{(1)} (\rho u_\alpha) \right) + \partial_\alpha^{(1)} \left(\partial_{\mathrm{t}}^{(1)} (\rho u_\alpha) + \partial_\beta^{(1)} \Pi^{(0)}_{\alpha\beta} \right) \Big) \\
&= \sum_i h_i^{(2)} + \frac{\delta t}{2} \Big(\partial_{\mathrm{t}}^{(1)} \sum_i h_i^{(1)} + \partial_\alpha^{(1)} \sum_i c_{i\alpha} h_i^{(1)} \Big).
\end{aligned}$$

Finally using Eq. (II.12) and (II.15) we get

$$\begin{aligned}
&\partial_{\mathrm{t}}^{(2)} \rho + \frac{\delta t}{2} \Big(\partial_{\mathrm{t}}^{(1)} \sum_i h_i^{(1)} + \partial_\alpha^{(1)} \sum_i c_{i\alpha} h_i^{(1)} \Big) \\
&= \sum_i h_i^{(2)} + \frac{\delta t}{2} \Big(\partial_{\mathrm{t}}^{(1)} \sum_i h_i^{(1)} + \partial_\alpha^{(1)} \sum_i c_{i\alpha} h_i^{(1)} \Big).
\end{aligned} \tag{II.16}$$

Rearranging the terms of Eq. (II.16) gives us rate of change of density with the diffusive time scale, i.e.,

$$\partial_{\mathrm{t}}^{(2)}\rho \;=\; \sum_i h_i^{(2)}. \tag{II.17}$$

We assume that the source term h_i^2 does not change the density at the diffusive time scale, i.e.,

$$\sum_i h_i^{(2)} = 0. \tag{II.18}$$

Using the relation ε(II.12)+ ε^2 (II.17) we get

$$\partial_{\mathrm{t}}\rho + \partial_\alpha(\rho u_\alpha) = \varepsilon \sum_i h_i^{(1)} + \varepsilon^2 \sum_i h_i^{(2)}. \tag{II.19}$$

If we choose

$$\varepsilon h_i^{(1)} \;=\; -\frac{w_i \rho u_{\mathrm{r}}}{r}, \tag{II.20}$$

then

$$\sum_i h_i^{(1)} = -\frac{1}{\varepsilon}\frac{\rho u_{\mathrm{r}}}{r}, \tag{II.21a}$$

$$\sum_i c_{i\alpha} h_i^{(1)} = 0, \tag{II.21b}$$

$$\sum_i c_{i\alpha} c_{i\beta} h_i^{(1)} = -c_s^2 \frac{1}{\varepsilon}\frac{\rho u_{\mathrm{r}}}{r}\delta_{\alpha\beta}. \tag{II.21c}$$

Using the Eqs. (II.19), (II.21a) and (II.18) gives us

$$\partial_{\mathrm{t}}\rho + \partial_\alpha(\rho u_\alpha) = -\frac{\rho u_{\mathrm{r}}}{r}. \tag{II.22}$$

Eq. (II.22) is the axisymmetric continuity Eq. (5.1).

Momentum conservation

Similarly, in order to calculate the rate of momentum change with respect to diffusive time scale, we take the first moment of Eq. (II.11)

$$\begin{aligned}
&\delta t\Big(\partial_{\mathrm{t}}^{(2)}\sum_i c_{i\gamma}f_i^{(0)}+\partial_{\mathrm{t}}^{(1)}\sum_i c_{i\gamma}f_i^{(1)}+\partial_\alpha^{(1)}\sum_i c_{i\alpha}c_{i\gamma}f_i^{(1)}\Big)\\
&\quad+\frac{(\delta t)^2}{2}\Big(\partial_{\mathrm{t}}^{(1)}\partial_{\mathrm{t}}^{(1)}\sum_i c_{i\gamma}f_i^{(0)}+\partial_\alpha^{(1)}\partial_\beta^{(1)}\sum_i c_{i\alpha}c_{i\beta}c_{i\gamma}f_i^{(0)}\\
&+2\partial_{\mathrm{t}}^{(1)}\partial_\alpha^{(1)}\sum_i c_{i\alpha}c_{i\gamma}f_i^{(0)}\Big)=-\frac{1}{\tau}\sum_i c_{i\gamma}f_i^{(2)}+\delta t\ \sum_i c_{i\gamma}h_i^{(2)}\\
&\quad+\frac{(\delta t)^2}{2}\Big(\partial_{\mathrm{t}}^{(1)}\sum_i c_{i\gamma}h_i^{(1)}+\frac{\delta t}{2}\partial_\alpha^{(1)}\sum_i c_{i\gamma}c_{i\alpha}h_i^{(1)}\Big),
\end{aligned}\tag{II.23}$$

using Eqs. (II.2), (II.5) and (II.21a) we get

$$\begin{aligned}
&\partial_{\mathrm{t}}^{(2)}(\rho u_\gamma)+\partial_\alpha^{(1)}\Pi_{\alpha\gamma}^{(1)}+\frac{\delta t}{2}\Big(\partial_{\mathrm{t}}^{(1)}\partial_{\mathrm{t}}^{(1)}(\rho u_\gamma)+\partial_\alpha^{(1)}\partial_\beta^{(1)}P_{\alpha\beta\gamma}^{(0)}\\
&\quad+2\partial_{\mathrm{t}}^{(1)}\partial_\alpha^{(1)}\Pi_{\alpha\gamma}^{(0)}\Big)=\sum_i c_{i\gamma}h_i^{(2)}-c_s^2\frac{1}{\varepsilon}\partial_\gamma^{(1)}\Big(\frac{\rho u_{\mathrm{r}}}{r}\Big),
\end{aligned}\tag{II.24}$$

where

$$P_{\alpha\beta\gamma}^{(0)}\equiv\sum_i c_{i\alpha}c_{i\beta}c_{i\gamma}f_i^{(0)},\tag{II.25}$$

$$\Pi_{\alpha\gamma}^{(1)}\equiv\sum_i c_{i\alpha}c_{i\gamma}f_i^{(1)}.\tag{II.26}$$

Using Eq. (3.22) and (II.1) in Eq. (II.25) we get

$$\begin{aligned}
P_{\alpha\beta\gamma}^{(0)}&=\frac{1}{c_s^2}\sum_i w_i c_{i\alpha}c_{i\beta}c_{i\gamma}c_{i\delta}(\rho u_\delta)\\
&=c_s^2\Big(\delta_{\alpha\beta}(\rho u_\gamma)+\delta_{\beta\gamma}(\rho u_\alpha)+\delta_{\alpha\gamma}(\rho u_\beta)\Big),
\end{aligned}\tag{II.27}$$

and Eq. (II.10) in Eq. (II.26) gives

$$\begin{aligned}
\Pi_{\alpha\gamma}^{(1)}&=\delta t\ \tau\sum_i c_{i\alpha}c_{i\gamma}\left(h_i^{(1)}-c_{i\delta}\partial_\delta^{(1)}f_i^{(0)}-\partial_{\mathrm{t}}^{(1)}f_i^{(0)}\right)\\
&=\delta t\ \tau\sum_i c_{i\alpha}c_{i\gamma}h_i^{(1)}-\delta t\ \tau\left(\partial_\delta^{(1)}P_{\alpha\gamma\delta}^{(0)}+\partial_{\mathrm{t}}^{(1)}\Pi_{\alpha\gamma}^{(0)}\right).
\end{aligned}\tag{II.28}$$

Substituting Eqs. (II.15) and (II.28) in (II.24) and rearranging gives

$$\begin{aligned}&\partial_{\mathrm{t}}^{(2)}(\rho u_\gamma) - \delta t\left(\tau - \frac{1}{2}\right)\left(\partial_\alpha^{(1)}\partial_\delta^{(1)}P_{\alpha\gamma\delta}^{(0)} + \partial_{\mathrm{t}}^{(1)}\partial_\alpha^{(1)}\Pi_{\alpha\gamma}^{(0)}\right)\\ &= c_s^2\frac{1}{\varepsilon}\delta t\left(\tau - \frac{1}{2}\right)\partial_\gamma^{(1)}\Big(\frac{\rho u_{\mathrm{r}}}{r}\Big) + \sum_i c_{i\gamma}h_i^{(2)}.\end{aligned} \tag{II.29}$$

In order to obtain the NS Eqs. (5.2) from the lattice Boltzmann Eq. (5.4) it is necessary that the hydrodynamic velocity satisfies the low Mach number, Ma condition i.e. $O(\mathrm{Ma}^3)$ terms are very small and can be neglected from the Eq. (II.29). For the LB method the Mach number is defined as $\mathrm{Ma} = u/c_s$, where u is the characteristic hydrodynamic velocity and c_s is the speed of sound in LB method. The third order velocity appears only in the expression $\partial_{\mathrm{t}}^{(1)}\partial_\alpha^{(1)}\Pi_{\alpha\gamma}^{(0)}$ in Eq. (II.29):

$$\begin{aligned}\partial_{\mathrm{t}}^{(1)}\partial_\alpha^{(1)}\Pi_{\alpha\gamma}^{(0)} &= \partial_{\mathrm{t}}^{(1)}\left(\partial_\alpha^{(1)}\Pi_{\alpha\gamma}^{(0)}\right)\\ &= \partial_{\mathrm{t}}^{(1)}\left(\partial_\alpha^{(1)}\left(\rho u_\alpha u_\gamma + c_s^2\rho\delta_{\alpha\gamma}\right)\right)\\ &= \partial_{\mathrm{t}}^{(1)}\partial_\alpha^{(1)}(\rho u_\alpha u_\gamma) + c_s^2\partial_\gamma^{(1)}(\partial_{\mathrm{t}}^{(1)}\rho)\\ &= \partial_\alpha^{(1)}\Big(\partial_{\mathrm{t}}^{(1)}(\rho u_\alpha)u_\gamma + \partial_{\mathrm{t}}^{(1)}(\rho u_\gamma)u_\alpha\\ &\quad - (\partial_{\mathrm{t}}^{(1)}\rho)u_\alpha u_\gamma\Big) + c_s^2\partial_\gamma^{(1)}(\partial_{\mathrm{t}}^{(1)}\rho).\end{aligned}$$

Using Eqs. (II.12), (II.15) and (II.21a) we get

$$
\begin{aligned}
&\partial_{\mathrm{t}}^{(1)}\partial_{\alpha}^{(1)}\Pi_{\alpha\gamma}^{(0)} \\
&= -\partial_{\alpha}^{(1)}\Big((\partial_{\mathrm{t}}^{(1)}\rho)u_\alpha u_\gamma + u_\gamma\partial_{\beta}^{(1)}\Pi_{\alpha\beta}^{(0)} + u_\alpha\partial_{\beta}^{(1)}\Pi_{\gamma\beta}^{(0)}\Big) \\
&\quad - c_s^2\partial_{\gamma}^{(1)}\Big(\partial_{\beta}^{(1)}(\rho u_\beta) + \frac{1}{\varepsilon}\frac{\rho u_{\mathrm{r}}}{r}\Big) \\
&= -\partial_{\alpha}^{(1)}\Big((\partial_{\mathrm{t}}^{(1)}\rho)u_\alpha u_\gamma + u_\gamma\partial_{\beta}^{(1)}\Big(\rho u_\alpha u_\beta + c_s^2\rho\delta_{\alpha\beta}\Big) \\
&\quad + u_\alpha\partial_{\beta}^{(1)}\Big(\rho u_\gamma u_\beta + c_s^2\rho\delta_{\gamma\beta}\Big)\Big) \\
&\quad - c_s^2\partial_{\gamma}^{(1)}\Big(\partial_{\beta}^{(1)}(\rho u_\beta) + \frac{1}{\varepsilon}\frac{\rho u_{\mathrm{r}}}{r}\Big) \\
&= -\partial_{\alpha}^{(1)}\Big((\partial_{\mathrm{t}}^{(1)}\rho)u_\alpha u_\gamma + u_\gamma\partial_{\beta}^{(1)}(\rho u_\alpha u_\beta) + u_\alpha\partial_{\beta}^{(1)}(\rho u_\gamma u_\beta) \\
&\quad + c_s^2\Big(u_\gamma(\partial_{\alpha}^{(1)}\rho) + u_\alpha(\partial_{\gamma}^{(1)}\rho)\Big)\Big) \\
&\quad - c_s^2\partial_{\gamma}^{(1)}\Big(\partial_{\beta}^{(1)}(\rho u_\beta) + \frac{1}{\varepsilon}\frac{\rho u_{\mathrm{r}}}{r}\Big).
\end{aligned}
$$

Neglecting the terms $u_\alpha\partial_{\beta}^{(1)}(\rho u_\beta u_\gamma)$, $(\partial_{\mathrm{t}}^{(1)}\rho)u_\alpha u_\gamma$ and $u_\gamma\partial_{\beta}^{(1)}(\rho u_\beta u_\alpha)$ ($O(Ma^3)$ terms) from the last equation we get

$$
\begin{aligned}
\partial_{\mathrm{t}}^{(1)}\partial_{\alpha}^{(1)}\Pi_{\alpha\gamma}^{(0)} = &-c_s^2\partial_{\alpha}^{(1)}\Big(u_\gamma(\partial_{\alpha}^{(1)}\rho) + u_\alpha(\partial_{\gamma}^{(1)}\rho)\Big) \\
&- c_s^2\partial_{\gamma}^{(1)}\Big(\partial_{\beta}^{(1)}(\rho u_\beta) + \frac{1}{\varepsilon}\frac{\rho u_{\mathrm{r}}}{r}\Big).
\end{aligned}
\tag{II.30}
$$

Hence using Eqs. (II.27) and (II.30), the second term on L.H.S. of Eq. (II.29) becomes

$$
\begin{aligned}
&\partial_{\alpha}^{(1)}\partial_{\delta}^{(1)}P_{\alpha\gamma\delta}^{(0)} + \partial_{\mathrm{t}}^{(1)}\partial_{\alpha}^{(1)}\Pi_{\alpha\gamma}^{(0)} \\
&= c_s^2\Big(\partial_{\delta}^{(1)}\partial_{\delta}^{(1)}(\rho u_\gamma) + 2\partial_{\delta}^{(1)}\partial_{\gamma}^{(1)}(\rho u_\delta)\Big) - c_s^2\partial_{\alpha}^{(1)}\Big(u_\gamma(\partial_{\alpha}^{(1)}\rho) \\
&+ u_\alpha(\partial_{\gamma}^{(1)}\rho) + \partial_{\gamma}^{(1)}(\rho u_\beta)\Big) - c_s^2\frac{1}{\varepsilon}\partial_{\gamma}^{(1)}\Big(\frac{\rho u_{\mathrm{r}}}{r}\Big),
\end{aligned}
$$

rearranging the terms we get

$$\begin{aligned}
&\partial_\alpha^{(1)}\partial_\delta^{(1)}P^{(0)}_{\alpha\gamma\delta}+\partial_{\mathrm{t}}^{(1)}\partial_\alpha^{(1)}\Pi^{(0)}_{\alpha\gamma}\\
&=c_s^2\Big(\partial_\delta^{(1)}\partial_\delta^{(1)}(\rho u_\gamma)+2\partial_\delta^{(1)}\partial_\gamma^{(1)}(\rho u_\delta)-\partial_\beta^{(1)}(u_\gamma\partial_\alpha^{(1)}\rho)\\
&\quad-\partial_\beta^{(1)}(u_\alpha\partial_\gamma^{(1)}\rho)-\partial_\beta^{(1)}\partial_\gamma^{(1)}(\rho u_\beta)\Big)-c_s^2\frac{1}{\varepsilon}\partial_\gamma^{(1)}\Big(\frac{\rho u_{\mathrm{r}}}{r}\Big)\\
&=c_s^2\Big(\partial_\delta^{(1)}\partial_\delta^{(1)}(\rho u_\gamma)+\partial_\delta^{(1)}\partial_\gamma^{(1)}(\rho u_\delta)\\
&\quad-\partial_\beta^{(1)}(u_\gamma\partial_\alpha^{(1)}\rho)-\partial_\beta^{(1)}(u_\alpha\partial_\gamma^{(1)}\rho)\Big)-c_s^2\frac{1}{\varepsilon}\partial_\gamma^{(1)}\Big(\frac{\rho u_{\mathrm{r}}}{r}\Big)\\
&=c_s^2\left(\partial_\delta^{(1)}(\rho\partial_\delta^{(1)}u_\gamma)+\partial_\delta^{(1)}(\rho\partial_\gamma^{(1)}u_\delta)\right)-c_s^2\frac{1}{\varepsilon}\partial_\gamma^{(1)}\Big(\frac{\rho u_{\mathrm{r}}}{r}\Big).
\end{aligned}\tag{II.31}$$

Substituting Eq. (II.31) back in to Eq. (II.29) gives us

$$\begin{aligned}
&\partial_{\mathrm{t}}^{(2)}(\rho u_\gamma)-c_s^2\delta t\left(\tau-\frac{1}{2}\right)\left(\partial_\delta^{(1)}(\rho\partial_\delta^{(1)}u_\gamma)+\partial_\delta^{(1)}(\rho\partial_\gamma^{(1)}u_\delta)\right)\\
&+c_s^2\frac{1}{\varepsilon}\delta t\left(\tau-\frac{1}{2}\right)\partial_\gamma^{(1)}\Big(\frac{\rho u_{\mathrm{r}}}{r}\Big)\\
&=c_s^2\frac{1}{\varepsilon}\delta t\left(\tau-\frac{1}{2}\right)\partial_\gamma^{(1)}\Big(\frac{\rho u_{\mathrm{r}}}{r}\Big)+\sum_i c_{i\gamma}h_i^{(2)}.
\end{aligned}\tag{II.32}$$

Using Eqs. (II.21a) and rearranging we get

$$\begin{aligned}
\partial_{\mathrm{t}}^{(2)}(\rho u_\gamma) &= c_s^2\delta t\left(\tau-\frac{1}{2}\right)\partial_\delta^{(1)}\Big(\rho\Big(\partial_\delta^{(1)}u_\gamma+\partial_\gamma^{(1)}u_\delta\Big)\Big)\\
&\quad+\sum_i c_{i\gamma}h_i^{(2)}.
\end{aligned}\tag{II.33}$$

Using relation ε (II.15) + ε^2 (II.33) along with Eq. (II.3) we get

$$\begin{aligned}
&\partial_{\mathrm{t}}(\rho u_\gamma)+\partial_\alpha(\rho u_\alpha u_\gamma)=-\partial_\gamma(c_s^2\rho)\\
&+c_s^2\delta t\left(\tau-\frac{1}{2}\right)\partial_\delta\Big(\rho\Big(\partial_\delta u_\gamma+\partial_\gamma u_\delta\Big)\Big)+\varepsilon^2\sum_i c_{i\gamma}h_i^{(2)}.
\end{aligned}\tag{II.34}$$

If we define $\nu=c_s^2\delta t(\tau-0.5)$ and $p=c_s^2\rho$ Eq. (II.34) becomes

$$\begin{aligned}
\partial_{\mathrm{t}}(\rho u_\gamma)+\partial_\alpha(\rho u_\alpha u_\gamma) &= -\partial_\gamma p+\nu\partial_\delta\Big(\rho\Big(\partial_\delta u_\gamma+\partial_\gamma u_\delta\Big)\Big)\\
&\quad+\varepsilon^2\sum_i c_{i\gamma}h_i^{(2)}.
\end{aligned}\tag{II.35}$$

Eq. (II.35) represents the axisymmetric NS equations if the source term $h_i^{(2)}$ satisfies the following conditions :

$$\varepsilon^2 \sum_i c_{i\mathrm{r}} h_i^{(2)} = 2\mu\partial_{\mathrm{r}}\Big(\frac{u_{\mathrm{r}}}{r}\Big) - \frac{\rho u_{\mathrm{r}}^2}{r}, \tag{II.36}$$

$$\varepsilon^2 \sum_i c_{i\mathrm{z}} h_i^{(2)} = \frac{\mu}{r}(\partial_{\mathrm{r}} u_z + \partial_{\mathrm{z}} u_{\mathrm{r}}) - \frac{\rho u_{\mathrm{r}} u_z}{r}. \tag{II.37}$$

Finally we summarize the conditions on $h_i^{(1)}$ and $h_i^{(2)}$ that give us axisymmetric NS equations in the long wavelength and small Mach number limit:

$$\sum_i h_i^{(1)} = -\frac{1}{\varepsilon}\frac{\rho u_{\mathrm{r}}}{r},$$

$$\sum_i c_{i\mathrm{r}} h_i^{(1)} = 0, \qquad \sum_i c_{i\mathrm{z}} h_i^{(1)} = 0,$$

and

$$\sum_i h_i^{(2)} = 0,$$

$$\sum_i c_{i\mathrm{r}} h_i^{(2)} = \frac{1}{\varepsilon^2}\Big(2\mu\partial_{\mathrm{r}}\Big(\frac{u_{\mathrm{r}}}{r}\Big) - \frac{\rho u_{\mathrm{r}}^2}{r}\Big),$$

$$\sum_i c_{i\mathrm{z}} h_i^{(2)} = \frac{1}{\varepsilon^2}\Big(\frac{\mu}{r}(\partial_{\mathrm{r}} u_z + \partial_{\mathrm{z}} u_{\mathrm{r}}) - \frac{\rho u_{\mathrm{r}} u_z}{r}\Big),$$

hence

$$\begin{aligned} h_i &= \varepsilon h_i^{(1)} + \varepsilon^2 h_i^{(2)}, \\ &= w_i\Big(-\frac{\rho u_{\mathrm{r}}}{r} + \frac{1}{c_s^2}(c_{i\mathrm{z}} H_{\mathrm{z}} + c_{i\mathrm{r}} H_{\mathrm{r}})\Big), \end{aligned}$$

which is the same as Eq. (5.6). This concludes our Chapman Enskog expansion procedure to obtain the axisymmetric NS equations from modified LB equation We do not impose any additional condition on ρ.

Bibliography

[1] A. Pimpin and W. Srituravanich. Review on Micro- and Nanolithography Techniques and their Applications, 2012. Cited on pages 1 and 2.

[2] B. J. Lin. Optical lithography-present and future challenges. *Comptes Rendus Physique*, 7(8):858–874, October 2006. Cited on page 2.

[3] M. Switkes and M. Rothschild. Resolution enhancement of 157-nm lithography by liquid immersion, 2002. Cited on page 2.

[4] B. Wu and A. Kumar. Extreme ultraviolet lithography: A review. *Journal of Vacuum Science & Technology B: Microelectronics and Nanometer Structures*, 25(6):1743, 2007. Cited on page 2.

[5] K. G. Winkels. *Fast contact line motion : fundamentals and applications*. PhD thesis, University of Twente, Enschede, 2013. Cited on page 3.

[6] C. W. J. Berendsen. *Controlled deformation, rupture and dewetting of thin liquid films on partially-wetting substrates*. PhD thesis, Eindhoven University of Technology, November 2013. Cited on page 3.

[7] I. M. Hutchings and G. D. Martin. *Inkjet Technology for Digital Fabrication*. Wiley, 2012. Cited on pages 3 and 111.

[8] H. Wijshoff. The dynamics of the piezo inkjet printhead operation. *Physics Reports*, 491(4-5):77–177, June 2010. Cited on pages 3, 4, 89, 104, 111, and 115.

[9] X. Shan and H. Chen. Lattice Boltzmann model for simulating flows with multiple phases and components. *Physical Review E*, 47(3):1815–1819, March 1993. Cited on pages 4, 9, 27, 35, 36, 42, 64, 90, 91, 101, 112, 125, and 164.

[10] X. Shan and H. Chen. Simulation of nonideal gases and liquid-gas phase transitions by the lattice Boltzmann equation. *Physical Review E*,

49(4):2941–2948, April 1994. Cited on pages 4, 27, 42, 43, 45, 46, 64, 90, 91, 99, 100, and 164.

[11] T. S. Chan, S. Srivastava, A. Marchand, B. Andreotti, L. Biferale, F. Toschi, and J. H. Snoeijer. Hydrodynamics of air entrainment by moving contact lines. *Physics of Fluids*, 25(7):074105, March 2013. Cited on pages 5, 23, and 27.

[12] L. D. Landau and E. M. Lifshitz. *Fluid Mechanics*, volume 6. Pergamon Press, October 1959. Cited on pages 7, 8, and 12.

[13] P. K. Kundu and I. M. Cohen. *Fluid Mechanics*. Acadmic press, second edi edition, 2002. Cited on pages 7 and 8.

[14] J. S. Rowlinson and B. Widom. *Molecular Theory of Capillarity*. Dover books on chemistry. Clarendon Press, 2002. Cited on pages 9 and 44.

[15] M. C. Sukop and D. T. Thorne. *Lattice Boltzmann modeling: An introduction for geoscientists and engineers*. Springer Verlag, 2006. Cited on pages 9, 10, 38, and 95.

[16] A. Marchand, J. H. Weijs, J. H. Snoeijer, and B. Andreotti. Why is surface tension a force parallel to the interface? *American Journal of Physics*, 79(10):999, 2011. Cited on page 11.

[17] P. G. de Gennes, F. Brochard-Wyart, and D. Quéré. *Capillarity and wetting phenomena: drops, bubbles, pearls, waves*. Springer Verlag, 2004. Cited on pages 12 and 23.

[18] J. H. Snoeijer and B. Andreotti. Moving Contact Lines: Scales, Regimes, and Dynamical Transitions. *Annual Review of Fluid Mechanics*, 45(1):269–292, January 2013. Cited on pages 16 and 75.

[19] D. Bonn, J. Eggers, J. Indekeu, J. Meunier, and E. Rolley. Wetting and spreading. *Reviews of Modern Physics*, 81(2):739–805, May 2009. Cited on pages 16, 17, 25, 69, 70, 72, 75, and 76.

[20] C. Huh and L. E. Scriven. Hydrodynamic model of steady movement of a solid/liquid/fluid contact line. *Journal of Colloid and Interface Science*, 35(1):85–101, January 1971. Cited on pages 17, 18, 25, 64, 69, 70, and 72.

[21] A. Oron, S. G. Bankoff, and S. H. Davis. Long-scale evolution of thin liquid films. *Reviews of Modern Physics*, 69(3):931–980, July 1997. Cited on pages 19, 21, 22, 53, and 70.

[22] J. H. Snoeijer, G. Delon, M. Fermigier, and B. Andreotti. Avoided Critical Behavior in Dynamically Forced Wetting. *Physical Review Letters*, 96(17):174504, May 2006. Cited on pages 19, 53, 54, 68, 70, 78, and 79.

[23] J. H. Snoeijer. Free-surface flows with large slopes: Beyond lubrication theory. *Physics of Fluids*, 18(2):021701, 2006. Cited on pages 19, 23, and 72.

[24] S. J. Weinstein and K. J. Ruschak. Coating Flows. *Annual Review of Fluid Mechanics*, 36(1):29–53, January 2004. Cited on page 24.

[25] L. Landau and B. Levich. Dragging of a liquid by a moving plate. *Acta Physicochim. URSS*, 17:42, 1942. Cited on pages 24 and 54.

[26] B. V. Deryaguin. On the thickness of a layer of liquid remaining on the walls of vessels after their emptying, and the theory of the application of photoemulsion after coating on the cine film. *Acta physico-chimica USSR*, 20:349, 1943. Cited on pages 24, 25, and 54.

[27] R. G. Cox. The dynamics of the spreading of liquids on a solid surface. Part 1. Viscous flow. *Journal of Fluid Mechanics*, 168(-1):169, April 2006. Cited on pages 25, 54, 70, 84, and 86.

[28] B. R. Duffy and S. K. Wilson. A third-order differential equation arising in thin-film flows and relevant to Tanner's law. *Applied Mathematics Letters*, 10(3):63–68, 1997. Cited on page 25.

[29] O. V. Voinov. Hydrodynamics of wetting. *Fluid Dynamics*, 11(5):714–721, 1976. Cited on pages 25 and 70.

[30] S. Chen and G. D. Doolen. Lattice Boltzmann Method For Fluid Flows. *Annual Review of Fluid Mechanics*, 30(1):329–364, January 1998. Cited on page 27.

[31] S. Succi. *The Lattice Boltzmann Equation for Fluid Dynamics and Beyond*. Numerical Mathematics and Scientific Computation. Clarendon Press, Oxford, 2001. Cited on pages 27, 38, 39, 40, and 41.

[32] A. J. Briant, P. Papatzacos, and J. M. Yeomans. Lattice Boltzmann simulations of contact line motion in a liquid-gas system. *Philosophical transactions. Series A, Mathematical, physical, and engineering sciences*, 360(1792):485–95, March 2002. Cited on page 27.

[33] A. J. Briant and J. M. Yeomans. Lattice Boltzmann simulations of contact line motion. II. Binary fluids. *Physical Review E*, 69(3):031603, March 2004. Cited on pages 27 and 66.

[34] A. J. Briant, A. J. Wagner, and J. M. Yeomans. Lattice Boltzmann simulations of contact line motion. I. Liquid-gas systems. *Physical Review E*, 69(3):031602, March 2004. Cited on page 27.

[35] M. Sbragaglia, K. Sugiyama, and L. Biferale. Wetting failure and contact line dynamics in a Couette flow. *Journal of Fluid Mechanics*, 614(1986):471, October 2008. Cited on pages 27, 64, 66, and 74.

[36] M. R. Kamali, J. J. J. Gillissen, S. Sundaresan, and H. E. A. van den Akker. Contact line motion without slip in lattice Boltzmann simulations. *Chemical Engineering Science*, 66(14):3452–3458, July 2011. Cited on page 27.

[37] S. Srivastava, P. Perlekar, L. Biferale, M. Sbragaglia, J. H. M. ten Thije Boonkkamp, and F. Toschi. A Study of Fluid Interfaces and Moving Contact Lines Using the Lattice Boltzmann Method. *Communications in Computational Physics*, 13(3):725–740, 2012. Cited on pages 27 and 85.

[38] M. C. Sukop. Lattice Boltzmann method for modeling liquid-vapor interface configurations in porous media. *Water Resources Research*, 40(1):W01509, 2004. Cited on page 27.

[39] U. Aaltosalmi. *Fluid Flow in Porous Media with the Lattice Boltzmann method*. PhD thesis, 2005. Cited on pages 27 and 38.

[40] R. Benzi and S. Succi. Two-dimensional turbulence with the lattice Boltzmann equation. *Journal of Physics A: Mathematical and General*, 23(1):L1–L5, January 1990. Cited on page 27.

[41] S. Succi, R. Benzi, and F. Higuera. The lattice Boltzmann equation: A new tool for computational fluid-dynamics. *Physica D: Nonlinear Phenomena*, 47(1-2):219–230, January 1991. Cited on page 27.

[42] H. Chen, S. Chen, and W. Matthaeus. Recovery of the Navier-Stokes equations using a lattice-gas Boltzmann method. *Physical Review A*, 45(8):R5339–R5342, April 1992. Cited on page 27.

[43] F. Higuera and C. Treviño. Lattice Boltzmann and Spectral Simulations of Nonlinear Stability of Kolmogorov Flows. *Rev. Mex. Fis.*, 40:878, 1994. Cited on page 27.

[44] D. O. Martínez, W. H. Matthaeus, S. Chen, and D. C. Montgomery. Comparison of spectral method and lattice Boltzmann simulations of two-dimensional hydrodynamics. *Physics of Fluids*, 6(3):1285, 1994. Cited on page 27.

[45] Y. H. Qian, S. Succi, and S. A. Orszag. Recent advances in lattice Boltzmann computing. *Annu. Rev. Comput. Phys*, 3:195, 1995. Cited on page 27.

[46] R. Benzi, M. V. Struglia, and R. Tripiccione. Extended self-similarity in numerical simulations of three-dimensional anisotropic turbulence. *Physical Review E*, 53(6):R5565–R5568, June 1996. Cited on page 27.

[47] D. Qian, J. B. McLaughlin, K. Sankaranarayanan, S. Sundaresan, and K. Kontomaris. Simulation of Bubble Breakup Dynamics in Homogeneous Turbulence. *Chemical Engineering Communications*, 193(8):1038–1063, August 2006. Cited on page 27.

[48] P. Perlekar, L. Biferale, M. Sbragaglia, S. Srivastava, and F. Toschi. Droplet size distribution in homogeneous isotropic turbulence. *Physics of Fluids*, 24(6):065101, 2012. Cited on page 27.

[49] M. L. Tan, Y. H. Qian, I Goldhirsch, and S. A. Orszag. Lattice-BGK approach to simulating granular flows. *Journal of Statistical Physics*, 81(1-2):87–103, October 1995. Cited on page 27.

[50] A. R. Da Silva. *Numerical Studies of Aeroacoustic Aspects of Wind Instruments*. PhD thesis, McGill University Montreal, Quebec, Canada, 2008. Cited on page 27.

[51] E. M. Viggen. The lattice Boltzmann method with applications in acoustics, 2009. Cited on page 27.

[52] S. Palpacelli. *Quantum lattice Boltzmann methods for the linear and nonlinear Schördinger equation in several dimensions*. PhD thesis, Università degli Studi "Roma Tre", 2009. Cited on page 27.

[53] S. Chen, H. Chen, D. Martnez, and W. Matthaeus. Lattice Boltzmann model for simulation of magnetohydrodynamics. *Physical Review Letters*, 67(27):3776–3779, December 1991. Cited on page 27.

[54] D. O. Martínez, S. Chen, and W. H. Matthaeus. Lattice Boltzmann magnetohydrodynamics. *Physics of Plasmas*, 1(6):1850, 1994. Cited on page 27.

[55] K. Huang. *Statistical Mechanics*, volume 8. Wiley Online Library, 1969. Cited on pages 28, 29, 30, and 32.

[56] L. S. Luo. *Lattice-Gas Automata and Lattice Boltzmann Equations for Two-Dimensional Hydrodynamics*. PhD thesis, Georgia Institute of Technology, 1993. Cited on page 29.

[57] C. Cercignani. *The Boltzmann Equation and Its Applications*, volume 67 of *Applied Mathematical Sciences*. Springer New York, New York, NY, 1988. Cited on pages 30 and 32.

[58] D. A. Wolf-Gladrow. *Lattice-gas cellular automata and lattice Boltzmann models: an introduction*. Springer, 2000. Cited on pages 30, 33, 34, 35, 112, 130, 131, and 133.

[59] S. Chapman and T. G. Cowling. *The mathematical theory of non-uniform gases*. Cambridge University Press, second edition, December 1953. Cited on page 30.

[60] P. Lallemand and Li-S. Luo. Theory of the lattice Boltzmann method: Dispersion, dissipation, isotropy, Galilean invariance, and stability. *Physical Review E*, 61(6):6546–6562, June 2000. Cited on pages 31 and 35.

[61] Eugene P. Gross and E. Atlee Jackson. Kinetic Models and the Linearized Boltzmann Equation. *Physics of Fluids*, 2(4):432, 1959. Cited on page 31.

[62] S. Kryszewski and J. Gondek. Eigenvalues of collision operators: Properties and methods of computation. *Physical Review A*, 56(5):3923–3936, November 1997. Cited on page 31.

[63] P. L. Bhatnagar, E. P. Gross, and M. Krook. A Model for Collision Processes in Gases. I. Small Amplitude Processes in Charged and Neutral One-Component Systems. *Physical Review*, 94(3):511–525, May 1954. Cited on pages 31 and 32.

[64] U. Frisch, B. Hasslacher, and Y. Pomeau. Lattice-Gas Automata for the Navier-Stokes Equation. *Physical Review Letters*, 56(14):1505–1508, April 1986. Cited on page 32.

[65] D H Rothman and S Zaleski. *Lattice-Gas Cellular Automata: Simple Models of Complex Hydrodynamics*. Cambridge University Press, 2004. Cited on page 32.

[66] J. D. Sterling and S. Chen. Stability Analysis of Lattice Boltzmann Methods. *Journal of Computational Physics*, 123(1):196–206, January 1996. Cited on page 32.

[67] Randall J LeVeque. *Numerical Methods for Conservation Laws*, volume 57. 1992. Cited on pages 32 and 34.

[68] Z. Guo, C. Zheng, and B. Shi. Discrete lattice effects on the forcing term in the lattice Boltzmann method. *Physical Review E*, 65(4):046308, April 2002. Cited on pages 35, 36, 37, 46, 99, 100, and 101.

[69] H. Huang, M. Krafczyk, and X. Lu. Forcing term in single-phase and Shan-Chen-type multiphase lattice Boltzmann models. *Physical Review E*, 84(4):046710, October 2011. Cited on pages 35 and 100.

[70] A. J. C. Ladd. Numerical simulations of particulate suspensions via a discretized Boltzmann equation. Part 1. Theoretical foundation. *Journal of Fluid Mechanics*, 271:285, April 2006. Cited on page 38.

[71] J. Latt. *Hydrodynamic limit of lattice Boltzmann equations*. PhD thesis, University de Geneve, 2007. Cited on page 38.

[72] Q. Zou and X. He. On pressure and velocity boundary conditions for the lattice Boltzmann BGK model. *Physics of Fluids*, 9(6):1591, 1997. Cited on page 38.

[73] R. Benzi, L. Biferale, M. Sbragaglia, S. Succi, and F. Toschi. Mesoscopic modeling of a two-phase flow in the presence of boundaries: The contact angle. *Physical Review E*, 74(2):021509, August 2006. Cited on pages 42, 45, 46, and 47.

[74] S. Hou, X. Shan, Q. Zou, G. D. Doolen, and W. E. Soll. Evaluation of Two Lattice Boltzmann Models for Multiphase Flows. *Journal of Computational Physics*, 138(2):695–713, December 1997. Cited on page 42.

[75] M. Sbragaglia, R. Benzi, L. Biferale, S. Succi, K. Sugiyama, and F. Toschi. Generalized lattice Boltzmann method with multirange pseudopotential. *Physical Review E*, 75(2):026702, February 2007. Cited on pages 43, 48, 64, and 112.

[76] H. Huang, D. T. Thorne, M. Schaap, and M. C. Sukop. Proposed approximation for contact angles in Shan-and-Chen-type multicomponent multiphase lattice Boltzmann models. *Physical Review E*, 76(6):66701, December 2007. Cited on pages 46 and 64.

[77] H. Li and H. Fang. Hysteresis and Saturation of Contact Angle in Electrowetting on a Dielectric Simulated by the Lattice Boltzmann Method. *Journal of Adhesion Science and Technology*, 26(12-17):1–9, January 2012. Cited on page 48.

[78] K. Connington and T. Lee. A review of spurious currents in the lattice Boltzmann method for multiphase flows. *Journal of Mechanical Science and Technology*, 26(12):3857–3863, January 2013. Cited on page 48.

[79] L. Scarbolo, D. Molin, P. Perlekar, M. Sbragaglia, A. Soldati, and F. Toschi. Unified framework for a side-by-side comparison of different multicomponent algorithms: Lattice Boltzmann vs. phase field model. *Journal of Computational Physics*, 234:263–279, February 2013. Cited on pages 48 and 64.

[80] X. Shan. Analysis and reduction of the spurious current in a class of multiphase lattice Boltzmann models. *Physical Review E*, 73(4):047701, April 2006. Cited on page 48.

[81] Zhaoli Guo, Baochang Shi, and Chuguang Zheng. Chequerboard effects on spurious currents in the lattice Boltzmann equation for two-phase flows. *Philosophical transactions. Series A, Mathematical, physical, and engineering sciences*, 369(1944):2283–91, June 2011. Cited on pages 48, 50, and 64.

[82] B. D. Kandhai. *Large Scale Lattice-Boltzmann Simulations: Computational Methods and Applications*. PhD thesis, University of Amsterdam, 1999. Cited on page 50.

[83] P. G. de Gennes. Wetting: statics and dynamics. *Reviews of modern physics*, 57(3), 1985. Cited on page 53.

[84] T. D. Blake, J. De Coninck, and U. D'Ortona. Models of Wetting: Immiscible Lattice Boltzmann Automata versus Molecular Kinetic Theory. *Langmuir*, 11(11):4588–4592, November 1995. Cited on page 53.

[85] J. G. M. Eggers. Existence of receding and advancing contact lines. *Physics of Fluids*, 17(8):082106, 2005. Cited on page 53.

[86] J. H. Snoeijer, J. Ziegler, B. Andreotti, M. Fermigier, and J. Eggers. Thick Films of Viscous Fluid Coating a Plate Withdrawn from a Liquid Reservoir. *Physical Review Letters*, 100(24):244502, June 2008. Cited on pages 53, 54, and 79.

[87] M. T. Ghannam and M. N. Esmail. Experimental study of the wetting of fibers. *AIChE Journal*, 39(2):361–365, February 1993. Cited on page 53.

[88] R. Golestanian and E. Raphaël. Dissipation in dynamics of a moving contact line. *Physical Review E*, 64(3):031601, August 2001. Cited on page 53.

[89] L. M. Hocking. Meniscus draw-up and draining. *European Journal of Applied Mathematics*, 12(03), August 2001. Cited on page 53.

[90] P. G. de Gennes. Deposition of Langmuir-Blodgett layers. *Colloid & Polymer Science*, 264(5):463–465, May 1986. Cited on page 54.

[91] J. A. Tallmadge. Withdrawal of flat plates from power law fluids. *AIChE Journal*, 16(6):925–930, November 1970. Cited on page 54.

[92] B. M. Deryagin and S. M. Levi. *Film Coating Theory.* Focal Press, London, 1964. Cited on page 54.

[93] A. de Ryck and D. Quéré. Gravity and Inertia Effects in Plate Coating. *Journal of Colloid and Interface Science*, 203(2):278–285, July 1998. Cited on page 54.

[94] O. Ou Ramdane and D. Quéré. Thickening Factor in Marangoni Coating. *Langmuir*, 13(11):2911–2916, May 1997. Cited on page 54.

[95] F. P. Bretherton. The motion of long bubbles in tubes. *Journal of Fluid Mechanics*, 10(02):166, March 1961. Cited on pages 54 and 56.

[96] H. Benkreira and M. I. Khan. Air entrainment in dip coating under reduced air pressures. *Chemical Engineering Science*, 63(2):448–459, January 2008. Cited on pages 54, 55, and 68.

[97] H. Benkreira and J. B. Ikin. Dynamic wetting and gas viscosity effects. *Chemical Engineering Science*, 65(5):1790–1796, March 2010. Cited on pages 54 and 68.

[98] A. Marchand, T. S. Chan, J. H. Snoeijer, and B. Andreotti. Air Entrainment by Contact Lines of a Solid Plate Plunged into a Viscous Fluid. *Physical Review Letters*, 108(20):204501, May 2012. Cited on pages 54, 55, 68, 75, 79, and 86.

[99] C. Duez, C. Ybert, C. Clanet, and L. Bocquet. Making a splash with water repellency. *Nature Physics*, 3(3):180–183, February 2007. Cited on pages 54, 68, 78, and 83.

[100] R. Ledesma-Aguilar, R. Nistal, A. Hernández-Machado, and I. Pagonabarraga. Controlled drop emission by wetting properties in driven liquid filaments. *Nature materials*, 10(5):367–71, May 2011. Cited on pages 54, 68, 78, and 83.

[101] R. Burley and B. S. Kennedy. A study of the dynamic wetting behaviour of polyester tapes. *British Polymer Journal*, 8(4):140–143, December 1976. Cited on page 54.

[102] J. Eggers. Air Entrainment through Free-Surface Cusps. *Physical Review Letters*, 86(19):4290–4293, May 2001. Cited on pages 55 and 86.

[103] É. Lorenceau, F. Restagno, and D. Quéré. Fracture of a Viscous Liquid. *Physical Review Letters*, 90(18):184501, May 2003. Cited on pages 55 and 86.

[104] L. Biferale, P. Perlekar, M. Sbragaglia, S. Srivastava, and F. Toschi. A Lattice Boltzmann method for turbulent emulsions. *Journal of Physics: Conference Series*, 318(5):052017, December 2011. Cited on page 64.

[105] F. Diotallevi, L. Biferale, S. Chibbaro, A. Lamura, G. Pontrelli, M. Sbragaglia, S. Succi, and F. Toschi. Capillary filling using lattice Boltzmann equations: The case of multi-phase flows. *The European Physical Journal Special Topics*, 166(1):111–116, February 2009. Cited on page 64.

[106] T. D. Blake and K. J. Ruschak. Wetting: static and dynamic contact lines. In S F Kistler and P M Schweizer, editors, *Liquid film coating*. London, Chapman and Hall, 1997. Cited on page 68.

[107] J. Eggers. Hydrodynamic Theory of Forced Dewetting. *Physical Review Letters*, 93(9):094502, August 2004. Cited on pages 68, 79, and 86.

[108] R. V. Sedev and J. G. Petrov. The critical condition for transition from steady wetting to film entrainment. *Colloids and Surfaces*, 53(1):147–156, January 1991. Cited on page 68.

[109] D. Quéré. On the minimal velocity of forced spreading in partial wetting (in French). *C. R. Acad. Sci. Paris, Serie II*, 313:313–318, 1991. Cited on page 68.

[110] J. H. Snoeijer, B. Andreotti, G. Delon, and M. Fermigier. Relaxation of a dewetting contact line. Part 1. A full-scale hydrodynamic calculation. *Journal of Fluid Mechanics*, 579:63, May 2007. Cited on pages 68, 79, and 86.

[111] G. Delon, M. Fermigier, J. H. Snoeijer, and B. Andreotti. Relaxation of a dewetting contact line. Part 2. Experiments. *Journal of Fluid Mechanics*, 604:55–75, May 2008. Cited on pages 68, 79, and 86.

[112] T. D. Blake and K. J. Ruschak. A maximum speed of wetting. *Nature*, 282(5738):489–491, November 1979. Cited on page 68.

[113] R. Burley and B. S. Kennedy. An experimental study of air entrainment at a solid/liquid/gas interface. *Chemical Engineering Science*, 31(10):901–911, January 1976. Cited on page 68.

[114] P. G. Simpkins and V. J. Kuck. Air entrapment in coatings by way of a tip-streaming meniscus. *Nature*, 403(6770):641–3, February 2000. Cited on page 68.

[115] J. Eggers. Toward a description of contact line motion at higher capillary numbers. *Physics of Fluids*, 16(9):3491, 2004. Cited on page 72.

[116] A. L. Bertozzi, M. Shearer, and R. Buckingham. Thin Film Traveling Waves and the Navier Slip Condition. *SIAM Journal on Applied Mathematics*, 63(2):722–744, January 2003. Cited on page 73.

[117] E. Rame and S. Garoff. Microscopic and macroscopic dynamic interface shapes and the interpretation of dynamic contact angles. *J. Colloid Interface Sci.*, 177:234–244, 1996. Cited on page 76.

[118] J. Ziegler, J. H. Snoeijer, and J. Eggers. Film transitions of receding contact lines. *The European Physical Journal Special Topics*, 166(1):177–180, February 2009. Cited on page 79.

[119] T. S. Chan, T. Gueudré, and J. H. Snoeijer. Maximum speed of dewetting on a fiber. *Physics of Fluids*, 23(11):112103, 2011. Cited on page 79.

[120] T. S. Chan, J. H. Snoeijer, and J. Eggers. Theory of the forced wetting transition. *Physics of Fluids*, 24(7):072104, 2012. Cited on page 79.

[121] I. Halliday, L. Hammond, C. Care, K. Good, and A. Stevens. Lattice Boltzmann equation hydrodynamics. *Physical Review E*, 64(1):1–8, June 2001. Cited on pages 90, 91, and 92.

[122] T. Reis. *The Lattice Boltzmann Method for Complex Flows*. PhD thesis, School of Mathematics, Cardiff University, UK, 2007. Cited on pages 90, 91, and 92.

[123] H. Huang and Xi-Y. Lu. Theoretical and numerical study of axisymmetric lattice Boltzmann models. *Physical Review E*, 80(1):016701, July 2009. Cited on page 90.

[124] Z. Guo, H. Han, B. Shi, and C. Zheng. Theory of the lattice Boltzmann equation: Lattice Boltzmann model for axisymmetric flows. *Physical Review E*, 79(4):046708, April 2009. Cited on page 90.

[125] Q. Li, Y. L. He, G. H. Tang, and W. Q. Tao. Improved axisymmetric lattice Boltzmann scheme. *Physical Review E*, 81(5):056707, May 2010. Cited on page 90.

[126] S. Chen, J. Tölke, S. Geller, and M. Krafczyk. Lattice Boltzmann model for incompressible axisymmetric flows. *Physical Review E*, 78(4):046703, October 2008. Cited on page 90.

[127] K. N. Premnath and J. Abraham. Lattice Boltzmann model for axisymmetric multiphase flows. *Physical Review E*, 71(5):056706, May 2005. Cited on pages 90 and 91.

[128] S. Mukherjee and J. Abraham. Lattice Boltzmann simulations of two-phase flow with high density ratio in axially symmetric geometry. *Physical Review E*, 75(2):026701, February 2007. Cited on pages 90 and 91.

[129] T. Reis and T. N. Phillips. Modified lattice Boltzmann model for axisymmetric flows. *Physical Review E*, 75(5):056703, May 2007. Cited on pages 91 and 92.

[130] T. Reis and T. N. Phillips. Numerical validation of a consistent axisymmetric lattice Boltzmann model. *Physical Review E*, 77(2):026703, February 2008. Cited on pages 91 and 92.

[131] S. Middleman. *Modeling Axisymmetric Flows: dynamics of films, jets, and drops*. Academic Press, Inc., 1995. Cited on pages 96 and 97.

[132] J. M. Buick and C. A. Greated. Gravity in a lattice Boltzmann model. *Physical Review E*, 61(5):5307–5320, May 2000. Cited on page 100.

[133] C. A. Miller and L. E. Scriven. The oscillations of a fluid droplet immersed in another fluid. *J. Fluid Mech*, 32(03):417–435, March 1968. Cited on pages 101 and 102.

[134] J. A. F. Plateau. *Statique Expérimentale et Théoretique des Liquides Soumis aux Seules Forces Moléculaires*, volume II. Gauthier Villars, Paris, 1873. Cited on pages 103 and 104.

[135] J. W. S. Rayleigh Lord. On the instability of jets. *Proc. R. Soc. London A*, 10(4):4–13, 1879. Cited on pages 103 and 104.

[136] P. Lafrance. Nonlinear breakup of a laminar liquid jet. *Physics of Fluids*, 18(4):428, 1975. Cited on page 104.

[137] S. Tomotika. On the Instability of a Cylindrical Thread of a Viscous Liquid Surrounded by Another Viscous Fluid. *Proceedings of the Royal Society A: Mathematical, Physical and Engineering Sciences*, 150(870):322–337, June 1935. Cited on page 104.

[138] D. F. Rutland and G. J. Jameson. A non-linear effect in the capillary instability of liquid jets. *Journal of Fluid Mechanics*, 46(02):267, March 2006. Cited on pages 104 and 106.

[139] T. Driessen and R. Jeurissen. A regularised one-dimensional drop formation and coalescence model using a total variation diminishing (TVD) scheme on a single Eulerian grid. *International Journal of Computational Fluid Dynamics*, 25(6):333–343, July 2011. Cited on pages 104, 105, 106, and 126.

[140] E. Villermaux. Fragmentation. *Annual Review of Fluid Mechanics*, 39(1):419–446, January 2007. Cited on page 104.

[141] P. Marmottant and E. Villermaux. Fragmentation of stretched liquid ligaments. *Physics of Fluids*, 16(8):2732, 2004. Cited on page 104.

[142] N. Bremond and E. Villermaux. Bursting thin liquid films. *Journal of Fluid Mechanics*, 524:121–130, February 2005. Cited on page 104.

[143] F. Veron, C. Hopkins, E. L. Harrison, and J. A. Mueller. Sea spray spume droplet production in high wind speeds. *Geophysical Research Letters*, 39(16), August 2012. Cited on page 104.

[144] J. Eggers and E. Villermaux. Physics of liquid jets. *Reports on Progress in Physics*, 71(3):036601, March 2008. Cited on page 105.

[145] R. M. S. M. Schulkes. The contraction of liquid filaments. *Journal of Fluid Mechanics*, 309(-1):277, April 2006. Cited on page 105.

[146] H. A. Stone, B. J. Bentley, and L. G. Leal. An experimental study of transient effects in the breakup of viscous drops. *Journal of Fluid Mechanics*, 173(-1):131, April 1986. Cited on page 105.

[147] P. K. Notz and O. A. Basaran. Dynamics and breakup of a contracting liquid filament. *Journal of Fluid Mechanics*, 512, July 2004. Cited on page 105.

[148] J. Eggers and T. F. Dupont. Drop formation in a one-dimensional approximation of the Navier-Stokes equation. *Journal of Fluid Mechanics*, 262(-1):205, April 1994. Cited on pages 105 and 107.

[149] X. D. Shi, M. P. Brenner, and S. R. Nagel. A cascade of structure in a drop falling from a faucet. *Science (New York, N.Y.)*, 265(5169):219–22, July 1994. Cited on page 105.

[150] E. D. Wilkes, S. D. Phillips, and O. A. Basaran. Computational and experimental analysis of dynamics of drop formation. *Physics of Fluids*, 11(12):3577, 1999. Cited on page 105.

[151] W. van Hoeve, S. Gekle, J. H. Snoeijer, M. Versluis, M. P. Brenner, and D. Lohse. Breakup of diminutive Rayleigh jets. *Physics of Fluids*, 22(12):122003, 2010. Cited on page 105.

[152] R. E. Saunders, J. E. Gough, and B. Derby. Delivery of human fibroblast cells by piezoelectric drop-on-demand inkjet printing. *Biomaterials*, 29(2):193–203, January 2008. Cited on page 111.

[153] S. M. Bidoki, J. Nouri, and A. A. Heidari. Inkjet deposited circuit components, 2010. Cited on page 111.

[154] H. Cho, M. Parameswaran, and H.-Zhong Yu. Fabrication of microsensors using unmodified office inkjet printers, 2007. Cited on page 111.

[155] Han-C. Liu, Chia-P. Chuang, Yi-T. Chen, and Chen-H. Du. Inkjet Printing for Silicon Solar Cells. *Water, Air, & Soil Pollution: Focus*, 9:495–498, 2009. Cited on page 111.

[156] A. J. Lennon, R. Y. Utama, M. A.T. Lenio, A. W.Y. Ho-Baillie, N. B. Kuepper, and S. R. Wenham. Forming openings to semiconductor layers of silicon solar cells by inkjet printing, 2008. Cited on page 111.

[157] S. Bruner, D. Xu, and C. Phillips. 54.3: Drop Landing Accuracy Improvements in Inkjet Printed OLED Displays. *SID Symposium Digest of Technical Papers*, 38(1):1611, 2007. Cited on page 111.

[158] H. P. Le. Progress and trends in ink-jet printing technology. *Journal of Imaging Science and Technology*, 42:49–62, 1998. Cited on page 111.

[159] J. R. Womersley. Method for the calculation of velocity, rate of flow and viscous drag in arteries when the pressure gradient is known. *The Journal of physiology*, 1(5):255–60, December 1955. Cited on page 113.

[160] R. J. M. Jeurissen. *Bubbles in inkjet printheads : analytical and numerical models*. PhD thesis, Enschede, October 2009. Cited on page 114.

[161] R. Jeurissen, H. Wijshoff, M. van den Berg, H. Reinten, and D. Lohse. Regimes of bubble volume oscillations in a pipe, 2011. Cited on page 114.

[162] H. N. Oğuz and A. Prosperetti. The natural frequency of oscillation of gas bubbles in tubes. *The Journal of the Acoustical Society of America*, 103(6):3301, June 1998. Cited on page 116.

[163] J. C. Butcher. *Numerical Methods for Ordinary Differential Equations*. John Wiley & Sons, Ltd, Chichester, UK, March 2008. Cited on page 119.

[164] X. He and Li-S. Luo. Lattice Boltzmann Model for the Incompressible Navier-Stokes Equation. *Journal of Statistical Physics*, 88(3/4):927–944, August 1997. Cited on page 119.

[165] S. D. Geschiere, I. Ziemecka, V. van Steijn, G. J. M. Koper, J. H. van Esch, and M. T Kreutzer. Slow growth of the Rayleigh-Plateau instability in aqueous two phase systems. *Biomicrofluidics*, 6(2):22007–2200711, June 2012. Cited on page 122.

[166] J. Hagedorn, N. Martys, and J. Douglas. Breakup of a fluid thread in a confined geometry: droplet-plug transition, perturbation sensitivity, and kinetic stabilization with confinement. *Physical Review E*, 69(5):056312, May 2004. Cited on page 122.

[167] A. D. Angelopoulos, V. N. Paunov, V. N. Burganos, and A. C. Payatakes. Lattice Boltzmann simulation of nonideal vapor-liquid flow in porous media. *Physical Review E*, 57(3):3237–3245, March 1998. Cited on page 122.

[168] S. Srivastava, Prasad Perlekar, Jan H. M. ten Thije Boonkkamp, Nishith Verma, and Federico Toschi. Axisymmetric multiphase lattice Boltzmann method. *Physical Review E*, 88(1):013309, July 2013. Cited on page 125.

[169] S. Srivastava, T. Driessen, R. Jeurissen, H. Wijshoff, and F. Toschi. Lattice Boltzmann Method to Study the Contraction of a Viscous Ligament. *International Journal of Modern Physics C*, 24(12):1340010, July 2013. Cited on page 126.

Summary

Lattice Boltzmann method for contact line dynamics

This PhD project deals with the study of the problems related to the contact line dynamics and moving fluid interfaces. The contact line here is refereed to the common borderline between two immiscible fluids and a solid surface. In our work, we use the lattice Boltzmann (LB) method to study the fundamental aspects of the moving contact line. This project is mainly inspired by two industrial applications: immersion lithography (ASML) and print head of an ink-jet nozzle (Océ), where the moving contact line plays a significant role in various instabilities occurring at the micro scale. Both of these problems involves more then one characteristic length scale and time scales, highly curved fluid interfaces, multiphase flows and complex boundary conditions, which make the analytical or numerical studies for these very challenging. In our study we develop, validate and apply the LB method for the problems related to the contact line motion and the moving interfaces.

From modeling point of view, the problems that involve contact line motion in Immersion lithography and ink-jet nozzle, fall in to a general categories of advancing and receding contact line. For our study, we consider the contact lines and interfaces that are: a) translational symmetric along one of the coordinate axis (2D), and b) axisymmetric.

In Chapter 4, we presented the studies based on the Lattice Boltzmann method and a generalized lubrication model. Our 2D numerical setup consists of a partially wetting smooth plate, vertically immersed in a pool of liquid. Depending on whether the plate is being pulled out or push into the fluid bath, we have dip coating (receding contact line) or plunging plate (advancing contact line) problems, respectively. For the receding contact line study, the gas viscosity is irrelevant. But, for the advancing contact line the second phase must be considered, this makes the study of the problems involving advancing contact lines much more complex. We apply the LB method for both of these problems for the different contact angle, the viscosity ratio and the dimensionless velocity (Capillary number). The different fluid phases and their

contact with the plate are simulated by means of the Shan-Chen model. We found a very good agreement between the LB simulations and the generalized lubrication model (GL) for the different viscosity ratios and the contact angles for small capillary numbers. Furthermore, we found that for the hydrophilic surfaces the matching between the LB method and GL is very good. This validates both the LB and the GL method, and presents the LB method as an effective alternative too for the study of the contact line in motion. We further extended our LB study of the dip-coating problem for: a) the liquid film deposited on the plate above critical capillary number, and b) for estimation of critical capillary number for hydrophobic surfaces.

The second part of this PhD is related to the print head of an ink-jet nozzle. In Chapter 6, we developed the LB model for axisymmetric multiphase flows. The model is an extension of the classic Shan-Chen multiphase model for axisymmetric flows. We benchmarked the model for its accuracy in reproducing the dynamics of the oscillations of an axially symmetric droplet and on the capillary breakup of a viscous liquid thread. Very good quantitative agreement between the numerical solutions and the analytical results is observed.

In Chapter 7, we presented an application of the axisymmetric multiphase lattice Boltzmann method to simulate drop formation in inkjet printers. We showed that given several geometrical and physical constraints, how one could choose the parameters for the lattice Boltzmann simulation. We validate the time varying pressure boundary condition in the LB model and showed that under some geometrical constraints the compressibility effects in the lattice Boltzmann simulations are negligible. We presented the unit conversion procedure, which helps to compare the LB simulation with realistic jetting cases. Finally, we showed a qualitative comparison between the LB and Flow3D simulation for a drop-formation in an inkjet nozzle.

In this work, we used the LB method to study the behavior of the contact line in two different geometrical setups, 2D and axisymmetric. The results from the 2D study contribute in to the validation of the GL model. For the axisymmetric study we developed a numerical tool that is applicable to the industrial problems. The LB study not only provides an alternate to the existing analytical and numerical models and commercial flow solvers, but also gives more insight in to the regimes where the problems are much more challenging. Using LB model as a numerical tool for above problems also reveled some drawback of multiphase/multicomponent Shan-Chen LB model. The range of viscosity ratio and Capillary number restricts the range of applicability of the Shan-Chen model for the case of plunging plate problem. Finite sound speed and dependence of density and surface tension on single parameter in Shan-

Chen model, gives the geometrical restriction in using the axisymmetric LB model for nozzle simulations. The multiphase model used is a diffuse interface method and introduces interface width as an addition parameter in the problem. It is self-evident that some problems are still remaining unsolved, but the LB method certainly provides a meaningful insight and vast applicability to many industrial problems.

Acknowledgments

Like many of those who have been through this path, my PhD has also been a journey with hindrances, lessons and an eventual triumph. I consider myself very lucky to have met people who kept me motivated which kept me going. Without their help and encouragement this work would not have been possible to be in this present shape. In this Chapter, I take the opportunity to express my gratitude to my teachers for their guidance, my collaborators for their scientific discussions and my friends for their wonderful company.

First of all, I would like to thank my supervisor and first promotor Prof. Federico Toschi for giving me the opportunity to do PhD on such an interesting topic. Unarguably he has been the most influential person during my PhD. I am indebted for his guidance, encouragement and trust in me. I am also thankful to him for proving me the financial support during the period of thesis writing. I am thankful to my second promotor and group head Prof. Herman Clercx for his critical evaluation of my work. I am thankful to my co-supervisor Dr. Jan ten Thije Boonkkamp for his critical reading of my thesis and scientific discussions.

I am grateful to my committee members Prof. Detlef Lohse, Prof. Barry Koren, Prof. Luca Biferale, Dr. Jens Harting and Dr. Herman Wijshoff, who have been kind enough to review my thesis.

I am thankful to stichting FOM and industrial partners ASML and Océ for funding this research as part of the industrial partnership program "Contact line control during wetting and dewetting". I found the quarterly project meetings very motivating, since it encouraged me to focus onto the industrial applicability of the research. I am thankful to Anton Darhuber, Hans Reinten, Jos Zeegers, Michel Riepen, Ramin Badie, and all the participants of the project for their useful comments and co-operation. I am also thankful to Martijn de Jager, Pieter de Witte and Maria Teuwissen for taking care of all my administrative matters at FOM.

I am extremely thankful to my co-supervisor Dr. Roger Jeurissen. Although he was officially supposed to supervise me once a week for the Océ

project, yet I have never been refused for any kind of scientific query or discussion at any time. My sincere thanks goes to Dr. Prasad Perlekar who helped me in the initial phases of my PhD. I definitely learned many things from him.

I would like to thank Luca Biferale, Jacco Snoeijer, Mauro Sbragaglia and Nishit Verma for their valuable comments and many interesting scientific discussions during my PhD. I would also like to thank Tak Shing Chan, Theo Driessen, Calin Dan for their collaborations in Chapters 4 and 5 of this thesis. I am also thankful to Sebastian and Florian for helping me with server issues and many interesting scientific and nonscientific discussions. I can not recall even a single instance when I have asked them a question and I have been refused help.

I thank to all the colleagues and friends at WDY, MTP, CASA group, and those who I met during my stay in Eindhoven for their wonderful company. I am also thankful to Marjan, Brigitte and Enna for taking care of my administrative matters at WDY, MTP and CASA.

I am thankful to Badr, Eugen, Inga, Kristina, Kundan, Manohar, Marta, Maxim, Nidhi, Qihong, Theo, Valeriu, and Yogesh for many many nice evenings consisting of tasty dinners, movies, trips, and tennis sessions. I will cherish the time spent in their company for the rest of my life.

Last but not least, I would like to thank my family for their love and affection. I am thankful to my parents for giving me full independence to take my own decisions and supporting it all the way. I humbly bow before my parents and dedicate this thesis to them.

Sudhir Srivastava
Eindhoven, Febrauary 2014

Curriculum Vitae

Sudhir Srivastava was born on 03-08-1982 in Bahraich, India. After finishing schooling in 1999 at S. M. B. Gita Sen. Sec. School in Kurukshetra, India, he pursued the Bachelor of Science in Physics and Mathematics at Dr. R. M. L Avadh University Faizabad, India. He studied Applied Mathematics at Indian Institute of Technology, Madras in Chennai, India. Subsequent to his master studies in India, he was awarded Erasmus Mundus scholarship from European Commission to pursue Double degree program at Johannes Kepler University Linz, Austria and at Eindhoven University of Technology, The Netherlands. In 2009 he graduated within the Department of Mathematics and Computer Science on Industrial Mathematics. From 2009 he started a PhD project at Eindhoven University of Technology at Eindhoven, The Netherlands, the results of which are presented in this dissertation.

Cover illustration

Snapshot of a 2D lattice Boltzmann simulation using the Shan-Chen multiphase model [9, 10]. The flow domain includes two wetting rectangular blocks ($\theta_{\mathrm{e}} = 0°$). Simulation parameters in lattice units (LU): $N_{\mathrm{x}} \times N_{\mathrm{y}} = 2432 \times 1420$, $G_{\mathrm{sc}} = -4.5$, $R_{\mu} = 0.17$, $\gamma = 0.0215$ and $g = 2 \times 10^{-5}$ is acting from left to right. Initially drops are generated at random spatial position (one drop in each 100×100 LU) with their radii varying from 40 to 100 LU. Photoshop has been used for the data rendering.